

**The Synthesis and Tunable Processing of Magnetic and Metallic Nanoparticles in a Functional Solvent System**

by

Jennifer Nichole Duggan

A dissertation submitted to the Graduate Faculty of  
Auburn University  
in partial fulfillment of the  
requirements for the Degree of  
Doctor of Philosophy

Auburn, Alabama  
May 4, 2014

Keywords: Nanoparticle Synthesis, Controlled Aggregation, Dimethyl Sulfoxide, Functional Solvent, Oxidation, Gas-Expanded Liquids

Copyright 2014 by Jennifer Nichole Duggan

Approved by

Christopher B. Roberts, Chair, Dean of Engineering  
Steve R. Duke, Associate Dean for Academics  
Mario R. Eden, Professor of Chemical Engineering  
Bart Prorok, Professor of Materials Engineering  
Michael Bozack, Professor of Physics

## Abstract

The concepts presented in this dissertation describe techniques that have been developed to produce metallic and magnetic nanoparticles using dimethyl sulfoxide (DMSO). The unique and size-dependent properties of nanoparticles require development of sustainable production techniques that allow for fine control over particle size and morphology. Typical methods that are used to produce specifically-sized nanoparticles involve either tedious synthesis methods or extensive post-synthesis processing. In addition, these methods often require the use of expensive solvents and reagents, produce significant amounts of waste, and are time-intensive. One way to simplify and improve nanoparticle synthesis is to develop a method that uses a single molecule “functional solvent” for both nanoparticle solvation and nanoparticle stabilization. Previously, it has been shown that DMSO can provide sufficient surface coverage and solvation of noble metal palladium nanoparticles via interactions involving the sulfur and oxygen moieties of the DMSO molecule. The studies outlined in this dissertation explore the production of magnetic cobalt nanoparticles and metallic gold nanoparticles using simple and sustainable synthesis techniques which employ the use of a DMSO functional solvent.

Magnetic nanoparticles can become overly oxidized and unstable during synthesis, ultimately leading to nanoparticle agglomeration and degradation. Popular methods typically employed to prevent excessive oxidation and agglomeration involve adding ligands during nanoparticle synthesis that attach directly to the particle surface to

provide particle surface coverage and improve nanoparticle dispersibility in solution. However, this dissertation contains a technique for the synthesis of amorphous  $3.7 \pm 1.5$  nm magnetic cobalt nanoparticles using DMSO as a functional solvent via a quick, solvent-based reduction of  $\text{Co}^{2+}$  with  $\text{NaBH}_4$  in a DMSO solvent. The DMSO functional solvent adsorbs to the cobalt nanoparticle surface via the sulfoxide functional group (particularly the oxygen component), thereby protecting the particle from excessive oxidation. Furthermore, the effects of synthesis temperature on cobalt nanoparticle size and stability are investigated using DMSO as a functional solvent. High synthesis temperature was found to induce the aggregation of 3.7 nm cobalt nanoparticles into 20 nm clusters, likely by weakening the interaction between DMSO and the cobalt nanoparticles. Co-solvent addition to the clusters was found to liberate the individual cobalt nanoparticles within the clusters and allow them to re-disperse into the solution. The thermal oxidation of the aforementioned amorphous cobalt nanoparticles are also investigated by annealing the particles in air up to  $800^\circ\text{C}$ . Upon annealing, the amorphous cobalt nanoparticles transition into ordered structures of spinel- $\text{Co}_3\text{O}_4$  nanoparticles. These  $\text{Co}_3\text{O}_4$  particles exhibit very unique magnetic properties, such as an increase in coercivity as a function of the annealing temperature.

Previous work has demonstrated that gas expanded liquid technology can be utilized for the controlled precipitation of non-polar, aliphatic, ligand-stabilized gold nanoparticles from conventional non-polar organic solvents (e.g., aliphatic hydrocarbons) by exploiting the pressure-tunable, physico-chemical properties of the mixture. Central to the research presented in this dissertation,  $\text{CO}_2$  can diffuse into DMSO to create a  $\text{CO}_2$ -gas expanded liquid. The dispersibility of gold nanoparticles in various  $\text{CO}_2$ -gas

expanded DMSO solvent systems is investigated and described in this dissertation. Contrary to the aliphatic ligand-stabilized nanoparticles in organic solvents, the dispersibility of gold nanoparticles in CO<sub>2</sub>-gas expanded DMSO is drastically different. Gold nanoparticles can be clustered within the DMSO+CO<sub>2</sub> mixture as a function of pressure, and, after a certain transition pressure is reached, the nanoparticle clusters become destabilized and precipitate from the solution as a function of time.

In essence, the research presented in this dissertation demonstrates that noble metal and magnetic nanoparticles can be synthesized and subsequently processed using a single molecule, DMSO, to function concomitantly as the solvent and the stabilizing ligand. Ultimately, the development of these simple, fast, and efficient nanoparticle production techniques is an important step in the evolution of nanoparticle engineering.

## Acknowledgments

First of all, I must thank my advisor, Dr. Christopher Roberts, for believing in me and giving me a chance at Auburn and in his research group. Dr. Roberts has taught me how to be patient and focused on my goals, and he has always been so supportive of all of the activities I have been involved in (both inside and outside of the lab) at Auburn. I am especially grateful that Dr. Roberts gave me the freedom and independence to work on my research project, and for helping me make the most out of my research experience. I cannot thank Dr. Roberts enough for all of the advice over the years, and the countless hours he has spent with me. I feel so lucky to have been able to work under his guidance in his lab. I sincerely appreciate absolutely everything.

I also want to thank Dr. Steve Duke, Dr. Mario Eden, and Dr. Bart Prorok, for agreeing to serve as the committee members for this dissertation. They have always been available to have thoughtful discussions with me about my research, or just about life, and I really appreciate it. Special thanks also go to Dr. Michael Bozack for undertaking the role as the outside reader, and for all of his support and work on my first publication.

There have also been several other folks who have positively contributed to my time at Auburn. Thanks goes to Dr. Michael Miller, for his technical assistance on the TEM and SEM, and for taking time to continuously fine-tune the instruments so that I can get the best possible images of the magnetic particles. Thanks

are due to Brian Schwieker and Steve Moore, for their technical assistance, and for being great friends who would always take time to chat with me when I needed to take a break. Karen Cochran, Sue Ellen Abner, Elaine Jimmerson, and Georgetta Dennis also deserve big thanks for their kindness and for all of their help over the years.

Thank you to the past and present members of the Roberts Research Group: Kendall Hurst, Steve Saunders, Rui Xu, Helena Sihe, and Jie Zhong, as well as Pranav Vengsarkar, Charlotte Stewart, David Roe for being awesome lab mates, and even better friends. I especially need thank Pranav, in particular, who has always been there for me for anything I ever needed. Also, I am so thankful to Hema Ramsurn and Courtney Ober for their friendship and for the hundreds of lunches we have shared. I also want to express my gratitude to my fellow graduate students, Hector Galacia, Arianna Tieppo-Rappo, Aaron Seetow, Kendall Hurst, Steve Saunders, and Matt Kayatin who helped me make the transition to graduate school in chemical engineering at Auburn and would spend countless hours with me discussing classwork.

Lastly, I want to thank my family for their support, in particular, my Papa and Granny and my Uncle Larry and Aunt Debbie for being great role models and encouraging me to succeed. I am also so very grateful for my mother- and father-in-law, Dr. James Duggan and Freda Duggan, who have always been so supportive throughout my entire college endeavors. Finally, I want to thank my sweet, supportive husband and best friend, Wayne Duggan. None of this would have been possible without him. Wayne has been by my side and has helped me achieve my goals. I could never thank him enough for all he has done to make my life better.

## Table of Contents

|   |      |
|---|------|
| Abstract.....   | ii   |
| Acknowledgments .....   | v    |
| List of Figures .....   | xii  |
| List of Tables .....  | xx   |
| List of Abbreviations .....   | xxii |
| Chapter 1: Introduction .....   | 1    |
| 1.1 Introduction to Nanotechnology .....                                      | 1    |
| 1.2 General Applications in Nanotechnology .....                              | 5    |
| 1.2.1 Optical Properties and Applications of Nanoparticles .....              | 6    |
| 1.2.2 Magnetism, Magnetic Properties, and Applications of Nanoparticles ..... | 10   |
| 1.3 Nanoparticle Synthesis Techniques .....                                   | 21   |
| 1.3.1 Solvent-Based Methods for Nanoparticle Synthesis .....                  | 22   |
| 1.4 Significance of Nanoparticle Stabilization .....                          | 26   |
| 1.4.1 Nanoparticle Stabilization Techniques .....                             | 27   |
| 1.5 Properties of DMSO .....  | 29   |
| 1.6 DMSO as a Functional Solvent for Nanoparticle Synthesis .....             | 32   |
| 1.7 Nanoparticle Processing Techniques .....                                  | 36   |
| 1.7.1 Liquid-Liquid Nanoparticle Processing Techniques .....                  | 36   |
| 1.7.2 Gas-Expanded Liquid Nanoparticle Processing Techniques .....            | 37   |

|   |     |
|---|-----|
| 1.8 Summary of Chapters .....   | 43  |
| 1.8.1 Chapter 2 Summary .....   | 43  |
| 1.8.2 Chapter 3 Summary .....   | 44  |
| 1.8.3 Chapter 4 Summary .....   | 44  |
| 1.8.4 Chapter 5 Summary .....   | 45  |
| 1.8.5 Chapter 6 Summary .....   | 45  |
| Chapter 2: The Synthesis and Arrested Oxidation of Amorphous Cobalt<br>Nanoparticles using Dimethyl Sulfoxide as a Functional Solvent ..... | 47  |
| 2.1 Introduction.....   | 48  |
| 2.2 Experimental .....  | 51  |
| 2.2.1 Materials .....   | 51  |
| 2.2.2 Co Nanoparticle Synthesis in DMSO .....   | 52  |
| 2.2.3 Characterization Techniques .....   | 55  |
| 2.3 Results and Discussion .....  | 58  |
| 2.3.1 Complete Reduction of Co Salt to Form Nanoparticles .....   | 58  |
| 2.3.2 Precipitation of Co Nanoparticles from DMSO using Acetone .....   | 66  |
| 2.3.3 Co Nanoparticle Surface Interactions with DMSO .....  | 73  |
| 2.4 Conclusions .....   | 92  |
| Chapter 3: Clustering and Solvation of Cobalt Nanostructures in Dimethyl Sulfoxide .....  | 93  |
| 3.1 Introduction .....  | 94  |
| 3.2 Experimental .....  | 97  |
| 3.2.1 Materials .....   | 97  |
| 3.2.2 Co Nanoparticle and Nanocluster Synthesis .....   | 98  |
| 3.2.3 Addition of Co-Solvents to Co Nanoparticles and Clusters .....  | 100 |



|   |     |
|---|-----|
| 3.2.3 Characterization Techniques .....   | 100 |
| 3.3 Results.....  | 101 |
| 3.3.1 TEM Analysis of Co Nanoparticle Cluster Formation .....   | 101 |
| 3.3.2 Co Nanoparticle Cluster Degradation by the Addition of Water .....  | 106 |
| 3.3.3 Co Nanoparticle Cluster Degradation by Co-Solvent Addition .....  | 111 |
| 3.4 Discussion of Co Nanoparticle Clustering and Cluster Degradation .....  | 113 |
| 3.5 Conclusions .....   | 117 |
| Chapter 4: Controlling the Crystallinity and Magnetism of Cobalt Nanoparticles<br>via Thermal Oxidative Treatment ..... | 118 |
| 4.1 Introduction .....  | 119 |
| 4.2 Experimental .....  | 123 |
| 4.2.1 Materials .....   | 123 |
| 4.2.2 Co Nanoparticle Synthesis .....   | 124 |
| 4.2.3 Precipitation of Co Nanoparticles from DMSO Solution .....  | 126 |
| 4.2.4 Post-Synthesis Annealing of Co Nanoparticles .....  | 126 |
| 4.2.5 Characterization Techniques .....   | 127 |
| 4.3 Results.....  | 129 |
| 4.3.1 Morphology of Co Nanoparticles Prior to Annealing .....   | 129 |
| 4.3.2 Thermal Stability of Co Nanoparticles Prior to Annealing .....  | 132 |
| 4.3.3 Effect of Thermal Treatment on Co Nanoparticle Structures .....   | 134 |
| 4.3.4 Effect of Annealing Time on Co Nanoparticle Structure .....   | 136 |
| 4.3.5 Effect of Thermal Treatment on Co Nanoparticle Size and<br>Morphology .....                                       | 138 |
| 4.3.6 Effect of Annealing Time on Co Nanoparticle Size and Morphology ....  | 143 |

|   |     |
|---|-----|
| 4.3.7 Effect of Thermal Treatment on Co Nanoparticle Magnetic Properties .....  | 146 |
| 4.3.4 Effect of Annealing Time on Co Nanoparticle Structure .....   | 136 |
| 4.4 Discussion of Temperature-Dependent Magnetism .....   | 152 |
| 4.5 Conclusions .....   | 157 |
| Chapter 5: Aggregation and Precipitation of Gold Nanoparticle Clusters in CO <sub>2</sub> -Gas Expanded Liquid-Dimethyl Sulfoxide Solvent Systems ..... | 158 |
| 5.1 Introduction .....  | 159 |
| 5.2 Experimental .....  | 161 |
| 5.2.1 Materials .....   | 161 |
| 5.2.2 Au Nanoparticle Synthesis .....   | 161 |
| 5.2.3 Characterization Techniques .....   | 163 |
| 5.3 Results.....  | 167 |
| 5.3.1 TEM Imaging Analysis of Au Nanoparticle Size and Morphology .....   | 167 |
| 5.3.2 Interaction Between Au Nanoparticle Surface and DMSO/Fatty Acid Molecules .....   | 171 |
| 5.3.3 Au Nanoparticle Stability as a Function of Time at Standard Ambient Temperature and Pressure .....  | 184 |
| 5.3.4 Volume Expansion of CO <sub>2</sub> -DMSO Solutions .....   | 188 |
| 5.3.5 Dispersibility of Au Nanoparticles in CO <sub>2</sub> -Gas Expanded DMSO Solvent Systems at Various Pressures .....                               | 189 |
| 5.4 Discussion of Au Nanoparticle Dispersibility in CO <sub>2</sub> -Gas Expanded DMSO Solvents .....   | 201 |
| 5.5 Conclusions .....   | 210 |
| Chapter 6: Overall Conclusions and Future Directions .....  | 211 |

|  |     |
|--|-----|
| 6.1 Summary and Conclusions .....  | 211 |
| 6.2 Future Directions .....  | 215 |
| 6.2.1 Synthesis of Au Nanoparticles in a CO <sub>2</sub> -Gas Expanded<br>Dimethyl Sulfoxide Solvent .....                       | 215 |
| 6.2.2 Co <sub>3</sub> O <sub>4</sub> Thin Film Formation .....   | 220 |
| References .....   | 222 |
| Appendix A: Supplemental TEM Images of Co Nanoparticles and Temperature<br>Programmed Desorption Data for Co Nanoparticles ..... | 240 |
| Appendix B: The Effect of Gold Coating on SEM Imaging Analysis .....   | 245 |
| Appendix C: UV-vis analysis of Au Nanoparticle Reductions and Au Nanoparticle<br>Syntheses at High Temperature .....             | 248 |
| Appendix D: List of Publications and Presentations .....   | 255 |

## List of Figures

|     |  |    |
|-----|--|----|
| 1.1 | Example of using scanning tunneling microscopy as a method to manipulate individual xenon atoms, spelling ‘IBM’ (Eigler & Schweizer 1990). .....   | 4  |
| 1.2 | Au NP structures of various aspect ratios: a) digital image of Au NP structure solutions, b) UV-vis spectral data of Au NP structure solutions, and c) TEM images of Au NP solutions. Vial ‘0’ is a solution of 4 nm Au nanospheres and vials 1-5 are solutions of Au nanorods with increasing aspect ratio (Murphy et al. 2008). .....  | 8  |
| 1.3 | Illustration of a generic magnetization curve to illustrate the variation of the magnetization, $M$ , of a material with the applied magnetic field, $H$ . .....   | 13 |
| 1.4 | An image of a neodymium magnet obtained using Kerr microscopy (Hubert & Schafer 2000). .....   | 15 |
| 1.5 | Schematics illustrating the interaction of particles in a magnetic field: (a) ferromagnetic and superparamagnetic nanoparticle domains both in the presence and absence of a magnetic field and (b) example magnetization curves of a ferromagnetic material (denoted by the black line) and a superparamagnetic material (denoted by the blue line) (Dave & Gao 2009; Daniel-da-silva & Trindade 2011). ..... | 16 |
| 1.6 | Molecular representation of dimethyl sulfoxide, DMSO, and its corresponding resonance hybrid structure. ....   | 31 |
| 1.7 | TEM image and corresponding histogram of Pd nanoparticles, stabilized by the functional solvent, DMSO (Liu et al. 2010). .....   | 34 |
| 1.8 | FT-IR spectra of neat DMSO and Pd nanoparticles synthesized in DMSO (Liu et al. 2010). .....   | 35 |
| 1.9 | An illustration to describe the dissolution of a gas (e.g., CO <sub>2</sub> ) into a liquid to create a gas-expanded liquid where the solution is a) a neat liquid before the addition of the gas and b) a mixture of a liquid and gas (e.g., a gas-expanded liquid) after the addition of the gas. ....   | 40 |

|      |   |    |
|------|---|----|
| 1.10 | Volumetric expansion of a) CO <sub>2</sub> +hexane (Mukhopadhyay 2003) and b) CO <sub>2</sub> +DMSO (adapted from (Calvignac et al. 2009; Kordikowski et al. 1995; Rajasingam et al. 2004; Elvassore et al. 2002)).   | 42 |
| 2.1  | Nitrogen-purged apparatus containing DMSO solution and a) dissociated CoCl <sub>2</sub> *6H <sub>2</sub> O salt and b) Co nanoparticle solution after the addition of NaBH <sub>4</sub> . The color change from blue (a) to dark gray (b) indicates the presence of Co nanoparticles.   | 54 |
| 2.2  | UV-visible spectra for the disappearance of the Co salt peak to form Co nanoparticles using a functional solvent, DMSO. Shown here, the Co salt peak is a 0.05M solution of Co <sup>2+</sup> salt solution (prior to the addition of NaBH <sub>4</sub> reducing agent). Then, the amounts of [Co <sup>2+</sup> ]:[NaBH <sub>4</sub> ] were increased to 4:1, 4:3, 4:5, 4:6, 4:7, 4:9. | 61 |
| 2.3  | Co nanoparticles stabilized by DMSO in the presence of a magnet. The left image shows a representative dispersion of the Co nanoparticles at t = 0 minutes and the right image shows the collection of the Co nanoparticles on the meniscus of the DMSO solvent due to their attraction to the magnet placed on the top of the vial at t = 10 minutes.                                | 63 |
| 2.4  | TEM image and corresponding histogram for Co nanoparticles synthesized in the presence of the functional solvent, DMSO.   | 65 |
| 2.5  | Digital image of the N <sub>2</sub> -inflated glove bag that was used to completely dry the Co nanoparticles after they had been removed from the DMSO solvent using acetone.   | 68 |
| 2.6  | Digital images of dried Co nanoparticles illustrating the separation of the Co nanoparticles from DMSO using acetone as liquid anti-solvent. Inset is a close-up of the Co nanoparticle powder.   | 69 |
| 2.7  | SEM image of Co nanoparticles (after subsequent precipitation from DMSO using acetone as an anti-solvent).  | 70 |
| 2.8  | Co nanoparticles redispersed in DMSO after having been precipitated from a DMSO + acetone solution (i.e. using acetone as an anti-solvent).   | 72 |
| 2.9  | FT-IR spectra for neat DMSO, neat acetone, and Co nanoparticles synthesized in DMSO (after subsequent precipitation from DMSO using acetone as an anti-solvent).  | 76 |
| 2.10 | Schematic representation of a Co nanoparticle stabilized by the oxygen component of DMSO.   | 78 |

|      |   |     |
|------|---|-----|
| 2.11 | XPS spectra of Co nanoparticles synthesized in DMSO (after subsequent precipitation from DMSO using acetone as an anti-solvent) for a) S2p, b) C1s, c) O1s, and d) Co2p.....  | 81  |
| 2.12 | XRD spectra of Co nanoparticle powder synthesized in DMSO a) after precipitation from DMSO using acetone as an anti-solvent and b) after a subsequent washing with DI-H <sub>2</sub> O.....   | 84  |
| 2.13 | TEM images of Co nanoparticles synthesized in DMSO when a) exposed to environmental air during synthesis, b) purged with air during synthesis, c) exposed to air for 4.5 days after synthesis, d) purged with air for 4.5 days after synthesis. ....  | 90  |
| 2.14 | Size histograms from TEM analysis for Co nanoparticles synthesized in DMSO when a) exposed to environmental air during synthesis, b) purged with air during synthesis, c) exposed to air for 4.5 days after synthesis, d) purged with air for 4.5 days after synthesis .....  | 91  |
| 3.1  | The recursive clustering cycle of individual nanoparticles and nanoparticle clusters, whereby the formation and/or degradation of clusters can be controlled. ....  | 96  |
| 3.2  | The reaction set-up for the high-temperature synthesis of Co nanoparticle clusters. ....  | 99  |
| 3.3  | TEM images and corresponding histograms of Co nanoparticles synthesized at different temperatures: a) 25°C, b) 50°C, and c) 150°C. ....   | 103 |
| 3.4  | HR-TEM image of Co nanoclusters synthesized at 150°C. The scale bar is 10 nm. ....  | 104 |
| 3.5  | Proposed reaction schemes for a) the formation of Co nanoparticles (~4 nm) in DMSO at 25°C and b) the formation of Co nanoclusters (~20 nm) at higher temperatures (e.g. 50°C and 150°C).....   | 105 |
| 3.6  | TEM images for Co nanoparticles stabilized by DMSO synthesized at different temperatures and diluted with different amounts of water after the solution was returned to room temperature (25°C). A ratio of 1:3 DMSO-Co nanoparticle dispersion to water was used to dilute the nanostructures in the first column: a) 25°C, b) 50°C, and c) 150°C. A ratio of 3:1 DMSO-Co nanoparticle dispersion to water was used to dilute the nanostructures in the second column: d) 25°C, e) 50°C, f) 150°C..... | 107 |
| 3.7  | Cartoon representation of Co nanostructures interacting with co-solvents (e.g., DI-H <sub>2</sub> O): a) at 25°C, b) at elevated temperatures (e.g., 50°C, 150°C) and c) detailed depiction of DMSO-stabilized Co nanoparticles being solvated by co-solvents (e.g., DI-H <sub>2</sub> O).....  | 116 |

|      |   |     |
|------|---|-----|
| 4.1  | Radley apparatus used to simultaneously synthesize up to six Co nanoparticle samples in DMSO. ....  | 125 |
| 4.2  | TEM image of Co-DMSO nanoparticles as synthesized at room temperature, prior to annealing. ....   | 130 |
| 4.3  | SEM image of Co nanoparticle powder after precipitation from DMSO prior to annealing. ....  | 131 |
| 4.4  | TGA analysis of Co-DMSO nanoparticle powder as synthesized at room temperature. Measurements were performed from 25°C to 500°C. ....  | 133 |
| 4.5  | XRD analysis for different samples of Co nanoparticle powder, (a) prior to annealing, and after annealing for 2 hours at (b) 200°C, (c) 400°C, (d) 600°C, and (e) 800°C, where ( ● ) indicates the peaks indexed to spinel Co <sub>3</sub> O <sub>4</sub> . ....  | 135 |
| 4.6  | XRD analysis for Co nanoparticle powder annealed to 800°C for a) 2 hours and b) 12 hours, where ( ● ) indicates the peaks indexed to spinel Co <sub>3</sub> O <sub>4</sub> . ....   | 137 |
| 4.7  | SEM images of the Co nanoparticle powder after annealing for 2 hours to a) 200°C, b) 400°C, c) 600°C, and d) 800°C. ....  | 139 |
| 4.8  | Digital image of Co nanoparticle powders redispersed in a fresh solution of DMSO after annealing to 200°C, 400°C, 600°C, and 800°C for 2 hours (pictured in order of increasing annealing time from left to right). ....  | 141 |
| 4.9  | TEM images of the Co nanoparticle powder samples that had been annealed for 2 hours and subsequently re-dispersed in fresh DMSO solution a) 200°C, b) 400°C, c) 600°C, and d) 800°C. ....   | 142 |
| 4.10 | SEM images of the Co nanoparticle powder a) prior to annealing, b) after annealing to 800°C for 2 hours, and c) after annealing to 800°C for 12 hours. ....   | 144 |
| 4.11 | TEM images of the Co nanoparticle powder a) prior to annealing, b) after annealing to 800°C for 2 hours, and c) after annealing to 800°C for 12 hours. ....   | 145 |
| 4.12 | M-H curve for amorphous Co nanoparticles, obtained prior to annealing, measured at 5, 40, and 300K, respectively. The M-H curve at 300 and 5K exhibit paramagnetic and ferromagnetic behaviors, respectively. The M-H curve at 40 K shows the mixture of both the para and ferromagnetic components. .... | 147 |

|      |  |     |
|------|--|-----|
| 4.13 | M-H curves for Co <sub>3</sub> O <sub>4</sub> nanoparticles, obtained after annealing at 800°C for 2 hours. The M-H curve exhibits para- and ferromagnetic behaviors at 300 and 5K, respectively, while the curve at 40 K shows the mixture of both the para and ferromagnetic components. ....  | 148 |
| 4.14 | M-H curves for Co <sub>3</sub> O <sub>4</sub> nanoparticles, obtained after annealing at 800°C for 12 hours. The M-H curve exhibits para- and ferromagnetic behaviors at 300 and 5K, respectively, while the curve at 40 K shows the mixture of both the para and ferromagnetic components. .... | 149 |
| 4.15 | M-H curves for Co <sub>3</sub> O <sub>4</sub> nanoparticles, obtained after annealing at 800°C for 15 hours. The M-H curve exhibits para- and ferromagnetic behaviors at 300 and 5 K, respectively, while the one at 40 K shows the mixture of both the para and ferromagnetic components ....   | 150 |
| 4.16 | M-H curves for Co <sub>3</sub> O <sub>4</sub> nanoparticles, obtained after annealing at 800°C for 20 hours. The M-H curve exhibits para- and ferromagnetic behaviors at 300 and 5 K, respectively, while the one at 40 K shows the mixture of both the para and ferromagnetic components ....   | 151 |
| 4.17 | Variation of coercivity (H <sub>c</sub> ) measured at 5 K as a function of the annealing time of the Co <sub>3</sub> O <sub>4</sub> nanoparticles, where the annealing temperature is 800°C. ....  | 156 |
| 5.1  | A digital image of the high-pressure, stainless steel view cell that has been specifically designed for the high-pressure UV-vis spectroscopy experiments. ....  | 166 |
| 5.2  | TEM image and corresponding histograms of the Au nanoparticles synthesized using a) DMSO as a functional solvent, b) oleic acid as a stabilizing ligand in a DMSO solvent, and c) stearic acid as a stabilizing ligand in a DMSO solvent.....  | 169 |
| 5.3  | Molecular representations of a) the DMSO functional solvent, and the other stabilizing ligands b) oleic acid and c) stearic acid used to synthesize Au nanoparticles. ....   | 170 |
| 5.4  | FT-IR spectra of a) neat DMSO solvent, b) Au-DMSO nanoparticles (DMSO as a functional solvent), and c) comparison of the neat DMSO and the Au-DMSO nanoparticles.....  | 172 |
| 5.5  | Illustration of the electrostatic coordination occurring between the sulfoxide functional groups of DMSO with the Au nanoparticle surface. ....  | 174 |



|      |   |     |
|------|---|-----|
| 5.6  | FT-IR spectra of a) neat oleic acid, b) Au-OA nanoparticles in DMSO solvent, and c) comparison of the neat oleic acid and the Au-OA nanoparticles. ....   | 176 |
| 5.7  | FT-IR spectra of a) neat stearic acid, b) Au-SA nanoparticles in DMSO solvent, and c) comparison of the neat stearic acid and the Au-SA nanoparticles. ....   | 177 |
| 5.8  | Illustration of monodentate chelating coordination occurring between the carboxylate functional groups of the fatty acid ligands (i.e., oleic acid and stearic acid) with the Au nanoparticle surface. ....   | 183 |
| 5.9  | UV-vis spectra of the Au nanoparticle dispersions as a function of extended aging time at standard ambient temperature and pressure: a) DMSO as a functional solvent, b) oleic acid as the stabilizing ligand and DMSO as the solvent, and c) stearic acid as the stabilizing ligand and DMSO as the solvent. ....  | 186 |
| 5.10 | Digital images of the Au nanoparticle dispersions as a function of extended aging time at standard ambient temperature and pressure for a) DMSO as a functional solvent, b) oleic acid as the stabilizing ligand and DMSO as the solvent, and c) stearic acid as the stabilizing ligand and DMSO as the solvent. In each image above, the dispersion on the left has aged for 24 hours after synthesis, while the dispersion on the right has aged for 3 months.....                          | 187 |
| 5.11 | Volume expansion as a function of applied CO <sub>2</sub> pressure for neat DMSO (◆), oleic acid + DMSO (■), and stearic acid + DMSO (▲). ....  | 189 |
| 5.12 | UV-vis spectra of a) the absorbance of the Au-DMSO nanoparticle dispersion as a function of the applied CO <sub>2</sub> pressure and b) the absorbance of the Au-DMSO nanoparticle dispersion before pressurization with CO <sub>2</sub> and after depressurization. Note that the spectrum labeled '55.2* bar' corresponds to the transition pressure, and the spectrum labeled '55.2 bar PPT' corresponds to the point at which all Au nanoparticles had precipitated from the mixture..... | 192 |
| 5.13 | UV-vis spectra of a) the absorbance of the Au-OA nanoparticle dispersion as a function of the applied CO <sub>2</sub> pressure and b) the absorbance of the Au-OA nanoparticle dispersion before pressurization with CO <sub>2</sub> and after depressurization. Note that the spectrum labeled '55.2* bar' corresponds to the transition pressure, and the spectrum labeled '55.2 bar PPT' corresponds to the point at which all Au nanoparticles had precipitated from the mixture. ....    | 197 |

|      |   |     |
|------|---|-----|
| 5.14 | UV-vis spectra of a) the absorbance of the Au-SA nanoparticle dispersion as a function of the applied CO <sub>2</sub> pressure and b) the absorbance of the Au-SA nanoparticle dispersion before pressurization with CO <sub>2</sub> and after depressurization. Note that the spectrum labeled '48.3* bar' corresponds to the transition pressure, and the spectrum labeled '48.3 bar PPT' corresponds to the point at which all Au nanoparticles had precipitated from the mixture. ....                      | 198 |
| 5.15 | Curves representing the precipitation of Au nanoparticles from CO <sub>2</sub> -gas expanded DMSO solvent systems as a function of time where a) is the Au-DMSO nanoparticle solution, b) is the Au-OA nanoparticle solution, and c) is the Au-SA nanoparticle solution. Pressure was held constant in each case and the graphs represent the precipitation that occurs once the transition pressure has been reached at a) 55.2 bar for 44 hours, b) 55.2 bar for 45 hours, and c) 48.3 bar for 28 hours. .... | 206 |
| 5.16 | Illustration of Au nanoparticle dispersibility in DMSO+CO <sub>2</sub> solvent systems at various applied pressures of CO <sub>2</sub> . ....   | 209 |
| 6.1  | The viscosity of DMSO as a function of the applied CO <sub>2</sub> pressure (Calvignac et al. 2009; Bhuiyan et al. 2007). ....  | 218 |
| 6.2  | Schematic illustration of nanoparticle formation via the processes of nucleation and growth (Cao 2004; Oskam 2006; Viswanatha & Sarma 2007) .....   | 219 |
| 6.3  | TEM image of a) an array of dodecanethiol-stabilized Au nanoparticles that have been deposited onto a TEM grid using the CO <sub>2</sub> -gas expanded deposition technique and b) Au nanoparticle array at higher magnification to show particle deposition uniformity (Liu et al. 2006). ....   | 221 |
| A1.1 | TEM images and corresponding histograms for Co nanoparticles stabilized by the functional solvent, DMSO, where the ratio of [Co <sup>2+</sup> ]:[NaBH <sub>4</sub> ] is a) 4:1, b) 4:3, c) 4:5, d) 4:6, e) 4:9 .....  | 241 |
| A2.1 | TPD data as obtained from Micromeritics, where the TCD signal is plotted as a function of time. ....  | 243 |
| A2.2 | TPD data as obtained from Micromeritics, where the measurements were carried out over the range from 0°C to 1000°C .....  | 244 |
| B1.1 | SEM images of Co nanoparticles without gold coating a) prior to annealing, b) annealed at 200°C, c) annealed at 400°C, d) annealed at 600°C, and e) annealed at 800°C. All images were taken at 20,000X magnification .....   | 246 |

|      |  |     |
|------|--|-----|
| B1.2 | SEM images of Co nanoparticles that have been sputter coated with gold a) prior to annealing, b) annealed at 200°C, c) annealed at 400°C, d) annealed at 600°C, and e) annealed at 800°C. All images were taken at 20,000X magnification .....                       | 247 |
| C1.1 | UV-vis absorption spectra of the Au nanoparticle synthesis in DMSO using different ratios of salt to reducing agent: 4:1, 4:5, 4:7, 4:9, 4:11, 4:17 .....  | 249 |
| C2.2 | TEM images and histograms of the Au nanoparticles synthesized in DMSO using different ratios of salt to reducing agent: a) 4:1, b) 4:3, c) 4:7, d) 4:9, e) 4:11, f) 4:13, g) 4:15, h) 4:17. ....   | 250 |
| C2.1 | TEM image of Au nanoparticles that were synthesized at 150°C using DMSO as the solvent and oleic acid as the ligand where a) is an image taken at 10,000 times magnification and b) is an image that has been zoomed in on a particular region of the image .....    | 253 |
| C2.2 | TEM image of Au nanoparticles that were synthesized at 150°C using DMSO as the solvent and stearic acid as the ligand, where a) is an image taken at 16,000 times magnification and b) is an image that has been zoomed in on a particular region of the image. .... | 254 |

## List of Tables

|     |  |     |
|-----|--|-----|
| 1.1 | Summary of several solvent-based synthesis procedures and corresponding reaction conditions for the preparation of different nanomaterials (from (Y. Liu, 2006)).....  | 25  |
| 1.2 | Comparison of the different classes of solvents and the corresponding volume expansion behavior at different CO <sub>2</sub> pressures and at 40°C (Heldebrant et al. 2006; Scurto et al. 2009; Jessop & Subramaniam 2007) .....   | 41  |
| 2.1 | Summary of wavenumbers for sulfur and oxygen FT-IR coordination (Smith 1999). .....  | 77  |
| 2.2 | Results from SEM-EDS elemental analysis for Co nanoparticle powder .....   | 87  |
| 3.1 | The average size of the Co nanostructures originally synthesized in DMSO at various temperatures before and after the addition of DI-H <sub>2</sub> O, where 10 mL of DI-H <sub>2</sub> O was added to 30 mL of each Co nanostructure dispersion .....   | 110 |
| 3.2 | A list of the co-solvents added to the Co nanostructures originally synthesized in DMSO at 150°C and the corresponding average Co nanoparticle size after the addition of the co-solvents, where 10 mL of each co-solvent was added to 30 mL the Co nanostructure dispersion. Solvents are listed in the order of decreasing dipole moments..... | 112 |
| 5.1 | FT-IR vibrational mode assignments for neat DMSO (Horrocks Jr. & Cotton 1961; Nakamoto 2009; Smith 1999).....  | 173 |
| 5.2 | FT-IR vibrational mode assignments for neat oleic acid (Wu et al. 2004; Nakamoto 1997).....  | 178 |
| 5.3 | FT-IR vibrational mode assignments for neat stearic acid (Wu et al. 2004; Nakamoto 1997; Smith 1999).....  | 179 |
| 5.4 | Types of complexation, wave number separation, and illustration of the possible nanoparticle surface interaction with carboxylate functional groups.....   | 182 |

|     |  |     |
|-----|--|-----|
| 5.5 | The amount of time spent at each CO <sub>2</sub> pressurization interval, as well as the elapsed time, for the Au-DMSO nanoparticle dispersion. .... | 194 |
| 5.6 | The amount of time spent at each CO <sub>2</sub> pressurization interval, as well as the elapsed time, for the Au-OA nanoparticle dispersion. ....   | 199 |
| 5.7 | The amount of time spent at each CO <sub>2</sub> pressurization interval, as well as the elapsed time, for the Au-SA nanoparticle dispersion. ....   | 200 |

## List of Abbreviations

|                                       |   |
|---------------------------------------|---|
| [bmim]BF <sub>4</sub>                 | Tetrafluoroborate                                     |
| $\Delta$                              | Wave Number Separation                                |
| Au                                    | Gold  |
| <i>B</i>                              | Magnetic Induction                                    |
| Co                                    | cobalt  |
| CO <sub>2</sub>                       | Carbon Dioxide  |
| Co <sub>3</sub> O <sub>4</sub>        | Cobalt Oxide  |
| CoCl <sub>2</sub> *6H <sub>2</sub> O  | Cobalt (II) chloride hexahydrate                      |
| D-H <sub>2</sub> O                    | Deionized Ultra Filtered Water                        |
| DMF                                   | N,N-Dimethylmethanamide                               |
| DMSO                                  | Dimethyl Sulfoxide                                    |
| EDS                                   | Energy-dispersive X-Ray Spectroscopy                  |
| FDA                                   | Food and Drug Administration                          |
| FTIR                                  | Fourier Transform Infrared Spectroscopy               |
| FWHM                                  | Full Width Half Maximum                               |
| <i>H</i>                              | Applied Magnetic Field                                |
| HAuCl <sub>4</sub> *3H <sub>2</sub> O | Hydrogen Tetrachloroaurate (III) Trihydrate           |
| H <sub>c</sub>                        | Coercivity  |
| K                                     | Magneto-Crystalline Anisotropy Energy per unit Volume |

|            |  |
|------------|--|
| $k_B$      | Boltzmann constant                     |
| $M$        | Magnetization                          |
| $m$        | Dipole Moment                          |
| MeCN       | Acetonitrile                           |
| M-H Curves | Magnetization Curves                   |
| MRI        | Magnetic Resonance Imaging             |
| $N_2$      | Nitrogen                               |
| $N_2H_5OH$ | Hydrazinium Hydroxide                  |
| $NaBH_4$   | Sodium Borohydride                     |
| NIR        | Near-Infrared                          |
| NP         | Nanoparticle                           |
| OA         | Oleic Acid                             |
| Pd         | Palladium                              |
| PEG-400    | Polyethylene Glycol                    |
| PPG-2700   | Poly(propylene glycol)                 |
| SA         | Stearic Acid                           |
| SDBS       | Sodium Dodecyl Benzenesulfonate        |
| SEM        | Scanning Electron Microscopy           |
| $T$        | Temperature                            |
| $t$        | Time                                   |
| $T_B$      | Superparamagnetic Blocking Temperature |
| TEM        | Transmission Electron Microscope       |
| TEOS       | Tetraethyl Orthosilicate               |

|          |                                   |
|----------|-----------------------------------|
| TGA      | Thermogravimetric Analysis        |
| TPD      | Temperature Programmed Desorption |
| UV-vis   | UV-Visible                        |
| V        | Particle Volume                   |
| VSM      | Vibrating Sample Magnetometry     |
| XPS      | X-ray Photoelectron Spectroscopy  |
| XRD      | X-ray Diffractometry              |
| $\theta$ | Diffraction angle                 |
| $\mu_o$  | Permeability of a Vacuum          |
| $\nu$    | Vibrational Modes                 |
| $\chi$   | Magnetic Susceptibility           |



## **Chapter 1**

### **Introduction**

#### **1.1 Introduction to Nanotechnology**

Nature has projected the evolution of nanotechnology in modern science and engineering. In fact, there is evidence to suggest that nature has been constructing materials at the nanoscale for billions of years (Poole & Owens 2003). For example, abalone shells are constructed of strong, calcium carbonate nano-structured brick-like shapes that have enhanced mechanical properties. Because of the method by which nature organizes these nano-structured bricks, cracks that form on the surface of the shell are unable to penetrate completely through the shell, providing substantial protection for the vulnerable body of the mollusk (Poole & Owens 2003). Thus, nature has provided the lessons necessary to understand the importance of constructing materials from the nano-scale and how these materials can be organized to have improved properties over materials at the bulk-scale.

Moving beyond these lessons, these same principles of miniaturization can be applied to a variety of different materials in order to exploit the properties of nano-scale materials. Nanotechnology allows for precise control over particle size and shape because these materials are often constructed one atom at a time (Goodsell 2004). As Richard Feynman predicted in his forward-thinking and very famous lecture in 1959

titled, *There's Plenty of Room at the Bottom*, working with matter on the atomic scale will become a reality and that human-kind would be able to manipulate single atoms with the use of advanced instrumentation (Feynman 1959). A couple of years later, Gordon Moore, founder of Intel, made a bold prediction that the number of transistors per circuit would double every 18-24 months (Moore 1965). This prediction, called Moore's Law, challenged researchers to assemble circuits with more transistors per unit area (Wu et al. 2013), and this ultimately led to the construction of smaller and more powerful devices.

Soon thereafter, other pioneers in nanotechnology began to publish numerous reports predicting the ability to manipulate single atoms. In fact, the term 'nanotechnology' was first reported to have been mentioned at a conference proceeding in Tokyo, Japan in 1974 (Taniguchi 1974). Later, Gerd Binnig and Henrich Rohrer at IBM developed the first scanning tunneling microscope, which allowed matter to be controlled on the atomic scale (Binnig & Rohrer 1983). An example of the 'nanoscale precision' provided by scanning tunneling microscopy can be seen in Figure 1.1, where xenon atoms were used to construct the letters 'IBM' (Eigler & Schweizer 1990; Baird & Shew 2004). In 1985, a group of researchers discovered an organized structure of 60 carbon atoms, the 'buckyball' (Kroto et al. 1985), which preceded the discovery of helical microtubules of graphitic carbon, termed 'carbon nanotubes' by Sumio Iijima in 1991 (Iijima 1991). Shortly thereafter in 1986, Eric Drexler published a book, *Engines of Creation*, to describe nanotechnology in detail, and predicted that nanocircuits and nanomachines will be created (Drexler 1986). All of these researchers contributed significantly to the development of nanotechnology, and their insights have challenged other scientists to create materials and devices which exhibit specifically-engineered,

size-dependent properties. Thus, nanotechnology has essentially become a sustainable branch of science and engineering that provides innovative methods that can be used to overcome technological barriers and continuously develop advanced materials and applications.

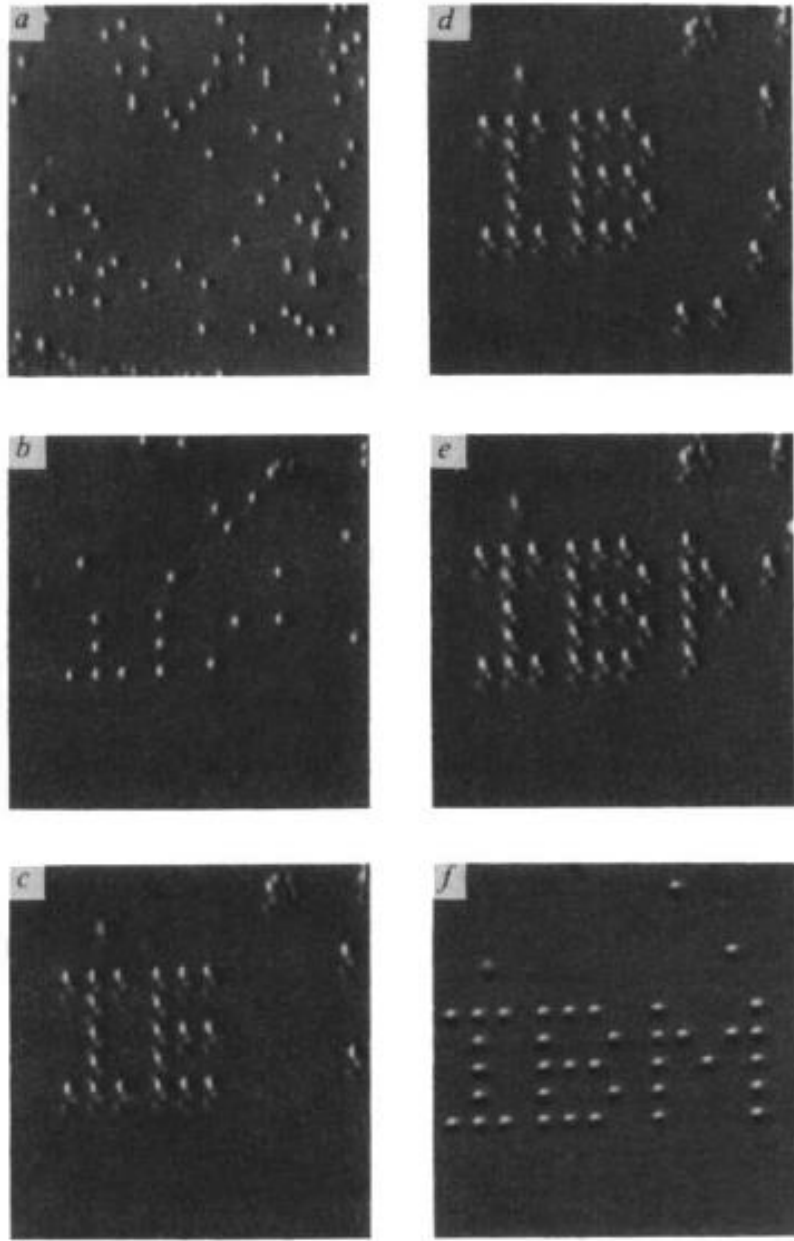


**Figure 1.1** Example of using scanning tunneling microscopy as a method to manipulate individual xenon atoms, spelling 'IBM' (Eigler & Schweizer 1990).

## 1.2 General Applications in Nanotechnology

The extreme miniaturization in size gives nano-scale materials unique and size-dependent properties that afford opportunities in a wide variety of applications. Specifically, devices constructed of nanomaterials have interesting optical (Beecroft & Ober 1997; Kelly et al. 2003; Murphy et al. 2005), mechanical (Shi et al. 2006; Zhang & Singh 2004), electronic (Grieve et al. 2000; McConnell et al. 2000), and magnetic properties (Frey et al. 2009; Pankhurst 2003).

In general, nanotechnology has applications in medicine as methods for advanced drug delivery. Nanoparticles can be functionalized on the surface with proteins and drugs, which essentially ‘program’ these particles to migrate to specific locations within the body for targeted drug delivery (Langer & Tirrell 2004; Panyam 2003; Cole et al. 2011). Magnetic nanoscale particles (e.g., cobalt – Co) also provide advancements in biological and magnetic imaging for cancer and disease detection and treatment (Berry & Curtis 2003; Jordan 1999; Hao et al. 2010; Xie et al. 2011). Additionally, since nanoparticles are much smaller than cells in the body, nanoparticles can preferentially interact with individual cells, and now *in vivo* migration of particles to various parts of the body is no longer limited to tissues (Berry & Curtis 2003), which provides many opportunities for improved targeting in drug delivery and disease diagnosis. Certain metallic nanoparticles (e.g., gold – Au) have interesting optical properties that allow for these particles to be utilized in various biomedical imaging applications (Huff et al. 2007; Murphy, Gole, Stone, et al. 2008; Huang et al. 2007). For example, Au nanostructures (such as Au nanorods) can be optically active in the near infrared region and can be used in laser irradiation treatment as a method to penetrate diseased tissues and induce

apoptosis of cancer cells (Murphy, Gole, Stone, et al. 2008). Nanoparticles can also be specifically engineered to have a magnetic core, which can be composed of a magnetic material (e.g., Co) and a optically active shell (e.g., Au) in order to combine the magnetic and optical properties in a single particle (Lee et al. 2005; Bao et al. 2007). A couple of examples describing the integration of nanoparticles and nanostructured materials into various applications are examined below, with emphasis on exploiting the optical and magnetic properties in various applications.

### **1.2.1 Optical Properties and Applications of Nanoparticles**

Various metallic nanoparticles have been investigated for their interesting and size-dependent optical properties (Huang et al. 2008; Link & El-Sayed 1999; Li et al. 2013; Huang & El-Sayed 2010; Murphy, Gole, Stone, et al. 2008; Huang et al. 2007). A straight-forward example can be seen in the case of Au nanoparticles where a solution of Au nanoparticles appears as a red wine color when observed with the naked eye, instead of the ‘gold’ color that is seen in bulk metallic Au. The difference in color is directly related to the size-dependent optical properties of Au, where Au particles in the range of 5 – 200 nm contain a conduction band (Murphy, Gole, Stone, et al. 2008). At this very small size scale, these particles can support a conduction band that is comparable to the mean free path of electrons in the metal, but smaller than the wavelengths of visible light. Therefore, excitation of the nano-scale particles with visible light produces collective oscillations of electrons, or plasmons, in the conduction band (Eustis & el-Sayed 2006; Murphy, Gole, Hunyadi, et al. 2008; Wetenschappen & Chemie 2006; Murphy, Gole,

Stone, et al. 2008). The surface plasmon bands can be conveniently observed using ultraviolet visible (UV-vis) spectroscopy (Wetenschappen & Chemie 2006).

The shape and positioning of the surface plasmon bands, which can be observed using UV-vis spectroscopy, can depend on several factors, such as the type of metal as well as the morphology, size, standard deviation, and surrounding media (Hutter & Fendler 2004; Mulvaney 1996; Underwood & Mulvaney 1994). In fact, subtle changes in a nanoparticle's surroundings (including agglomerating with other nanoparticles or metal ions in solution) can induce color changes in the nanoparticle dispersions, as well as changes in the peak positioning and shape of the UV-vis spectral data (Huang & El-Sayed 2010; Murphy, Gole, Hunyadi, et al. 2008) as shown in Figure 1.2. Particle agglomerations disrupt plasmon oscillations in the conduction band, and thereby induce plasmon coupling. The plasmon band shifts to higher wavelengths as a result of the plasmon coupling occurring within the aggregates (Murphy, Gole, Stone, et al. 2008). This plasmon coupling is sensitive enough to be detected by UV-vis spectroscopy, and can therefore be used to verify the presence of anisotropic nanoparticles and aggregates of nanoparticles in solution (Lin et al. 2005). This particular topic is central to the contents presented in this dissertation because *in-situ* UV-vis spectroscopy will be utilized to investigate Au nanoparticle clustering in Chapter 5.

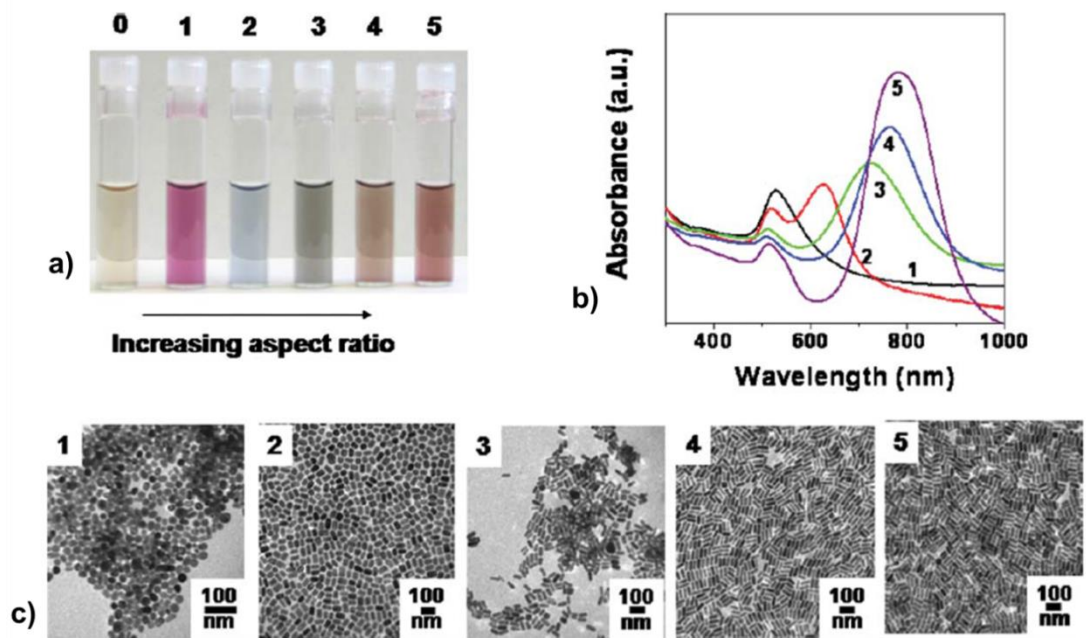


**Figure 1.2** Au nanoparticle structures of various aspect ratios: a) digital image of Au nanoparticle structure solutions, b) UV-vis spectral data of Au nanoparticle structure solutions, and c) TEM images of Au nanoparticle solutions. Vial ‘0’ is a solution of 4 nm Au nanospheres and vials 1-5 are solutions of Au nanorods with increasing aspect ratio (Murphy, Gole, Hunyadi, et al. 2008).



### **1.2.1.1 NIR Applications of Au Nanoparticles**

Au nanostructures of particular shapes have been reported to be optically active in the near-infrared (NIR) region of light (Huang & El-Sayed 2010; Huang et al. 2007; Perezjuste et al. 2005; Tong et al. 2009; Huang et al. 2006), i.e., at wavelengths  $> 700$  nm (Michalet et al. 2005). As a result of their size- and shape-dependent optical properties, Au nanostructures can be utilized in cancer diagnostic and treatment technologies.

Au nanostructures can be specifically functionalized on the surface such that they preferentially bind to receptors that are overexpressed on cancerous cells (Eustis & el-Sayed 2006; Huang et al. 2008; Day et al. 2010; Weissleder 2001; Ramos 2012). Other Au nanostructures, such as Au nanorods, can be used as contrast agents to detect cancer cells (Huang et al. 2006; Tong et al. 2009; Kim et al. 2007) and as drug delivery systems (Huang et al. 2007; Ramos 2012). In many cases where Au nanostructures are used to image cancerous cells, it was also found that these structures can be used to induce apoptosis of infected cells (Day et al. 2010; Huang et al. 2006), thereby serving as a potentially viable and non-invasive means of cancer treatment (e.g., hyperthermia). As stated earlier, Au nanostructures exhibit a strong plasmon band that can be finely tuned depending on shape and size of the structure, and these particles can therefore be used to controllably and effectively transduce NIR light to heat in photothermal therapeutic applications. In this technique, abnormal cells in biological tissues can be targeted using Au nanostructures, and the infected cells are subjected to high temperatures in order to prompt cell destruction (van der Zee 2002). Therefore, these tunable optical properties of various Au nanoparticles are particularly relevant to the Au nanoparticle clustering studies that are presented in Chapter 5.

### 1.2.2 Magnetism, Magnetic Properties, and Applications of Nanoparticles

In order to understand the magnetism of nanomaterials, it is first important to make some general, introductory comments on magnetism. Applied magnetic fields certainly have an effect on materials. The relationships between the applied magnetic field,  $H$ , the magnetic induction,  $B$ , and the magnetization,  $M$ , are described in the equations below. In a vacuum with no materials present,  $B$  and  $H$  can be related by

$$B = \mu_o H, \quad (1.1)$$

where  $B$  and  $H$  are parallel and  $\mu_o$  a universal constant for the permeability of a vacuum (Jakubovics 1987). When a material is present within the magnetic field, the material develops a dipole moment in the field,  $m$ . The dipole moment is proportional to the volume of the material and can be written as  $M$  (magnetization). Then,  $M$  can be related to  $B$  and  $H$  by the following equation

$$B = \mu_o (H + M). \quad (1.2)$$

A material's magnetization is dependent on the magnetic field that is acting on the material, and  $M$  is proportional to  $H$ . Therefore, the following equation can be written to describe the relationship

$$M = \chi H, \quad (1.3)$$

where  $\chi$  is the magnetic susceptibility, which is a property that is unique to the material (Jakubovics 1987; Pankhurst 2003).

The electrons orbiting an atom give rise to the magnetic properties of a material. Electrons orbit around the nucleus of an atom, and there is a magnetic moment associated with each orbit. However, if the moments are opposing, there is no resulting magnetic moment. For these materials, there is no magnetic moment when there is no applied magnetic field, and these materials are classified as diamagnetic (Jakubovics 1987). In essence, if the orbital motion of the electrons does not cancel, there will be a net magnetic moment on the atom. These materials are called permanent magnets, and one classification of permanent magnetics is paramagnetic materials, which possess atoms with permanent magnetic dipole moments. In permanent magnets the moments point in random directions in zero applied magnetic field (Anon 2014; Jakubovics 1987). Another type of permanent magnet is ferromagnetic materials, which can develop significant magnetization in relatively small applied magnetic fields (Anon 2014; Jakubovics 1987). Also, ferromagnetic materials do not maintain magnetic saturation upon the removal of the magnetic field, which is largely in part due to the magnetic domains present in the material (Jakubovics 1987), which will be discussed in Section 1.2.2.1.

The magnetization curve is a key component in understanding the magnetism of materials. An illustration of a generic magnetization curve is presented in Figure 1.3. Starting from point 1, the magnetism increases, and reaches a constant value at point 2. Point 2 is known as the magnetic saturation. Upon reducing the applied magnetic field ( $H$ ), the magnetism decreases and follows a different path until  $H = 0$  at point 3. Then, when  $H$  is reversed, the magnetization increases in the direction of the reversed applied field  $H$  until the magnetic saturation point is reached at point 4. This process can be

repeated and magnetism will follow the shape of the loop, also known as the hysteresis loop.

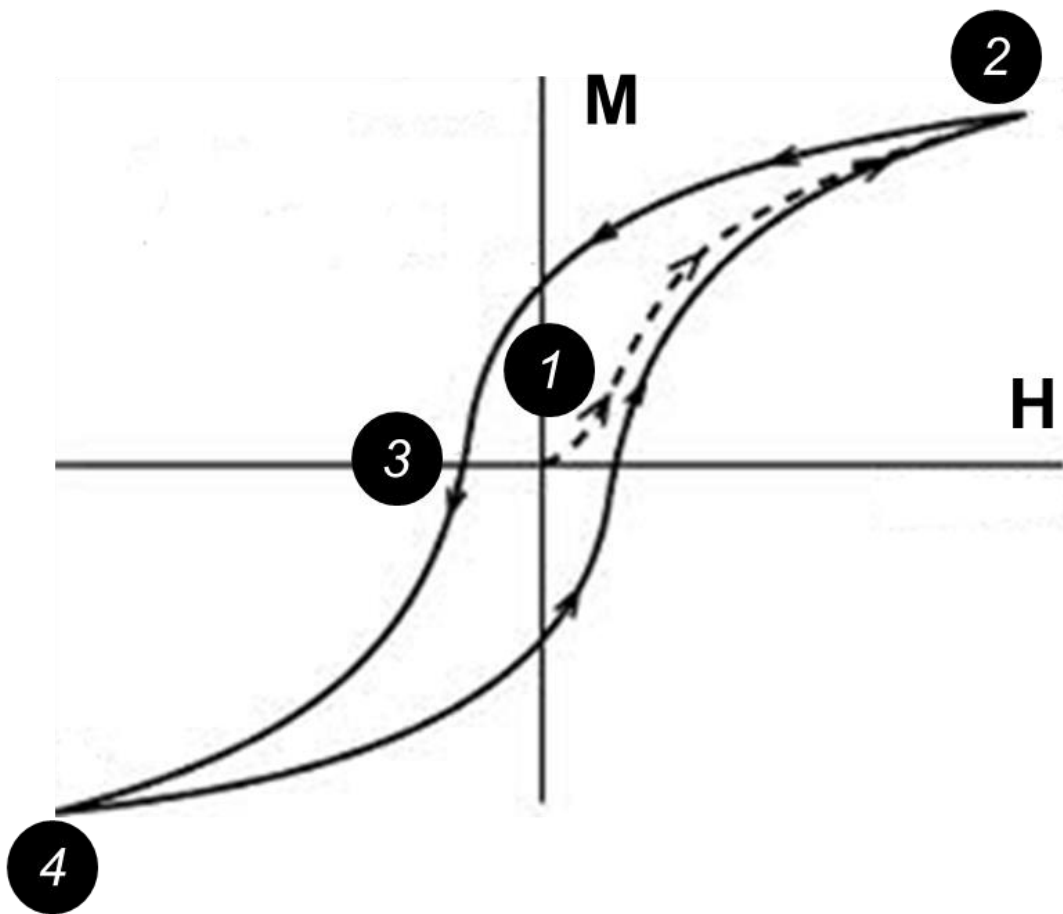


**Figure 1.3** Illustration of a generic magnetization curve to illustrate the variation of the magnetization,  $M$ , of a material with the applied magnetic field,  $H$ .

### **1.2.2.1 Importance of Magnetic Domains in Nanoparticles**

Magnetic materials are sub-divided into small sections, called domains. Each domain has its own magnetism, but the domains generally contribute to the net magnetism of the material by following the direction of the easy axis, or the direction of spontaneous magnetization (Hubert & Schafer 2000). An image of the magnetic domains (and grain boundaries) in a neodymium magnet are shown in Figure 1.4. The magnetic domains are the shaded regions in the figure with corresponding arrows, which indicate the direction of magnetization in each domain (Hubert & Schafer 2000). Nanoparticles exhibit size-dependent magnetic properties, and this unique characteristic arises from the differences between a bulk material and a single domain material (i.e., nanoparticles). For example, domain walls in bulk metals can nucleate and rotate with the rotation of magnetization vector; however, domain wall movement does not occur in single domain nanoparticles because the domain size is on the nanoscale (Frey et al. 2009). Typically, the critical diameter of a single domain magnetic nanoparticle is in the range of 10-100 nm (Frey et al. 2009), however, the single domain limit can reach several hundred nanometers for particles with high magnetic anisotropy (Skomski & Coey 1999). The difference between a multi-domain ferromagnetic material and a single-domain nanoparticle is illustrated in the schematics in Figure 1.5. Moreover, it is important to emphasize that the key function of the domains is to lower the overall energy of the material (Jakubovics 1987), therefore, materials will preferentially form domains in order to minimize the free energy (Hubert & Schafer 2000).



**Figure 1.4** An image of a neodymium magnet obtained using Kerr microscopy (Hubert & Schafer 2000).

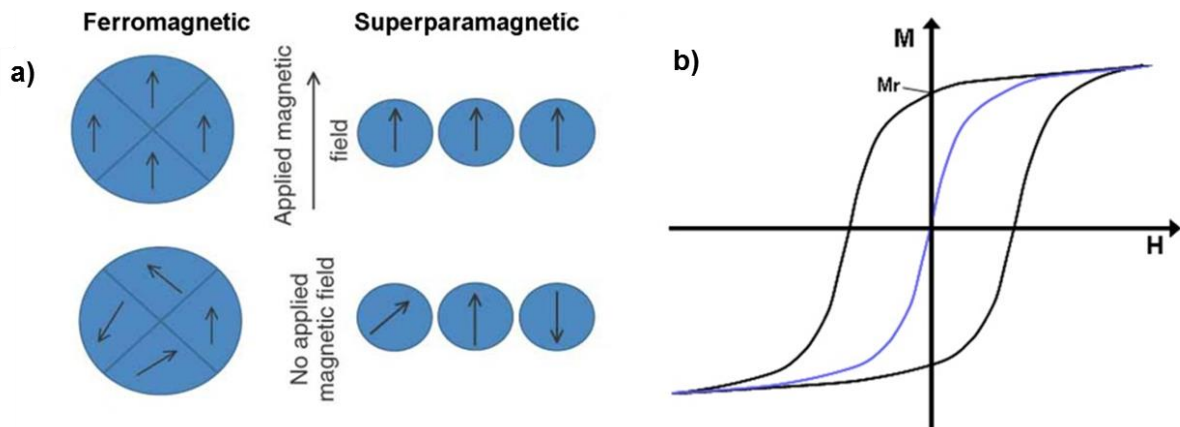


**Figure 1.5** Schematics illustrating the interaction of particles in a magnetic field: (a) ferromagnetic and superparamagnetic nanoparticle domains both in the presence and absence of a magnetic field and (b) example magnetization curves of a ferromagnetic material (denoted by the black line) and a superparamagnetic material (denoted by the blue line) (Dave & Gao 2009; Daniel-da-silva & Trindade 2011).



### 1.2.2.2 Magnetism in Nanoparticles

Nanoparticles can exhibit very unique magnetic properties, which largely depend on particle size. Magnetism in materials can be paramagnetic, diamagnetic, ferromagnetic, and these characteristics can be observed in either bulk or nanoscale materials. However, as material's dimensions are decreased to the nanoscale, the magnetic properties can drastically change. In fact, nanoparticles can exhibit a different form of magnetism, a superparamagnetic behavior. Materials that are classified as 'superparamagnetic' possess higher magnetic susceptibility (at the same applied magnetic field as ferromagnetic materials), there is no pattern of hysteresis and no residual magnetism after the magnetic field is removed (Bean & Livingston 1959). A comparison between ferromagnetic and superparamagnetic magnetism is illustrated in Figure 1.5.

Examples of the ability to manipulate the magnetic properties of materials as a function of particle size have been demonstrated in the literature. Bulk palladium (Pd) metal is paramagnetic (Gray et al. 2013), but as the particle dimensions are decreased into the nanoscale (e.g., 7 nm), the particles' magnetism transitions from paramagnetic to ferromagnetic (Seehra et al. 2012). Similarly, bulk Au is diamagnetic (Gray et al. 2013), but as the Au particle size is decreased to the nanoscale (e.g., 5 nm), the particles become ferromagnetic and even exhibit a superparamagnetic blocking temperature  $T_B \approx 50$  K (Dutta et al. 2007). Moreover, it has also been reported that ferromagnetic bulk Co can exhibit different magnetisms as the size and shape of the Co particles are altered. Specifically, 5 x 20 nm ferromagnetic Co nanodisks were found to be ferromagnetic, but spherical 10 nm Co nanoparticles were found to be superparamagnetic (Bao & Krishnan 2005). Thus, particles of different sizes can have drastically different magnetic properties

and this dissertation is largely focused on the ability to produce Co nanoparticles and clusters of different sizes for their potential use in a variety of applications.

### **1.2.2.3 Biomedical Applications of Magnetic Co Nanoparticles**

An application of magnetic nanoparticles that is of particular interest at Auburn involves exploiting the magnetic properties of nanoparticles for their potential use as contrast agents in magnetic resonance imaging. Magnetic Resonance Imaging (MRI) is a method for high-quality imaging of soft tissues inside the human body. Magnetic nanoparticles can be used as a method to improve image resolution as contrast agents. In traditional MR imaging, gadolinium complexes (Gd (III)) is the most common paramagnetic contrasting agent because it has seven unpaired electrons with a relatively long relaxation time in water (Pérez-Mayoral et al. 2008). However, Gd (III) is not inherently attracted to certain tissue types and is found to preferentially accumulate in the liver (Berry & Curtis 2003). These types of contrast agents have size-related limitations and cannot interact with individual cells. However, image contrast and resolution, as well as the access to smaller components within the body (e.g., cells) can be improved by decreasing the size of the metals to the nanoscale.

The most common material currently being explored for its use as nano-scale contrast agents is iron oxide. Iron oxide and other nanoscale particles interact by a few different mechanisms in the body. These particles enter the body primarily by intravenous administration. Depending on their size and surface functionality, these particles can be specifically tailored to concentrate within cells or tissues as they circulate in the blood stream (Gellissen et al. 1999; Na et al. 2009; Larsen et al. 2009; Schoepf et al. 1998). For example, iron oxide nanoparticles have been observed to assist in the detection of tumor cells. Growth of cancerous tumors is very rapid and gaps within endothelial cells that line the blood vessels develop. Since nanoparticles are at such

small dimensions, these materials can penetrate the gaps and group together inside the tumor by self-assembly, facilitated by enzymes in the cell. Once the nanoparticles are in the cell, they agglomerate and are too large to escape the cell (Cho et al. 2007; Farokhzad et al. 2006). Increases in the local concentration resulting from the accumulation in the tumor cells produce strong magnetic signals, allowing for the MR detection of these cells (Harris et al. 2006). This type of accumulation mechanism occurs inside the body and the surface modifications of the nanoparticle bind with the receptors of defective target cells and form a local concentration of magnetic nanoparticles to be detected using MRI (Na et al. 2009). Hence, magnetic nanoparticles can be functionalized on the surface with biocompatible coatings and can accumulate in defective cells to allow for improved MR imaging. Central to the research presented in this dissertation (Chapters 2, 3, & 4), Co is a promising candidate for magnetic imaging applications because Co particles have appreciable saturation magnetization (Bao & Krishnan 2005).

#### **1.2.2.4 Energy and Data Storage Applications**

Current technological advancements are focused on improving magnetic recording and energy storage devices. Magnetic recording devices can be improved by utilizing magnetic nanoparticles where the information recording density in nanostructured devices is increased by 1000 – 10,000 times over the bulk-scale counterparts (Gubin et al. 2005). This is due, in part, to the magnetization per unit atom and the increase in magnetic anisotropy as particle size decreases to the nanoscale. Magnetic anisotropy is the alignment of the magnetization along a specific direction (Gambardella et al. 2003). Moreover, the magnetic anisotropy depends largely on the crystalline structure and atomic composition as well as the particle size and morphology

(Gubin et al. 2005). There is also much interest centered on creating new materials that have high coercivity values, which would make these materials particularly interesting for energy applications in order to maintain long-term magnetic stability (Frey et al. 2009; Gubin et al. 2005). Magnetic nanoparticles can be used in a variety of potential applications where high magnetic anisotropy and high coercivity are essential. Thus, developing methods by which these magnetic materials can be produced is significant and relevant to the current technological needs, and this topic will be discussed in more complete detail in Chapter 4.

### **1.3 Nanoparticle Synthesis Techniques**

Methods by which to synthesize nanoparticles are of contemporary interest due to their increasing demand for their use in the rapidly-expanding applications, as discussed above. Nanoscale materials are typically constructed via two different mechanisms by either the top-down approach or the bottom-up approach (Poole & Owens 2003). In the top-down method, the nanoscale materials are mechanically sculpted from a bulk material by gradually reducing the dimensions of the bulk material to the nanoscale (Poole & Owens 2003). Examples of the top-down approach are lithography, ball milling, and etching (Poole & Owens 2003). Nanoscale materials can also be constructed by assembling nanoscale building blocks in the bottom-up approach. Bottom-up synthesis techniques are chemically-based methods, such as chemical vapor deposition (Adachi et al. 2003), microemulsion-based synthesis (Lin & Samia 2006), pyrolysis (Puntes et al. 2001), thermal decomposition (Dinega & Bawendi 1999), and polyol techniques (Komarneni et al. 2002) to name a few. Of particular interest to the research presented in this document, bottom-up, solvent-based nanoparticle synthesis techniques will be

explored because these methods allow for the judicious control over size, shape, composition, and physical properties of the nanostructure by controlling the nucleation and growth of the particles (Lin & Samia 2006; Hyeon 2003).

### **1.3.1 Solvent-based Methods for Nanoparticle Synthesis**

Popular methods used to synthesize inorganic nanoparticles involve the solvent-based reduction of metal ions by a reducing agent. These methods require fine control of the reaction conditions, and produce relatively uniform nanoparticles. For example, the solvothermal method specifically involves synthesis in non-aqueous solutions at elevated temperatures (often greater than the boiling point of the solvent) and likewise, the hydrothermal methods involve synthesis in aqueous solutions (often above the boiling point of the water) (Feng & Li 2011). Additionally, both involve careful and fine control over the reaction conditions and occur in a sealed and heated solution (usually in an autoclave) at the appropriate temperature (100-1000°C) and pressure (1-100 MPa) (Feng & Li 2011). These methods have been used for mineral extraction (Habashi 2005), synthesis of geological materials (Goranson 1931; Hosaka 1991), synthesis of novel materials (Demazeau 1999; Feng & Xu 2001; Demianets 1999), crystal growth (Rabenau & Rau 1969), deposition of thin films (Gogotsi & Yoshimura 1994), sintering processes (Yamasaki et al. 1986), and the controlled synthesis of particles of particular size and morphology (Demazeau 2007; Rajamathi & Seshadri 2003).

A variety of materials such as metal, magnetic, and semiconductor nanoparticles can be synthesized with a high degree of size control using solvent-based methods (Feng et al. 2010); however, it is important to emphasize that these methods often require the use of harsh, unsafe, and expensive solvents and reagents (Liu 2006). Table 1.1 shows a

summary of several solvent-based synthesis techniques and corresponding reaction conditions for the preparation of different nanomaterials. From this table, it is easy to see that many harsh and expensive reagents, solvents, and surfactants are utilized in these synthesis procedures such as SDBS (sodium dodecyl benzenesulfonate),  $N_2H_5OH$  (hydrazine hydrate), hexachlorobenzene, and benzene to name a few. Also, the Table 1.1 identifies the reaction time and reaction temperatures many of the methods lasting upwards of 20 hours to complete under extreme heating conditions around  $200^{\circ}C$ . As such, solvent-based methods have been cited numerous times in the literature as a viable method to synthesize nanoparticles of controlled size and shape, as a method to create nanomaterials that are versatile in a wide variety of applications. However, these methods are often tedious and time intensive since much effort must be focused on fine-tuning these parameters to obtain the optimum reaction conditions in order to yield the desired product. Moreover, many experimental factors and conditions that have an impact on nanoparticle size and morphology (Liu 2006) and particular consideration must be given to choose the appropriate starting materials and solvent as well as the reaction temperature and time. Thus, the research presented in this dissertation will be primarily focused on improving and simplifying these synthesis methods in order to create new sustainable techniques for nanoparticle synthesis and processing that will allow for the precise control of nanoparticle size and morphology.

| <b>Element</b>                       | <b>Type of Nanostructure</b> | <b>Dimensions (nm)</b> | <b>Reagents, Temperature(°C), &amp; Time</b>  | <b>Reference</b>        |
|--------------------------------------|------------------------------|------------------------|---|-------------------------|
| <b>Cu</b>                            | nanowires                    | 85 x 10,000 - 90,000   | Cu <sup>II</sup> -glycerol + HPO <sub>3</sub> <sup>2+</sup> + SDBS, 120, 20h  | (Liu et al. 2003)       |
| <b>CdO</b>                           | nanocrystals                 | 4.5                    | Cd(cup) <sub>2</sub> + TOPO + toluene, 240, 2.5 h   | (Ghosh & Rao 2004)      |
| <b>CuFeS<sub>2</sub></b>             | nanorods                     | 20 x 5000              | CuCl + FeCl <sub>3</sub> + (NH <sub>4</sub> ) <sub>2</sub> S, 200, 10h  | (Hu et al. 1999)        |
| <b>CoAl<sub>2</sub>O<sub>4</sub></b> | nanocubes                    | 70                     | CoCl <sub>2</sub> + AlCl <sub>3</sub> + 3M NaOH, 210, 24h   | (Chen et al. 2002)      |
| <b>Ni-Cu</b>                         | nanoparticles                | 12                     | NiAc <sub>2</sub> + CuAc <sub>2</sub> + SDBS + PEG, ammonia, 150, 3h  | (Niu et al. 2004)       |
| <b>Co</b>                            | nanodisks                    | 5 x 20                 | Co <sub>2</sub> (CO) <sub>8</sub> + DCB + TOPO/OA, 182  | (Puntes et al. 2002)    |
| <b>Co</b>                            | nanoparticles                | 10                     | Co <sub>2</sub> (CO) <sub>8</sub> + DCB + TOPO/OA, 182  | (Bao 2003)              |
| <b>Co@Au</b>                         | nanoparticles (seeds)        | 6                      | Co <sub>2</sub> (CO) <sub>8</sub> + (C <sub>6</sub> H <sub>5</sub> ) <sub>3</sub> P]AuCl + DCB + OA + TOA + Hydrazine, Toluene, 95, 2hr | (Bao et al. 2007)       |
| <b>Co@SiO<sub>2</sub></b>            | nanoparticles                | 5 - 77                 | CoCl <sub>2</sub> *6H <sub>2</sub> O + NaBH <sub>4</sub> + citric acid + APS + TEOS, 200-700, 2h  | (Kobayashi et al. 2003) |
| <b>CoO</b>                           | nanoparticles                | 4.5 - 18               | Co(cup) <sub>2</sub> +Decalin + toluene + methanol, 270 6 - 48 hr   | (Ghosh et al. 2005)     |

**Table 1.1** Summary of several solvent-based synthesis procedures and corresponding reaction conditions for the preparation of different nanomaterials (adapted from (Y. Liu, 2006)).



## 1.4 Significance of Nanoparticle Stabilization

Stabilizing agents/ligands play a critical role in nanoparticles synthesis. Strong interactions between neighboring nanoparticles, such as van der Waals forces and even magnetic attractions, can lead to nanoparticle agglomeration (Cushing et al. 2004). In addition, stabilizing agents also function to suppress nanoparticle growth by effectively passivating the surface of newly formed metal clusters and seeds that could agglomerate due to interparticle attractions (Liu et al. 2009). Since nanoparticle activity and reactivity is highly related to the available surface area, nanoparticle agglomeration must be avoided in order to maintain high specific surface area and interfacial free energy of individual nanoparticles (He et al. 2007). To overcome the attractive interactions between nanoparticles, stabilizing agents can be used which function to enhance dispersion via electrostatic repulsion and steric hindrance. Specifically, electrostatic repulsion between nanoparticles exists when an electrical double layer is formed by the addition of counter ions such as citrate, chloride, or sulfide molecules. The highly charged nanoparticles are prevented from agglomerating by the Coulombic repulsions between neighboring nanoparticles (Finke 2002; Fendler 1996). As the distance between the nanoparticles increases, the Coulombic charge between neighboring nanoparticles decreases exponentially (Fendler 1996). Nanoparticles can also be stabilized by steric repulsions created by engineering bulky molecules, such as polymers, on the surfaces on the particles. Steric stabilization of nanoparticles is related to entropy effects and osmotic effects. Entropic effects occur when the nanoparticles are forced to reorganize due to the large molecular interactions of the surfactant when the nanoparticles are tightly packed. The entropy of the system will decrease when the distance between the nanoparticles is

decreased to force the surfactants into smaller and restricted configurations, resulting in a thermodynamically unfavorable system. The osmotic effect functions to stabilize the nanoparticles by solvating the surfactant or polymer chains between neighboring nanoparticles (Fendler 1996). Another function of stabilizing agents is to protect the highly reactive nanoparticle surfaces from oxidation that can occur from the contents of the surrounding media. Even though the surfactants protect nanoparticles from environmental contaminants, the surfactants do not hinder any potential reaction that may occur with a target molecule because the particles still possess increased reactivity due to increased surface areas resulting from particle stabilization (He et al. 2007). In particular for the work presented in this dissertation, an ideal stabilizing agent will be able to effectively suppress nanoparticle growth, relatively non-toxic to the environment, and cost effective.

#### **1.4.1 Nanoparticle Stabilization Techniques**

There are a variety of molecules that can be used to achieve nanoparticle stabilization in solution. For example, organic thiol-derived ligands have been used as ligands to stabilize Au nanoparticles (Brust et al. 1994; Shields et al. 2010), as well as other metal nanoparticles such as silver and platinum (Sarathy et al. 1997) in organic solvents by forming a covalent bond with the Au (Hirsch et al. 2006; Badia et al. 1997).

Simple, inexpensive and benign molecules have also been explored for their use as stabilizing agents in nanoparticle synthesis. It has been shown that starch can serve as a surfactant to improve the reactivity and dispersibility of iron, silver, and gold, silver-gold alloy nanoparticles (Raveendran, J. Fu, et al. 2006; Raveendran, J. Fu, et al. 2003). Other methods have been developed to use beta-D-glucose to serve as both the reducing

agent and stabilizing agent in the synthesis of Au nanoparticles (J. C. Liu et al. 2006). Even though starch and beta-D-glucose are cost effective and non-toxic, these molecules were only able to stabilize nanoparticles for short durations (Raveendran, Jie Fu, et al. 2003; Raveendran, Jie Fu, et al. 2006; Juncheng C. Liu et al. 2006). More relevant to the work presented in this dissertation, fatty acid, such as oleic acid and stearic acid (Wu et al. 2004; Shafi et al. 2001) can also be used to function as stabilizing ligands in nanoparticle synthesis, and this topic will be explored more extensively in Chapter 5.

#### **1.4.1.1 Functional Solvent**

One method to further improve nanoparticle synthesis could be to develop a synthesis technique that eliminates excess reagents by combining nanoparticle stabilization and solvation through the use of a single, multifunctional solvent system. The molecule dimethyl sulfoxide (DMSO) has been found to sufficiently serve as both the solvent and the stabilizing agent (Liu et al. 2010), and the unique ability for DMSO to stabilize and solvate nanoparticles will be referred to as a “functional solvent” henceforth. A functional solvent can concomitantly function as the solvent as well as the stabilizing agent/ligand for nanoparticles, thereby allowing more complete and unrestricted access to the nanoparticle surface. Further requirements for a functional solvent to be effective include the ability to dissolve all reagents and provide sufficient interaction with the nanoparticle surface in order to keep the nanoparticles solvated and dispersed in solution. Moreover, nanoparticle synthesis using a functional solvent reduces the number of reagents employed during synthesis and eliminates the need for post-processing separations of any excess stabilizing agents. This provides a direct route for generating nanoparticles with high purity and yield.

## 1.5 Properties of DMSO

Dimethyl sulfoxide (DMSO) is a polar, aprotic solvent, meaning it has appreciable solvation strength due to a moderate dielectric constant and polarity. In particular, DMSO molecules possess significant charge separation between other DMSO molecules that is quantified by its dielectric constant of 46.7 (Steiner & Gilbert 1965). DMSO has comparable ion dissolving quality to that of protic solvents, but it lacks acidic hydrogens and is therefore unable to hydrogen bond with other molecules. DMSO is a symmetrical molecule containing a sulfoxide group with a methyl group on each side, as shown in Figure 1.6. DMSO also is a suitable green solvent because it has low toxicity and a high boiling point of 189°C and low vapor pressure of 0.01psia. Even though DMSO has a somewhat oily appearance, it has a relatively high freezing point of 18°C, making solvent removal from nanoparticles a very simple process (Liu et al. 2010). These properties minimize potential solvent emissions into the atmosphere at ambient conditions. Furthermore, DMSO has the ability to dissolve polar and nonpolar molecules and is miscible in water (Andreatta et al. 2007) as well as a variety of other solvents (Anon 2007). For medicinal application purposes, it was approved in 1978 by the FDA to treat interstitial cystitis and can be used transdermal drug delivery as well (Muir 2005). In addition, DMSO is also a class III solvent according to the pharmaceutical industry which is the lowest toxicity class for humans with no health-based exposure limits (Robert 2000). DMSO is a commonly used reactant and is very effective as a solvent. Additionally, DMSO can readily interact with organisms by penetrating biological membranes (Rodríguez-Gattorno et al. 2002), making DMSO an

important transport medium for drug delivery and medicinal applications for nanoparticle systems.

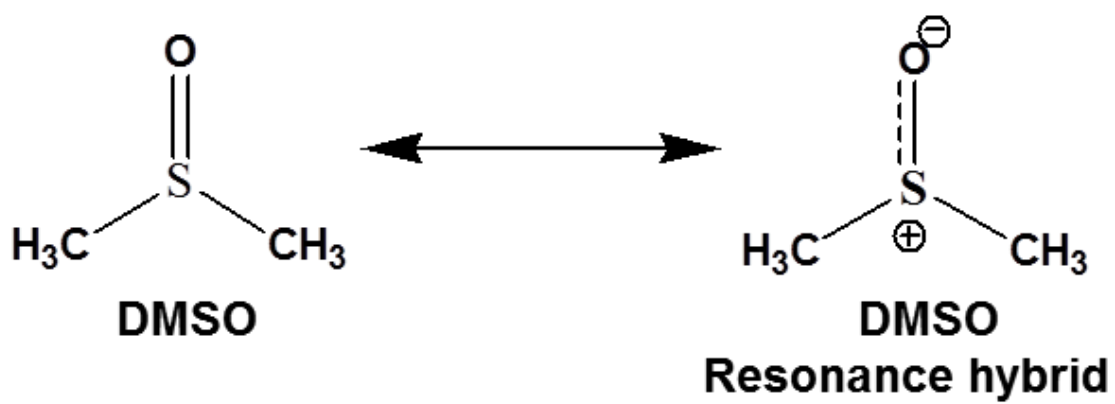


**Figure 1.6** Molecular representation of dimethyl sulfoxide, DMSO, and its corresponding resonance hybrid structure.

## 1.6 DMSO as a Functional Solvent for Nanoparticle Synthesis

There are several nanoparticles synthesis techniques that use DMSO during synthesis. Iron oxide nanoparticles were synthesized using a thermal decomposition technique, but high temperature refluxing conditions had to be carefully maintained up to 24 hours after the addition of reagents (Guin et al. 2006). Ruthenium dioxide nanoparticles were also synthesized using DMSO as well as several other harsh reagents, such as methanol and hydrochloric acid, under high refluxing temperatures (Borah & Sharma 2011). Another study attempted to produce silver nanoparticles using DMSO as a stabilizing agent using a spontaneous reduction of the silver ions at room temperature, but this nanoparticles synthesis attempt was at first unsuccessful (Rodríguez-Gattorno et al. 2002). This silver nanoparticle synthesis was improved to produce a polydisperse silver nanoparticles population upon the addition of sodium citrate and 2-ethylhexanoate to function together as stabilizing agents instead of DMSO at elevated temperatures (Rodríguez-Gattorno et al. 2002). DMSO has also been reported to serve as a phase transfer catalyst to move metal and semiconductor nanoparticles from an aqueous phase into an organic phase of toluene (Vijaykumar et al. 2007). Each of these techniques describes the ability to produce nanoparticles using DMSO in some capacity, but these methods involve utilizing extreme temperatures, long reaction times, harsh reactants, and tedious control over the reaction conditions.

Recently in the Roberts Lab, DMSO has been successfully employed as a functional solvent to be utilized as both the solvent and stabilizing agent to produce monodisperse palladium (Pd) nanoparticles ( $3.5 \text{ nm} \pm 0.5 \text{ nm}$ ) via a simple, fast, homogeneous reduction of a Pd salt using  $\text{NaBH}_4$  (Liu et al. 2010). Even though DMSO

was exclusively used as the stabilizing agent, these Pd nanoparticles possessed a high degree of stability, i.e. nanoparticles agglomeration and precipitation was not observed. The TEM image as well and the size histogram of the DMSO-stabilized Pd nanoparticles are shown in Figure 1.7 and the uniform nanoparticle size and spherical morphology can be observed. FT-IR was used to study the molecular interactions of the DMSO molecule with the surface of the Pd nanoparticles as shown in Figure 1.8. FT-IR spectra reveal that the DMSO molecule exists as a resonance hybrid structure as coordination occurs between the oxygen and sulfur groups of the molecule. A molecular representation of the resonance hybrid structure of DMSO is shown in Figure 1.6. The peak at  $1031\text{ cm}^{-1}$  from the neat DMSO sample split into two peaks at  $1128\text{ cm}^{-1}$  and  $1020\text{ cm}^{-1}$  to offer substantial evidence that DMSO serves as an essential component in uniform Pd nanoparticle synthesis and subsequent stabilization, and no additional molecules or moieties are needed to stabilize the particles.



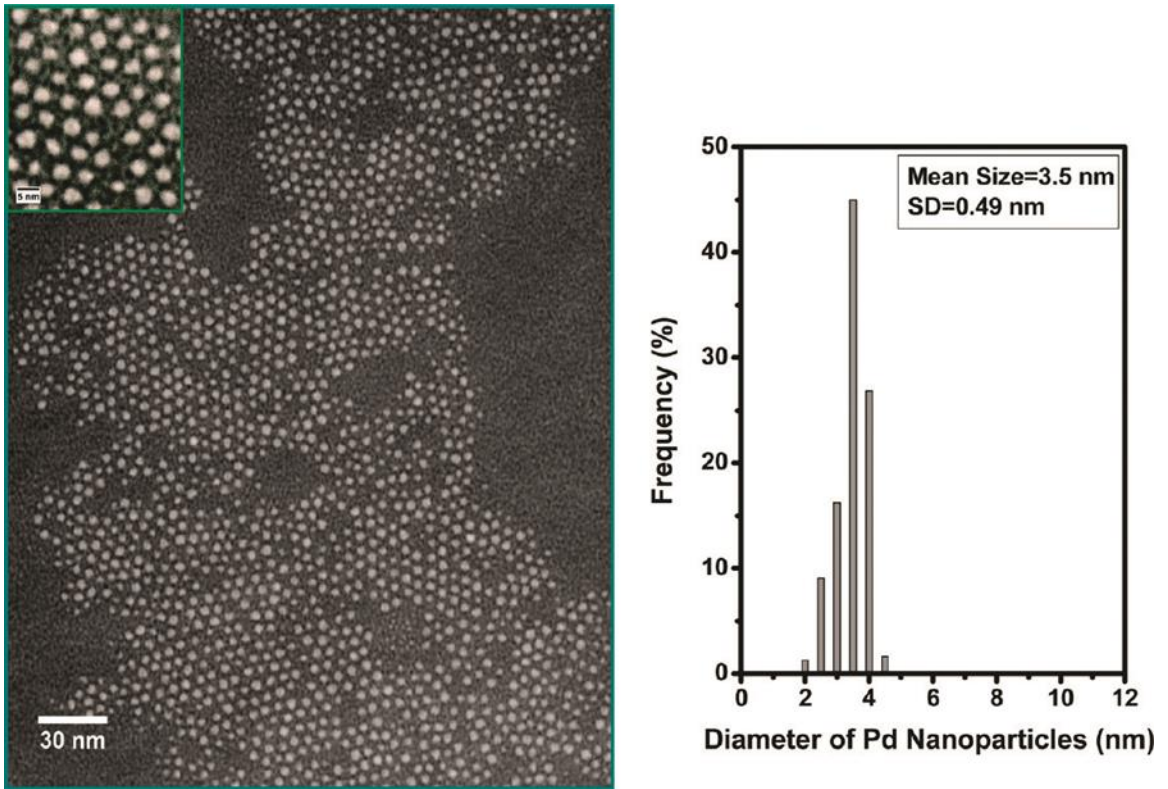


**Figure 1.7** TEM image and corresponding histogram of Pd nanoparticles, stabilized by the functional solvent, DMSO (Liu et al. 2010).

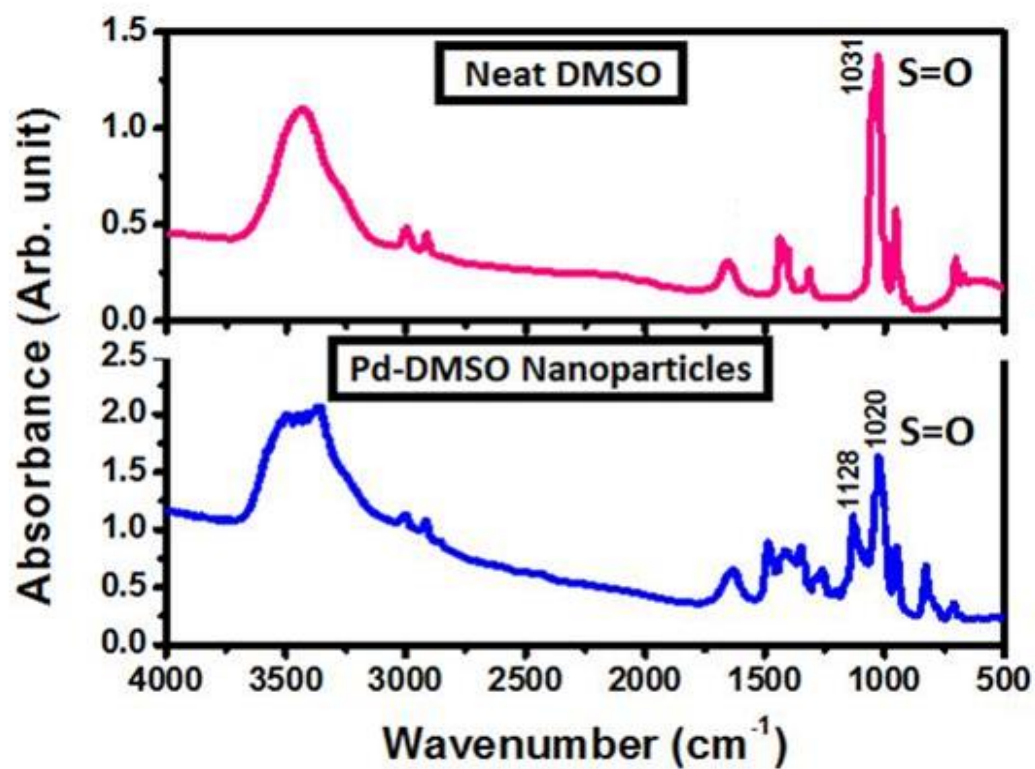


**Figure 1.8** FT-IR spectra of neat DMSO and Pd nanoparticles synthesized in DMSO (Liu et al. 2010).

## **1.7 Nanoparticle Processing Techniques**

Nanoparticles exhibit very unique and highly size-dependent properties as mentioned above, therefore, it is essential to explore methods by which nanoparticles of controlled sizes and shapes can be produced. It is possible to directly produce monodisperse nanoparticle samples by controlled-growth synthesis procedures, such as seeded growth methods (Nikhil R. Jana et al. 2001b; Liu et al. 2009) and citrate reduction methods (Ji et al. 2007; Nikhil R. Jana et al. 2001a), however, these procedures can often be tedious and produce low concentrations of nanoparticle samples. To eliminate the need for synthesis procedures to produce nanoparticles of highly size-controlled sizes, several nanoparticle post-processing techniques have been developed. Methods that have been previously employed to size-selectively fractionate nanoparticle dispersions include size-exclusion liquid chromatography (Wilcoxon et al. 1998), high pressure liquid chromatography (Jimenez et al. 2003; Fischer et al. 1989), diafiltration (Sweeney et al. 2006), and gel electrophoresis (Hanauer et al. 2007). These techniques involve complex equipment, are expensive, and produce relatively low throughputs, thus, new methods for post-synthesis nanoparticle processing need to be developed.

### **1.7.1 Liquid-Liquid Nanoparticle Processing Techniques**

A popular method for post-synthesis nanoparticle processing exploits the interactions between a solvent and anti-solvent in a liquid-liquid system. In this technique, the addition of a liquid anti-solvent can induce nanoparticle precipitation from the original solvent by destabilizing the ligands that are attached to the surfaces of the particles (Murray et al. 2000). This method can be used to further purify nanoparticle dispersions by separating the nanoparticles from the original solvent. This method

typically requires the use of a centrifugation device, can be time intensive, and may produce large amounts of waste with small nanoparticle yields (Murray et al. 2000). This technique can also be utilized as a post-synthesis method to size-selectively separate nanoparticles into very narrow size ranges in order to use the nanoparticles in applications that require extreme control over the nanoparticle size (Vossmeier et al. 1994; Murray et al. 2000) (Murray et al. 1993).

### **1.7.2 Gas-Expanded Liquid Nanoparticle Processing Techniques**

Another method employs a similar solvent-antisolvent ideology, but with a liquid-gas system instead of a liquid-liquid system (Saunders & Roberts 2009; McLeod, Anand, et al. 2005; McLeod, Kitchens, et al. 2005; Anand et al. 2007; Anand et al. 2005). Using this method, a gas-expanded liquid system is created, which eliminates the production of waste and centrifugation is not necessary.

A gas-expanded liquid is a solvent mixture that is composed of an organic solvent containing a dissolved compressible gas, like carbon dioxide (CO<sub>2</sub>) or ethane (Jessop & Subramaniam 2007). In a gas expanded liquid system, the gas dissolves in the organic solvent, creating a gas expanded mixture at greater than atmospheric pressures, but less than the vapor pressure of the pure gas. An illustration of the dissolution of a gas into a liquid to create a gas-expanded liquid is shown in Figure 1.9. As the applied pressure of the pure gas increases, the amount of gas dissolved in the organic phase increases, thus increasing the overall volume of the liquid solvent (Jessop & Subramaniam 2007). Furthermore, as the applied pressure of the gas is changed, the physico-chemical properties and the composition of the solvent can be tuned to behave more like a gas (at higher pressures) or more like the solvent (at lower pressures). Gas expanded liquid

systems also offer enhanced transport properties and higher gas miscibility as compared to organic solvents alone (Jessop & Subramaniam 2007).

There are three classes of CO<sub>2</sub> gas expanded liquids, Class I, II, and III, which are based on the solubility of CO<sub>2</sub> within the liquid (Scurto et al. 2009; Jessop & Subramaniam 2007). Table 1.2 lists a short comparison of the volumetric expansion for the different classes of solvents. Class I liquids, like water, do not easily dissolve CO<sub>2</sub> and with no appreciable volumetric expansion (Scurto et al. 2009; Jessop & Subramaniam 2007). Class II liquids expand considerably upon dissolving large amounts of CO<sub>2</sub>. Examples of Class II liquids include most traditional organic solvents (hexane, methanol, ethyl acetate) and these liquids experience extreme changes in physical properties (as described above) when used as a gas expanded liquid (Scurto et al. 2009; Jessop & Subramaniam 2007). Class III liquids (ionic liquids, liquid polymers, crude oil) dissolve smaller amounts of CO<sub>2</sub> and expand only moderately due to their poor capability of dissolving CO<sub>2</sub> (Scurto et al. 2009; Jessop & Subramaniam 2007). Thus, it is important to understand both how CO<sub>2</sub> dissolves in a liquid and the degree to which the liquid volumetrically expands, and this topic will be revisited in Chapter 5 for the gas expanded DMSO system.

CO<sub>2</sub> gas expanded liquids have highly tunable solvent properties, which can be exploited by adjusting the applied CO<sub>2</sub> pressure in order to vary the solvent strength of organic solvents (J. Liu, Anand, et al., 2006; McLeod, Kitchens, et al., 2005; J. Zhang et al., 2001). It has been reported that CO<sub>2</sub> can be used as an anti-solvent to induce a controlled nanoparticle precipitation process in a gas expanded liquid system for aliphatic ligand-stabilized nanoparticles dispersed in organic solvents (e.g., hexane) (McLeod,

Anand, et al. 2005; Anand et al. 2005; Anand et al. 2007; Saunders & Roberts 2009). However, the work presented in this dissertation (Chapter 5) focuses on investigating the dispersibility of Au nanoparticles in a new CO<sub>2</sub>-gas expanded liquid system, where DMSO is used as both a solvent and a functional solvent for nanoparticle stabilization. For comparison purposes that are particularly relevant to the work presented Chapter 5, the volumetric expansion of CO<sub>2</sub>+hexane and CO<sub>2</sub>+DMSO is shown in Figure 1.10, whereby both of the solutions expand considerably upon CO<sub>2</sub> pressurization.

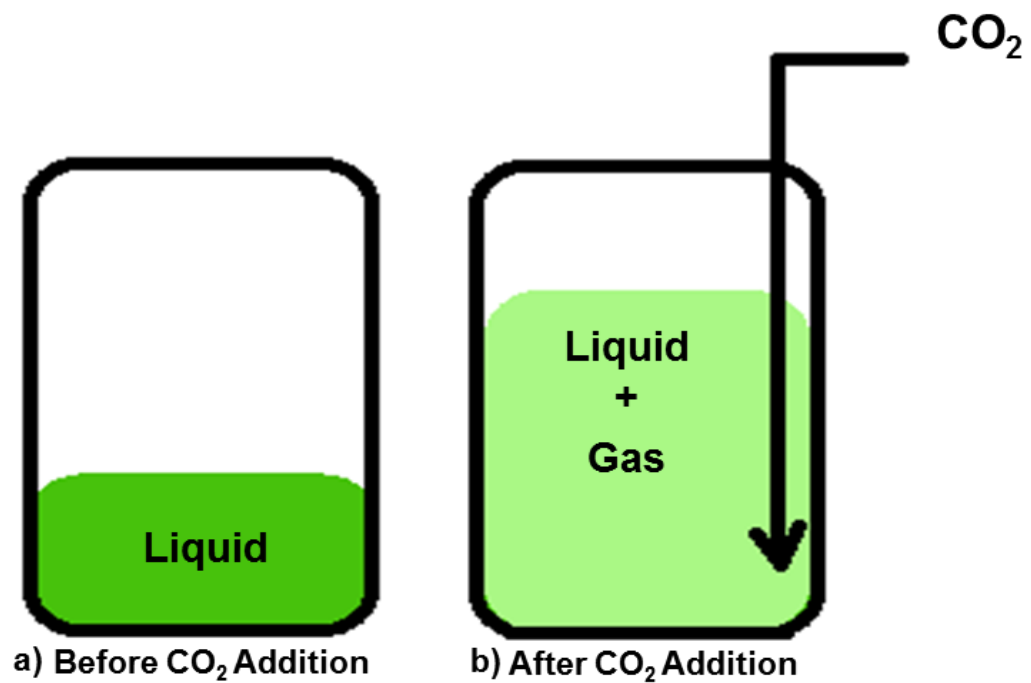


**Figure 1.9** An illustration to describe the dissolution of a gas (e.g., CO<sub>2</sub>) into a liquid to create a gas-expanded liquid where the solution is a) a neat liquid before the addition of the gas and b) a mixture of a liquid and gas (e.g., a gas-expanded liquid) after the addition of the gas.

| Class      | Solvent               | P (bar) | Volumetric Expansion (%) | wt % CO <sub>2</sub> | mol% CO <sub>2</sub> |
|------------|-----------------------|---------|--------------------------|----------------------|----------------------|
| <b>I</b>   | H <sub>2</sub> O      | 70      | n/a                      | 4.8                  | 2.0                  |
| <b>II</b>  | MeCN                  | 69      | 387                      | 83                   | 82                   |
|            | 1,4-dioxane           | 69      | 954                      | 79                   | 89                   |
|            | DMF                   | 69      | 281                      | 52                   | 65                   |
| <b>III</b> | [bmim]BF <sub>4</sub> | 70      | 17                       | 15                   | 47                   |
|            | PEG-400               | 80      | 25                       | 16                   | 63                   |
|            | PPG-2700*             | 60      | 25                       | 12                   | 89                   |

\*data obtained at 35°C

**Table 1.2** Comparison of the different classes of solvents and the corresponding volume expansion behavior at different CO<sub>2</sub> pressures and at 40°C (Heldebrant et al. 2006; Scurto et al. 2009; Jessop & Subramaniam 2007).



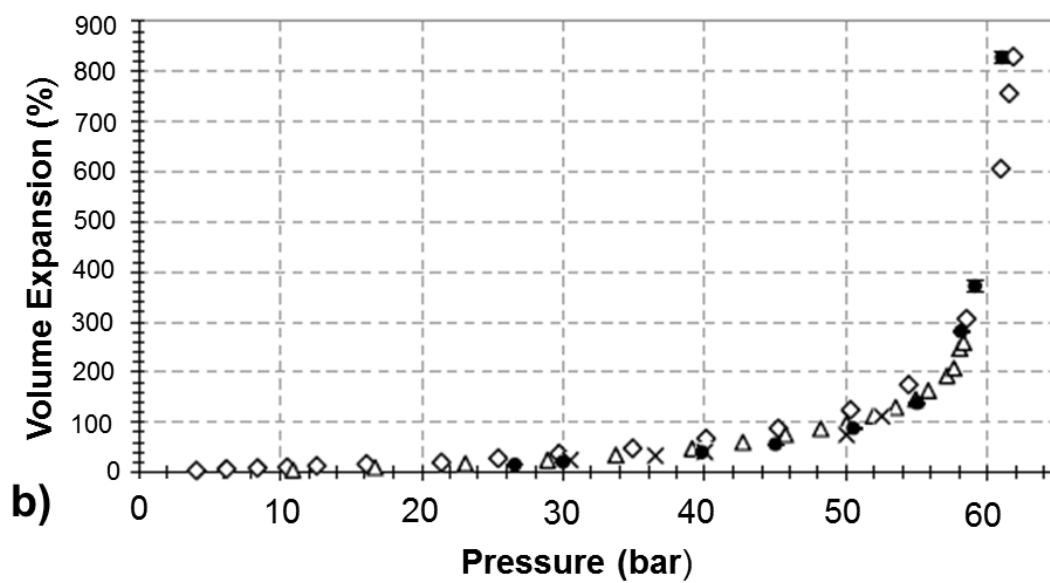
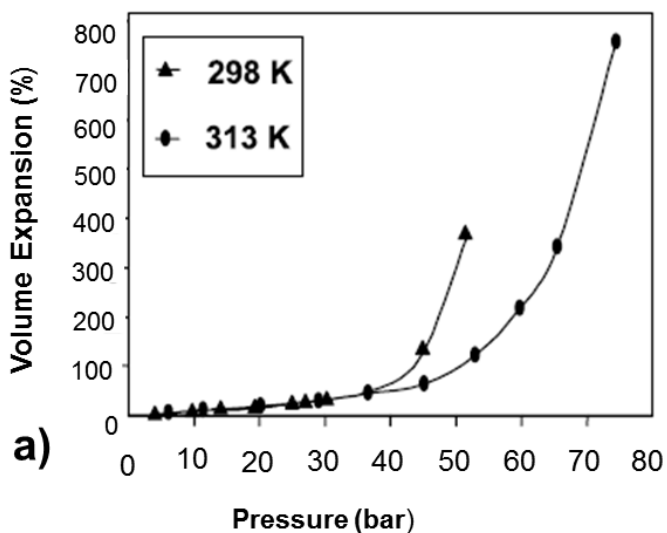


**Figure 1.10** Volumetric expansion of a) CO<sub>2</sub>+hexane (Mukhopadhyay 2003) and b) CO<sub>2</sub>+DMSO (adapted from (Calvignac, Letourneau, et al. 2009; Kordikowski et al. 1995; Rajasingam et al. 2004; Elvassore et al. 2002)).

## **1.8 Summary of Chapters**

The overall goals of this research were to provide a sustainable method to produce nanoparticles by simplifying current nanoparticle synthesis techniques (e.g., utilizing DMSO as a functional solvent), and then utilizing the already existing post-synthesis nanoparticle processing techniques to produce nanoparticles and clusters of nanoparticles with specific sizes (e.g., using CO<sub>2</sub>-gas expanded technologies to induce nanoparticle clustering). Moreover, this research has provided depth to understanding nanoparticle dispersibility in a new and unique solvent under a variety of conditions.

### **1.8.1 Chapter 2 – Cobalt Nanoparticle Synthesis using Dimethyl Sulfoxide as a Functional Solvent**

The ability to easily produce Co nanoparticles is typically a time consuming, and often difficult task due to the tendency of magnetic nanoparticles to readily oxidize. This chapter describes a simple solvent-based synthesis method to produce amorphous Co nanoparticles using DMSO as a functional solvent at ambient conditions, where the DMSO can function as both the solvent and the stabilizing ligand. It was found that the DMSO sufficiently protects the surface of the Co nanoparticles from oxidation at ambient conditions. In addition, the Co nanoparticles can be conveniently removed from DMSO by using acetone as a liquid anti-solvent, and the Co nanoparticles can be easily re-dispersed in a fresh solution of DMSO. This synthesis technique provides a quick and straight-forward method to produce Co nanoparticles in an FDA-approved solvent (DMSO), which is particularly relevant to the biomedical imaging applications (e.g., MRI) discussed above.

### **1.8.2 Chapter 3 – Clustering and Solvation of Cobalt Nanostructures in Dimethyl Sulfoxide**

Typical metal nanoparticle clustering techniques allow for nanoparticles to be controllably aggregated using a variety of techniques, and this can be accomplished by several different methods, including pH variations in the nanoparticle solution as well as adding polymer surfactants. This chapter reports a Co nanoparticle clustering technique that can be used to aggregate individual Co nanoparticles (that are produced from Chapter 2) into various cluster sizes as a function of the reaction temperature. Moreover, it is reported that these Co clusters can be reversibly dissociated into the individual Co nanoparticles by simply adding various co-solvents to the dispersion. At high temperatures, Co nanoparticle solvation by DMSO is weakened due to the added thermal energy of the reaction, thereby forming successively larger Co nanoclusters as a function of the reaction temperature. Then, the adsorbed DMSO molecules present on the surface of the Co nanoparticles are preferentially solvated upon addition of the co-solvent, liberating the individual Co nanoparticles from the clusters. This clustering feature is attributed to the unique solvation properties of DMSO.

### **1.8.3 Chapter 4 – Controlling the Crystallinity and Magnetism of Cobalt Nanoparticles via Thermal Oxidative Treatment**

Producing magnetic nanoparticles of high magnetic and crystalline compositions is gaining significant recent interest due to the ability to use these materials in energy storage and magnetic data storage devices. This chapter describes a technique that can be easily employed to controllably oxidize amorphous Co nanoparticles (that are produced from Chapter 2) by annealing the particles in air. It was found that upon annealing, the

amorphous Co nanoparticles transition into ordered structures of spinel-Co<sub>3</sub>O<sub>4</sub> nanoparticles. Furthermore, annealing induces unique magnetism in the particles, whereby the Co<sub>3</sub>O<sub>4</sub> particles were found to exhibit high coercivity. This particular magnetic property of the Co<sub>3</sub>O<sub>4</sub> nanoparticles is central to the potential use of these particles in magnetic storage devices.

#### **1.8.4 Chapter 5 – Aggregation and Precipitation of Gold Nanoparticle Clusters in CO<sub>2</sub>-Gas Expanded Liquid DMSO Solvent Systems**

Post-synthesis nanoparticles processing methods can be used to produce metal nanoparticles of various sizes. Traditional nanoparticle processing methods have utilized CO<sub>2</sub>-gas expanded liquids to carefully produce nanoparticles of narrow size ranges, however, these nanoparticles contained organic, aliphatic ligands and were dispersed in organic, aliphatic solvents. This chapter explores the dispersibility of Au nanoparticles in various CO<sub>2</sub>-gas expanded DMSO solvents. It was found that Au nanoparticles can be aggregated into clusters as a function of the applied CO<sub>2</sub> pressure, and these clusters could be kinetically precipitated from the mixture as a function of time at high pressures. This chapter demonstrates the versatility of using DMSO as a solvent for nanoparticle synthesis and processing techniques. The findings reported in this chapter also suggest that other CO<sub>2</sub>-gas expanded polar solvents should be explored for their potential use as nanoparticle processing media.

#### **1.8.5 Chapter 6 –Overall Conclusions and Future Work**

This chapter first summarizes the scientific contributions of the research presented in this dissertation and also describes the future directions for this research. In the future

directions sections, two distinct research projects are described which represent extensions of the work that has been described in this dissertation.

The first project involves the synthesis of Au nanoparticles in CO<sub>2</sub>-gas expanded DMSO solutions. Previous work (presented in this dissertation) has indicated that the post-synthesis dispersibility of Au nanoparticles can be manipulated by modest changes in applied CO<sub>2</sub> pressure. The dynamic dispersibility of these particles may be linked to the tunable viscosity upon the application of CO<sub>2</sub> pressure. It is advantageous to synthesize Au nanoparticles in CO<sub>2</sub>-gas expanded DMSO because their surface plasmon absorption band can be monitored during the entire nanoparticle nucleation and growth process using in situ UV visible spectroscopy. Furthermore, it is postulated that nanoparticle size (and even shape) may be manipulated by simply changing the amount of applied CO<sub>2</sub> pressure during nanoparticle nucleation and growth.

The second project describes future directions for Co<sub>3</sub>O<sub>4</sub> thin film formation. Thin films that are composed of magnetic materials can be used for magnetic recording of data. Highly-ordered structures of Co<sub>3</sub>O<sub>4</sub> nanoparticles will be prepared by using the simple Co synthesis technique that is described in Chapter 2 of this dissertation along with annealing, as described in Chapter 4. Moreover, CO<sub>2</sub>-gas expanded DMSO may be used as a viable method to controllably deposit Co<sub>3</sub>O<sub>4</sub> nanoparticles on a substrate. This project will also examine the unique magnetic properties of these Co<sub>3</sub>O<sub>4</sub> particles with the primary purpose of testing these magnetic thin film materials into magnetic recording devices.

## **Chapter 2**

### **The Synthesis and Arrested Oxidation of Amorphous Cobalt Nanoparticles using Dimethyl Sulfoxide as a Functional Solvent**

Magnetic nanoparticles exhibit a strong tendency to become overly oxidized and unstable during synthesis, ultimately leading to nanoparticle agglomeration and degradation. Capping agents can be used during nanoparticle synthesis to provide particle surface coverage and to improve nanoparticle dispersibility in solution, while preventing excessive oxidation and agglomeration. This chapter describes a technique to synthesize amorphous  $3.7 \pm 1.5$  nm cobalt (Co) nanoparticles using dimethyl sulfoxide (DMSO) to function as both the stabilizing agent and the solvent for Co nanoparticles via a quick, solvent-based reduction of  $\text{Co}^{2+}$  with  $\text{NaBH}_4$  in a DMSO solvent. This synthesis method demonstrates that Co nanoparticles can be successfully synthesized by simply using DMSO as a functional solvent, thereby avoiding excessive oxidation and agglomeration in solution.

## 2.1 Introduction

Nano-scale materials exhibit very unique and size-dependent properties that benefit a wide variety of applications. Specifically, devices constructed of nanomaterials have interesting optical (Beecroft & Ober 1997; Murphy et al. 2005), mechanical (Shi et al. 2006; Zhang & Singh 2004), electronic (Zhang & Singh 2004; McConnell et al. 2000), and magnetic properties (Frey et al. 2009; Pankhurst 2003). Thus, developing methods and techniques to precisely control the size and size distribution of magnetic nanoparticles has been of significant contemporary interest, especially in light of the wide variety of applications in which these particles can be employed. In particular, nanoparticles constructed of magnetic materials, such as iron oxide ( $\text{Fe}_2\text{O}_3$  and  $\text{Fe}_3\text{O}_4$ ) and cobalt (Co), have biomedical applications in part due to their magnetic properties (Gellissen et al. 1999; Park et al. 2005; Hyeon 2003; Bao et al. 2010; Della & Lin 2010; Kobayashi et al. 2003; Frey et al. 2009). Co metal is ferromagnetic at the bulk scale, but as the dimensions of the metal are decreased to below 10 nm, it can become superparamagnetic, meaning that higher magnetic susceptibility and no hysteresis pattern is observed (Bao & Krishnan 2005; Bao et al. 2005; Bean & Livingston 1959). Furthermore, excessive oxidation of Co nanoparticles can lead to loss of magnetism and dispersibility (Lu et al. 2007). Therefore, it is particularly important to carefully control the synthesis conditions of Co nanoparticles in order to successfully protect the nanoparticles from unwanted oxidation and degradation.

There are a variety of different solvent-based methods that are traditionally used to produce magnetic nanoparticles (Ghosh et al. 2005; Wang et al. 2004; Park et al. 2002; Kobayashi et al. 2003; Bao et al. 2005; Bao et al. 2010; Bao et al. 2007; Puentes et al.

2002), but these methods often require the use of expensive solvents and reagents as well as elevated synthesis temperatures and prolonged reaction times. Recently, these methods have been replaced and modified by focusing on greener, more sustainable, and alternative synthesis techniques (Nadagouda & Varma 2007; Polshettiwar et al. 2009). It is important to emphasize that these popular techniques often require the use of additional reagents to function as capping/stabilizing agents that are attached directly to the surface of the nanoparticles. As such, stabilizing agents play a critical role in nanoparticle synthesis. Strong interactions between neighboring nanoparticles, such as van der Waals forces and even magnetic attractions, can lead to nanoparticle agglomeration (Cushing et al. 2004). In addition, stabilizing agents also function to suppress nanoparticle growth by effectively passivating the surface of newly formed metal clusters and seeds that could otherwise agglomerate due to interparticle attractions (Liu et al. 2009). However, there are some potential disadvantages of using stabilizing agents. For example, stabilizing agents that are covalently bound to the nanoparticle surface could restrict access to the surface of the nanoparticle, which is an important consideration for many surface-dependent applications like catalysis. Furthermore, using stabilizing agents that are different from the solvent often require excessive downstream processing to eliminate waste (and excess stabilizing agents). Thus, nanoparticle stability must be maintained in order to prevent degradation and maintain favorable magnetic behavior (Lu et al. 2007).

One method to improve nanoparticle synthesis could be to develop a synthesis technique that eliminates excess reagents by combining nanoparticle stabilization and solvation through the use of a single, multifunctional solvent system. The molecule dimethyl sulfoxide (DMSO) has been found to sufficiently serve as both the solvent and



the stabilizing agent (Liu et al. 2010). In this dissertation, this characteristic of the solvent will be termed “functional solvent.” Employing a functional solvent to synthesize nanoparticles can allow for improved access to a nanoparticle’s surface and its surface energy. More importantly, using a functional solvent can impact nanoparticle magnetic saturation capacities because bulky stabilizing agents, such as tetraoctyl ammonium bromide, polyethylene glycol, and oleic acid, that are directly attached to the nanoparticle surfaces have been reported to impact the magnetic behavior of the particle (Duan et al. 2008; Crespo et al. 2004).

Thus, a functional solvent can concomitantly function as the solvent as well as the stabilizing agent for nanoparticles, thereby allowing more complete and unrestricted access to the nanoparticle surface. Further requirements for a functional solvent to be effective includes the ability to dissolve all reagents and provide sufficient interaction with the nanoparticle surface in order to keep the nanoparticles solvated and dispersed in solution. Moreover, nanoparticle synthesis using a functional solvent reduces the number of reagents employed during synthesis and eliminates the need for post-processing separations of any excess stabilizing agents. This provides a direct route for generating nanoparticles with high purity and yield.

Recently, dimethyl sulfoxide (DMSO) has been successfully employed as a functional solvent to be utilized as both the solvent and stabilizing agent to produce  $3.5 \text{ nm} \pm 0.5 \text{ nm}$  monodisperse nanoparticles composed of a noble metal, i.e. palladium (Pd), via a simple, fast, homogeneous reduction of a Pd salt using  $\text{NaBH}_4$  (Liu et al. 2010), as discussed in Section 1.6. Even though DMSO served as the only stabilizing agent, the Pd nanoparticles that were produced possessed a high degree of stability, i.e. nanoparticles

agglomeration, and precipitation was not observed. Furthermore, this study revealed that the DMSO molecule must exist as a resonance hybrid structure as coordination occurs between the oxygen and sulfur groups of the molecule. Thus, DMSO can serve as an essential component in the formation and stabilization of uniform noble metal Pd nanoparticles, and no additional molecules or moieties are needed to stabilize the particles. The unique properties of DMSO are discussed in more detail in Section 1.5, and these discussions reveal that DMSO is a commonly used reactant and is very effective as a solvent. As such, DMSO is particularly interesting to explore as a functional solvent in nanoparticle synthesis because of the potential magnetic and biomedical applications.

In this chapter, a technique is presented for the synthesis of amorphous Co nanoparticles using DMSO as a functional solvent. Then, the interaction between DMSO and the Co nanoparticles is investigated and it is found that the DMSO can serve as a stabilizing agent for these Co nanoparticles. The Co nanoparticles obtained by this process were found to be stable, even when exposed to excessive amounts of air, thereby further indicating DMSO plays an important role in preventing unwanted and excessive Co nanoparticle oxidation, agglomeration, and subsequent precipitation.

## **2.2 Experimental**

### **2.2.1 Materials**

Dimethyl sulfoxide ((CH<sub>3</sub>)<sub>2</sub>SO, 99.9%) was obtained from BDH Chemicals. Deionized ultrafiltered water (DI-H<sub>2</sub>O) was obtained from Fisher Scientific. Cobalt (II) chloride hexahydrate (CoCl<sub>2</sub>\*6H<sub>2</sub>O, 99+%) was obtained from Strem Chemicals. Sodium

borohydride ( $\text{NaBH}_4$ , 99%) was obtained from Sigma Aldrich. Acetone ( $(\text{CCH}_3)_2\text{CO}$ ) was obtained from BDH. Nitrogen (UHP grade) was obtained from Airgas.

### 2.2.2 Co Nanoparticle Synthesis in DMSO

Co nanoparticles were synthesized via a solvent-based reduction of  $\text{Co}^{2+}$  in a solution of DMSO using  $\text{NaBH}_4$  as the reducing agent at room temperature. In a typical reaction, 50 mL of DMSO was added to a 250 mL flask along with a magnetic stir bar, and this flask was continuously stirred ( $\sim 700$  rpm) on a magnetic stir plate prior to the addition of any other reagents. An airtight apparatus was constructed over the flask to ensure the contents of the flask would be free of possible external oxygen contamination from exposure to air. A digital image of the set-up is shown in Figure 2.1a. Nitrogen gas ( $\text{N}_2$ ) was purged through the system and bubbled through the DMSO solution starting 30 minutes prior to the addition of any reagents and continuing throughout the entire duration of the reaction. A 0.05 M solution of  $\text{CoCl}_2 \cdot 6\text{H}_2\text{O}$  was added to the reaction flask via the injection port, as well as a 0.05 M solution of  $\text{NaBH}_4$  using the appropriate reagent ratios. For example, for a ratio of  $[\text{Co}^{2+}]:[\text{NaBH}_4]$  of 4:7, 7020  $\mu\text{L}$  of a 0.05 M  $\text{NaBH}_4$  solution was added (through multiple sequential injections using a 1000  $\mu\text{L}$  pipette) to the reaction flask that already contained 4000  $\mu\text{L}$  of 0.05 M Co salt solution. It is important to note that both the Co salt ( $\text{CoCl}_2 \cdot 6\text{H}_2\text{O}$ ) and  $\text{NaBH}_4$  were prepared in a solution of DMSO. The Co salt displayed favorable solubility upon the addition of DMSO, contrary to the  $\text{NaBH}_4$ , which needed to be heated using warm tap water and mixed using a vortex mixer for several minutes before dissolving in the DMSO. Upon addition of the reagents to the reaction flask, the solution evolved from a bright blue color

to a dark grayish color as shown in Figure 2.1. The reaction was stirred and purged with  $N_2$  for 2 hours after the addition of the reactants. After 2 hours, the  $N_2$  purge was stopped, the flask was securely capped, and the contents of the reactor were allowed to continuously stir for 24 hours.

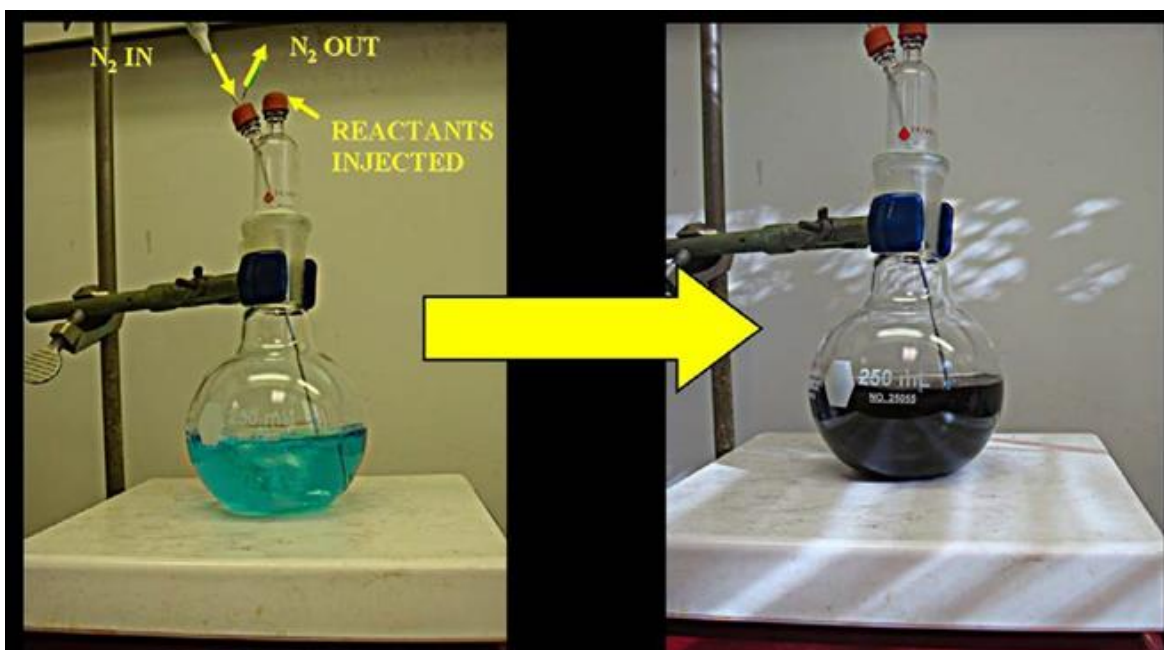


**Figure 2.1** Nitrogen-purged apparatus containing DMSO solution and a) dissociated  $\text{CoCl}_2 \cdot 6\text{H}_2\text{O}$  salt and b) Co nanoparticle solution after the addition of  $\text{NaBH}_4$ . The color change from blue (a) to dark gray (b) indicates the presence of Co nanoparticles.

### 2.2.3 Characterization Techniques

*UV Visible Spectroscopy (UV-vis)* - UV-vis absorption measurements were made on a Cary 3E UV-vis spectrophotometer by pipetting 2 mL of the Co nanoparticle dispersion into a 1 cm path length quartz cuvette.

*Fourier Transform Infrared Spectroscopy (FT-IR)* – FT-IR spectroscopy was performed using a Nicolet Avatar 360. A solid sample of Co nanoparticle powder was obtained by isolating the Co nanoparticles from the DMSO solvent using acetone as an anti-solvent in combination with centrifugation. Subsequently, a thin pellet of the Co nanoparticles (5 mg) and KBr (100 mg) was formed using a pellet press. A neat KBr pellet was utilized as the background for the FT-IR spectrum of the Co nanoparticles. FT-IR spectra of neat acetone and DMSO were also obtained by placing a few drops of each solvent between two KBr salt disk windows in a standard liquid cell holder.

*Transmission Electron Microscopy (TEM)* - TEM was used to investigate the morphology of the Co nanoparticles using a Zeiss EM 10 TEM at an operating voltage of 60 kV. TEM samples were prepared by placing a single drop of sample onto a carbon type B, 300 mesh copper grid. The grid was contained in a plastic petri dish and placed in the vacuum oven to dry for several days prior to TEM analysis. The average particle size and size distribution of the Co nanoparticles were obtained using the Image J software package to size hundreds of particles from multiple TEM images taken from the same sample grid.

*X-ray diffractometry (XRD)* - XRD was performed by Intertek (Allentown, PA) and was used to analyze the crystallinity and surface oxidation of the Co nanoparticles. The sample was prepared by placing a portion of the Co nanoparticle powder in the

recessed area of a low-background mount and pressed flat using a glass slide. The sample was scanned on the Panalytical X'Pert Pro MPD over the range  $3^\circ \leq 2\theta \leq 85^\circ$  using Co-K $\alpha$  radiation, a  $0.033^\circ$  step size, and an 400 sec/step count time. Incident beam optics included a  $\frac{1}{4}^\circ$  fixed divergence slit, a 15 mm beam mask, 0.04 rad Soller slits, and a  $\frac{1}{2}^\circ$  fixed anti-scatter slit. Diffracted beam optics included a 5 mm fixed anti-scatter slit and anti-scatter shield, 0.04 rad Soller slits, the Fe filter, and the X'Celerator strip detector with an active length of  $2.122^\circ$ . A blank zero-background mount was also scanned to more accurately determine the contribution of the sample mount and instrument background to the sample data.

*X-ray photoelectron spectroscopy (XPS)* – XPS measurements were performed in order to investigate the surface oxidation of the Co nanoparticle powder. These measurements were performed on the Co nanoparticle powder using a load-locked Kratos XSAM 800 surface analysis system equipped with a hemispherical energy analyzer. The base pressure of this ion- and turbo-pumped system was  $8 \times 10^{-9}$  torr as read on a nude ion gauge. The XPS analyzer was a 127 mm radius double-focusing concentric hemispherical energy analyzer (CHA) equipped with an aberration compensated input lens (ACIL). XPS spectra were recorded in the fixed analyzer transmission (FAT) mode with a pass energy of 80 eV, appropriate for acquisition of medium resolution, high signal-to-noise spectra. The magnification of the analyzer in the FAT mode was selected to collect electrons from the smallest allowable ( $5 \text{ mm}^2$ ) area on the specimen. The resolution of the instrument at the operating parameters was measured from FWHM of the Ag3d $_{5/2}$  peak to be 1.0 eV. The XPS energy scale was calibrated by setting the Ag3d $_{5/2}$  line on clean silver to exactly 368.3 eV referenced to the Fermi level. Due to

specimen charging during X-ray irradiation, the energy axis of each XPS spectra has been shifted to make the C1s binding energy line equal to 285.0 eV, which is a standard hydrocarbon energy (C-H and C-C bonds) used to reference charge affected materials. The potential measured on a typical sample was 0.5 V. The photoelectrons were excited by a water-cooled, conventional (i.e., non-monochromatic) dual anode X-ray gun equipped with an Al window. The angle of the incidence of the x-ray beam with the specimen normal was 51.5°. MgK $\alpha$  (1253.6 eV) radiation was used exclusively. In cases when the peaks were low in amplitude, such as S2p, the Savitsky-Golay (Savitzky & Golay 1964) smoothing routine was used in order to help determine the peak binding energies. The XPS surface composition was calculated based on the Scofield cross-sectional values (Scofield 1973) accounting for the instrumental transmission function in the FAT mode of operation. After compound synthesis, the powdered specimens were transferred to the surface laboratory under a nitrogen atmosphere. The specimen was pressed into double-sided carbon tape to a thickness which insured that the emitted photoelectrons would originate only from the specimen.

*Scanning Electron Microscope (SEM)* – SEM was linked to an energy dispersive X-ray spectrometer (EDS) in order to obtain images of the Co nanoparticle powder and information on the elemental composition of the Co nanoparticle powder using a JEOL JSM-7000F SEM at an operating voltage of 20 kV. SEM images were obtained by covering a SEM sample holder with double-sided carbon tape and adhering the dried Co nanoparticle powder to the tape. The SEM images shown herein are digital images. EDS microanalysis was performed by obtaining an average of twelve different spectra taken from representative areas of the Co nanoparticle powder sample.



*Temperature Programmed Desorption (TPD)* - TPD in combination with Mass Spectrometry was performed by Micromeritics (Norcross, GA) in order to determine the amount of residual DMSO present on the surface of the dried Co nanoparticle powder. These experiments were carried out using a 200 amu Cirrus model quadruple mass spectrometer. A sample tube was prepared by loading glass wool in the bottom, followed by 0.005g of the Co nanoparticle sample. The instrument was equilibrated at 25°C. Helium gas was used as the carrier gas for mass spectrometry analysis and was delivered at a rate of 50cc/min. The mass spectrometry analysis was initiated and the desorption of the Co nanoparticles was monitored using AutoChem II 2904 V4.03 software with a temperature range from 25 - 1000°C. A measurement was taken once every second. The sample was maintained at 1000°C for 10 minutes before cooling to room temperature.

## **2.3 Results and Discussion**

### **2.3.1 Complete Reduction of Co Salt to Form Co Nanoparticles**

A series of experiments were performed in order to determine the minimum amount of reducing agent (NaBH<sub>4</sub>) required to achieve complete reduction of the Co salt and to produce nanoparticles. An appropriate amount of the Co<sup>2+</sup> salt and NaBH<sub>4</sub> reagents were added to each flask to achieve [Co<sup>2+</sup>]:[NaBH<sub>4</sub>] reagent ratios of 4:1, 4:3, 4:5, 4:6, 4:7, 4:9. For each reaction, the concentration of the Co salt solution added to the reaction was kept constant along with the stir rate and the purge time/reaction time, and the only variable was the amount of reducing agent added. Each reaction was continuously stirred and purged for 2 hours after the addition of the reactants, then the flask was securely sealed, and the reaction was stirred at a constant stir rate (~700 rpm) for 24 hours. After each experiment was complete, some of the solution was removed

from each sample and placed in a 20 mL vial, and each of the vials were placed on a permanent magnet in order to separate the larger (bulk) Co structures from the Co nanostructures that are responsive to the magnet and remain dispersed in solution. These larger Co structures are simply aggregates of the smaller Co nanoparticles, and are therefore composed of the same material as the larger Co structures. It is necessary to separate the larger Co structures from the Co nanoparticles because the larger structures result in a lack of transmittance due to their size and therefore interfere with the resulting spectra during UV-vis analysis. Thus, the magnet-induced removal of the larger Co structures prior to UV-vis spectroscopy analysis allowed the results to be representative of absorption of the Co salt in solution without interference from the large Co structures. Additionally, a sample of the Co nanoparticle structures resulting from the addition of each of the different concentrations of reducing agent was analyzed using TEM.

The results from the UV-vis analysis of the different Co salt reduction experiments (corresponding to each of the  $[\text{Co}^{2+}]:[\text{NaBH}_4]$  reagent ratios given above) are shown in Figure 2.2. An initial UV-vis curve, corresponding to the spectrum with the largest overall absorption in Figure 2.2, was obtained for the Co salt solution prior to the addition of any reducing agent. The peak for this Co salt solution is centered at 679 nm and dissipates as the amount of reducing agent added to the reaction mixtures is increased. Specifically, as the  $[\text{Co}^{2+}]:[\text{NaBH}_4]$  ratio increased from 4:1 to 4:7 and beyond, the absorbance of this band decreased, indicating that complete reduction of the Co salt solution is achieved at a  $[\text{Co}^{2+}]:[\text{NaBH}_4]$  ratio of 4:7. The UV-vis spectrum for the  $[\text{Co}^{2+}]:[\text{NaBH}_4]$  ratio of 4:9 shows that excess reducing agent is not necessary in order to achieve a complete reduction of the Co salt and form nanoparticles since there is

no peak at this concentration. Also, it is important to note that the spectrum in Figure 2.2 that corresponds to the 4:9 ratio, while still flat, seems to be increasing in overall absorbance compared to the 4:7 concentration sample. This phenomenon is attributed to large agglomerations of Co nanoparticles that have aggregated within the UV cuvette causing an increase in sample absorbance. An increase in observed particle size can affect an increase in sample absorbance during UV-vis analysis (Nath and Chilkoti 2002; Templeton et al. 2000).

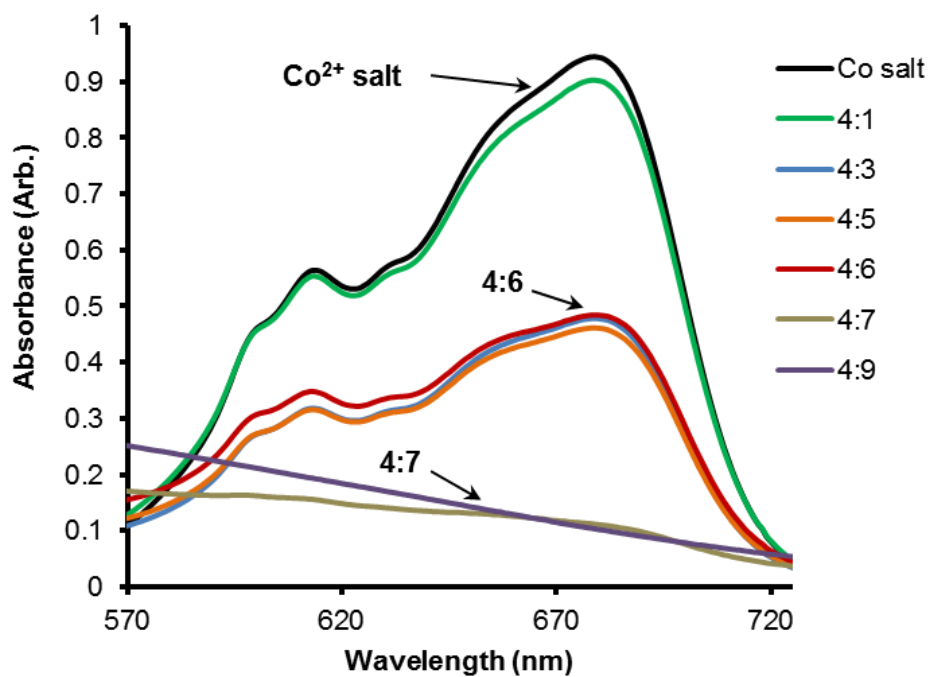


**Figure 2.2** UV-visible spectra for the disappearance of the Co salt peak to form Co nanoparticles using a functional solvent, DMSO. Shown here, the Co salt peak is a 0.05M solution of Co<sup>2+</sup> salt solution (prior to the addition of NaBH<sub>4</sub> reducing agent). Then, the amounts of [Co<sup>2+</sup>]:[NaBH<sub>4</sub>] were increased to 4:1, 4:3, 4:5, 4:6, 4:7, 4:9.

It should be noted here that these Co nanoparticles that were synthesized in and stabilized by the DMSO functional solvent can be agglomerated using a magnet. Figure 2.3 shows a digital image of the magnetic response of a 1 mL sample of DMSO-stabilized Co nanoparticles. The left side of the image shows the Co nanoparticle dispersion at  $t = 0$ , and the right side of the image shows the agglomeration of the Co nanoparticles at the meniscus of the DMSO solvent after  $t = 10$  minutes. The Co nanoparticles can move to the meniscus of the solvent when the magnet is placed at the top because of the inherent magnetic properties of Co. This simple demonstration illustrates that it is possible to synthesize nanoparticles with magnetic properties using a functional solvent such as DMSO.

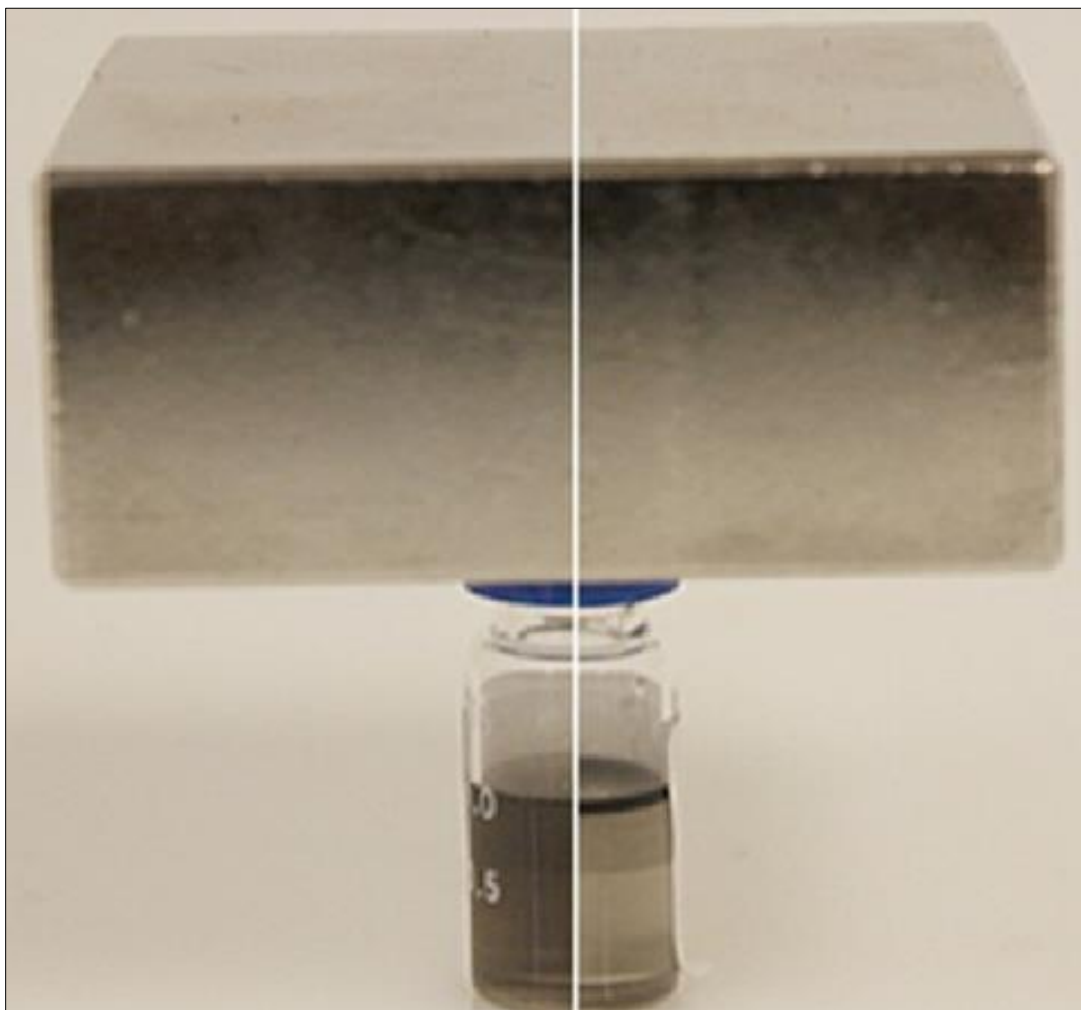


**Figure 2.3** Co nanoparticles stabilized by DMSO in the presence of a magnet. The left image shows a representative dispersion of the Co nanoparticles at  $t = 0$  minutes and the right image shows the collection of the Co nanoparticles on the meniscus of the DMSO solvent due to their attraction to the magnet placed on the top of the vial at  $t = 10$  minutes.

TEM analysis of each of the samples that were prepared using different  $[\text{Co}^{2+}]:[\text{NaBH}_4]$  reagent concentrations was also performed to determine if there were any concentration-related effects on the Co nanoparticle size and distribution. The TEM image and corresponding histogram for the  $[\text{Co}^{2+}]:[\text{NaBH}_4]$  ratio of 4:7 is shown in Figure 2.4. As can be observed in this figure, the average size of the Co nanoparticles is  $3.7 \pm 1.5$  nm. These results suggest that the DMSO alone can efficiently function as a capping agent to suppress particle growth and produce relatively uniform Co nanoparticles. More detailed TEM imaging analysis is provided in Appendix A, which shows the TEM images and histograms for the Co nanoparticle sizes and distributions that correspond to the samples obtained from the other  $[\text{Co}^{2+}]:[\text{NaBH}_4]$  ratio experiments; however, there is no substantial difference in average size for any of the different reagent concentration experiments.

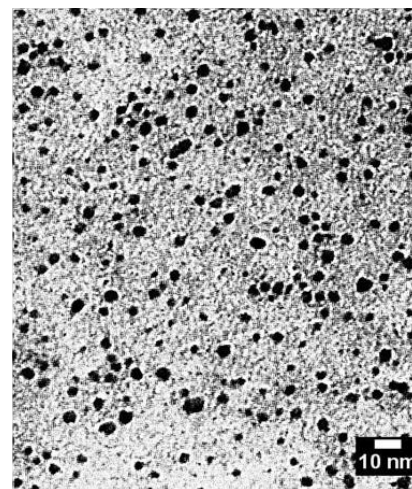
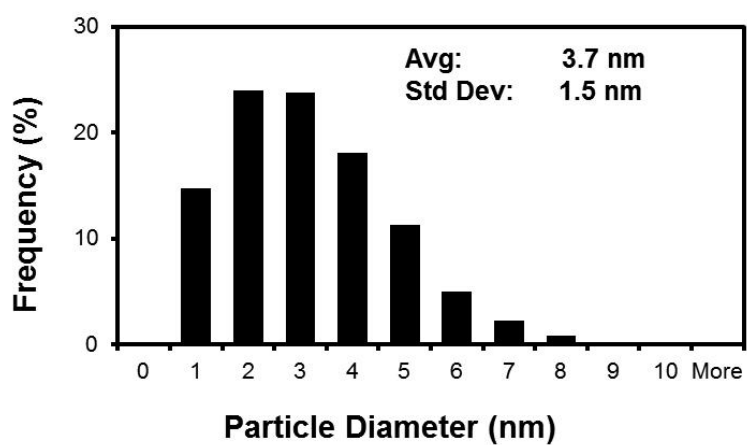


**Figure 2.4** TEM image and corresponding histogram for Co nanoparticles synthesized in the presence of the functional solvent, DMSO.



### **2.3.2 Precipitation of Co Nanoparticles from DMSO Using Acetone**

A popular method for nanoparticle purification and precipitation exploits the interactions between a solvent and anti-solvent in a liquid-liquid system. Adding an anti-solvent to nanoparticle dispersions can induce nanoparticle precipitation from the original solvent and can therefore be used to further purify nanoparticle dispersions by separating the nanoparticles from the solvent (Thorat & Dalvi 2012; Sigman et al. 2004; Murray et al. 2000; Saunders & Roberts 2011b). This technique is often used after synthesis to size-selectively separate nanoparticles into very narrow size ranges in order to use the nanoparticles in applications that require extreme control over the nanoparticle size (Vossmeier et al. 1994; Murray et al. 2000). Conveniently, the Co nanoparticles dispersed in and stabilized by DMSO can be precipitated by simply adding a liquid anti-solvent to the dispersion. For example, acetone serves as an excellent anti-solvent for the DMSO-stabilized Co nanoparticle solution because acetone is miscible with DMSO, but the carbonyl (C=O) group in the acetone molecule will not form hydrogen bonds with the sulfoxide (S=O) group of DMSO. Furthermore, the addition of acetone results in a diminished overall solvent strength of the solvent mixture (DMSO + acetone), thereby reducing the ability of the solvent mixture to stabilize the Co nanoparticle dispersion. The addition of acetone, therefore, promotes interparticle attractions and can ultimately cause nanoparticle precipitation once a threshold amount of anti-solvent is added to the dispersion (Saunders & Roberts 2011b; Saunders & Roberts 2009). To achieve Co nanoparticle precipitation from DMSO, 5 mL of acetone was added to 3 mL of the Co-DMSO nanoparticle dispersion in a centrifuge tube. The Co nanoparticle dispersion in the liquid DMSO + acetone mixture was mixed for about 30 seconds using a vortex

mixer. Visual observations indicate that the Co nanoparticles were destabilized by the addition of acetone, resulting in the formation of precipitates within the solution. The sample was then centrifuged for 5 minutes at 5000 rpm. The clear supernatant was carefully removed, leaving a precipitate of Co nanoparticle agglomerates on the bottom of the centrifuge tube. This process of acetone addition and centrifugation was repeated twice. The precipitated Co nanoparticles that remained at the bottom of the centrifuge tube were dried completely with N<sub>2</sub> using a nitrogen-inflated polyethylene glove bag (shown in Figure 2.5) to ensure complete removal of acetone prior to any further analysis. Figure 2.6 presents a digital image of the Co nanoparticle powder that was isolated from the DMSO solvent using acetone to induce nanoparticle precipitation. The inset in Figure 2.6 shows a close-up of the Co nanoparticle agglomerates within the dried powder. Figure 2.7 shows the SEM image of this Co nanoparticle powder. From Figure 2.7, it can be seen that the Co nanoparticles have agglomerated into larger structures (supra-particle clusters) upon DMSO removal and appear to be roughly 300 nm or so after drying using this acetone anti-solvent method.



**Figure 2.5** Digital image of the N<sub>2</sub>-inflated glove bag that was used to completely dry the Co nanoparticles after they had been removed from the DMSO solvent using acetone.

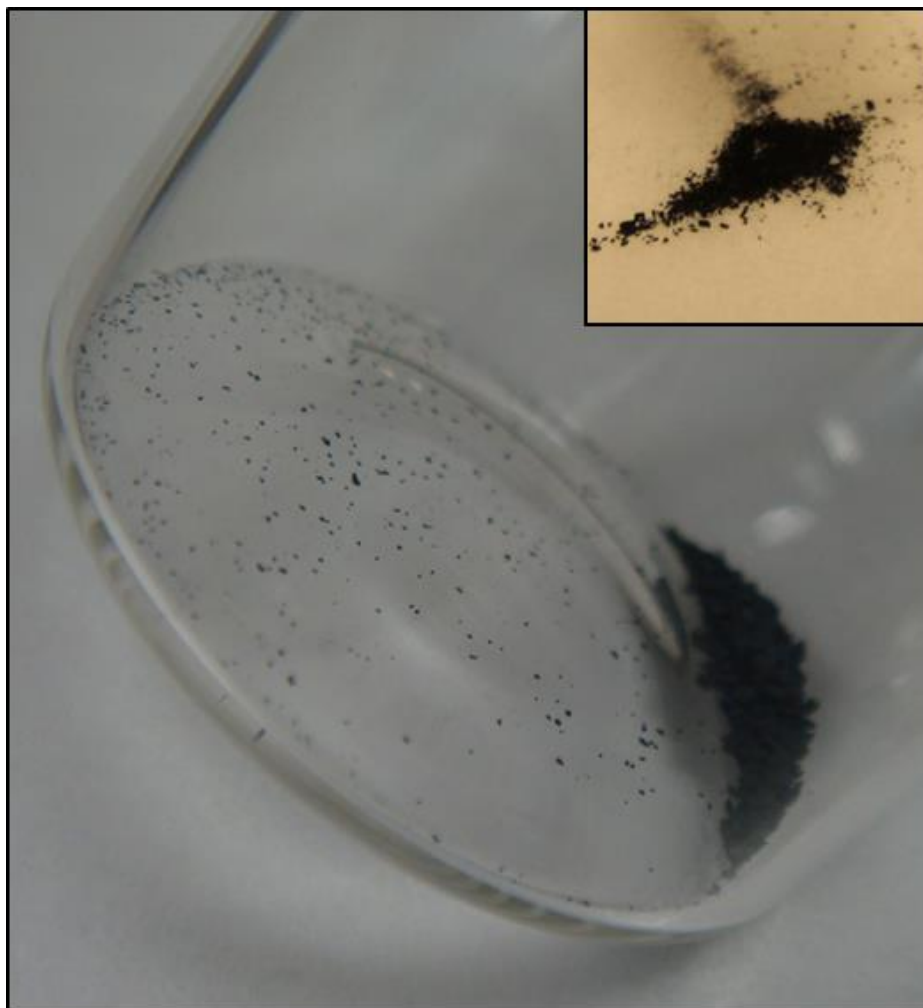


**Figure 2.6** Digital images of dried Co nanoparticles illustrating the separation of the Co nanoparticles from DMSO using acetone as liquid anti-solvent. Inset is a close-up of the Co nanoparticle powder.

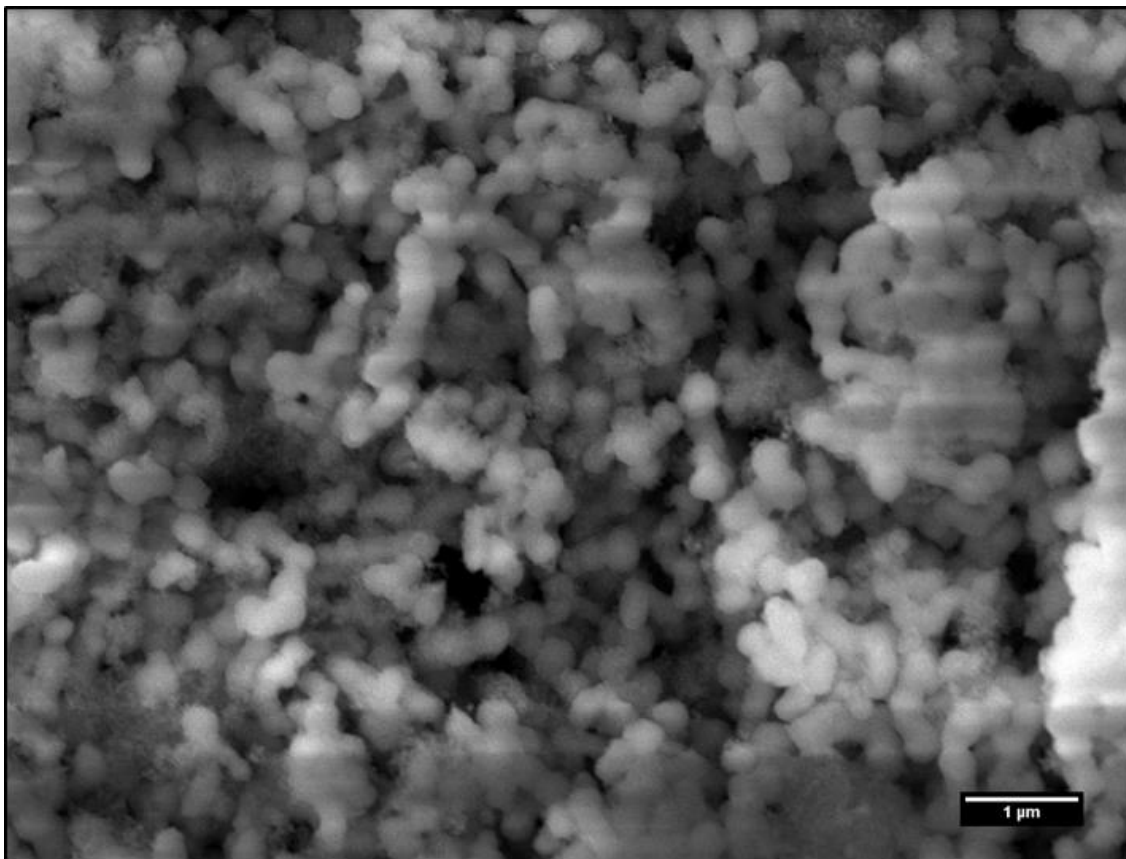


**Figure 2.7** SEM image of Co nanoparticles (after subsequent precipitation from DMSO using acetone as an anti-solvent).

It is important to point out that the individual Co nanoparticles that make up the agglomerates in the cobalt nanoparticle powder can be re-dispersed in a fresh solution of DMSO illustrating that solvent removal has little effect on the fundamental nanoparticle size. The TEM image in Figure 2.8 shows the re-dispersed Co nanoparticles (from the Co nanoparticle powder) in DMSO. This image illustrates that the size of the Co nanoparticles appears to be unchanged from the original TEM image of Co nanoparticles presented in Figure 2.4.

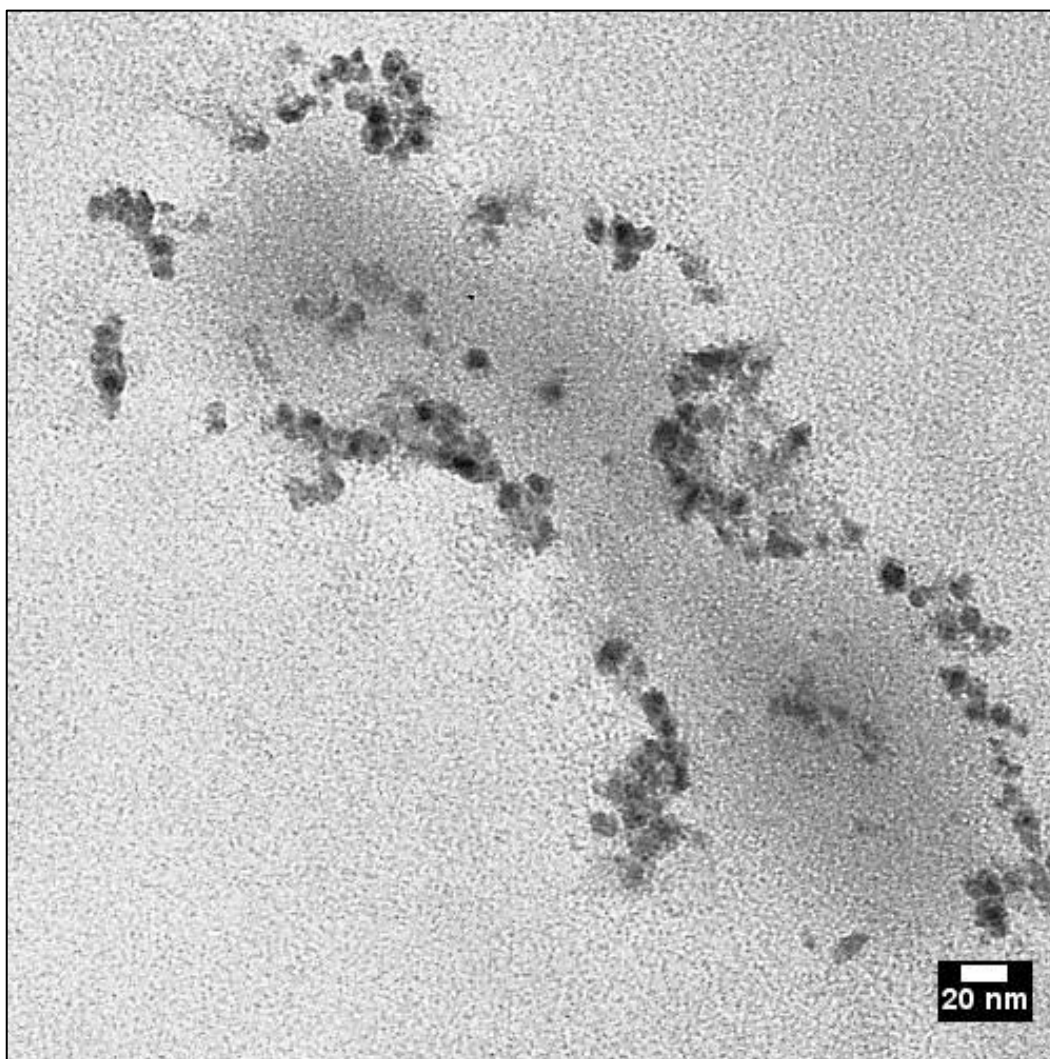


**Figure 2.8** Co nanoparticles redispersed in DMSO after having been precipitated from a DMSO + acetone solution (i.e. using acetone as an anti-solvent).

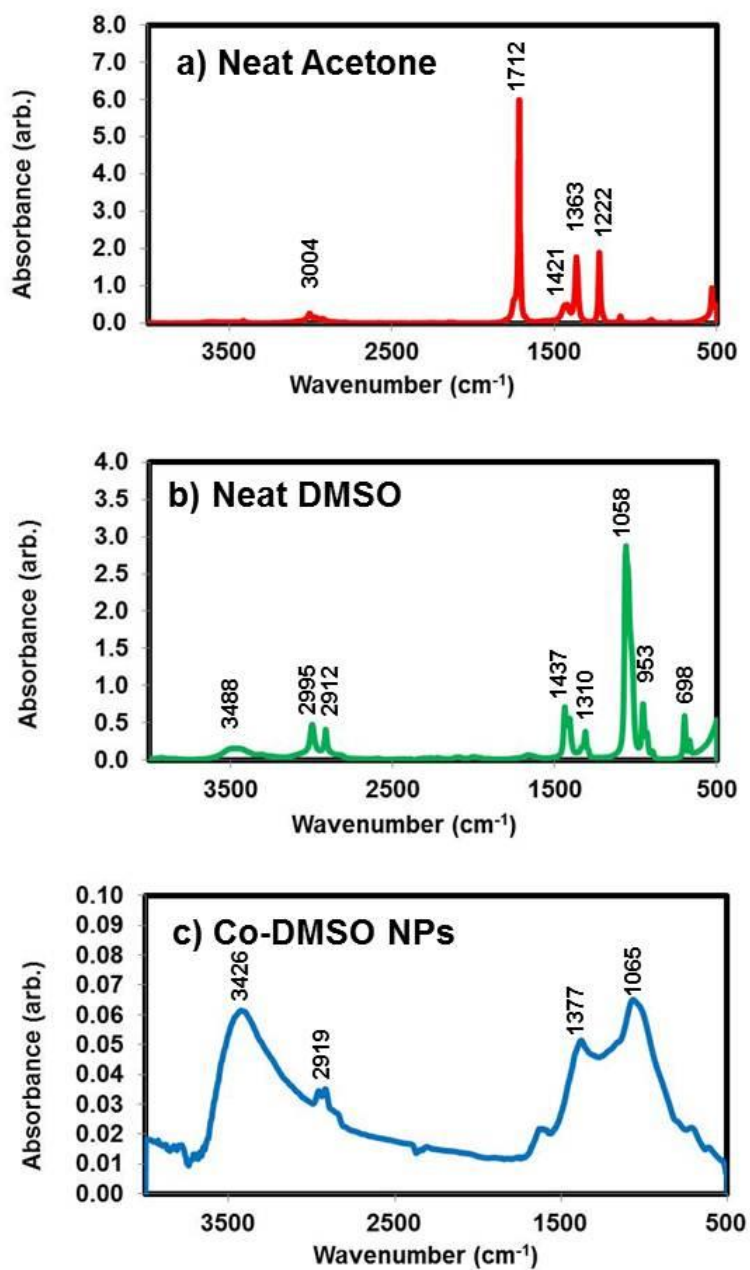
### 2.3.3 Co Nanoparticle Surface Interactions with DMSO

FT-IR spectroscopy is frequently used as a tool to understand the coordination between nanoparticle surfaces and capping ligands (Liu et al. 2007; Hong et al. 2006; Chen & Liu 2006; Li et al. 2006). In particular, FT-IR studies have been performed on Pd nanoparticles that have been stabilized by and dispersed in DMSO, similar to the synthesis technique described in this chapter for Co nanoparticle synthesis using DMSO (Liu et al. 2010). Liu et al. (2010) described that the coordination between the Pd nanoparticle surface and the DMSO occurs via a resonance hybrid structure of the sulfoxide functional group of DMSO, as was shown in Figure 1.6 (Chapter1), where there is an electrostatic contribution around the Pd nanoparticle from both the oxygen and sulfur moieties of DMSO. Similar coordination chemistries have been reported for  $[\text{Pd}(\text{DMSO})_4]^{2+}$  ions, whereby the metal interacts with the sulfoxide functional group by both the S-bond (at 1150 and 1140  $\text{cm}^{-1}$ ) and the O-bond (at 920 and 905  $\text{cm}^{-1}$ ) (Wayland & Schramm 1969; Nakamoto 2009).

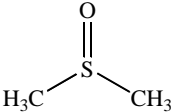
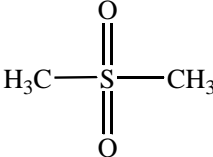
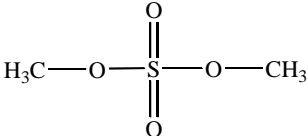
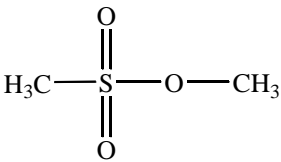


Similarly, the interaction between the Co nanoparticle surface and the DMSO solvent was studied using FT-IR spectroscopy. The FT-IR spectra for neat DMSO, acetone, and DMSO-stabilized Co nanoparticles are shown in Figure 2.9. The spectrum for neat DMSO in Figure 2.9b shows the sulfoxide functional group stretch  $\nu$  (S=O) at  $1058\text{ cm}^{-1}$ , which is in agreement with results reported in the literature for the sulfoxide stretch  $\nu$  (S=O) (Smith 1999). The increase in peak wavenumber from  $1058\text{ cm}^{-1}$   $\nu$ (S=O) that corresponds to the neat DMSO sample (Figure 2.9b) to  $1065\text{ cm}^{-1}$  corresponding to the Co-DMSO nanoparticle sample (Figure 2.9c) indicates that there may be some coordination between the S-bond of the sulfoxide functional group and the Co nanoparticle surface (Nakamoto 2009). However, literature suggests that coordination of DMSO with Co often occurs via the O-group of the sulfoxide functional group (Nakamoto 2009), and Co nanoparticles are prone to oxidation (Kobayashi et al. 2003; Su et al. 2010; Yang et al. 2003). Therefore, it is postulated that there is moderate coordination between the surface of the Co nanoparticles and the O within the sulfoxide functional group based upon the observed broadening of the spectrum peaks at  $1377\text{--}1065\text{ cm}^{-1}$ , corresponding to the Co-DMSO nanoparticle sample. Specifically, the broadness of the peak at  $1377\text{--}1065\text{ cm}^{-1}$  suggests that further intermolecular coordination may be occurring with the DMSO molecules situated around the Co nanoparticles and thereby behaving as ligands. For example, it may be possible that sulfate-, sulfone-, or sulfonate-like interactions are occurring on the surfaces of the Co nanoparticles. For comparison purposes, the structures and wavenumbers for S—O coordinations are listed in Table 2.1. Figure 2.10 shows a cartoon representation and interpretation of this interaction. With the proposed coordination occurring at the Co

nanoparticle surface, it is easy to see how this broad peak (at 1377-1065  $\text{cm}^{-1}$ ) in Figure 2.9c might resemble the sulfur-oxygen stretches of sulfate, sulfone, or sulfonate functional groups. Smith (1999) reports that these peaks can be observed around 1340-1310  $\text{cm}^{-1}$  and 1450-1350  $\text{cm}^{-1}$  respectively, which is in accordance with the broad peaks observed at 1377-1065  $\text{cm}^{-1}$  in the Co-DMSO nanoparticle sample in Figure 2.9c. It is also noted that the carbonyl peak at 1712  $\text{cm}^{-1}$  for the neat acetone spectrum in Figure 2.9a is not observed in the Co-DMSO spectrum, indicating that there is no residual acetone present in the Co-DMSO nanoparticle sample powder. Therefore, the evidence from FT-IR spectroscopy indicates that the Co nanoparticles are being modestly oxidized by the O-group of the sulfoxide functional group of DMSO. It is noted that this coordination between Co and DMSO is markedly different from the coordination that was observed by Liu et al. (2010), whereby the sulfoxide stretching of DMSO at 1031  $\text{cm}^{-1}$  is split into 1128  $\text{cm}^{-1}$  and 1020  $\text{cm}^{-1}$ , indicating the DMSO interacts with the Pd nanoparticle surface via both the sulfur and oxygen moieties of DMSO.



**Figure 2.9** FT-IR spectra for neat DMSO, neat acetone, and Co nanoparticles synthesized in DMSO (after subsequent precipitation from DMSO using acetone as an anti-solvent).

| Compound  | $\nu$ (cm <sup>-1</sup> )                                |
|---|--|
| Dimethyl Sulfoxide<br> | 1070—1030<br><i>(S = O Stretch)</i>                      |
| Sulfone<br>            | 1340—1310<br><i>(Assymmetric SO<sub>2</sub> Stretch)</i> |
| Sulfate<br>          | 1450—1350<br><i>(Assymmetric SO<sub>2</sub> Stretch)</i> |
| Sulfonate<br>        | 1430—1330<br><i>(Asymmetric SO<sub>2</sub> Stretch)</i>  |

**Table 2.1** Summary of wavenumbers for sulfur and oxygen FT-IR coordination (Smith 1999).

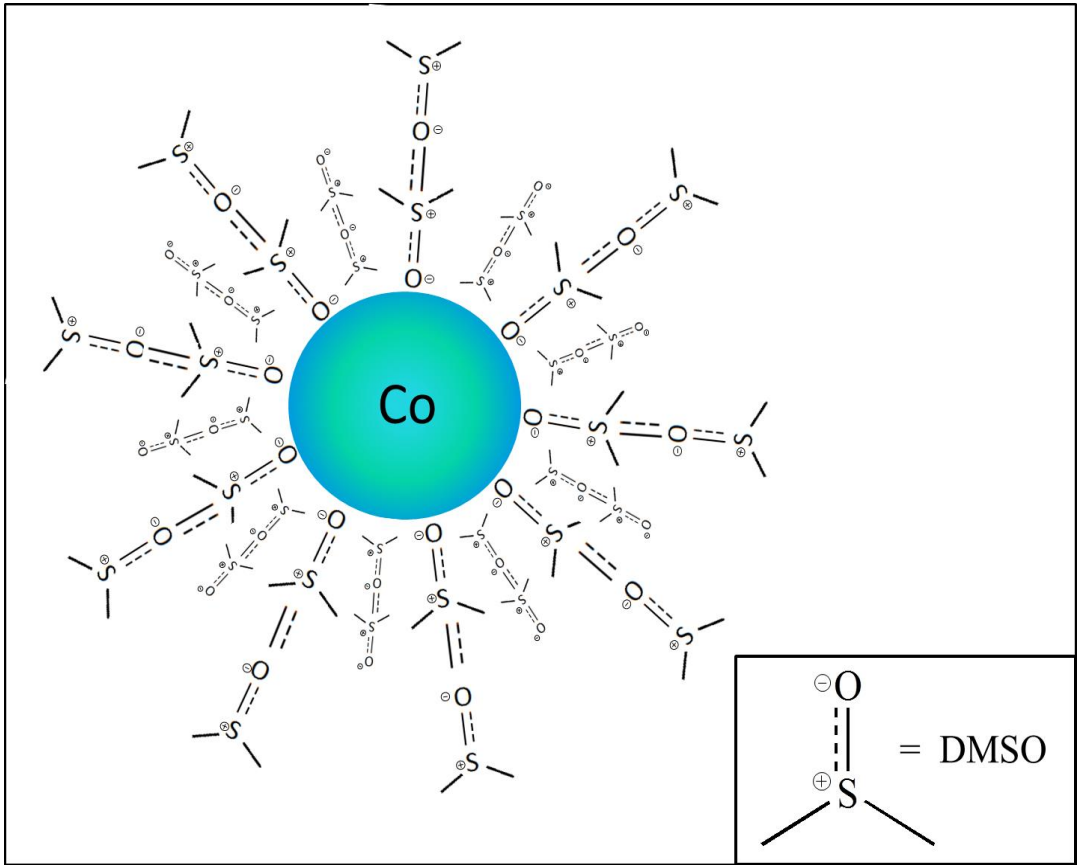


**Figure 2.10** Schematic representation of a Co nanoparticle stabilized by the oxygen component of DMSO.

XPS studies were also performed on the dried Co nanoparticle powder to further investigate the interaction of the oxygen and sulfur functional groups of DMSO with the Co nanoparticles. Figure 2.11 shows the XPS spectra from the Co nanoparticle powder. Figure 2.11a shows the S2p region, and the peaks present at 157 eV, 167 eV, and 171.5 eV are related to the sulfur complexes from the DMSO molecules that are adsorbed on the surface of the Co nanoparticles. For example, it has been reported in the literature that “oxidized sulfur” and Co-S-thiolate complexes can be referenced to the peak present at 167 eV (Sandhyarani & Pradeep 2001; Bao et al. 2008), which is a likely contribution from the sulfur moiety of DMSO. In Figure 2.11b, the C1s region is shown and the peak at 285 eV corresponds to the adventitious carbon peak resulting from the C-C or C-Hx bonds from adsorbed carbonaceous species on the Co nanoparticles, which is likely due to atmospheric exposure (Heide 2012). The O1s region, shown Figure 2.11c, presents a strong, symmetric peak centered at 532 eV. Similar results in the literature report the oxygen component from the DMSO molecule to be present around 530 eV (Burness et al. 1975), which is in agreement with the findings herein; however, it is noted that the peak at 532 eV in Figure 2.11c is broad. Figure 2.13d shows the Co2p region and the peaks present at 797 eV and 785 eV in the Co nanoparticle sample. These peaks are characteristic for the formation of typical Co oxides such as CoO and Co<sub>3</sub>O<sub>4</sub> (Wang et al. 2011) and Co sulfides (Yuan et al. 2009). However, the presence of these entities cannot be confirmed in this Co nanoparticle sample because the Co2p binding energies can inhibit the distinction between various sulfidic compounds that may surround the Co nanoparticles (Yuan et al. 2009). Therefore, the peaks present in the O1s and Co2p region are likely due to the native oxidation present on the surface of the Co

nanoparticles that has resulted from the room temperature atmospheric exposure of the Co nanoparticles (Burness et al. 1975). These findings strongly indicate that there is residual DMSO present on the Co nanoparticle surface, even after drying to a powder using acetone.

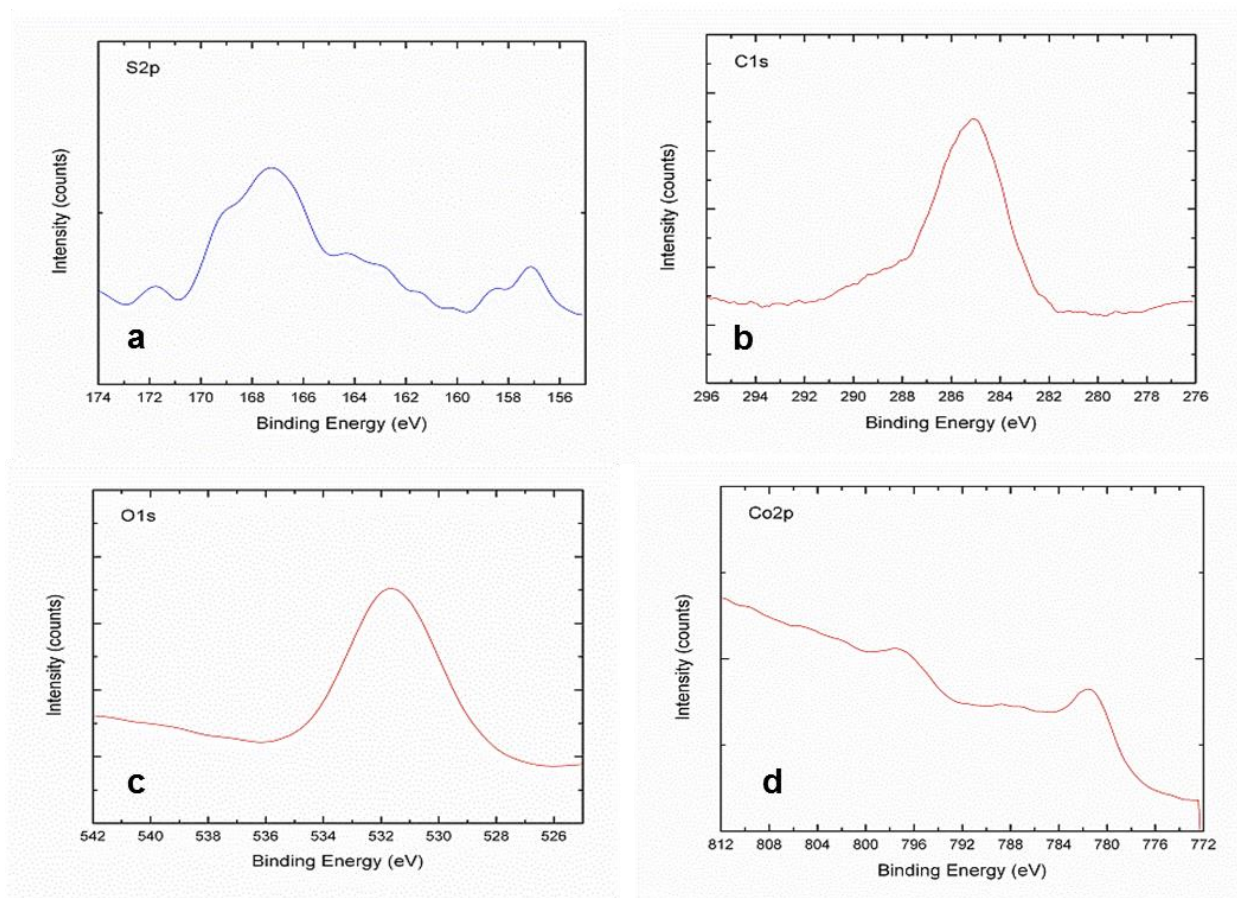


**Figure 2.11** XPS spectra of Co nanoparticles synthesized in DMSO (after subsequent precipitation from DMSO using acetone as an anti-solvent) for a) S2p, b) C1s, c) O1s, and d) Co2p.



XRD measurements on the dried Co powder were performed to investigate the bulk and surface morphology of the Co nanoparticle powder. Figure 2.12a shows the spectrum for the Co nanoparticle powder. The various sharp diffraction peaks in the spectrum in Figure 2.12a are due to unreacted species that may be present in the sample as well as NaCl, which is formed as a byproduct during the reduction of the  $\text{Co}^{2+}$  salt by  $\text{NaBH}_4$ . The Co nanoparticle powder was then washed using DI- $\text{H}_2\text{O}$  to remove any of these possible contaminants that may be interfering with the underlying spectrum of the Co nanoparticles. Figure 2.12b shows the spectrum for the Co nanoparticle powder after subsequent washings with DI- $\text{H}_2\text{O}$ . The data in Figure 2.12b indicates that the water successfully removed the unwanted by-products and contaminants, and the resulting spectrum in Figure 2.12b reveals that the Co nanoparticles are largely amorphous in structure. Thus, from the XRD analysis, no Co oxide signals were detected, indicating that the oxide layer on the Co nanoparticle surface is likely very thin. A similar observation has been reported in the literature and suggests that the XRD will not show a significant signal from the oxide layer if the oxide layer on the surface is miniscule (Bao et al. 2005). Furthermore, there were no diffraction peaks present for ordered structures of Co or Co oxides, and the Co nanoparticles are believed to be amorphous structures of cobalt metal. It is important to note that the all of the Co nanoparticle synthesis experiments were performed at room temperature and further XRD studies to determine the effect of temperature on the structure of the Co nanoparticles was not performed at this stage (but will be discussed in Chapter 4). However, there have been other reports for the formation of amorphous Co at room temperature, and after thermal treatment in

air, ordered structures of  $\text{Co}_3\text{O}_4$  nanoparticles were produced from these materials (Yang 2004; Kobayashi et al. 2003).

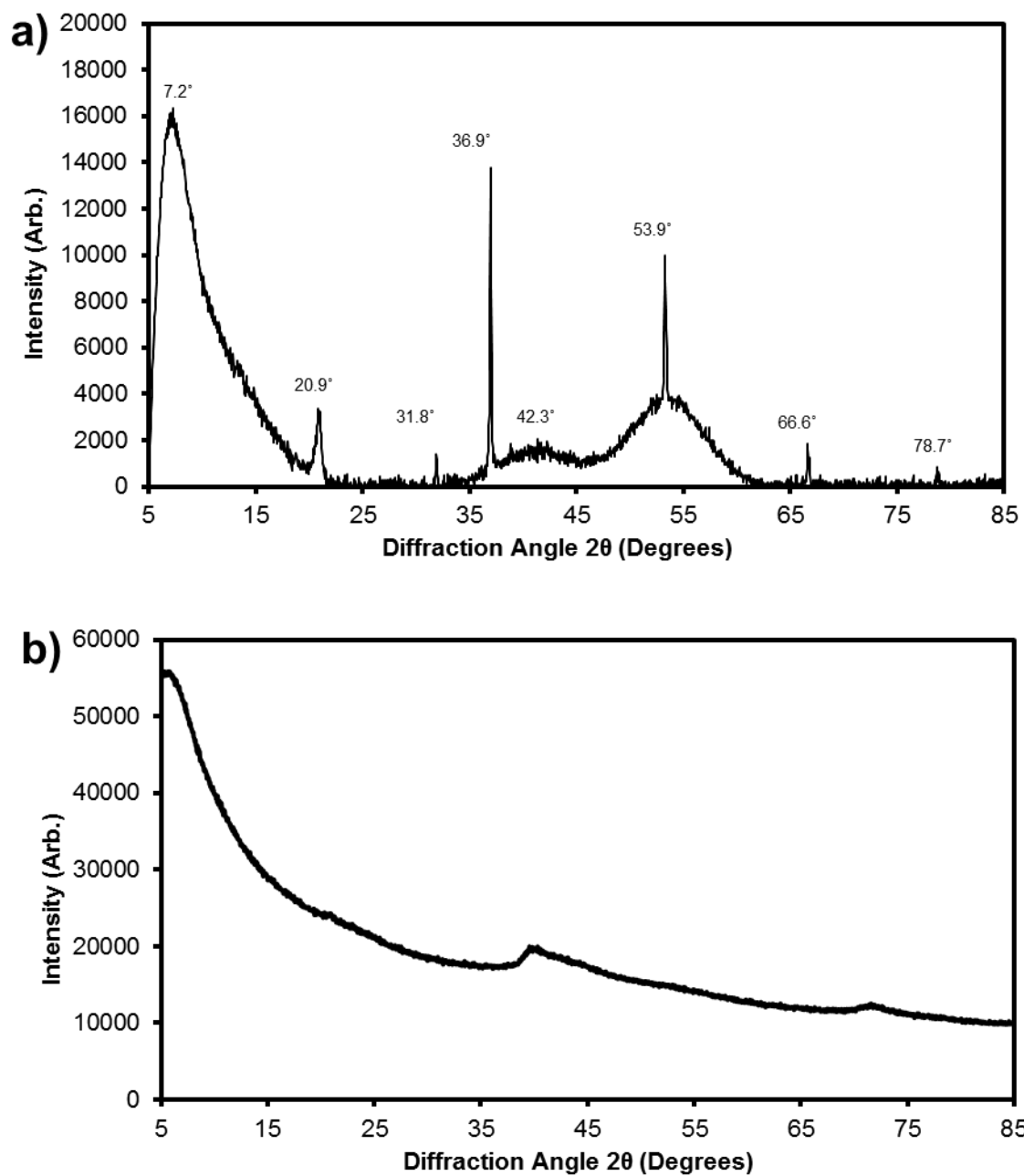


**Figure 2.12** XRD spectra of Co nanoparticle powder synthesized in DMSO a) after precipitation from DMSO using acetone as an anti-solvent and b) after a subsequent washing with DI- $H_2O$ .

The elemental composition of the Co nanoparticle powder was obtained using SEM-EDS. Recall that no residual acetone was found on the Co nanoparticle surface after drying. Table 2.2 summarizes the elemental analysis of the Co nanoparticle powder. These results confirm the presence of the Co metal, along with a considerable amount of oxygen. There are trace amounts of sulfur, which likely comes from the DMSO solvent remaining on the Co nanoparticle surface, as well as trace amounts of sodium and chlorine, which likely comes from the reducing agent and Co salt precursors. The mole-percent of each element was calculated and summarized in Table 2.2. These calculations illustrate that there are more moles of oxygen present than Co, and this further suggests that there is native oxidation occurring on the surface of the Co nanoparticles due to environmental exposure, as was observed in the XPS studies. It is also likely that Co-O intermediates are the result of the coordination chemistry occurring between the surface of the Co nanoparticles and the O-bond of the sulfoxide functional group of the DMSO solvent, as was observed in the FT-IR studies. Since the contents of the reaction were sufficiently protected by utilizing a nitrogen purge during and after synthesis, it is doubtful that the Co oxide intermediates have formed due to environmental contaminants. Furthermore, it may be possible that these Co oxide intermediates may have formed during the precipitation process of the Co nanoparticles from the DMSO solvent. It is also important to note that the Co nanoparticle sample for TEM-EDS analysis was prepared on a carbon type B, 300 mesh copper grid, and it is possible that the copper substrate may have mildly oxidized during sample handling to contribute to some of the oxygen content observed in EDS analysis. Thus, these SEM-EDS results, combined with the results obtained from FT-IR analysis, indicate that the Co nanoparticles likely have a

thin layer of oxide present at the surface, therefore, further investigations of the oxidation state and the surface of the Co nanoparticles is warranted.

| <b>Element</b> | <b>wt % *</b> | <b>mol %</b> |
|----------------|---------------|--------------|
| Co             | 68.0          | 37.3         |
| O              | 29.9          | 60.5         |
| Cl             | 1.1           | 1.0          |
| S              | 0.9           | 1.0          |
| Na             | 0.1           | 0.2          |

\*wt% is taken from EDS data

**Table 2.2** Results from SEM-EDS elemental analysis for Co nanoparticle powder.

TPD analysis was performed on the dried Co nanoparticle powder in combination with mass spectrometry analysis. The intention of this study was to determine if DMSO could be desorbed from the Co nanoparticle surface by exposing the sample to excessive temperatures (25°C - 1000°C). The results from this experiment indicated that there is no DMSO present on the surface of the Co nanoparticles, as evidenced by a very noisy TCD signal (Appendix A2) from the mass spectrometry analysis from 25°C - 1000°C. It is important to note that even though the experiment was performed from 25°C – 1000°C, all organic materials had been removed at temperatures greater than 400°C. Recall that some coordination with DMSO and the Co nanoparticles was confirmed by FT-IR and XPS analysis. Therefore, it is expected that there is a miniscule amount of DMSO, possibly a monolayer of DMSO, present on the Co nanoparticle surface, which is a sufficient amount that could be detected using FT-IR spectroscopy, but too little to be detected using mass spectrometry.

As a side note, additional investigations were performed to understand the impact of oxygen (environmental exposure to air) on the DMSO-stabilized Co nanoparticles, both during and after synthesis. Co nanoparticle synthesis was first repeated with no N<sub>2</sub>-purge (i.e. complete exposure to environmental air at room temperature), and a second time using air as the purge gas. Then, an aliquot of Co nanoparticle sample (that had been protected from air by the N<sub>2</sub> purge, as originally described in Section 2.2.2) was exposed to environmental air for 4.5 days, while a second aliquot of this Co nanoparticle sample was purged with air for 4.5 days. The TEM images for each of these studies are shown in Figure 2.13 and the corresponding size distribution histograms are shown in Figure 2.14. In each case, exposing the Co nanoparticles to air during or after synthesis

had little effect on the particle size or morphology. Likewise, purging the system with air had little effect on the Co nanoparticles. Furthermore, each of these dispersions exhibited little to no precipitation from the DMSO solvent after contact with air. Thus, this demonstrates that DMSO serves as a significant component for Co nanoparticle stabilization, thereby protecting the surface of the Co nanoparticles from subsequent oxidation (and agglomeration) even when the particles are deliberately subjected to air.



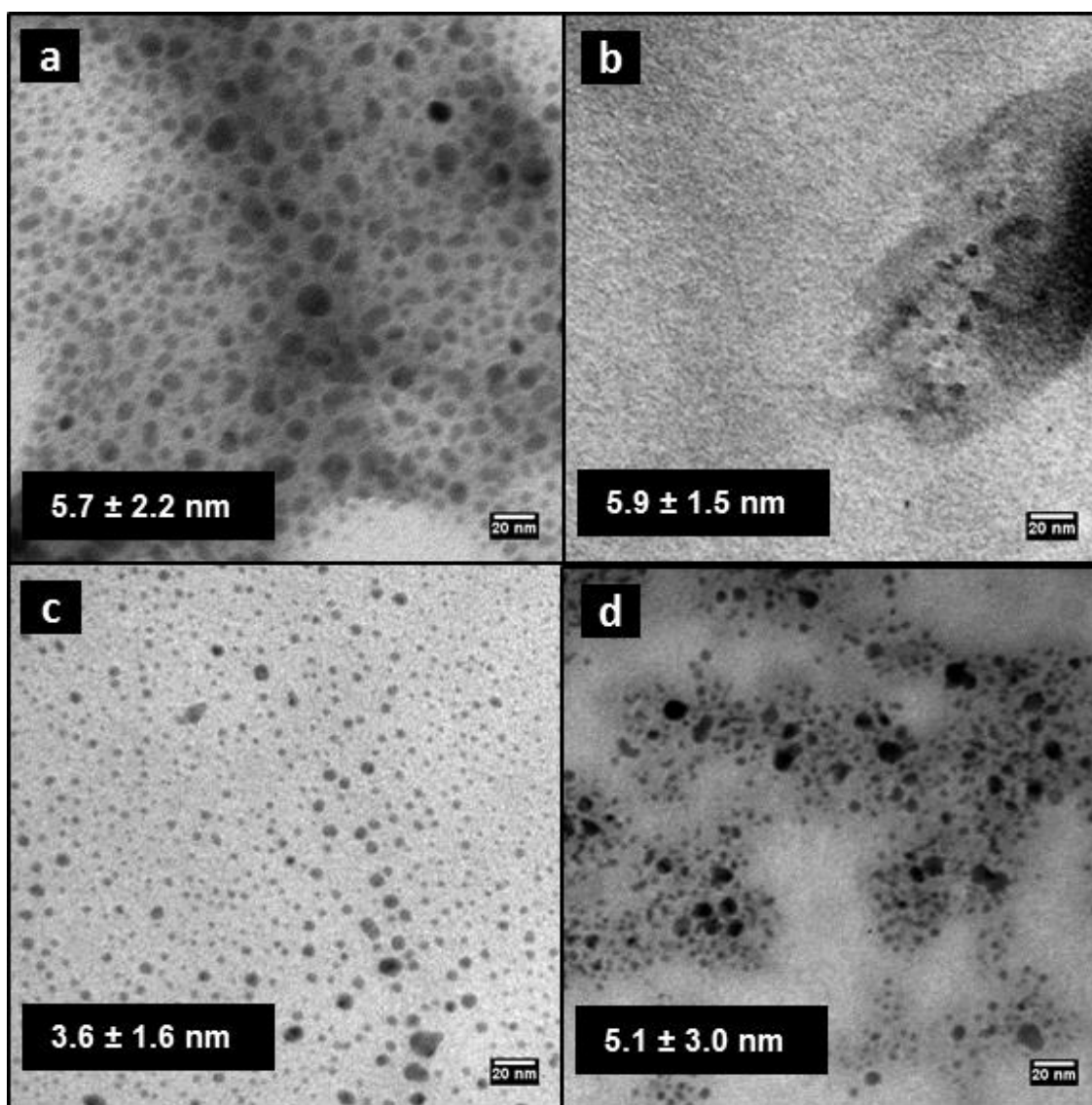


**Figure 2.13** TEM images of Co nanoparticles synthesized in DMSO when a) exposed to environmental air during synthesis, b) purged with air during synthesis, c) exposed to air for 4.5 days after synthesis, d) purged with air for 4.5 days after synthesis.

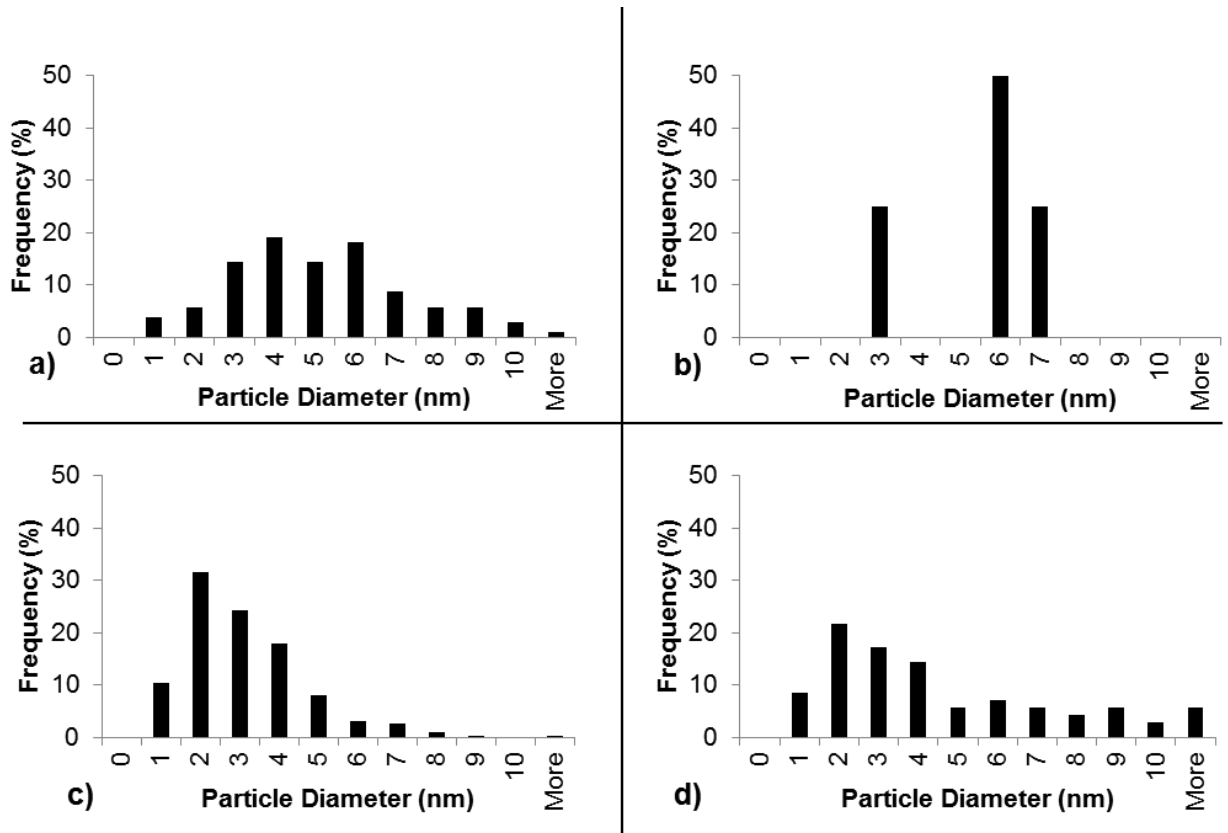


**Figure 2.14** Size histograms from TEM analysis for Co nanoparticles synthesized in DMSO when a) exposed to environmental air during synthesis, b) purged with air during synthesis, c) exposed to air for 4.5 days after synthesis, d) purged with air for 4.5 days after synthesis.

## 2.4 Conclusions

Certain magnetic nanoparticles, such as Co, are extremely susceptible to excessive and undesirable oxidation, and it is essential to be able to controllably synthesize these nanoparticles in a manner that impedes excessive oxidation. This chapter presented a simple synthesis technique to produce amorphous  $3.7 \pm 1.5$  nm Co nanoparticles by using DMSO as a functional solvent, whereby DMSO effectively functions as both the stabilizing agent and solvent for Co nanoparticle synthesis. These Co nanoparticles can be precipitated and extracted from the DMSO solvent by simply adding acetone to function as an anti-solvent to the Co-DMSO nanoparticle dispersion. SEM imaging analysis indicated that the Co nanoparticle powder consisted of larger, 300 nm supra-particle clusters that formed due to removal of the DMSO functional solvent. FT-IR studies indicate that the Co nanoparticles are likely stabilized by both the sulfur and oxygen moieties of DMSO, with a greater contribution from the oxygen component. Therefore, FT-IR and XPS spectroscopy analysis along with elemental mapping from EDS indicate that these DMSO-stabilized Co nanoparticles are mildly oxidized (via exposure to the atmosphere at room temperature). Furthermore, the Co nanoparticles remain homogeneously dispersed in solution and are uniform in shape, demonstrating that DMSO effectively interacts with the Co nanoparticle surfaces and behaves favorably as both a solvent and a capping agent. These investigations demonstrate that excessive nanoparticle oxidation and unwanted nanoparticle agglomeration and degradation can be avoided by simply using DMSO as a functional solvent during synthesis.

## **Chapter 3**

### **Clustering and Solvation of Cobalt Nanostructures in Dimethyl Sulfoxide**

It has been reported that the molecule DMSO, dimethyl sulfoxide, can be effectively utilized as both a stabilizing ligand and a solvent during cobalt (Co) nanoparticle synthesis. Accordingly, stabilization of the nanostructures is provided by electrostatic contributions from the molecular sulfoxide components. This chapter reports the synthesis of Co nanoparticles and nanoclusters (i.e., nanoparticle aggregates) of various sizes in DMSO at 25°C, 50°C, and 150°C. This study illustrates that the size of the resulting Co nanoclusters is a direct function of the synthesis temperature. Moreover, these Co nanoclusters are composed of smaller Co nanoparticles that preferentially aggregate at increased temperatures during synthesis, where the largest nanoclusters are constructed at the highest synthesis temperatures. Furthermore, it is demonstrated that the smaller Co nanoparticles that makeup the larger Co nanoclusters can be liberated in solution upon the addition of various co-solvents.

### **3.1 Introduction**

Nano-scale materials have become the focus of numerous applications due to their unique and size-dependent optical (Beecroft & Ober 1997; Murphy et al. 2005), mechanical (Shi et al. 2006; Zhang & Singh 2004), electronic (Zhang & Singh 2004; McConnell et al. 2000) , and magnetic (Frey et al. 2009; Pankhurst 2003) properties. It is important to be able to control the size and dispersibility of individual nanoparticles in solution in order to exploit the properties of these particles. For example, dispersions of individual nanoparticles, such as semiconductor quantum dots, can be used in electroluminescent (Mattoussi et al. 1998) and biomedical imaging applications (Michalet et al. 2005), whereby the light absorption and emission properties are determined by the particle size and shape (Michalet et al. 2005; Anand et al. 2007). Individual dispersions of nanoparticles can also have a profound impact on the catalytic activity of a reaction when they are used as catalysts due to their large surface-to-volume ratio (Narayanan & El-Sayed 2005). Thus, there are a variety of uses for nanoparticles in dispersions which function to improve current technologies.

It is essential to be able to produce dispersions of individual nanoparticles, however, recent studies have described the advantages of using agglomerations of nanoparticles (nanoparticle clusters) in a wide variety of applications. In particular, nanoparticle clusters can be used in magnetic imaging applications, (Ingram et al. 2010), biolabeling and biosensing applications (Xie et al. 2009), and magnetic recording applications (Lee et al. 2002), to name a few. In some cases, the properties of nanoparticle clusters may have distinct advantages over individual nanoparticles because

they can have higher magnetism in some cases (Qiang et al. 2004) and improved surface plasmon coupling (Lin et al. 2005).

Johnston and coworkers have demonstrated the ability to produce a variety of nanoclusters. For example, Ma et al. (2009) have constructed small multifunctional nanoroses, which have a superparamagnetic iron oxide core and are active in the near-infrared (NIR) regime due to a thin gold coating on the surface of the iron oxide nanoparticles. In this study, kinetic control of the cluster size is achieved by varying the iron oxide nanoparticle concentration and gold precursor concentration in the presence of dextran stabilizer molecules (Ma et al. 2009). In another study, Tam et al. (2010) described the kinetic assembly of 5 nm gold nanoparticles to produce biodegradable gold nanoclusters of 100 nm. The assembly and size of the gold nanoclusters were controlled by polymer adsorption to the nanoparticle surface and by simply varying the volume fractions of the particles during solvent evaporation. Controllable degradation of the gold nanoclusters occurred by decreasing the pH of the solution from pH 7 to pH 5 (Jasmine M. Tam et al. 2010). In some instances, nanoparticles can be controllably assembled into nanoclusters, which can be reversibly dissociated. In particular, Johnston and coworkers have developed techniques to produce nanoparticle clusters of various sizes whereby the cluster size is dependent on the concentration of the protein and ‘crowder’ molecules in the dispersion (Johnston et al. 2012). Therefore, a variety of different methods can be used as in order to controllably influence the size of nanoclusters, and a schematic of this process is illustrated in Figure 3.1.

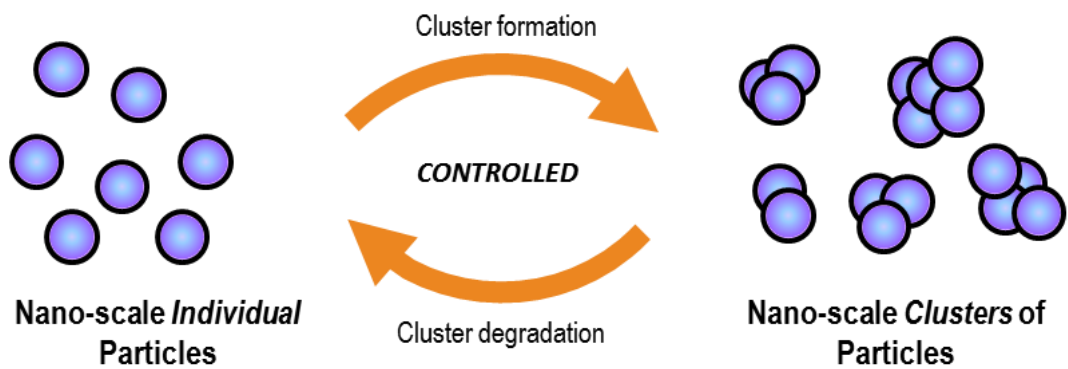


**Figure 3.1** The recursive clustering cycle of individual nanoparticles and nanoparticle clusters, whereby the formation and/or degradation of clusters can be controlled.

The studies described in Chapter 2 demonstrated the successful synthesis of cobalt (Co) nanoparticles in a dimethyl sulfoxide (DMSO) functional solvent, where the DMSO molecule can function as both the solvent and the stabilizing ligand in solution. Additionally, it was found that DMSO was adsorbed to the surface of the Co nanoparticles via the sulfoxide functional group of DMSO. In the present chapter, a method to achieve Co nanoparticle clustering in DMSO is described, whereby Co nanoparticle cluster size can be controlled by increasing the temperature of the reaction during synthesis. Subsequently, the smaller Co nanoparticles which make up the clusters can be re-dispersed by adding various co-solvents to the solutions of Co nanoparticle clusters post-synthesis. These experiments will provide valuable insights about the unique nanoparticle dispersibility properties of DMSO at different temperatures, as well as the distinct solvation capabilities of DMSO with other solvents.

## **3.2 Experimental**

### **3.2.1 Materials**

Dimethyl sulfoxide ((CH<sub>3</sub>)<sub>2</sub>SO, 99.9%) and ethanol (CH<sub>2</sub>CH<sub>3</sub>OH, 95%) were obtained from BDH Chemicals. Deionized ultrafiltered water (DI-H<sub>2</sub>O), Isopropanol ((CH<sub>3</sub>)<sub>2</sub>CHOH), dichloromethane (CH<sub>2</sub>Cl<sub>2</sub>), toluene (C<sub>7</sub>H<sub>8</sub>), and methanol (CH<sub>3</sub>OH) were obtained from Fisher Scientific. Cobalt (II) chloride hexahydrate (CoCl<sub>2</sub>\*6H<sub>2</sub>O, 99+%) was obtained from Strem Chemicals. Sodium borohydride (NaBH<sub>4</sub>, 99%) and chloroform (CHCl<sub>3</sub>) were obtained from Sigma Aldrich. Nitrogen (UHP grade) was obtained from Airgas. Acetone ((CCH<sub>3</sub>)<sub>2</sub>CO) was obtained from BDH. Acetic acid (CH<sub>3</sub>COOH, 99+%) was obtained from Alfa Aesar.



### 3.2.2 Co Nanoparticle and Nanocluster Synthesis

Co nanoparticle synthesis was carried out as described in Chapter 2. Nanoparticle and nanocluster synthesis was performed at 25°C, 50°C, and 150°C. A reaction system equipped with a nitrogen (N<sub>2</sub>) purge inlet, a thermocouple, and a reflux column was arranged on a 250 mL flask. A magnetic stir bar was added to the flask and filled with 50 mL of DMSO. The flask was situated in a heating mantle and placed on a magnetic stir plate. The reaction set-up is shown in Figure 3.2. Nitrogen was purged through the system for 30 minutes prior to the addition of any reagents as well as throughout the entire duration of the reaction. In addition, the solution was heated to the desired temperature (e.g., 50°C or 150 °C) before the addition of any reagents. Next, a 4000 µL of a 0.05 M solution of CoCl<sub>2</sub>\*6H<sub>2</sub>O was added to the reaction flask via the injection port as well as a 7020 µL of a 0.05 M solution of NaBH<sub>4</sub>. The reaction was stirred, purged with N<sub>2</sub>, and refluxed at the appropriate temperature for 3 hours after the addition of the reactants. After 3 hours, the nitrogen purge was stopped, the temperature was returned to 25°C, and the contents of the reactor were allowed to continuously stir for 24 hours.



**Figure 3.2** The reaction set-up for the high-temperature synthesis of Co nanoparticle clusters.

### 3.2.3 Addition of Co-Solvents to Co Nanoparticles and Clusters

Two different amounts of DI-H<sub>2</sub>O were added to each of the three Co nanoparticle/nanoclusters dispersions, after returning the solutions to room temperature, in order to determine if the amount of added co-solvent would have any influence on the size or morphology of the nanostructures. In the first set of experiments, water was added to each sample in order to produce a 1:3 ratio of Co nanostructure solution to water, e.g., a 10 mL sample of each of the DMSO/Co nanostructure dispersions resulting from the three different temperature syntheses was pipetted into separate vials and 30 mL of de-ionized water was added to the solution. The same procedure was followed for the second set of experiments, except that 30 mL of each of the different DMSO/Co nanostructure dispersions were combined with 10 mL of water to create a 3:1 ratio of Co nanostructure solution to water. Each new dispersion of Co nanostructures in DMSO with the added water was sealed and vigorously shaken for approximately 10 seconds.

Following a similar procedure, co-solvents with different polarities were added to the Co nanoclusters that were synthesized at 150°C. For these experiments, 10 mL of each co-solvent was added to the Co nanocluster dispersion to create a 1:3 ratio of the Co nanocluster solution to co-solvent. A list of the co-solvents used can be found in Table 3.2.

### 3.2.4 Characterization Techniques

*Transmission Electron Microscopy (TEM)* – TEM was used to investigate the size and morphology of each of the samples of Co nanoparticles and nanoclusters using a Zeiss EM 10 TEM at an operating voltage of 60 kV. TEM samples were prepared by placing a drop of sample onto a carbon type B, 300 mesh copper grid. The grid was

contained in a plastic petri dish and placed in the vacuum oven to dry for several days prior to TEM analysis. The average particle size and size distribution of the Co nanoparticles were obtained using the Image J software package to more than a hundred particles from multiple TEM images taken from the same sample grid. A high-resolution TEM image was also obtained, where noted, using JEOL JEM-2010 at an operating voltage of 200 kV.

### **3.3 Results**

#### **3.3.1 TEM Analysis of Co Nanoparticle Cluster Formation**

The TEM images and corresponding histograms for Co nanoparticles in the DMSO functional solvent that have been synthesized at 25°C, 50°C, and 150°C are shown in Figure 3.3 a, b, and c, respectively. In Figure 3.3a, the Co nanoparticles are synthesized at 25°C and are an average diameter of  $3.8 \text{ nm} \pm 2.7 \text{ nm}$ . As the temperature of the reaction was increased from 25°C to 50°C, the average diameter and standard deviation of the nanostructures obtained increased to  $6.5 \text{ nm} \pm 5.6 \text{ nm}$ , as shown in Figure 3.3b. As the temperature was increased even further to 150°C, as shown in Figure 3.3c, the average nanostructure diameter increased further to  $16.4 \text{ nm} \pm 7.8 \text{ nm}$ . Overall, the average diameter and size distribution of the nanostructures obtained drastically increased from  $3.8 \text{ nm} \pm 2.7 \text{ nm}$  at 25°C to  $16.4 \text{ nm} \pm 7.8 \text{ nm}$  at 150°C. Thus, this series of Co nanoparticle synthesis experiments performed at different temperatures illustrates that these synthesis temperatures can have a profound influence on the observed nanostructure sizes and distributions. The HR-TEM image of the Co nanostructures that have been synthesized at 150°C is shown in Figure 3.4, confirming that these larger Co

structures are the result of the smaller-sized particles clustering into larger agglomerates at elevated synthesis temperature. Thus, proposed reaction schemes are shown in Figure 3.5, which illustrate the role of temperature in Co nanocluster synthesis.

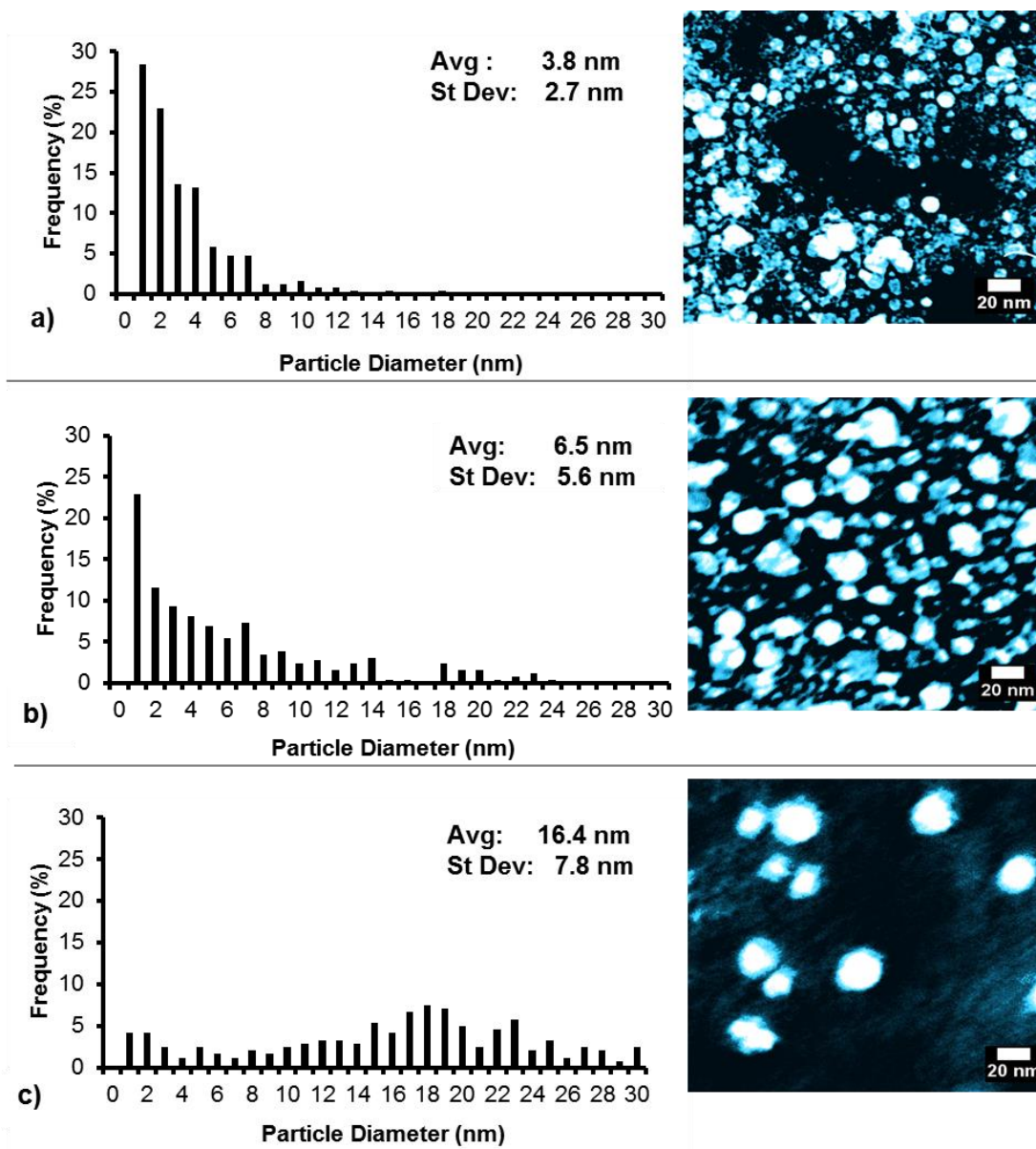


**Figure 3.3** TEM images and corresponding histograms of Co nanoparticles synthesized at different temperatures: a) 25°C, b) 50°C, and c) 150°C. Images have been re-processed using color for illustration purposes only in order to clearly show the increase in particle size as a function of synthesis temperature.

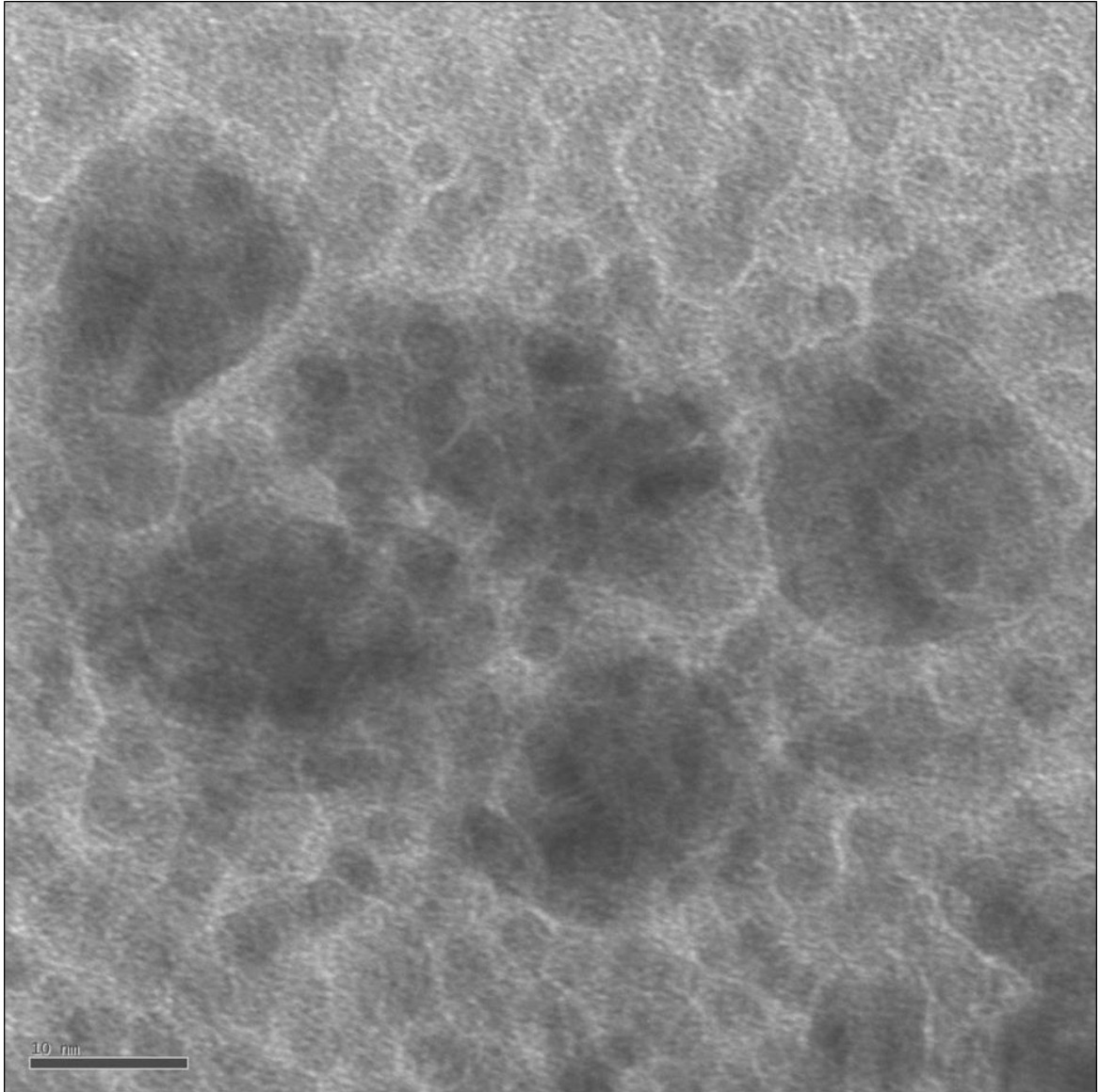


**Figure 3.4** HR-TEM image of Co nanoclusters synthesized at 150°C. The scale bar is 10 nm.

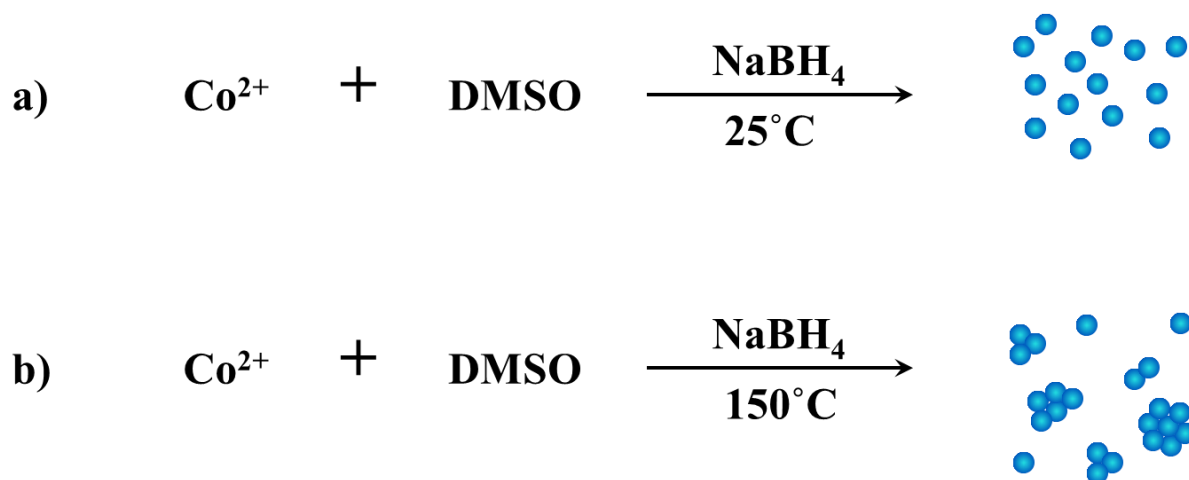


**Figure 3.5** Proposed reaction schemes for a) the formation of Co nanoparticles (~4 nm) in DMSO at 25°C and b) the formation of Co nanoclusters (~20 nm) at higher temperatures (e.g. 50°C and 150°C).



### 3.3.2 Co Nanoparticle Cluster Degradation by the Addition of Water

Two different amounts of DI-H<sub>2</sub>O were added to the three dispersions of nanostructures (resulting from the three syntheses conditions) in order to determine if the addition of water could influence their size or distribution. Visual observations indicated that the DI-H<sub>2</sub>O in combination with the already present DMSO enables the Co nanoparticles to be stabilized in a uniform dispersion of DMSO/water solution. Figure 3.6 shows the TEM imaging results for the average nanoparticle size and distributions of each of the DMSO-stabilized Co nanoparticles (synthesized at different temperatures and returned to room temperature) after adding different amounts of water to each of the dispersions. Figure 3.6a, b, and c show the TEM imaging analysis results after each solution had been diluted by a 1:3 ratio of Co dispersion to water; likewise, Figure 3.6d, e, and f shows the results for diluting the system to a 3:1 ratio of Co dispersion to water.

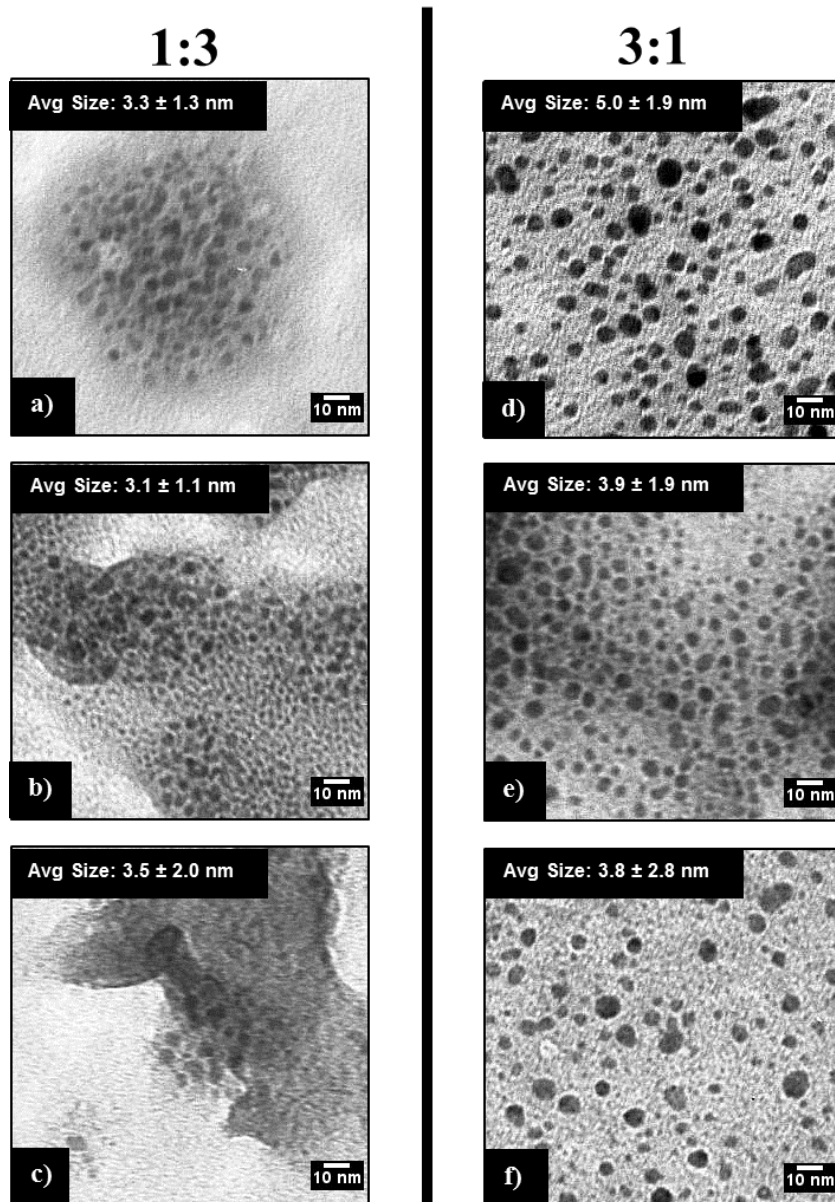


**Figure 3.6** TEM images for Co nanoparticles stabilized by DMSO synthesized at different temperatures and diluted with different amounts of water after the solution was returned to room temperature (25°C). A ratio of 1:3 DMSO-Co nanoparticle dispersion to water was used to dilute the nanostructures in the first column: a) 25°C, b) 50°C, and c) 150°C. A ratio of 3:1 DMSO-Co nanoparticle dispersion to water was used to dilute the nanostructures in the second column: d) 25°C, e) 50°C, f) 150°C.

TEM imaging analysis demonstrated that after adding different amounts of water, the resulting fundamental particle size was ~3.5 nm in each case. This result illustrates that the larger structures obtained at the high temperature synthesis condition in DMSO were simply a construct of these smaller fundamental particles that likely resulted from aggregation at the high temperature due to the weak DMSO solvent capacity at those conditions. The addition of water liberates the particles by providing a favorable interaction between the water and the adsorbed DMSO on nanoparticle surface. For example, the larger Co nanostructures resulting from the synthesis in neat DMSO at 150°C (Figure 3.3c) were 16.4 nm with a very broad size distribution; however, the average size of these structures dramatically decreased to 3.5 nm and 3.8 nm (Figure 3.6 c, f) when both small and large concentrations of water were added. It is also noted that these reductions in size also corresponded to much lower standard deviations than reported for the structures obtained at the higher temperatures. The same trend was observed for the particles synthesized at 50°C in neat DMSO where these structures decreased in size from 6.5 nm (Figure 3.3b) to approximately 3 nm (Figure 3.6b, e) with smaller size distributions upon addition of water. Lastly, the particles that were synthesized at 25°C in neat DMSO and reported in Figure 3.3a remain effectively the same size upon the addition of water (Figure 3.6a, d). It should be noted that the average particle size shown in Figure 3.6d is 5.0 nm and this likely represents an outlier due to statistical limitations of the imaging analysis. Nonetheless, adding water to the nanostructure dispersions obtained at the elevated temperatures has a profound effect on the particle size and distribution, regardless of the amount of water added.

For comparison purposes, the effect of adding water to the already synthesized Co nanoparticles in DMSO at different temperatures is summarized in Table 3.1. In this table, it can be seen that the average nanoparticle size after the addition of water is decreased. For example, the smaller nanoparticles that make up the 16.4 nm nanoclusters resulting from the synthesis at 150°C, were liberated and re-dispersed after water was added to the solution. Therefore, it can be inferred that the overall effect of adding water to the DMSO-Co nanoparticle dispersions is significant, and that the average size of the fundamental particle building blocks in each sample is ~3.5 nm with low deviations in average size.

| Synthesis Temperature (°C) | Size (nm) of Co Nanostructures after Synthesis | Size (nm) of Co Nanoparticles after DI-H <sub>2</sub> O Addition |
|----------------------------|--|--|
| 25                         | 3.8 ± 2.7                                      | 3.3 ± 1.3  |
| 50                         | 6.5 ± 5.6                                      | 3.1 ± 1.1  |
| 150                        | 16.4 ± 7.8                                     | 3.5 ± 2.0  |

**Table 3.1.** The average size of the Co nanostructures originally synthesized in DMSO at various temperatures before and after the addition of DI-H<sub>2</sub>O, where 10 mL of DI-H<sub>2</sub>O was added to 30 mL of each Co nanostructure dispersion.

### 3.3.3 Co Nanoparticle Cluster Degradation by Co-Solvent Addition

Other polar protic, polar aprotic, and non-polar co-solvents were added to the Co nanostructure dispersion that were synthesized at 150°C in order to determine if the co-solvent polarity or the hydrogen bonding capabilities of the co-solvent could influence the average Co nanoparticle size. A list of the co-solvents added to the Co nanostructures originally synthesized in DMSO at 150°C is provided in Table 3.2, as well as the corresponding average Co nanoparticle size after the addition of the co-solvents, where 10 mL of each co-solvent was added to 30 mL of the Co nanostructure dispersion in each case. Each of the different co-solvents that were added to the Co nanostructure dispersion (i.e. the 16 nm Co nanostructures) caused an overall decrease in the average Co nanoparticle size, as shown in Table 3.2. The addition of a co-solvent liberates the individual Co nanoparticles, which construct the larger (~16 nm) structures, by providing a favorable interaction between the DMSO molecules adsorbed on the Co nanoparticle surface and the added co-solvent. It is necessary to point out that the addition of DMSO had essentially no effect on the average nanoparticle size, because the interactions between the added co-solvents and DMSO are more preferred than the interactions between neighboring DMSO molecules, thereby preventing the smaller (~4nm) Co nanoparticles from being liberated from the larger (~16 nm) nanostructures in this case.

| Co-Solvent          | Average Co Nanoparticle Size (nm) after the Addition of Co-Solvent |
|---------------------|--|
| DMSO                | 15.9 ± 5.6   |
| Acetone             | 2.9 ± 1.6  |
| DI-H <sub>2</sub> O | 3.5 ± 2.0  |
| Acetic Acid         | 2.8 ± 0.9  |
| Methanol            | 3.3 ± 1.9  |
| Ethanol             | 2.7 ± 1.1  |
| Isopropanol         | 4.9 ± 2.9  |
| Dichloromethane     | 4.0 ± 2.0  |
| Chloroform          | 3.5 ± 1.5  |
| Toluene             | 3.3 ± 1.7  |

**Table 3.2** A list of the co-solvents added to the Co nanostructures originally synthesized in DMSO at 150°C and the corresponding average Co nanoparticle size after the addition of the co-solvents, where 10 mL of each co-solvent was added to 30 mL the Co nanostructure dispersion. Solvents are listed in the order of decreasing dipole moments.

### 3.4 Discussion of Co Nanoparticle Clustering and Cluster Degradation

The results presented in Chapter 2 indicated that DMSO interacts favorably with Co nanoparticles, and DMSO has been shown to provide sufficient and simultaneous particle stabilization and solvation (Liu et al. 2010). In the present chapter, various co-solvents were added to the different Co nanostructure dispersions (resulting from the three syntheses conditions). A step-wise illustration is provided in Figure 3.7 to supplement this discussion, where water is used as the example co-solvent.

Specifically, Figure 3.7a first illustrates what likely occurs when DI-H<sub>2</sub>O is introduced into the system of nanoparticles (~4 nm) that were synthesized at 25°C in DMSO, where ‘Stage 1’ shows that the Co nanoparticles are actually composed of individual particles that are dispersed in the DMSO solution. In this solution, the DMSO solvent molecules interact with the DMSO molecules that are adsorbed to the surface of the Co particles, thereby resulting in sufficient osmotic repulsion between neighboring particles so as to keep the individual Co nanoparticles dispersed in the DMSO solution. These osmotic repulsive forces result from the solvation of the nanoparticle ligands (in this case the DMSO molecules adsorbed to the surface of the Co nanoparticles). Upon the addition of DI-H<sub>2</sub>O to Co nanostructure dispersion in ‘Stage 2’ (Figure 3.7a), these Co nanoparticles remain individually dispersed and therefore maintain the same average size, distribution, and shape (as reported in Table 3.1).

Figure 3.7b shows the different steps that may occur when nanostructures are introduced initially to a co-solvent (e.g., DI-H<sub>2</sub>O) after their synthesis at elevated temperatures. In ‘Stage 1’ individual nanoparticles capped with DMSO are formed at higher temperatures (as shown from TEM imaging analysis in Figure 3.3b, c). At higher



temperatures (e.g. 50°C and 150°C), the intermolecular interactions occurring between DMSO solvent molecules in solution and the DMSO molecules attached to the particle surface become less favorable, causing the van der Waals forces between neighboring particles to dominate over the osmotic repulsive forces (Kitchens et al. 2003; Cushing et al. 2004). This, in turn, causes the initially formed Co particles to agglomerate into a polydisperse sample of clustered Co nanostructures, as depicted in ‘Stage 2’. In ‘Stage 3’, the solution is returned to 25°C before DI-H<sub>2</sub>O is added to the system and the particle size distribution remains the same. In ‘Stage 4’, DI-H<sub>2</sub>O is added to the Co nanostructures, where the DMSO-capped nanoparticles likely form favorable interactions with DI-H<sub>2</sub>O. ‘Stage 5’ shows the re-dispersion of one of these agglomerated nanoclusters by DI-H<sub>2</sub>O, and since the DI-H<sub>2</sub>O interacts favorably with the DMSO ligands on the nanoparticles, the DI-H<sub>2</sub>O effectively ‘pushes’ apart the individual particles in these clusters through preferential (i.e. improved) solvation. Thus, ‘Stage 6’ illustrates that the larger particle agglomerates can be completely separated and, therefore, re-dispersed by preferential solvation that is occurring between the added DI-H<sub>2</sub>O and the DMSO ligands on the nanoparticles. ‘Stages 4-6’ are summarized in Figure 3.7c, which illustrates that the DI-H<sub>2</sub>O molecules can solvate the DMSO ligands that are adsorbed on the Co nanoparticle surface and effectively separate the agglomerated DMSO-stabilized nanoclusters.

Many of the reports in the literature for controlled cluster formation and degradation involve adding other reagents, adjusting the metal ion concentration, or changing the pH of the solution in order to achieve nanoparticle clustering (as was discussed in Section 3.1). Very few reports have directly investigated the effect of

temperature on nanoparticle aggregation to form stable nanoparticle clusters. However, one study did show that 5 nm magnetic nanoparticles can be assembled into stable 90 nm clusters by coating the smaller particles with a temperature-dependent polymer (Isojima et al. 2008). In this particular study, the individual nanoparticles were composed of a hydrophilic coating that would become amphiphilic and self-assemble into 90 nm clusters as a function of the solution temperature (Isojima et al. 2008). The clustering synthesis technique described in the present chapter is different from other reports in the literature for nanoparticle clustering because a small molecule, DMSO, is used as both the solvent and the ligand, and is adsorbed to the surface by electrostatic interactions. Herein, the thermal energy provided by the increased synthesis temperatures effectively weakened the intermolecular interactions between the DMSO molecules adsorbed on the surface of the Co nanoparticles and the DMSO solvent molecules in solution. This effect subsequently promoted Co nanoparticle agglomeration at these conditions. The process of Co nanocluster formation at high temperatures in DMSO and subsequent nanocluster solvation by the addition of co-solvents occurs because of the distinct solvation characteristics provided by DMSO. DMSO is an aprotic polar solvent and it has the capabilities to dissolve both polar and non-polar compounds (Andreatta et al. 2007) (Gaylord Chemical Company LLC 2007), and this unique solvation characteristic allows DMSO to form preferential interactions with other solvents.

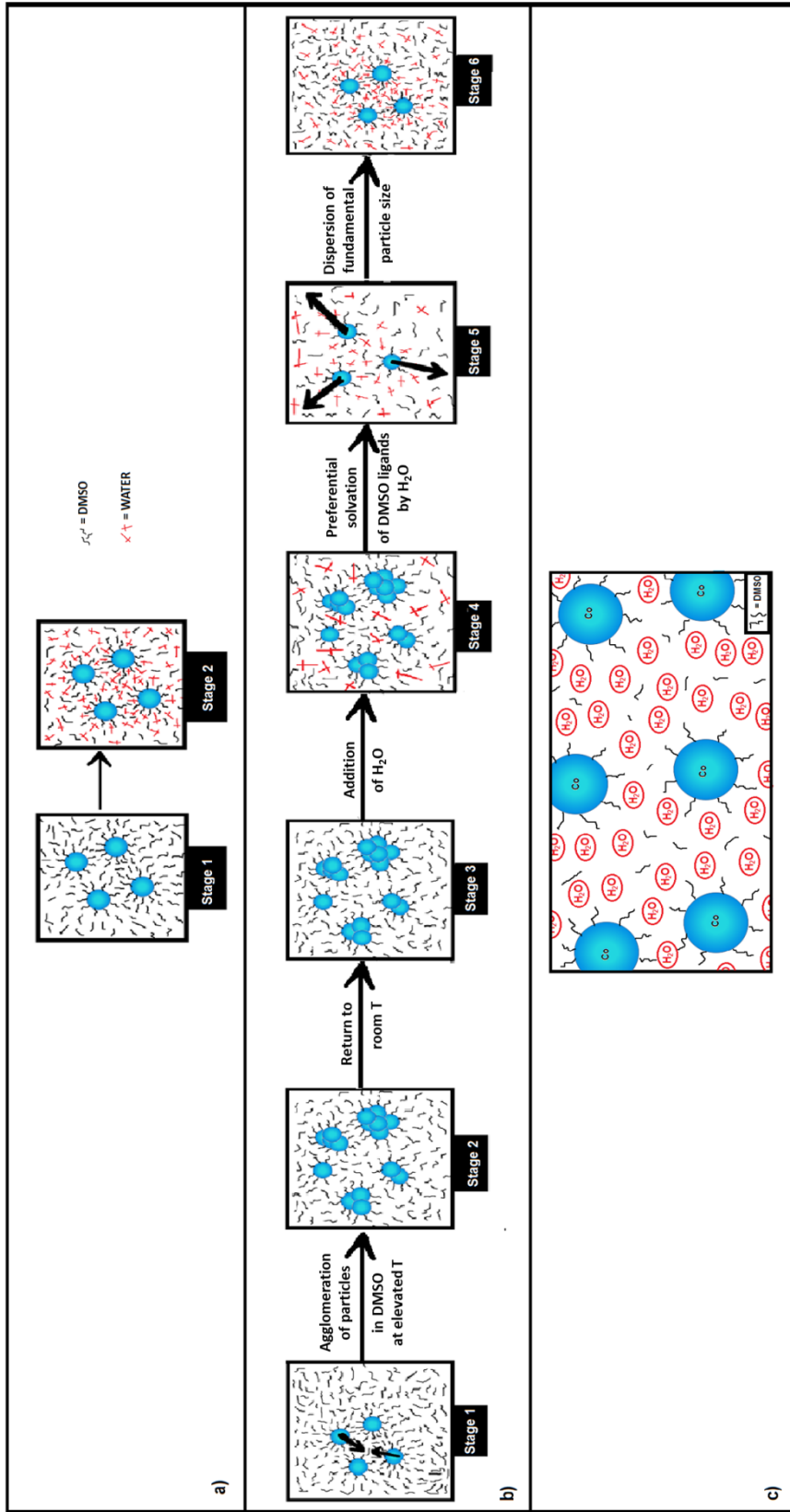


**Figure 3.7** Cartoon representation of Co nanostructures interacting with co-solvents (e.g., DI-H<sub>2</sub>O): a) at 25°C, b) at elevated temperatures (e.g., 50°C, 150°C) and c) detailed depiction of DMSO-stabilized Co nanoparticles being solvated by co-solvents (e.g., DI-H<sub>2</sub>O).

### **3.5 Conclusions**

The ability to induce nanoparticle clustering in solution is of contemporary interest, and it has been reported that individual nanoparticles can be aggregated into clusters by controlling the reaction conditions. It has already been shown in Chapter 2 that DMSO can be used to function simultaneously as a capping ligand and a solvent during nanoparticle synthesis. The present chapter demonstrated that Co nanoparticles (~4 nm) in DMSO can aggregate into larger (~16 nm) structures in DMSO by simply increasing the reaction temperature during synthesis, where the largest clusters form at the highest synthesis temperatures. Additionally, these Co nanoclusters were found to be composed of smaller Co nanoparticle building blocks, which will aggregate into clusters at increased reaction temperatures. These small Co nanoparticles (which construct the larger Co nanoclusters) in DMSO can be subsequently liberated and redispersed by adding various co-solvents to the nanocluster dispersion.

## **Chapter 4**

### **Controlling the Crystallinity and Magnetism of Cobalt Nanoparticles via Thermal Oxidative Treatment**

It is of contemporary interest to be able to utilize convenient methods to produce magnetic nanoparticles due to the significant demand for improvements and miniaturization of energy and information storage devices. Magnetic nanoparticles are easily oxidized if the surface is not properly protected (i.e., if the stabilizing ligand cannot sufficiently adsorb to the particle surface due to weak electrostatic attractions between the particle and the ligand). Bulky stabilizing ligands that can be attached directly to the nanoparticle surface to prevent oxidation can consequently impede the particles' magnetism. These issues can be addressed by utilizing a single, small molecule (e.g., dimethyl sulfoxide - DMSO) to function simultaneously as the solvent and the stabilizing ligand during nanoparticle synthesis, which effectively protects the particles from oxidation. This chapter describes a technique that allows for the facile production of spinel structures of  $\text{Co}_3\text{O}_4$  nanostructures via a simple synthesis and post-synthesis annealing process, and these novel particles have been shown to exhibit high magnetic anisotropy and coercivity.

## 4.1 Introduction

Magnetic nanoparticles have been used in a wide variety of applications including numerous biomedical applications (Cole et al. 2011; Mornet et al. 2004; Corot et al. 2006; Cormode et al. 2010) as well as in magnetic data (Tanase et al. 2007; Gubin et al. 2002; Warne et al. 2000) and energy storage devices (Frey et al. 2009; Li et al. 2011; Zhang et al. 2010). Devices constructed of nanomaterials offer significant improvements over traditional technologies, because the properties, including the particles' magnetism, can be uniquely altered as the dimensions of a material are decreased to the nanoscale (Gubin et al. 2005; Bucher & Bloomfield 1993). Magnetic nanoparticles are of contemporary interest because the size-scale of the nanoparticle is similar to the size of the magnetic domain, and this characteristic can generate very distinct magnetic properties for nanoparticles (Frey et al. 2009). The extraordinary magnetic behavior of nanoparticles arises from the difference between the domain walls of a bulk material and single domain nanoparticles. The domain walls in bulk metals can nucleate and rotate with the rotation of the magnetization vector; however, domain wall movement does not occur in single domain nanoparticles because the domain size is on the nanoscale (Frey et al. 2009). Typically, the critical diameter of a single domain magnetic nanoparticle is in the range of 10-100 nm (Frey et al. 2009), however, the single domain limit can reach several hundred nanometers for particles with high magnetic anisotropy (Skomski & Coey 1999).

There is also much interest focused on creating new materials that have high magnetic anisotropy and coercivity, which can be used to improve energy and data storage devices. In fact, Gubin et al., (2005) emphasizes that modern magnetic materials

should exhibit significant coercivity, preferably in the range of 2 – 3 kOe. A large value of coercivity is desired for energy storage applications in order to maintain long-term (magnetic) stability (Frey et al. 2009). Moreover, magnetic nanoparticles have attracted considerable interest in recent years due to their unique properties, potential for various applications including permanent magnet where high magnetic anisotropy and high coercivity are essential. Recently, it was reported that nano-particles of Co-carbide synthesized via polyol reaction exhibited very high coercivity, leading to magnet performance  $((BH)_{\max})$  higher than  $20 \text{ kJm}^{-3}$  (Harris et al. 2010). Recent work on spinel ferrites indicate that bulk spinel ferrites can exhibit soft or hard magnetic properties depending on its electronic structure, i.e., bulk  $\text{CoFe}_2\text{O}_4$  (hard) and  $\text{MnFe}_2\text{O}_4$  (soft). Moreover, thin films of  $(\text{CoFe})_3\text{O}_4$  have been shown to exhibit magnetic anisotropy of  $6 \times 10^6 \text{ erg/cc}$  at room temperature (Kita 2013). However, there is little work reported in literature which investigates the magnetism of spinel-type cobalt oxide nanoparticles (Farhadi et al. 2013).

Numerous techniques have been employed to produce magnetic cobalt (Co) and cobalt oxide nanoparticles of specific sizes, including various solution-based methods (Sun & Murray 1999) (Yuan et al. 2009), laser vaporization methods (Glaspell et al. 2004), thermal decomposition methods (Salavati-Niasari et al. 2009), and mechanical methods (Yang 2004). Solvent-based methods are particularly attractive techniques because careful control over nanoparticle size can be achieved (Yang et al. 2003). However, it is important to note that the magnetic properties of nanoparticles can be influenced by the chemical composition, the crystal lattice structure, particle size and

shape, morphology, and the interaction with the nanoparticle with the surrounding media (Gubin et al. 2005).

Standard solution-based nanoparticle synthesis methods typically require additional molecules to function as stabilizing ligands, which are directly attached to the nanoparticle surface in order to prevent nanoparticle agglomeration and precipitation from the solution. These stabilizing ligands are used in many of the popular magnetic nanoparticle synthesis technique in order to control particle growth and inhibit oxidation (Yikun Su, Xing OuYang, Jiaoning Tang 2009). However, bulky stabilizing ligands directly attached to the nanoparticle surfaces have been reported to impact the magnetic behavior of the particle (Duan et al. 2008; Crespo et al. 2004). Therefore, it is imperative that nanoparticle stability is maintained in order to prevent degradation and maintain favorable magnetic behavior (Lu et al. 2007).

A major theme in this dissertation has been to use the molecule, DMSO, as a functional solvent during Co nanoparticle synthesis. This is particularly important for the studies performed in the present chapter because eliminating the use of stabilizing ligands that are different from the solvent during the synthesis of magnetic nanoparticles can allow for the improved access to a nanoparticle's surface and its surface energy. Recall that the techniques utilized in Chapter 2 used DMSO to function concomitantly as both the solvent and the stabilizing ligand during synthesis, which allows more complete and unrestricted access to the nanoparticle surface. The studies in Chapter 2 also found that DMSO coordinates with the surface of the Co nanoparticles via the oxygen component of the sulfoxide functional group, and a monolayer of DMSO is remnant on the surface of the Co nanoparticles after solvent removal. Gubin et al., (2009) suggests that the surface



composition of a nanoparticle can influence the surface anisotropy and contributes to the total magnetic anisotropy of the particle. Utilizing a functional solvent in magnetic nanoparticle synthesis allows for the control of the surface composition of the nanoparticles, which could ultimately influence the surface anisotropy and overall magnetism. Hence, investigating the magnetism of Co and cobalt oxide nanoparticles produced by using DMSO as a functional solvent is of great interest because these studies may shed light on the benefits of using small molecules as functional solvents to produce nanoparticles with unique magnetic properties.

It has long been reported that the crystalline structure of metals can be altered by heat treatments (Folen & Rado 1958). There are numerous reports in the literature which describe how annealing amorphous metals at high temperatures can induce crystallization, and several studies have reported the evolution of ordered Co nanoparticles from amorphous Co after heat treatment (Yang 2004; Chou et al. 2008). Chou and co-workers describe (2008) a process to prepare ordered structures of  $\text{Co}_3\text{O}_4$  by heating amorphous cobalt ( $\text{Co}(\text{OH})_2$ ) structures in air to  $300^\circ\text{C}$ . A solvent-based synthesis technique has also been reported to produce silane-coated, amorphous cobalt nanoparticles that can be crystallized after annealing in air up to  $700^\circ\text{C}$  for 2 hours (Kobayashi et al. 2003). Another group has reported the mechanochemical synthesis of cobalt oxide nanoparticles from an amorphous precursor, which were produced after heat treatment up to  $600^\circ\text{C}$  for 2 hours (Yang 2004). It has also been reported that different crystal structures of Co can have different magnetic properties (Park et al. 2002; Sun & Murray 1999). Petit and co-workers have successfully produced hcp-structured cobalt nanoparticles with high magnetic anisotropy and high-order crystallinity which occurred

after annealing (Petit et al. 2005), and these particles were annealed for 30 minutes at 300°C. Thus, it is of great interest to investigate the influence of higher annealing temperatures (e.g., 800°C) and annealing times (e.g., 20 hours) on the formation of various cobalt nanostructures.

In this chapter, we present a technique to advance the methods by which magnetic nanomaterials are prepared by combining a straightforward nanoparticle synthesis technique, where DMSO is used as the functional solvent, with a controlled, post-synthesis thermal oxidative treatment process. We investigate the effect of temperature on the Co nanoparticle morphology, crystal structure, and magnetism of the Co nanoparticles that were produced using DMSO as the solvent and as the stabilizing agent. Co nanoparticles are annealed in air for 2 hours at 200°C, 400°C, 600°C, and 800°C in a furnace, and these particles were studied using TEM, SEM, and XRD. Additionally, Co nanoparticles are annealed at 800°C for 2, 12, 15, and 20 hours to investigate the influence of annealing time on Co nanoparticle magnetism.

## **4.2 Experimental**

### **4.2.1 Materials**

Dimethyl sulfoxide ((CH<sub>3</sub>)<sub>2</sub>SO, 99.9%) was obtained from BDH Chemicals. Deionized ultrafiltered water (DI-H<sub>2</sub>O) was obtained from Fisher Scientific. Cobalt (II) chloride hexahydrate (CoCl<sub>2</sub>\*6H<sub>2</sub>O, 99+%) was obtained from Strem Chemicals. Sodium borohydride (NaBH<sub>4</sub>, 99%) was obtained from Sigma Aldrich. Acetone ((CCH<sub>3</sub>)<sub>2</sub>CO) was obtained from BDH. Nitrogen (UHP grade) was obtained from Airgas.

### 4.2.2 Co Nanoparticle Synthesis

Co nanoparticles were synthesized via the solvent-based reduction of  $\text{Co}^{2+}$  using  $\text{NaBH}_4$  as a reducing agent at room temperature as described in Chapter 2. An airtight apparatus was constructed around the reaction flask so as to prevent any possible oxygen contamination from environmental exposure to air during synthesis. In a typical reaction, 4 mL of a 0.05 M  $\text{Co}^{2+}$  salt solution and 10 mL of 0.05 M  $\text{NaBH}_4$  were added to 50 mL DMSO solution. The solution was continuously stirred using a magnetic stirrer (at  $\sim 700$  rpm) and purged with  $\text{N}_2$  for 30 minutes prior to the addition of any reagents, during reagent addition, and for 2 hours after reagent addition. After 2 hours, the  $\text{N}_2$  purge was stopped, and the contents of the reaction flask were securely capped and allowed to stir continuously for 24 hours. It is noted that a Radley apparatus was used to synthesize several (up to six) Co nanoparticle samples at a time (as shown in Figure 4.1), where the same experimental procedure was followed as defined above.



**Figure 4.1** Radley apparatus used to simultaneously synthesize up to six Co nanoparticle samples in DMSO.

### **4.2.3 Precipitation of Co Nanoparticles from DMSO Solution**

Co nanoparticles were removed from DMSO solvent and dried to a powder by using acetone as a liquid anti-solvent in combination with centrifugation, as described in Chapter 2. To accomplish Co nanoparticle precipitation from DMSO, 5 mL of acetone was added to 3 mL of the Co-DMSO in a centrifuge tube and placed in a centrifuge for 5 minutes at 5000 rpm. Co nanoparticle agglomerates were precipitated on the bottom of the centrifuge tube, and the clear supernatant layer was removed from the centrifuge tube using a pipette. The process of acetone addition and centrifugation was repeated twice. After removal of the acetone supernatant, 5 mL of DI-H<sub>2</sub>O was added to the centrifuge tube and the tube was placed on the vortex mixer for 30 seconds prior to centrifugation at 5000 rpm for 5 minutes. Water is used in this step to remove any water-soluble byproducts that were still present on the Co nanoparticles. The water supernatant was removed and the process of washing the Co nanoparticles with water was repeated twice. A final addition of acetone, followed by centrifugation, and supernatant removal was also performed. The precipitated Co nanoparticle powder that remained at the bottom of the centrifuge tube was dried completely with N<sub>2</sub> using a nitrogen-inflated polyethylene glove bag (shown in Figure 2.5) to ensure complete removal of acetone prior to any further analysis. If necessary, A Zerostat Antistatic Gun was used to assist transfer the dried Co nanoparticle powder into a new vial.

### **4.2.4 Post-Synthesis Annealing of Co Nanoparticles**

Thermal treatment of the Co nanoparticle powder was performed using a Type 30400 Thermolyne Furnace equipped with a digital temperature controller. Each Co nanoparticle sample was contained in a ceramic crucible and placed in the center of the

furnace. The sample was then heated (i.e., annealed) in the furnace at room temperature in air to the desired temperature. Each sample was annealed independently in air to 200°C, 400°C, 600°C, and 800°C. All samples were heated for 2 hours, and an additional sample of Co nanoparticles was heated using the same procedure at 800°C for 12 hours, 15 hours, and 20 hours.

#### **4.2.5 Characterization Techniques**

*Transmission Electron Microscopy (TEM)* – TEM was used to investigate the particle size of the Co nanoparticles before and after thermal treatment using a Zeiss EM 10 TEM at an operating voltage of 60 kV. Co nanoparticle size measurements were performed on the Co nanoparticle sample before and after heating. Each of the Co nanoparticle samples were dispersed in a fresh solution of DMSO after heat treatment, where approximately 0.001 g of Co nanoparticle powder was dissolved in 1 mL of DMSO. TEM samples were made by placing a single drop of sample in DMSO onto a carbon type B, 300 mesh copper grid. The grid was contained in a plastic petri dish and placed in the vacuum oven to dry for several days prior to TEM analysis. The average particle size and size distribution of the Co nanoparticles were obtained using the Image J software package to size more than a hundred particles from multiple TEM images taken from the same sample grid..

*Scanning Electron Microscopy (SEM)* – SEM was used to study the particle size and morphology of the Co nanoparticle powder samples that were obtained after heating using a Zeiss EVO 50VP SEM. In each case, the Co nanoparticle powder was placed on double-sided adhesive carbon tape and mounted on an aluminum SEM stub. The mounted Co nanoparticle samples were coated with a thin layer of gold (~14 nm) using

an EMS 550X Sputter Coating Device prior to SEM imaging. Coating the Co particles with a thin layer of gold helped to improve the image resolution and more details on this topic are provided in Appendix B.

*X-ray diffractometry (XRD)* - XRD was used to investigate the crystallinity and surface oxidation of each of the Co nanoparticles after annealing using a Bruker D8 diffractometer with Cu-K $\alpha$  radiation ( $\lambda = 1.54056 \text{ \AA}$ ) and operated at 40 kV and 40 mA. The diffraction patterns were collected using a step size of  $0.01^\circ$  and 0.1 s/step count time from  $20^\circ \leq 2\theta \leq 90^\circ$ . Each sample was prepared by placing a portion of the Co nanoparticle powder on a glass slide and pressed flat using a glass slide.

*Thermogravimetric Analysis (TGA)* – TGA was performed on the Co nanoparticle powder, that was obtained prior to annealing, in order to study the desorption of the DMSO solvent and any other compounds from the surface of the particles as a function of temperature. Measurements were collected using a Q50 TA Instruments TGA. The microbalance was purged with 10 mL/min argon and argon was also used as the purge gas with a flow rate of 90 mL/min. An aliquot of Co nanoparticle powder was placed in acetone and transferred to a ~100  $\mu\text{L}$  platinum sample pan for a total mass of 4.0510 mg of Co nanoparticle powder sample. The sample temperature was first ramped to  $70.00^\circ\text{C}$  at a rate of  $10.0^\circ/\text{min}$  and held at this temperature for 30 minutes. Then, the temperature was increased to  $250^\circ\text{C}$  at a ramp rate of  $2^\circ\text{C}/\text{min}$  and held isothermally for 60 minutes. Next, the temperature was increased to  $500^\circ\text{C}$  at a rate of  $5^\circ\text{C}/\text{min}$  and held at this temperature for 30 minutes.

*Vibrating Sample Magnetometry (VSM)* – VSM was used to study the magnetism of the Co samples prior to annealing and after annealing at  $800^\circ\text{C}$  for 2 hours, 12 hours,

15 hours, and 20 hours. These measurements and analyses were performed at the Materials for Information Technology (MINT) Center at the University of Alabama in Tuscaloosa, Alabama, as part of a collaborative project. In a typical measurement, a sample of the annealed Co nanoparticles was carefully wrapped in teflon tape and each sample was annealed at 350°C to remove any oxygen trapped within the sample. The total mass of the particles for each magnetic measurement was about 10 mg. The VSM was used to carry out measurements over the temperature range from 4 to 300 K in applied fields up to 90 kOe. Magnetization curves (hereafter referred to as M-H curves) were measured as a field sweep rate of 20 Oe/s with 1 s averaging time.

## **4.3 Results**

### **4.3.1 Morphology of Co Nanoparticles Prior to Annealing**

Co-DMSO nanoparticles were synthesized at room temperature, using DMSO as a functional solvent. The average nanoparticle size was determined using TEM imaging analysis and found to be  $5.2 \pm 2.2$  nm. Figure 4.2 shows a digital TEM image of the Co-DMSO nanoparticle dispersion, and the particles appear to be relatively spherical in shape after synthesis. After synthesis, the Co nanoparticles were dried to a powder using acetone, and an SEM image of the dried powder was obtained, as shown in Figure 4.3. This image indicates that the Co nanoparticle powder appears to be composed of non-uniform structures prior to annealing.



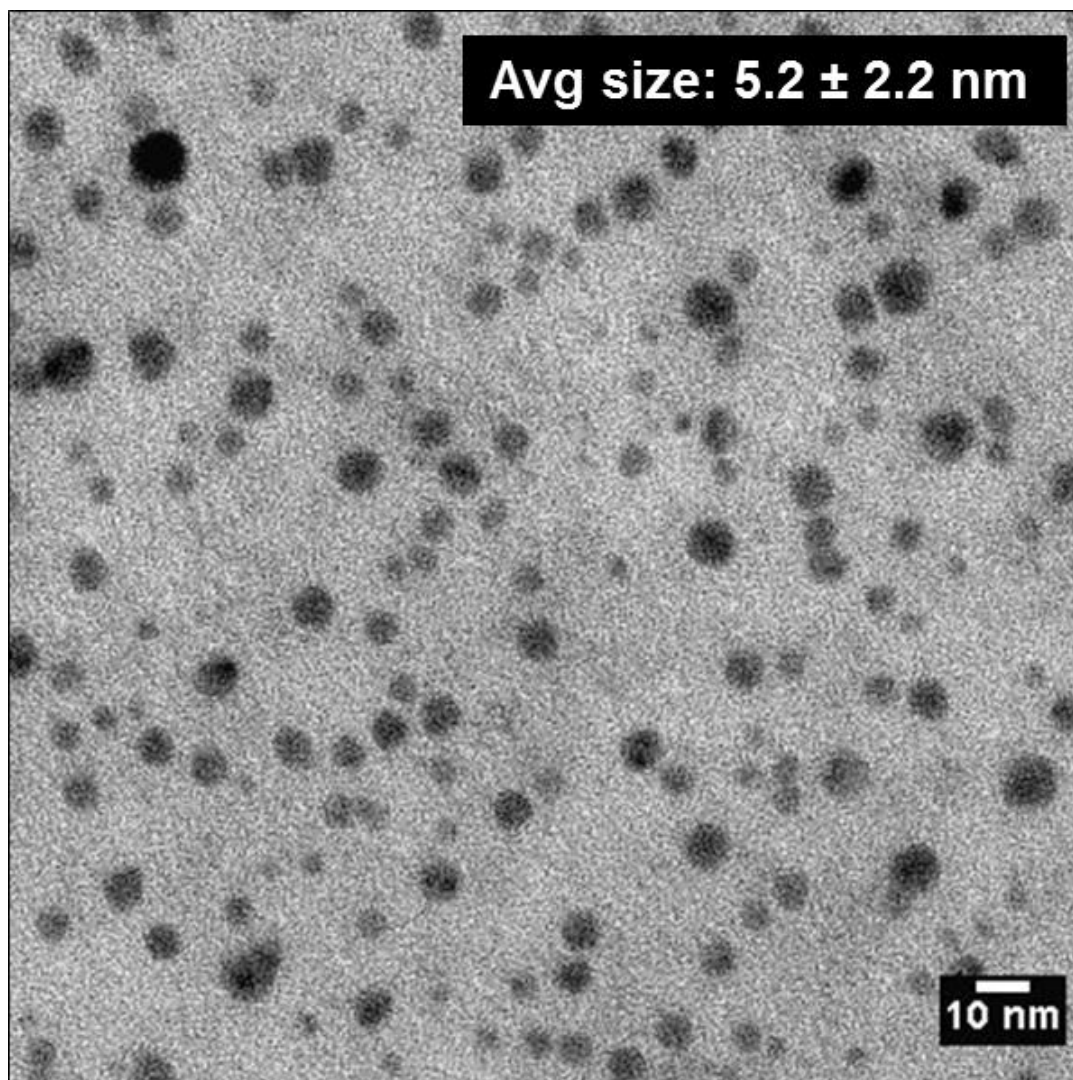


**Figure 4.2** TEM image of Co-DMSO nanoparticles as synthesized at room temperature, prior to annealing.

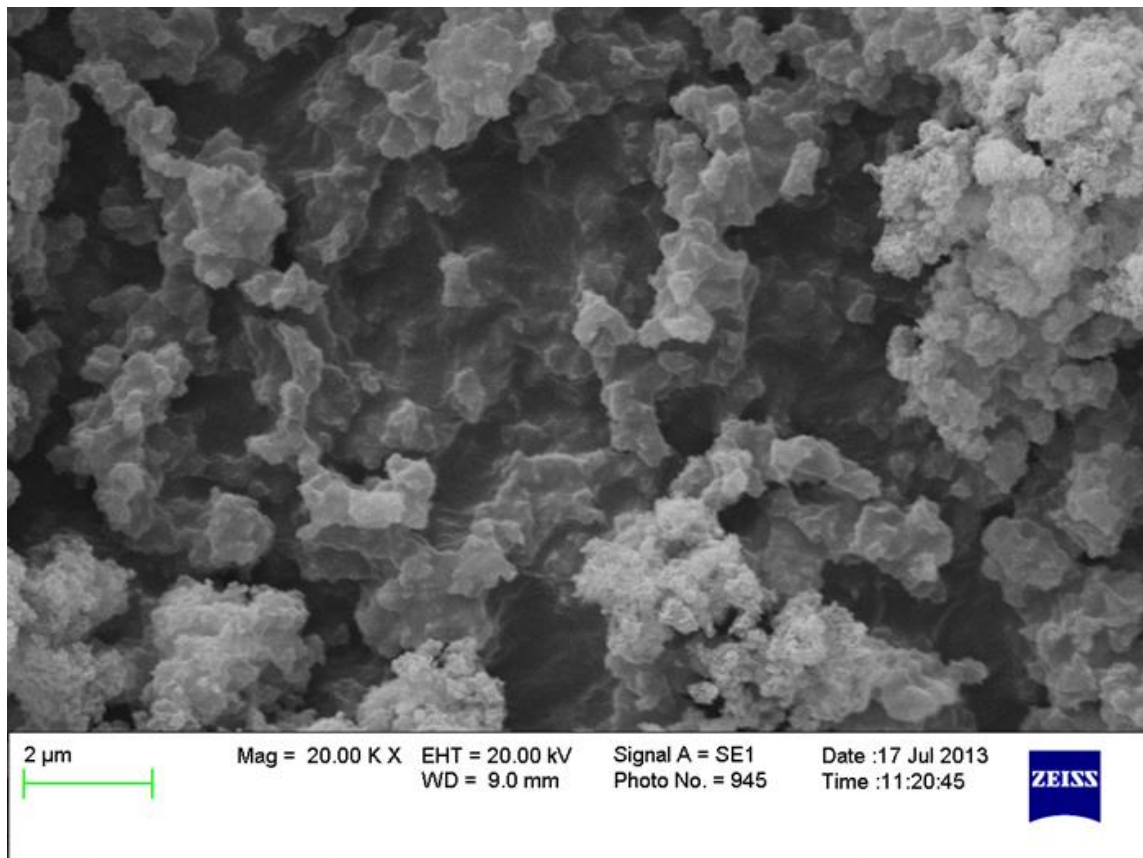


**Figure 4.3** SEM image of Co nanoparticle powder after precipitation from DMSO prior to annealing.

### 4.3.2 Thermal Stability of Co Nanoparticles Prior to Annealing

TGA was performed to investigate the thermal behavior of the Co nanoparticles. The results from TGA analysis are presented in Figure 4.4 and show that the majority of the weight-loss occurs in two-steps from 25°C to 79°C and from 79°C to 252°C. First, there is weight loss of 8.8 wt. % as the temperature is increased from 25°C to 79°C, which corresponds to residual acetone present in the solution likely remaining from TGA sample preparation. Another decrease in the weight (13.5 wt. %) is noticed from 79°C to 252°C, which is attributed to the desorption of water and DMSO from the Co nanoparticle powder. The gradual decrease in the slope over this temperature range can be attributed to the hydrogen bonding occurring between the hydrogen atoms in water and the sulfidic oxygen atoms of the DMSO molecule. There is likely residual acetone, water, and DMSO present in the interior of the Co nanoparticle powder (i.e., within pores), which can cause the gradual decrease in weight percent over the temperature range. There is little change in the Co nanoparticle powder at temperatures greater than 252°C, indicating any residual compounds have been removed from the surface of the Co nanoparticle powder. The findings from TGA analysis indicate that the Co nanoparticle powder is composed of acetone, water, and DMSO, and the annealing temperature will need to be increased well beyond 200°C so as to remove all remnant materials (e.g., residual acetone, water, and DMSO) in order for any possible changes to occur in the morphology or crystal structure of the Co nanoparticles.

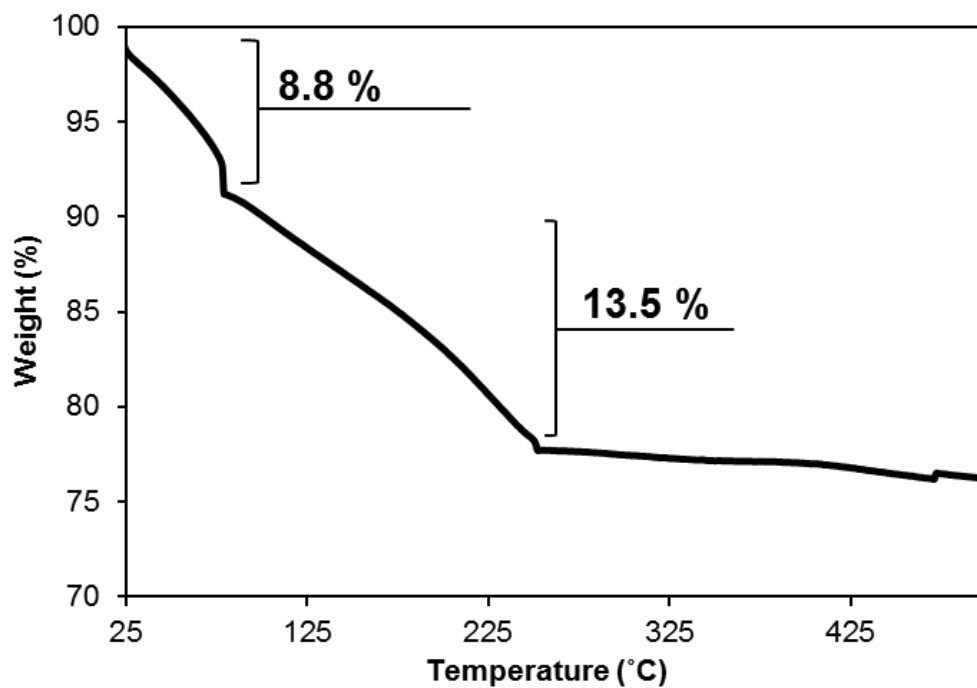


**Figure 4.4** TGA analysis of Co-DMSO nanoparticle powder as synthesized at room temperature. Measurements were performed from 25°C to 500°C.

### 4.3.3 Effect of Thermal Treatment on Co Nanoparticle Structures

Four samples of Co nanoparticle powder were heated separately in a furnace to 200°C, 400°C, 600°C, and 800°C in air for 2 hours in order to determine if the annealing temperature could have any influence on the Co nanoparticle size, morphology, crystal structure, or magnetism. The XRD analysis results are presented in Figure 4.5. Figure 4.5a is the spectrum from the Co nanoparticle powder prior to annealing. There is an absence of defined peaks, indicating the Co nanoparticle powder is amorphous, as described in Chapter 2. Figure 4.5b-e shows the evolution of various peaks, which correspond to the annealing temperature of each of the samples. The Co nanoparticle sample annealed at 200°C remains amorphous after annealing. This is likely due to the fact that DMSO is still present on the surface at this temperature (as confirmed by TGA analysis) and is effectively protecting the particles from crystallization and oxidation at this stage. However, as the temperature is increased further to 400°C and 600°C, small aberrations in the spectra appear for the Co nanoparticles annealed at these temperatures, as can be observed in Figure 4.5c and d. As the temperature is further increased to 800°C in Figure 4.5e, the peaks have become more defined and can be indexed to the peaks of <220>, <311>, <400>, <511>, and <440>, which correspond to the spinel structure of Co<sub>3</sub>O<sub>4</sub>. The results from this study clearly illustrate that the Co nanoparticles undergo a temperature-dependent transition from amorphous Co to an ordered structure of spinel-Co<sub>3</sub>O<sub>4</sub>.

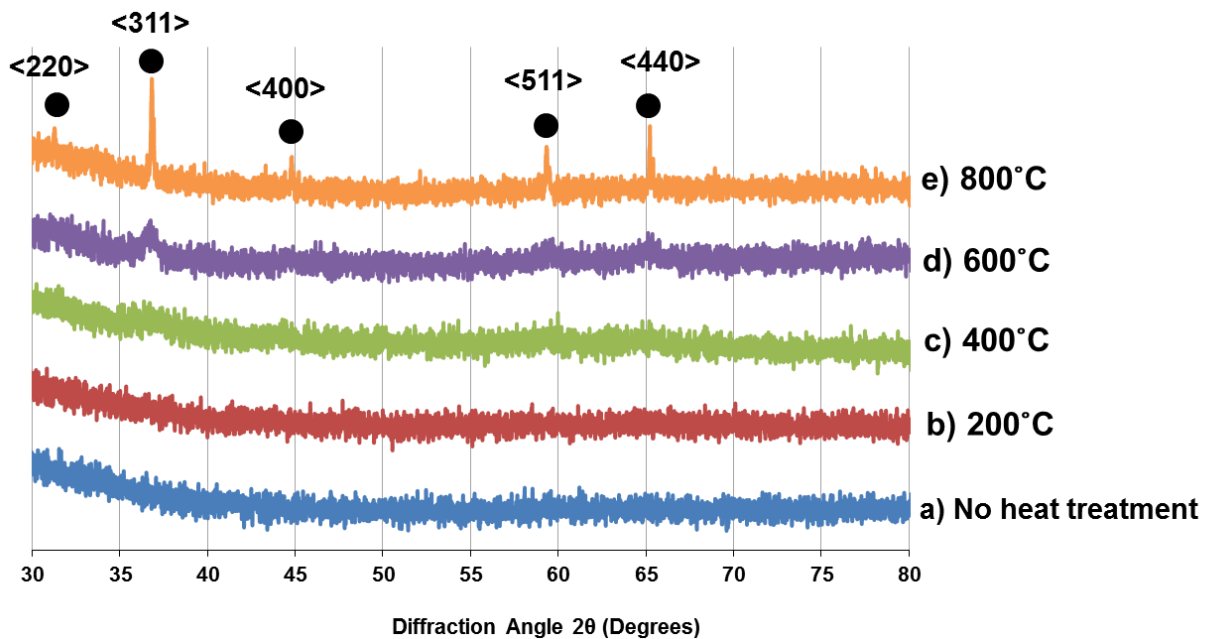


**Figure 4.5** XRD analysis for different samples of Co nanoparticle powder, (a) prior to annealing, and after annealing for 2 hours at (b) 200°C, (c) 400°C, (d) 600°C, and (e) 800°C, where ( ● ) indicates the peaks indexed to spinel  $\text{Co}_3\text{O}_4$ .

#### 4.3.4 Effect of Annealing Time on Co Nanoparticle Structure

Another sample of Co nanoparticle powder was annealed at 800°C for 12 hours in order to determine if the annealing time could influence the crystalline structure of the Co nanoparticles. The results from XRD analysis of Co nanoparticles heated to 800°C for  $t = 2$  hours and  $t = 12$  hours are shown in Figure 4.6. Figure 4.6a shows the Co nanoparticle powder heated to 800°C for 2 hours and the spinel structure  $\text{Co}_3\text{O}_4$  peaks are indicated on the figure. After exposure to 800°C for 12 hours, the Co nanoparticles seem to have developed a more crystalline structure, as can be observed from sharp peaks in the spectrum in Figure 4.6b. In the sample that was annealed for 12 hours, more peaks are present that correspond to the spinel structure of  $\text{Co}_3\text{O}_4$ , and these peaks can be indexed to  $\langle 220 \rangle$ ,  $\langle 311 \rangle$ ,  $\langle 222 \rangle$ ,  $\langle 400 \rangle$ ,  $\langle 422 \rangle$ ,  $\langle 511 \rangle$ ,  $\langle 440 \rangle$ , and  $\langle 622 \rangle$ . A report in the literature has indicated that the formation of the  $\text{Co}_3\text{O}_4$  structure can also result in the formation of randomly oriented crystals (Allaedini & Muhammad 2013), which likely explains the presence of the unlabeled peaks in Figure 4.6b.

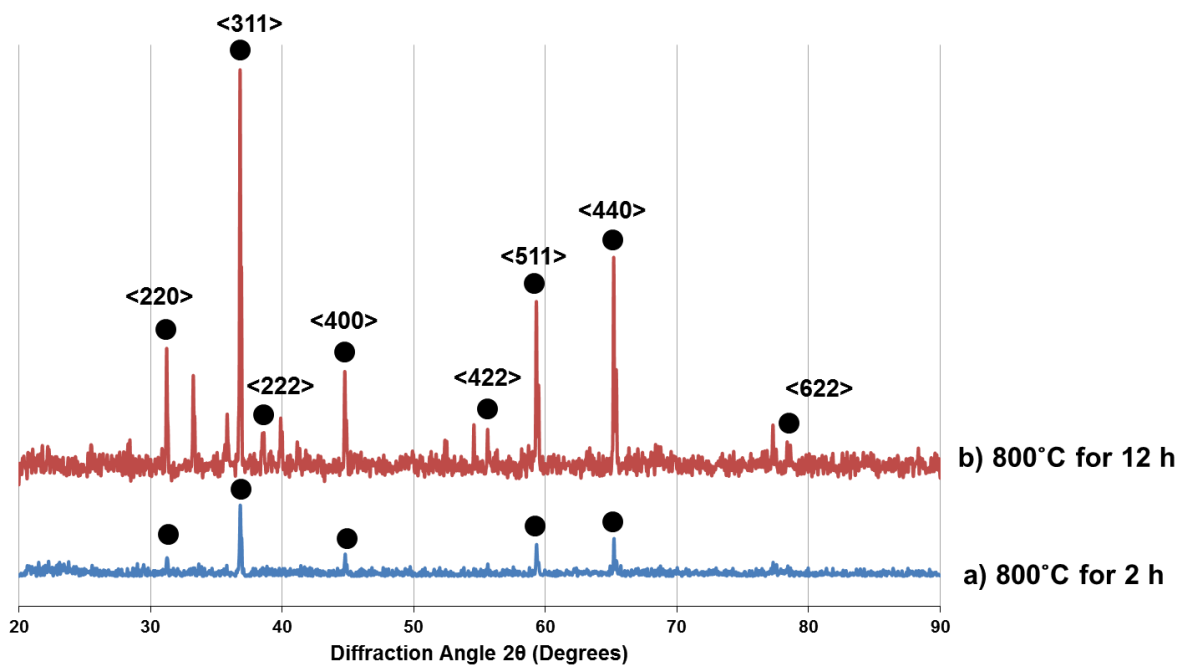


**Figure 4.6** XRD analysis for Co nanoparticle powder annealed to 800°C for a) 2 hours and b) 12 hours, where ( ● ) indicates the peaks indexed to spinel  $\text{Co}_3\text{O}_4$ .



#### **4.3.5 Effect of Thermal Treatment on Co Nanoparticle Size and Morphology**

Each of the Co nanoparticle powder samples were studied after annealing using SEM and TEM imaging analysis in order to study the effects of the different annealing temperatures on Co nanoparticle size and morphology. The SEM images of the Co nanoparticle powder are shown in Figure 4.7 and can be compared to the image of the Co nanoparticle powder prior to annealing (Figure 4.3). It can be observed from Figure 4.7 that as the Co nanoparticles are exposed to higher temperatures (e.g., 200°C, 400°C, 600°C, and 800°C), the apparent morphology of the particles becomes more uniform. In particular, Figure 4.7d presents the Co nanoparticle powder after having been annealed at 800°C for 2 hours. These particles have evolved from non-uniform, flaky structures shown in Figure 4.3, to more spherical structures of ~300 nm, and it is very clear by comparing these images that exposure to heat influences the morphology of the Co nanoparticles.

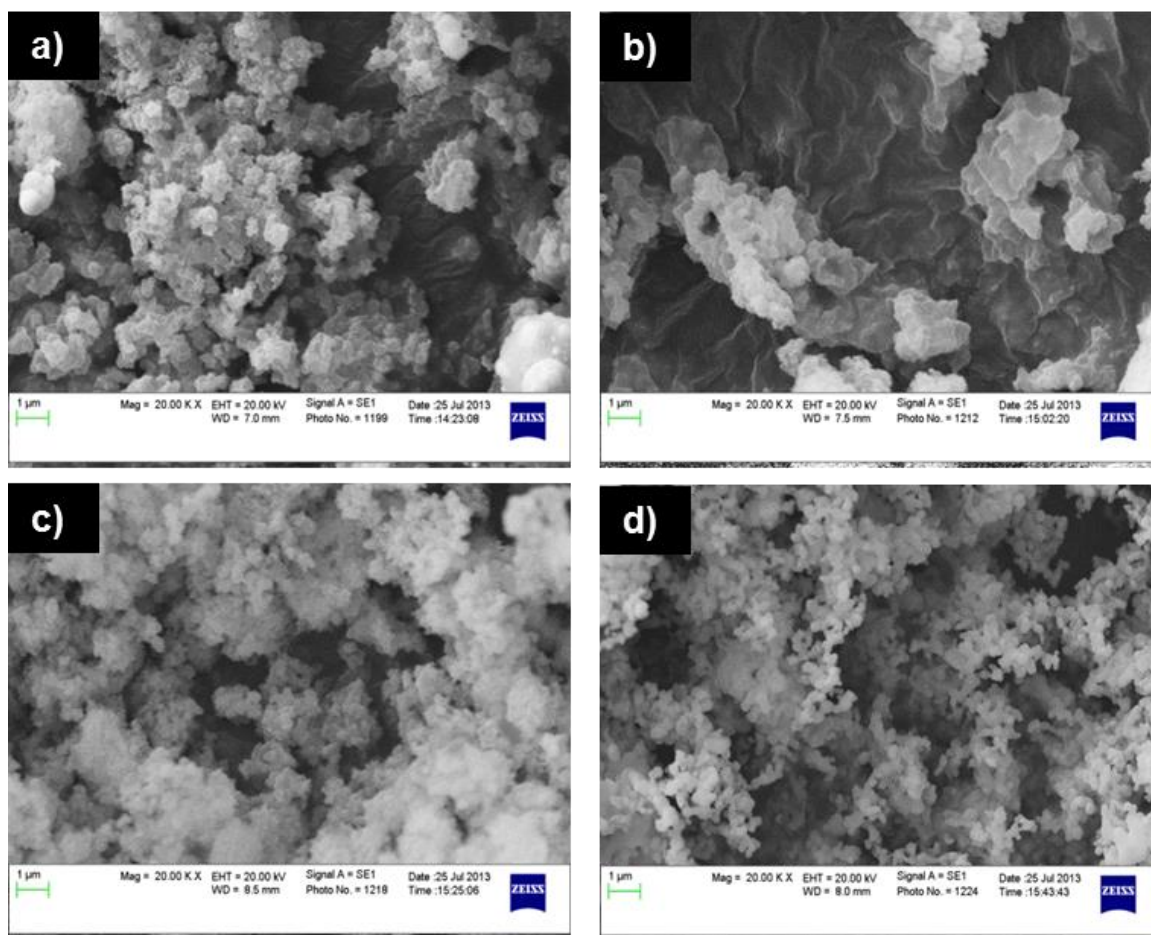


**Figure 4.7** SEM images of the Co nanoparticle powder after annealing for 2 hours to a) 200°C, b) 400°C, c) 600°C, and d) 800°C.

The Co nanoparticle powder was also analyzed using TEM imaging where the Co nanoparticle powder was re-dispersed in a fresh solution of DMSO after annealing, as shown in Figure 4.8. The TEM images of each of the Co nanoparticles re-dispersed in DMSO are shown in Figure 4.9. There were no notable changes in the average Co nanoparticle size with heat treatments shown in Figure 4.9; however, the particle sizes reported in Figure 4.9 are ~1nm smaller than the original Co nanoparticles that had not been annealed (Figure 4.2).



**Figure 4.8** Digital image of Co nanoparticle powders redispersed in a fresh solution of DMSO after annealing to 200°C, 400°C, 600°C, and 800°C for 2 hours (pictured in order of increasing annealing time from left to right).

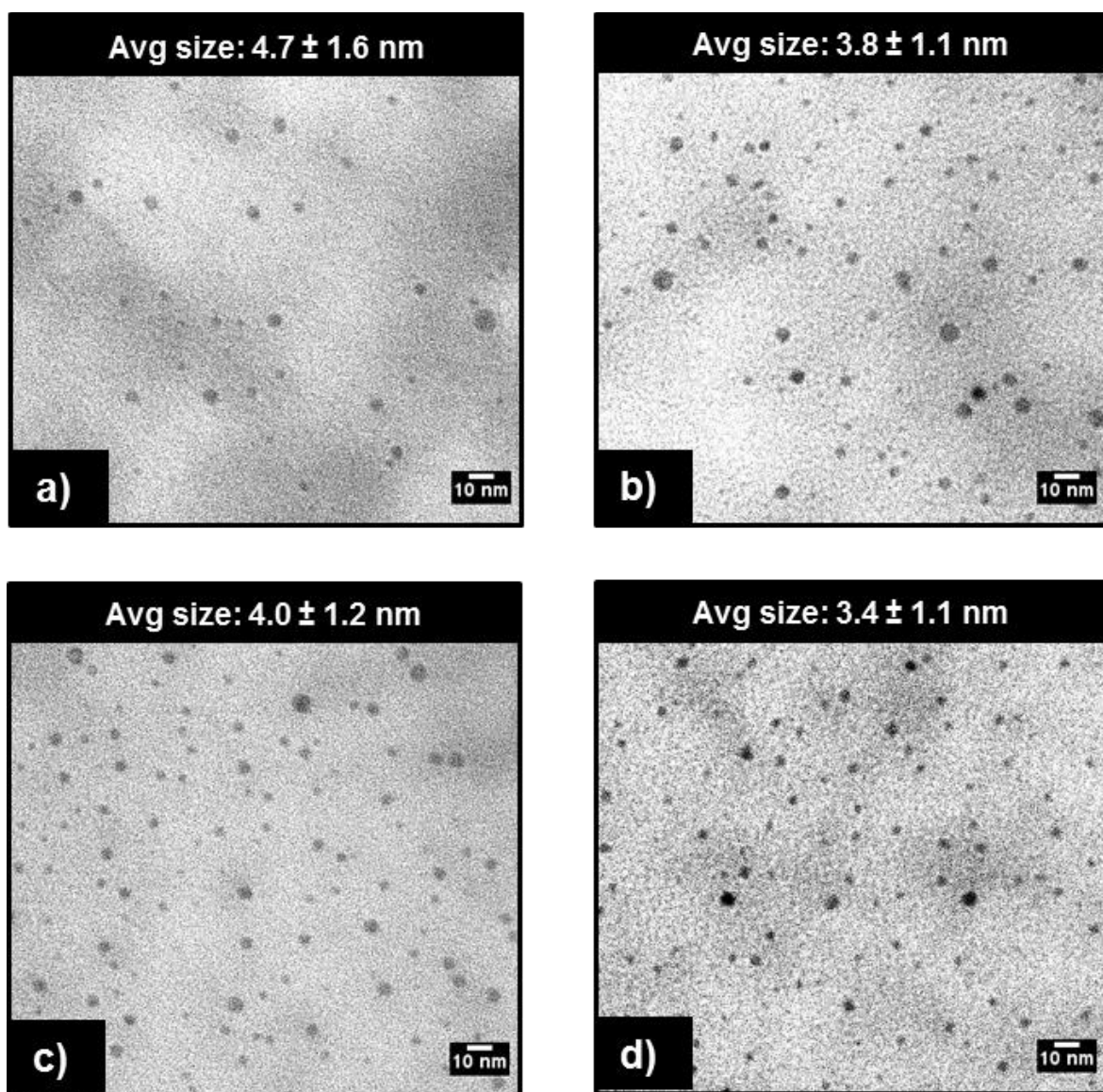


**Figure 4.9** TEM images of the Co nanoparticle powder samples that had been annealed for 2 hours and subsequently re-dispersed in fresh DMSO solution a) 200°C, b) 400°C, c) 600°C, and d) 800°C.

#### 4.3.6 Effect of Annealing Time Co Nanoparticle Size and Morphology

A sample of Co nanoparticle powder was annealed for 12 hours to investigate if the annealing time (at 800°C) could influence particle morphology of the resulting Co<sub>3</sub>O<sub>4</sub> nanoparticles. Figure 4.10 shows SEM images of Co nanoparticle powder a) prior to annealing, b) after annealing at 800°C for 2 hours, and c) after annealing at 800°C for 12 hours. The Co<sub>3</sub>O<sub>4</sub> nanoparticles in Figure 4.10b and c are more uniform in shape than the Co nanoparticles prior to annealing in Figure 4.10a, however, there is no noticeable difference in morphology of the Co nanoparticle powder at the different annealing times.

Similarly, TEM imaging analysis was performed on the Co<sub>3</sub>O<sub>4</sub> sample that had been annealed at 800°C for 12 hours. Figure 4.11 shows the TEM images of Co nanoparticle powder a) prior to annealing, b) after annealing at 800°C for 2 hours, and c) after annealing at 800°C for 12 hours. The Co nanoparticles in Figure 4.11b and c are smaller in size and have a more narrow particle size distribution than the Co nanoparticles prior to heat exposure in Figure 4.11a. However, there is no noticeable difference in morphology of the Co nanoparticle powder at the different heating times.

It is important to note that the Co particles that are dispersed in DMSO (TEM images in Figure 4.2, Figure 4.9, and Figure 4.11) are noticeably smaller than the Co nanoparticle powder (SEM images in Figure 4.3, Figure 4.7, and Figure 4.10). This large difference in size can be attributed to the Co nanoparticles agglomerating in the drying and annealing process. Thus, the large clusters in the Co nanoparticle powder are agglomerations of the smaller particles (~5 nm clusters) that have aggregated due to the removal of DMSO during annealing.

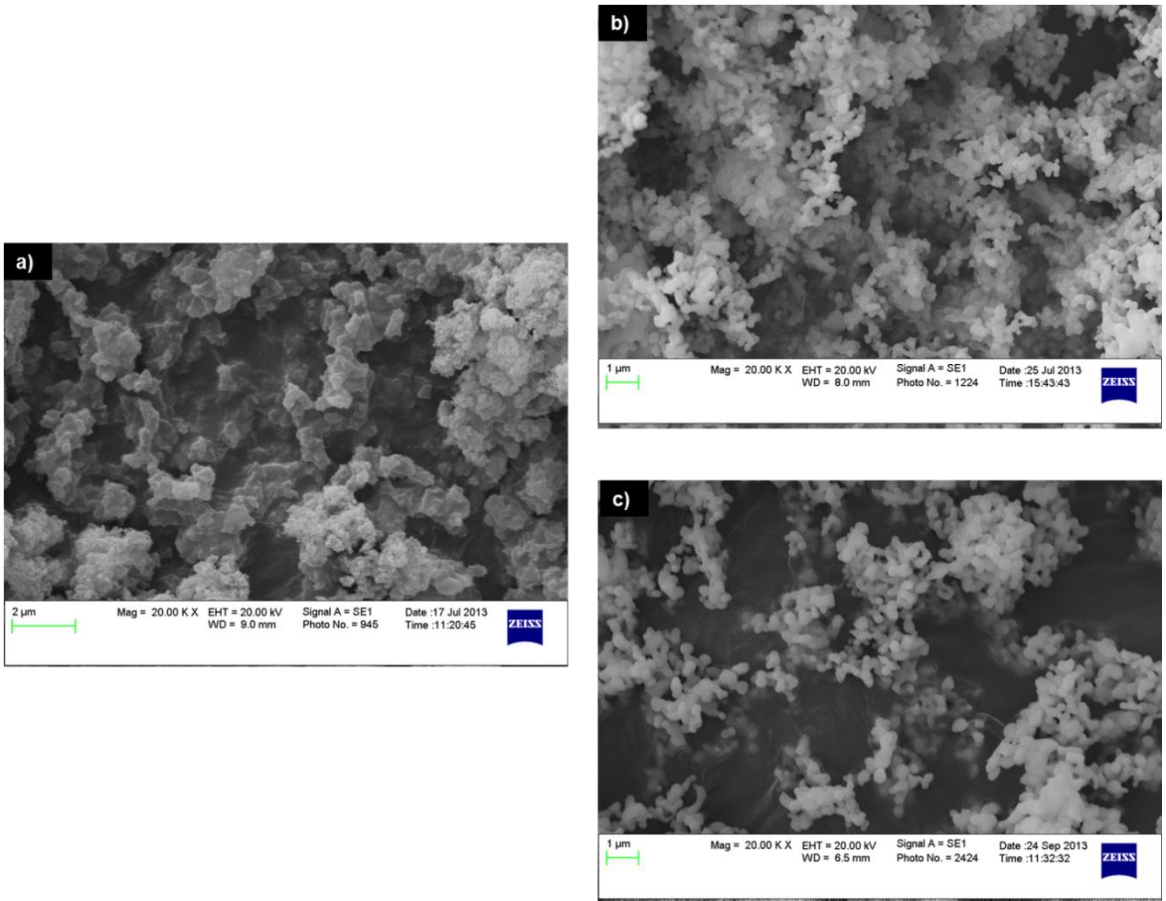


**Figure 4.10** SEM images of the Co nanoparticle powder a) prior to annealing, b) after annealing to 800°C for 2 hours, and c) after annealing to 800°C for 12 hours.

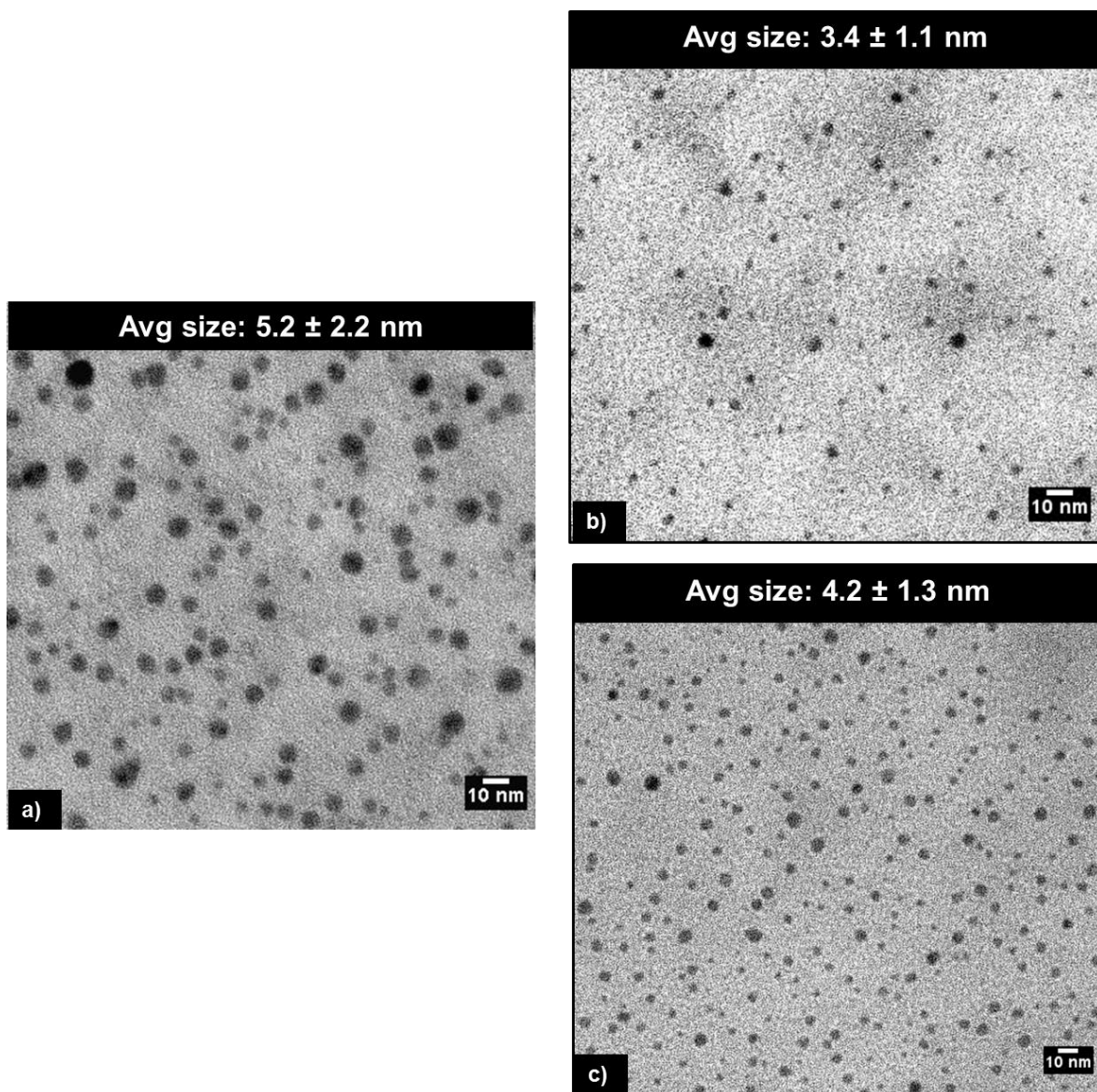


**Figure 4.11** TEM images of the Co nanoparticle powder a) prior to annealing, b) after annealing to 800°C for 2 hours, and c) after annealing to 800°C for 12 hours.



#### 4.3.7 Effect of Thermal Treatment on Co Nanoparticle Magnetic Properties

The effect of annealing on the magnetism of the Co nanoparticle powder samples prior to annealing, annealing at 800°C for 2 hours, 12 hours, 15 hours, and 20 hours was investigated using VSM at 5 K, 40 K and 300 K and the results are shown in Figure 4.12. At 300 K, these Co nanoparticles exhibit paramagnetic behavior. However, ferromagnetic behavior was observed at 5 K with coercivity ( $H_c$ ) ~150 Oe. The M-H curve at 40 K exhibits the behavior for both paramagnetic and ferromagnetic properties. Figures 4.13 and 4.14 show the M-H curves for the annealed samples at 800°C for 2 hours and 12 hours, respectively. Both samples exhibit a paramagnetic behavior at 300K and a ferromagnetic behavior at 5K. Even though the magnetic properties appear to be very similar for these Co nanoparticle samples, particles annealed for 12 hours at 800°C show higher coercivity ( $H_c = 5.7$  kOe) than the sample annealed for only 2 hours ( $H_c = 4.3$  kOe).

Figures 4.15 and 4.16 show the M-H curves for the annealed samples at 800°C for 15 and 20 hours, respectively. Similar to the previous two samples (i.e. samples annealed at 2 and 12 hours at the same temperature), these two samples exhibit paramagnetic and ferromagnetic behaviors at 300 and 5 K respectively while at 40 K the mixture of both the para and ferromagnetic components was observed. The slope of magnetization with H is nearly the same for both the particles at high fields. The Co nanoparticles annealed for 15 hours at 800°C (Figure 4.15) shows the  $H_c \sim 6.7$  kOe at 5 K which is highest among all of the samples measured at the same temperature. The nanoparticles annealed for 20 hours (Figure 4.16) shows  $H_c \sim 6.2$  kOe at 5 K.

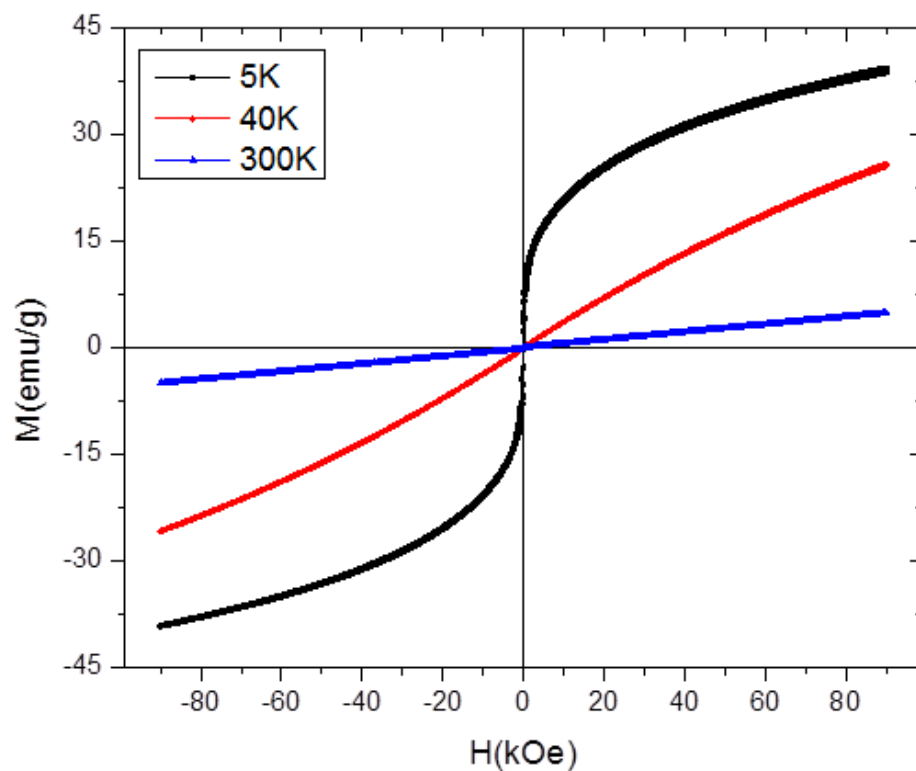


**Figure 4.12** M-H curve for amorphous Co nanoparticles, obtained prior to annealing, measured at 5, 40 and 300K, respectively. The M-H curve at 300 and 5K exhibit paramagnetic and ferromagnetic behaviors, respectively. The M-H curve at 40 K shows the mixture of both the para and ferromagnetic components.

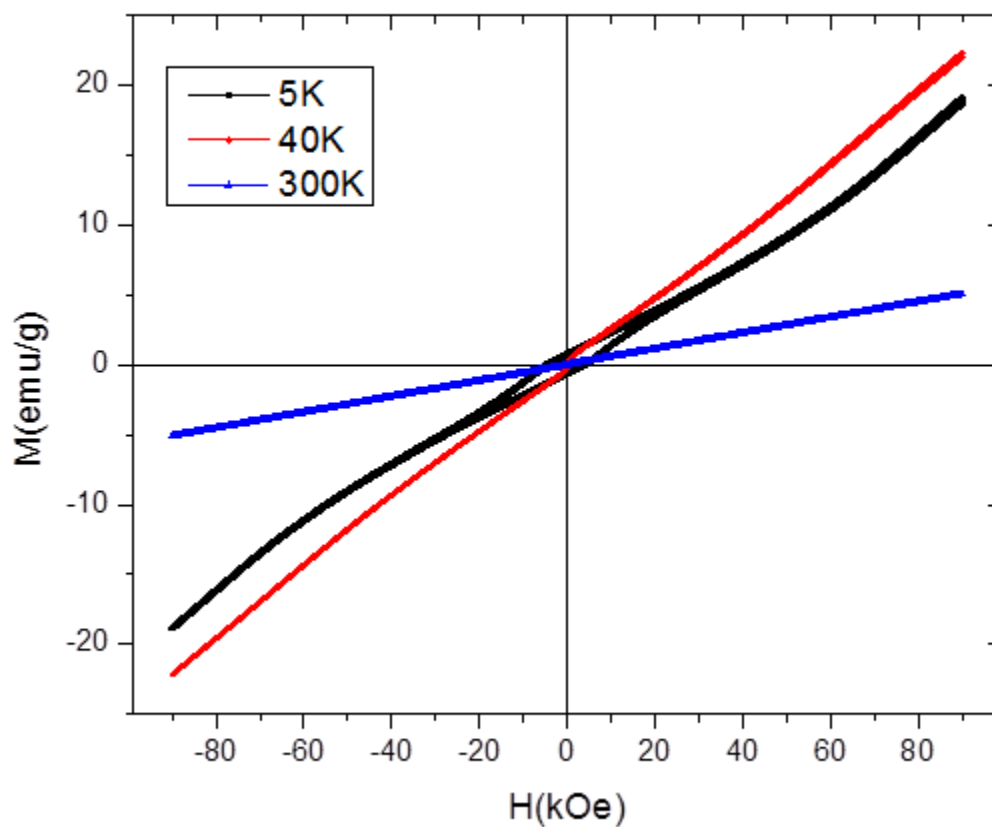


**Figure 4.13** M-H curves for  $\text{Co}_3\text{O}_4$  nanoparticles, obtained after annealing at  $800^\circ\text{C}$  for 2 hours. The M-H curve exhibits para- and ferromagnetic behaviors at 300 and 5K, respectively, while the curve at 40 K shows the mixture of both the para and ferromagnetic components.

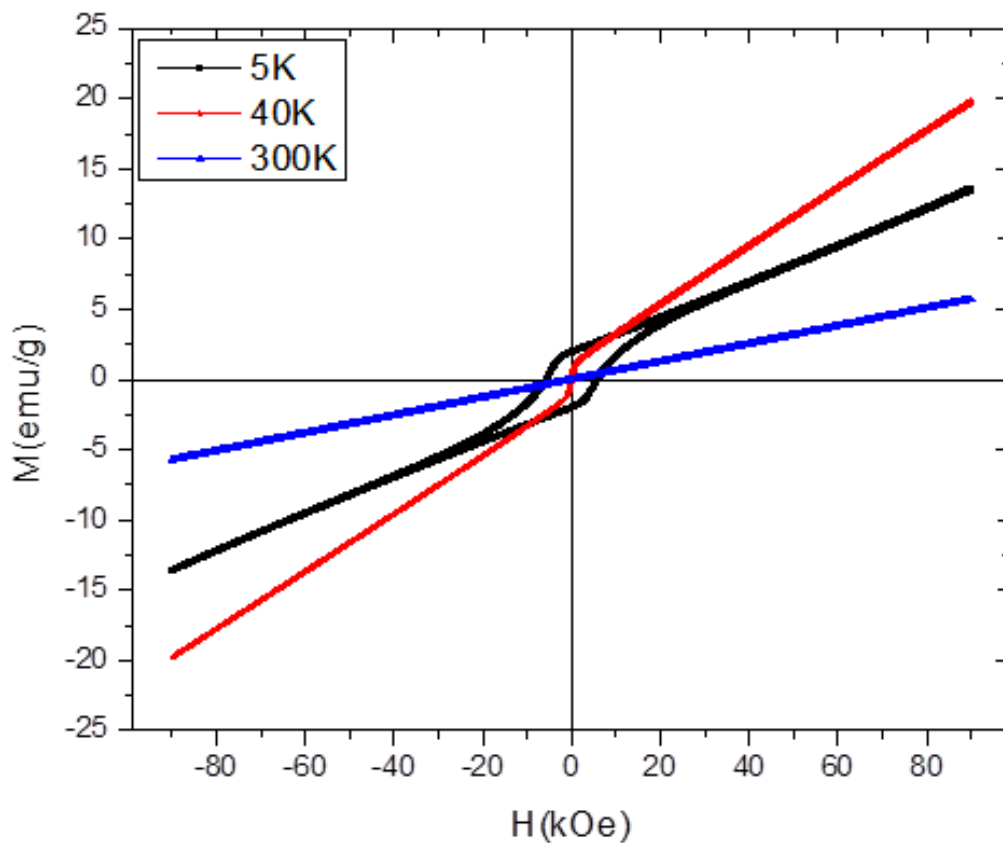


**Figure 4.14** M-H curves for  $\text{Co}_3\text{O}_4$  nanoparticles, obtained after annealing at  $800^\circ\text{C}$  for 12 hours. The M-H curve exhibits para- and ferromagnetic behaviors at 300 and 5K, respectively, while the curve at 40 K shows the mixture of both the para and ferromagnetic components.

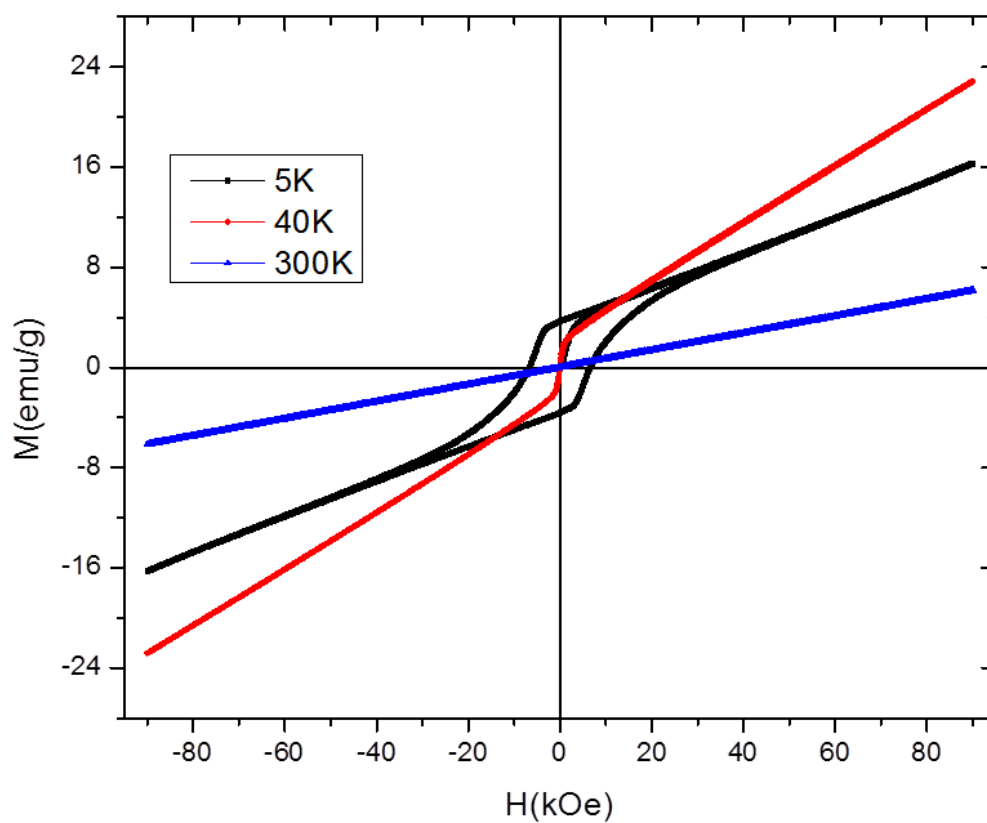


**Figure 4.15** M-H curves for  $\text{Co}_3\text{O}_4$  nanoparticles, obtained after annealing at  $800^\circ\text{C}$  for 15 hours. The M-H curve exhibits para- and ferromagnetic behaviors at 300 and 5 K, respectively, while the one at 40 K shows the mixture of both the para and ferromagnetic components.

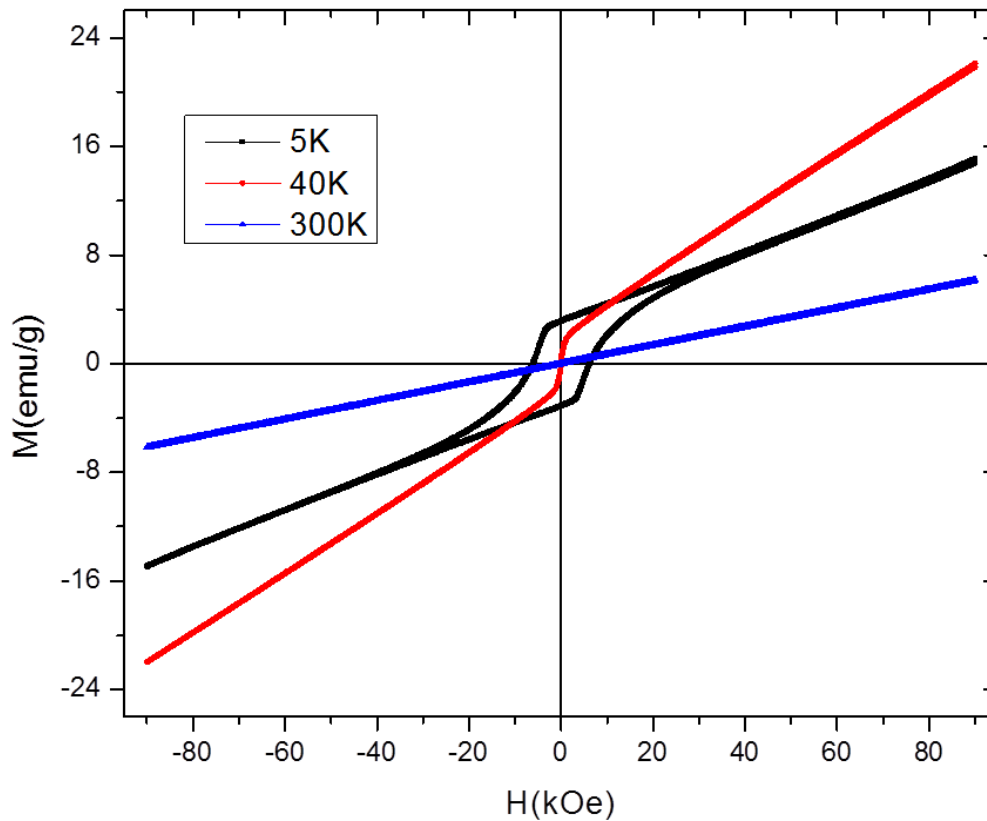


**Figure 4.16** M-H curves for  $\text{Co}_3\text{O}_4$  nanoparticles, obtained after annealing at  $800^\circ\text{C}$  for 20 hours. The M-H curve exhibits para- and ferromagnetic behaviors at 300 and 5 K, respectively, while the one at 40 K shows the mixture of both the para and ferromagnetic components.

#### 4.4 Discussion of Temperature-Dependent Magnetism

The results presented above in Figure 4.12 – Figure 4.16 indicate that the amorphous Co nanoparticles and the Co<sub>3</sub>O<sub>4</sub> nanoparticles exhibit various magnetic properties. It may be of interest to note that the M-H curve at 5 K for the sample annealed for 2 hours (Figure 4.13) shows a kink at approximately 60 kOe, beyond which magnetism increases with a higher slope. The reason for this behavior could be related to the magnetic coupling that may be occurring among the nanoparticles, which can contribute to this magnetization reversal mechanism. It is also noted that the slope of magnetization with H is nearly the same for both the particles at high fields.

In general, the ordering of magnetic moments (ferromagnetic state) of a nanoparticle becomes disorderly (“super- paramagnetic state”) above a temperature  $T_b$  (called the super-paramagnetic blocking temperature). This phenomenon occurs at  $T > T_b$  as thermal agitation energy ( $k_B T$ ) overcomes the total magnetic binding energy  $KV$  of the particle, where  $K$  is the magneto-crystalline anisotropy energy per unit volume,  $V$  is the volume of the particle and  $k_B$  is the Boltzmann constant. The critical particle radius ( $R_b$ ) at a given temperature,  $T$ , is given by  $(6k_B T/K)^{1/3}$ . If one assumes that the  $K$  value for a cobalt nanoparticle is the same as the bulk  $K$  value ( $K= 5 \times 10^6$  erg/cc at  $T= 300$ K (Takahashi & Suzuki 1979)), the value of  $R_b$  at  $T=300$ K would be about 4nm (Koeby 2010).

As mentioned above, the Co nanoparticles prior to annealing exhibit ferro-, mixture of ferro- and para- and ferromagnetism, at  $T= 5, 40$  and  $300$ K, respectively (Figure 4.12). If the cobalt particle possess the  $K$ -value same as that bulk, then one would expect the ferromagnetic behavior at  $300$  K, but that is not the case. Therefore,

these Co nanoparticles do not possess the same magnetic anisotropy constant,  $K$ , as the bulk value, but much smaller. This result is reasonable since the magnetic anisotropy constant generally decreases with decreasing nanoparticle size. The fact that the ferromagnetic behavior is observed at 40 K suggests that some particles are magnetically coupled (presumably due to aggregation, as evidenced by SEM imaging analysis), leading to a larger volume,  $V$ , thus becoming ferromagnetic. It is noted that the M-H curve at 40 K suggests that a significant portion of the cobalt particles still remains paramagnetic, as there is no clear evidence of saturation in magnetization even at fields at 90 kOe.

Regarding the samples annealed for 2 and 12 hours (Figures 4.13 and 4.14), it is of interest to note that a longer annealing time (12 hours) leads to a higher coercivity (5.7 kOe) than that (4.3 kOe) for a shorter one, even though the particle size is somewhat smaller (3.2 nm) for the former than that (5.2 nm) for the latter. As the structural analyses from XRD measurements indicate that those annealed samples are found to be  $\text{Co}_3\text{O}_4$ , one would expect the value of  $R_b$  at 300 K to be around 5 nm (Koey 2010), provided that the  $K$ -value is nearly the same as that for  $\text{Fe}_2\text{CoO}_3$  ( $6 \times 10^6 \text{ erg/cc}$  at 300K) (Kita 2013). The M-H curves for both the annealed samples do not exhibit the ferromagnetic behavior at 300 K, as shown in Figure 4.13 and 4.14. Therefore, the  $K$  value for those samples is believed to be much smaller than the bulk value. With decreasing measurement temperatures down to 40 K and 5 K, some portion of the samples become ferromagnetic, but there is still a significant portion of para-magnetism even at 5 and 40 K, as shown by a continuous increment of magnetization at fields above 20 kOe.



It is noted that the M-H curves do not show magnetic saturation in any of the cases studied, which is an indication that the magnetic moments are not uniformly aligned in the same direction with the applied magnetic field (Frey et al. 2009). Furthermore, this suggests that the particles do not consist of a single domain, which is plausible because the  $\text{Co}_3\text{O}_4$  particles are clusters of smaller Co structures, which have agglomerated after annealing.

It is important to emphasize that the coercivity increases as a function of 1) annealing temperature and 2) annealing time at  $800^\circ\text{C}$ , where a maximum coercivity is reached at 15 hours. Figure 4.17 shows the variation in coercivity at 5 K as a function of annealing time for the  $\text{Co}_3\text{O}_4$  nanoparticles annealed at  $800^\circ\text{C}$ . It can be seen that there is an overall increase in coercivity with increasing heating time; however, at 15 hours, a maximum coercivity was reached, which was only slightly greater than the other measurements. Furthermore, the magnetic anisotropy constant of the annealed  $\text{Co}_3\text{O}_4$  nanoparticles is on the order of  $4 \times 10^6$  erg/cc at 5 K. Recall from Section 4.1 that desired coercivity values should be  $\sim 2 - 3$  kOe (Gubin et al. 2005), and the anisotropy value should be  $\sim 6 \times 10^6$  erg/cc (Kita 2013). These results indicate that the  $\text{Co}_3\text{O}_4$  nanoparticles described in this chapter have potentially developed exceptional magnetic properties after annealing, which could allow for their use in advanced data storage or energy storage applications; however, further testing is required (and will be discussed in the Future Directions in Chapter 6).

Additionally, these  $\text{Co}_3\text{O}_4$  nanoparticles were prepared in the absence of a capping ligand (e.g., DMSO was used as a functional solvent), and are relatively spherical in shape, hence there is negligible surface and shape anisotropy. It can then be

assumed that crystalline anisotropy is likely the key factor contributing to the overall magnetic anisotropy of the  $\text{Co}_3\text{O}_4$  nanoparticles. Thus, it is possible that the increase in coercivity is related to the crystalline anisotropy of the  $\text{Co}_3\text{O}_4$  nanoparticles under these conditions, and it has been reported in the literature that crystalline anisotropy can induce high coercivity (Hyeon 2003).

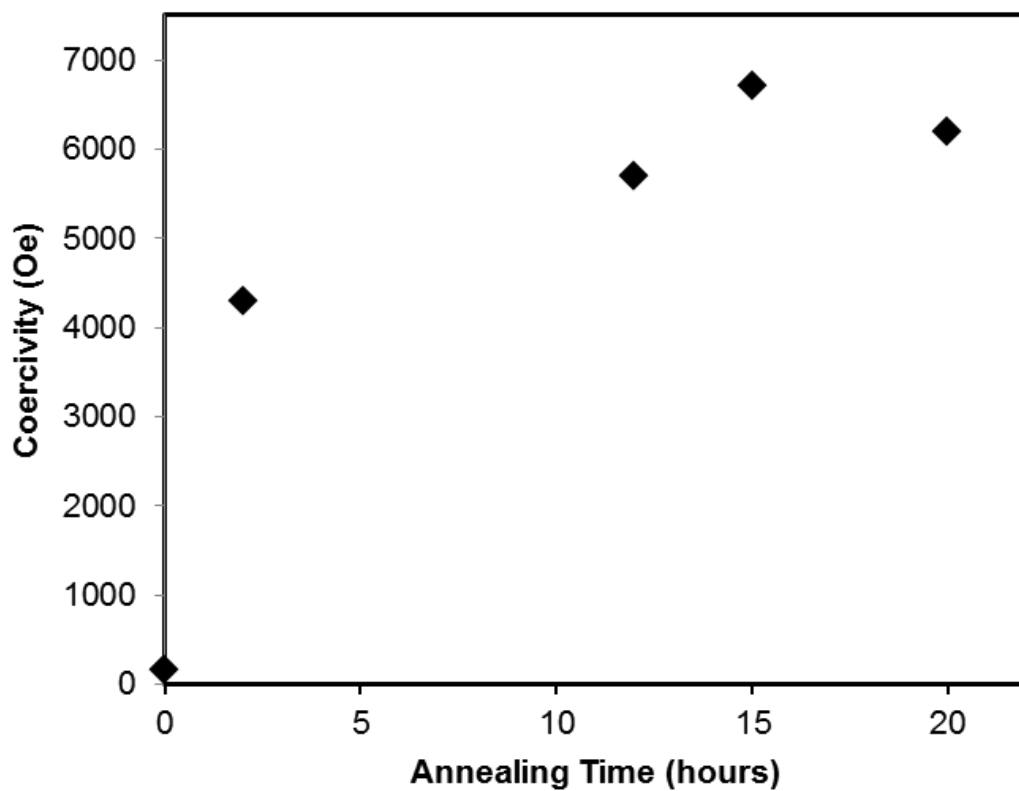


**Figure 4.17** Variation of coercivity ( $H_c$ ) measured at 5 K as a function of the annealing time of the  $\text{Co}_3\text{O}_4$  nanoparticles, where the annealing temperature is  $800^\circ\text{C}$ .

## 4.5 Conclusions

A method to easily produce high-quality magnetic nanoparticles is critical in order to continuously advance current technologies. A simple annealing technique was presented in this chapter, which produced spinel  $\text{Co}_3\text{O}_4$  nanoparticles with unique magnetic properties. First, amorphous Co nanoparticles were easily synthesized using DMSO as a functional solvent by following the procedures described in Chapter 2. After post-synthesis annealing in air up to  $800^\circ\text{C}$ , these Co nanoparticles were found to be ordered structures of spinel  $\text{Co}_3\text{O}_4$ . Furthermore, amorphous Co nanoparticles prepared at  $25^\circ\text{C}$  and  $\text{Co}_3\text{O}_4$  nanoparticles prepared at  $800^\circ\text{C}$  were found to be paramagnetic at 300K, and become ferromagnetic at 5K. This result suggests that the magnetic anisotropy constant of those particles is believed to be much smaller than that for bulk values. It is also noted that  $\text{Co}_3\text{O}_4$  nanoparticles annealed for 12 hours at  $800^\circ\text{C}$  exhibit higher coercivity than that for a shorter annealing time (2hr), even though the average particle size is smaller. However, maximum coercivity was reached for  $\text{Co}_3\text{O}_4$  particles annealed for 15 hours. This result suggests that a longer annealing time (~15 hours) produces particles of high crystalline quality of spinel  $\text{Co}_3\text{O}_4$  particles. These findings ultimately indicate that preparing  $\text{Co}_3\text{O}_4$  nanoparticles (and possibly other magnetic materials) using small molecules, such as DMSO, to function concomitantly as both the ligand and the solvent can allow the particles to develop unique and distinct magnetic properties.

## Chapter 5

### **Aggregation and Precipitation of Gold Nanoparticle Clusters in CO<sub>2</sub>-Gas Expanded Liquid-Dimethyl Sulfoxide Solvent Systems**

Previous post-synthesis nanoparticle processing techniques have demonstrated that CO<sub>2</sub>-gas expanded liquids can be used as a tool to controllably induce nanoparticle precipitation and size-selective fractionation. These previous studies have been limited to using non-polar solvents (e.g., hexane) in CO<sub>2</sub>-gas expanded liquids as a method to control nanoparticle precipitation by exploiting subtle changes in dispersive forces. In this chapter, a facile, post-synthesis nanoparticle processing technique is described, which allows for the controlled aggregation of gold (Au) nanoparticles into supra-particle clusters using CO<sub>2</sub>-gas-expanded DMSO (a polar, aprotic solvent), as well as the subsequent ability to precipitate these Au nanoparticle clusters from the DMSO solvent media at moderate applied CO<sub>2</sub> pressures. UV-vis spectroscopy was used to monitor the surface plasmon resonance band of the Au nanoparticle dispersions where it was determined that the post-synthesis aggregation and subsequent precipitation of the Au nanoparticles in DMSO is a direct function of the applied CO<sub>2</sub> pressure.

## 5.1 Introduction

Metal nanoparticles have very unique, size-dependent properties that allow for their use in a wide variety of contemporary applications. Among the most useful applications involves the exploitation of the tunable optical and electronic properties of gold (Au) nanoparticles for their use in biomedical applications (Murphy, Gole, Stone, et al. 2008; Day et al. 2010; Jasmine M Tam et al. 2010; Huang et al. 2008). It is important to be able to controllably produce nanoparticles of particular shapes and sizes in order to more fully utilize their unique size-dependent properties (Dutta et al. 2007; El-Brollossy et al. 2008; Murphy et al. 2005; Link & El-Sayed 1999; Jain et al. 2006; Kelly et al. 2003).

The work previously described in Chapter 2 as well as the results published by Liu et al. (2010), Roberts and coworkers have previously demonstrated that the molecule dimethyl sulfoxide (DMSO) can be an effective component in size-specific nanoparticle synthesis because DMSO can effectively serve as both the solvent and the stabilizing ligand during nanoparticle synthesis. Thus, using DMSO as a functional solvent to produce dispersions of Au nanoparticles is of particular interest since Au nanoparticles have a characteristic plasmon absorption band centered around 520 nm (Huang et al. 2008; Turkevich 1985), making these particles excellent candidates for investigations of their use in biomedical applications. Based on previous findings, the DMSO molecules are adsorbed to the nanoparticle surfaces by electrostatic attractions (Liu et al. 2010), allowing for further molecular functionalization of the particle surfaces. The ability to easily perform surface functionalization of Au nanoparticles allows these particles to be specifically tailored for numerous biomedical applications, such as sensing and diagnosis

(Jain et al. 2006; Shafer-Peltier et al. 2003) as well as targeted cancer treatment (Murphy, Gole, Stone, et al. 2008; Day et al. 2010; Huang et al. 2008). More important to the current investigation, when DMSO is pressurized with CO<sub>2</sub>, the CO<sub>2</sub> readily dissolves into the DMSO solution and creates a pressure-tunable gas-expanded liquid. More details on gas-expanded liquids are provided in Section 1.7.2 of this dissertation, and the discussions in the present chapter will be focused on examining the dispersibility of Au nanoparticle solutions in these CO<sub>2</sub>-gas expanded DMSO systems.

Gas-expanded liquid systems can be used to precipitate and size-selectively fractionate ligand-stabilized metal nanoparticle dispersions to produce nanoparticles of controlled size by simply controlling the applied CO<sub>2</sub> pressure (Anand et al. 2005; Anand et al. 2007; Saunders & Roberts 2009; Saunders & Roberts 2011a; Saunders & Roberts 2011b). In particular, Roberts and coworkers have previously investigated the dispersibility of various nanoparticles in organic solvents with aliphatic ligands (Saunders & Roberts 2009; Vengsarkar & Roberts 2013). The dispersibility of these nanoparticles can be manipulated by tuning the applied CO<sub>2</sub> pressure in gas expanded liquid systems. For example, the successful post-synthesis size fractionation of various Au (Saunders & Roberts 2009; Vengsarkar & Roberts 2013) and silver (Von White & Kitchens 2010; McLeod, Kitchens, et al. 2005) nanoparticles, as well as CdSe/ZnS quantum dots (Anand et al. 2007) have been demonstrated, all of which contained both organic ligands and organic solvents. Considering the unique nanoparticle solvation properties of DMSO and advantages of using DMSO during nanoparticle synthesis (as described in Chapter 2 and by Liu et al., (2010), this chapter specifically investigates the aggregation and subsequent precipitation of Au nanoparticle dispersions in a CO<sub>2</sub>-gas expanded DMSO solvent.

A synthesis method to produce Au nanoparticles using DMSO as a functional solvent, both with and without the use of fatty acid stabilizing ligands (e.g. oleic acid, stearic acid) is described in this chapter. When the fatty acid ligands are included, the addition of these stabilizing ligands can be used to more controllably produce Au nanoparticles of different sizes. In addition, the post-synthesis dispersibility and stability of these Au nanoparticles in three different CO<sub>2</sub>-gas expanded-DMSO systems (DMSO as the functional solvent, oleic acid + DMSO, and stearic acid + DMSO) is examined through the use of *in-situ* UV-vis spectroscopy investigations.

## **5.2 Experimental**

### **5.2.1 Materials**

Dimethyl sulfoxide ((CH<sub>3</sub>)<sub>2</sub>SO, 99.9%) was obtained from BDH Chemicals. Deionized ultrafiltered water (DI-H<sub>2</sub>O) was obtained from Fisher Scientific. Hydrogen tetrachloroaurate trihydrate (HAuCl<sub>4</sub>\*3H<sub>2</sub>O, 99+ %) and sodium borohydride (NaBH<sub>4</sub>, 99%) were obtained from Sigma Aldrich. Stearic acid (C<sub>18</sub>H<sub>34</sub>\*O<sub>2</sub>, 98%) was obtained from Alfa Aesar. Oleic acid (C<sub>18</sub>H<sub>34</sub>\*O<sub>2</sub>) was obtained from Fisher Scientific. n-Hexane HPLC grade (C<sub>6</sub>H<sub>14</sub>, 95+ %) was obtained from Alfa Aesar. Carbon Dioxide (SCF/SFE grade) was obtained from Airgas.

### **5.2.2 Au Nanoparticle Synthesis**

Au nanoparticles were synthesized via a solvent-based reduction of 0.05 M Au<sup>3+</sup> salt by 0.05 M NaBH<sub>4</sub> in a DMSO functional solvent using a modified procedure from Liu et al. (2010) and the procedure described in Chapter 2. The appropriate amounts of reagents necessary to produce Au nanoparticles were determined using UV-vis and TEM



imaging analyses, and these results are provided in Appendix C1 in Figures C1.2 and C1.2, respectively.

In a typical synthesis procedure, where DMSO is the functional solvent (denoted as Au-DMSO), the amount of reagents was adjusted to ensure complete reduction of the Au<sup>3+</sup> salt by the NaBH<sub>4</sub> (i.e., 500 uL of 0.05 M Au<sup>3+</sup> salt solution and 2175 uL of 0.05 M NaBH<sub>4</sub> were added to 50 mL DMSO), and the contents of the reaction were mixed using a magnetic stir plate. Upon addition of the reagents to the reaction flask, the solution transitioned from a bright yellow color to a dark red wine color. The Au-DMSO solution was then continuously stirred for at least 24 hours prior to further analysis.

Au nanoparticles were also synthesized using fatty acids as the ligands and DMSO as the solvent. The same reagent concentrations of [Au<sup>3+</sup>]:[NaBH<sub>4</sub>] were used in each case as described above. For Au nanoparticles stabilized by oleic acid (denoted as Au-OA), 10 mL of oleic acid was added to the DMSO in the reaction flask prior to the addition of the Au<sup>3+</sup> salt solution and NaBH<sub>4</sub>. For Au nanoparticles stabilized by stearic acid (denoted as Au-SA), 0.15wt % of stearic acid was added to the DMSO in the reaction flask prior to adding the Au<sup>3+</sup> salt solution and NaBH<sub>4</sub>. Upon addition of the reagents to the reaction flask, the solution transitioned from a bright yellow color to a dark red wine color. After the addition of the reactants, the flask was securely capped, and the contents of each flask were stirred continuously for 24 hours. The Au-OA nanoparticle sample and the Au-SA nanoparticle samples were subsequently washed using n-hexane so as to remove any excess fatty acids that may be remaining in the DMSO solvent (not adsorbed to Au nanoparticle surface). For example, 10 mL of n-hexane was added to 20 mL of Au-OA nanoparticle sample and vigorously shaken. A

milky, white phase formed at the top of the solution in the n-hexane phase, which was decanted and discarded. The n-hexane washing procedure was repeated three times, prior to subsequent nanoparticle analysis.

### **5.2.3 Characterization Techniques**

*UV Visible Spectroscopy (UV-vis)* - UV-vis was used post-synthesis in order to monitor the change in the Au nanoparticles' surface plasmon resonance band of the three different Au nanoparticle solutions in DMSO (Au-DMSO, Au-OA, and Au-SA). UV-vis absorption measurements of the nanoparticle dispersions were obtained using a Shimadzu UV-2700 spectrophotometer to monitor the change in the absorbance spectrum caused by nanoparticle clustering or precipitation. UV-vis analysis was first performed to investigate the stability of the Au nanoparticle dispersion over the period of 3 months.

UV-vis spectroscopy was also used to investigate the effect of the applied CO<sub>2</sub> pressure on Au nanoparticle dispersibility in DMSO. A high-pressure, stainless steel view cell, specifically designed for these high-pressure UV-vis spectroscopy measurements, was used to monitor any changes in the absorbance spectrum of the dispersions caused by nanoparticle clustering or precipitation during pressurization. An image of the high pressure apparatus is shown in Figure 5.1. The apparatus is fitted with transparent windows and can be conveniently placed into the UV-vis spectrophotometer. A 1 cm path length quartz cuvette containing a small aliquot of liquid nanoparticle dispersion was placed inside the apparatus and the cuvette was positioned precisely in line with the viewing windows such that the liquid nanoparticle dispersion could be viewed through the windows of the apparatus prior to and during pressurization. It is important to point out that the expansion of the liquid mixture due to pressurization

occurs within the cuvette. CO<sub>2</sub> is introduced to the apparatus via a high pressure syringe pump (ISCO 260D), and the applied CO<sub>2</sub> pressure is measured using a digital pressure gauge attached to the apparatus. Before each experiment, neat DMSO was pipetted into a cuvette and loaded into the high-pressure stainless steel view cell, and a background of the neat DMSO solution was collected.

In a typical experiment, an aliquot of the liquid nanoparticle dispersion was loaded into the cuvette and placed inside the high-pressure apparatus. The apparatus was then sealed and purged of any nitrogen and oxygen using CO<sub>2</sub>. The system was then pressurized to the desired value using CO<sub>2</sub>, and the applied CO<sub>2</sub> pressure was measured using a digital pressure gauge directly attached to the high-pressure apparatus. A UV-vis absorbance spectrum was collected once the system reached equilibrium, which was determined when the UV-vis absorbance spectrum remained unchanged at each applied CO<sub>2</sub> pressure setting. Then, the pressure was increased to a higher applied CO<sub>2</sub> pressure, and a UV-vis spectrum was collected. This process was repeated until the absorbance reached zero, as evidenced by a spectrum with a flat line. In each case, the system was first pressurized to 28 bar, then up to 55.2 bar in increments of 100 psig (i.e., 6.9 bar).

*Fourier Transform Infrared Spectroscopy (FT-IR)* –A Nicolet Avatar 360 was used to perform FT-IR spectroscopy analysis of the Au nanoparticle dispersions. The spectra for the neat oleic acid and stearic acid were obtained by preparing a KBr pellet. The spectra of the neat DMSO as well as the spectra for each of the Au nanoparticle dispersions were obtained by placing a few drops of each sample between two KBr salt disk windows in a standard liquid cell holder. FT-IR analysis of the three different Au nanoparticle solutions were performed: the Au-DMSO nanoparticle dispersion (using

DMSO as a functional solvent), the Au-OA nanoparticle dispersion (using oleic acid as the stabilizing ligand and DMSO as the solvent), and the Au-SA nanoparticle dispersion (using stearic acid as the stabilizing ligand and DMSO as the solvent).

*Transmission Electron Microscopy (TEM)* - TEM was used to investigate the morphology of the Au nanoparticles using a Zeiss EM 10 TEM at an operating voltage of 60 kV. TEM samples were prepared by placing a single drop of sample onto a carbon type B, 300 mesh gold grid. The grid was contained in a plastic petri dish and placed in the vacuum oven to dry for several days prior to TEM analysis. Digital images of each of the Au nanoparticle samples were obtained, and the average particle size and size distribution of the Au nanoparticle dispersions were determined using the Image J software package to size more than a hundred particles in each case.

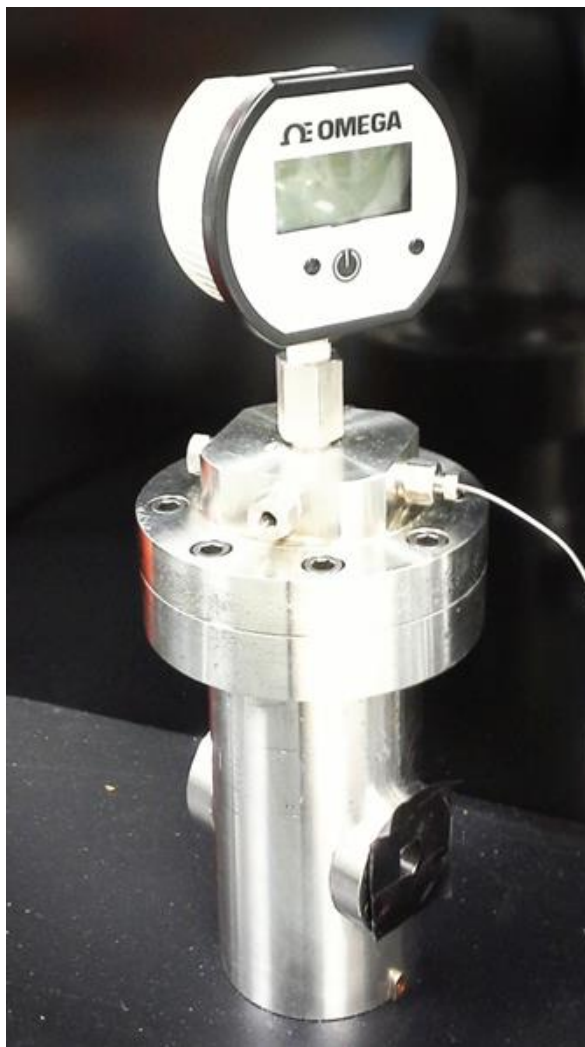


**Figure 5.1** A digital image of the high-pressure, stainless steel view cell that has been specifically designed for the high-pressure UV-vis spectroscopy experiments.

## 5.3 Results

### 5.3.1 TEM Imaging Analysis of Au Nanoparticle Size and Morphology

The TEM imaging analysis was performed to study the Au nanoparticle size and morphology resulting from each of the three Au nanoparticle synthesis procedures. The TEM images, size histogram are shown in Figure 5.2 and the molecular representation of each stabilizing ligand are shown in Figure 5.3. As can be observed in Figure 5.2a, the average size of the Au-DMSO nanoparticles is  $4.3 \pm 2.3$  nm. These results suggest that the DMSO alone (i.e., DMSO as a functional solvent) can efficiently function as a capping ligand to suppress particle growth and produce relatively uniform Au nanoparticles. Additionally, the average size of the Au-OA nanoparticles was found to be  $9.7 \pm 3.5$  nm (Figure 5.2b) and the average size of the Au-SA nanoparticles was determined to be  $8.5 \pm 3.2$  nm (Figure 5.2c). Thus, the addition of the fatty-acid stabilizing agents to the DMSO produces a slight increase in the average nanoparticle size. We postulate that this modest difference in Au nanoparticle size between the Au-DMSO nanoparticles vs. the Au+fatty acid nanoparticles may result from the ‘availability’ of the DMSO molecules in each case: For instance, there is an abundance of DMSO molecules available to provide immediate stabilization for the newly formed Au nanoparticles in the Au-DMSO solution, and this may form the smaller sizes ( $\sim 4.3$  nm) nanoparticles. However, in the Au+fatty acid nanoparticle solutions, the fatty acid molecules have to compete with the DMSO molecules during nanoparticle growth/stabilization, thereby hindering the stabilization of smaller nanoparticles and promoting the formation of larger ( $\sim 8+$  nm) nanoparticles. Moreover, both of the Au

nanoparticles synthesized using fatty acid stabilizing ligands are roughly the same size and shape, as can be observed in Figure 5.2b and c.

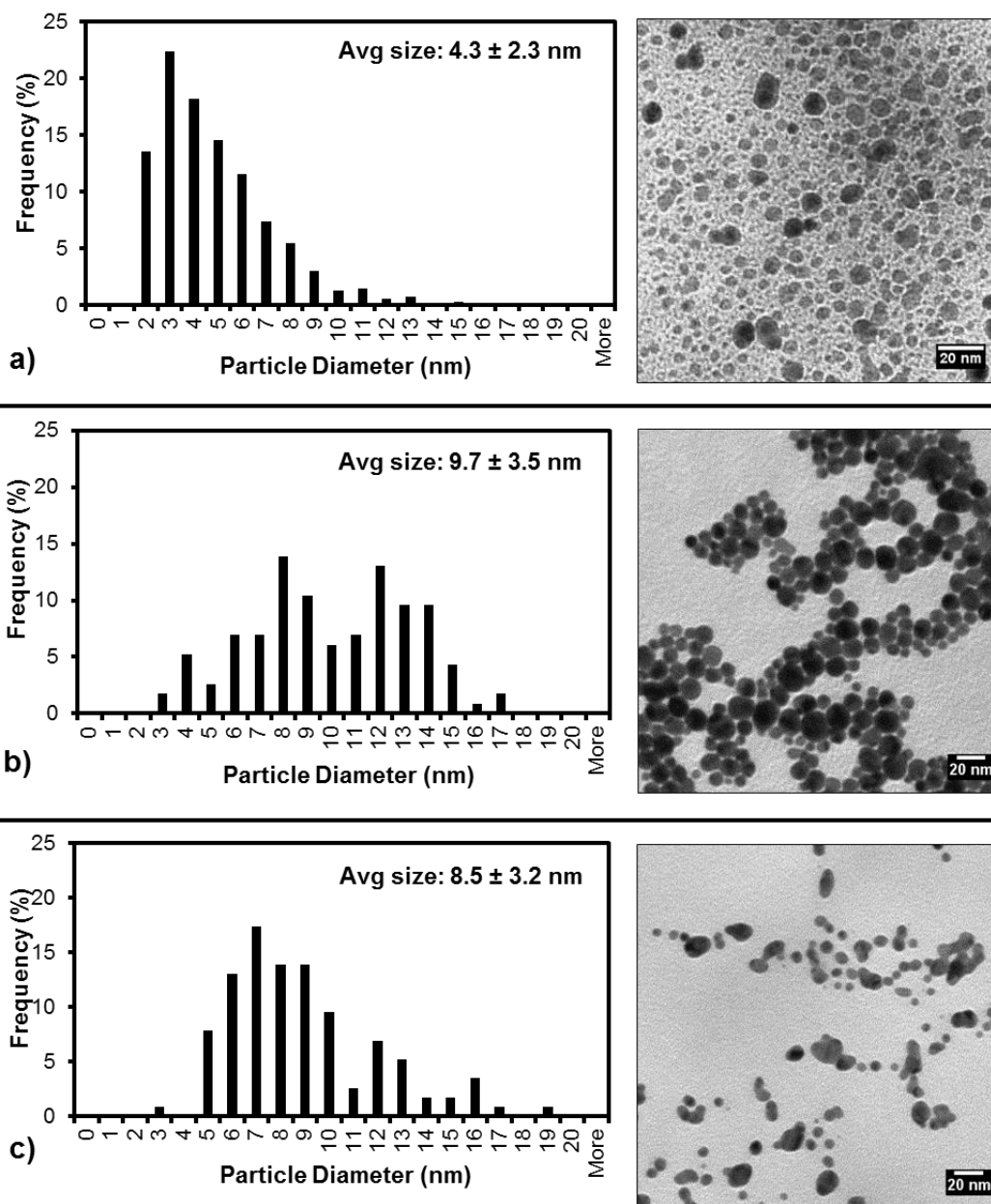


**Figure 5.2** TEM image and corresponding histograms of the Au nanoparticles synthesized using a) DMSO as a functional solvent, b) oleic acid as a stabilizing ligand in a DMSO solvent, and c) stearic acid as a stabilizing ligand in a DMSO solvent.



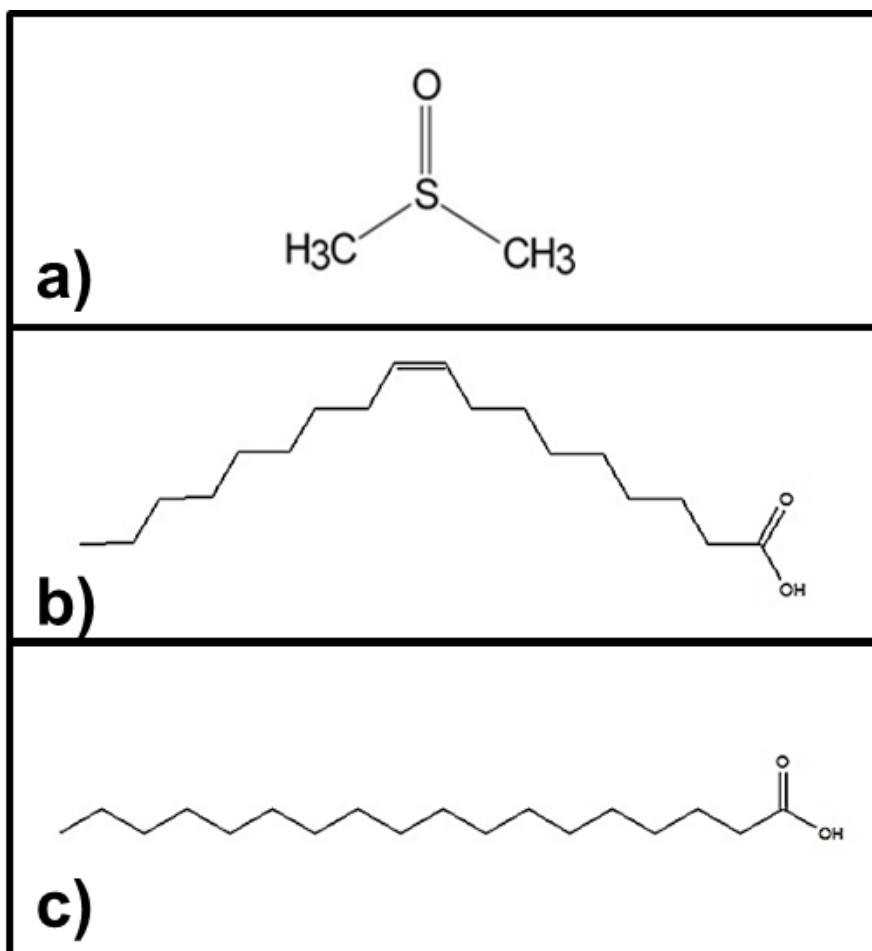


**Figure 5.3** Molecular representations of a) the DMSO functional solvent, and the other stabilizing ligands b) oleic acid and c) stearic acid used to synthesize Au nanoparticles.

### 5.3.2 Interaction Between Au Nanoparticle Surface and DMSO/Fatty Acid Molecules

FT-IR spectroscopy was used to examine the coordination between the Au nanoparticle surfaces and the DMSO solvent/fatty acid solutions' stabilizing ligands. Figure 5.4 shows the FT-IR spectra of the Au-DMSO nanoparticle dispersion and neat DMSO. The peak assignments for neat DMSO are listed in Table 5.1. The sulfoxide functional group stretch  $\nu$  (S=O) is located at  $1057\text{ cm}^{-1}$ , which is in agreement with results reported in the literature for the sulfoxide stretch  $\nu$  (S=O) (Smith 1999). In the Au-DMSO nanoparticle system in Figure 5.4, the sulfoxide functional peak splits into two different peaks, one at  $1071\text{ cm}^{-1}$  and one at  $1015\text{ cm}^{-1}$ , indicating an equal contribution from the sulfoxide functional group. This peak splitting is highlighted in Figure 5.4c, which shows an overlay of the neat DMSO spectrum with the Au-DMSO nanoparticle spectrum. The illustration in Figure 5.5 represents the interaction of the DMSO molecules with the Au nanoparticle surface. The coordination chemistry of the Au nanoparticles with DMSO found in this study coincides with the study by Liu et al. (2010) for Pd-DMSO nanoparticles.

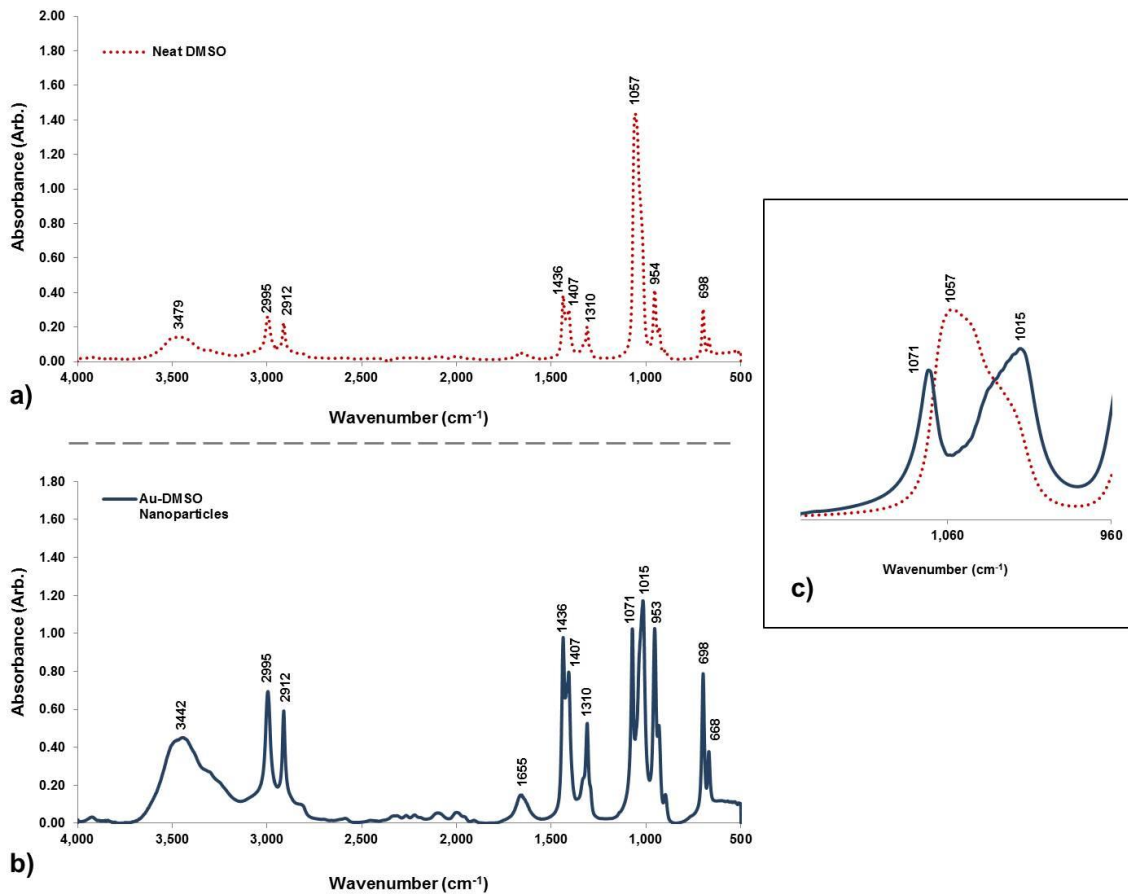


**Figure 5.4** FT-IR spectra of a) neat DMSO solvent, b) Au-DMSO nanoparticles (DMSO as a functional solvent), and c) comparison of the neat DMSO and the Au-DMSO nanoparticles.

| Peak Position (cm <sup>-1</sup> ) | Assignment                   |
|-----------------------------------|------------------------------|
| 3479                              | O—H stretch                  |
| 2995                              | Asymmetric C—H stretch       |
| 2912                              | Symmetric C—H stretch        |
| 1436                              | Degenerate C—H deformation   |
| 1407                              | Degenerate C—H deformation   |
| 1310                              | Symmetric C—H deformation    |
| 1057                              | S = O stretch                |
| 954                               | CH <sub>3</sub> rocking      |
| 698                               | Anti-symmetric stretch C—S—C |

**Table 5.1** FT-IR vibrational mode assignments for neat DMSO (Horrocks Jr. & Cotton 1961; Nakamoto 2009; Smith 1999).

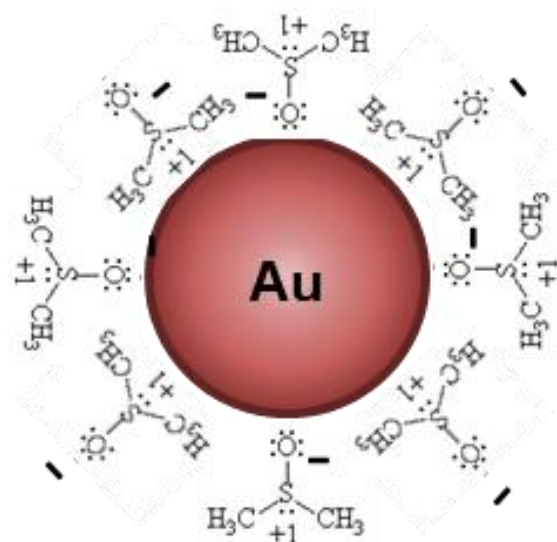


**Figure 5.5** Illustration of the electrostatic coordination occurring between the sulfoxide functional groups of DMSO with the Au nanoparticle surface.

Additionally, the interactions between the Au nanoparticle surface and the oleic acid and stearic acid stabilizing ligands were also studied using FT-IR spectroscopy. The spectra of neat oleic acid and the Au-OA nanoparticles are presented in Figure 5.6, and the spectra of neat stearic acid and the Au-SA nanoparticles are shown in Figure 5.7. The peak assignments for the neat oleic acid and the neat stearic acid are listed in Table 5.2 and Table 5.3, respectively. The peak positioning and assignments are very similar for these two Au nanoparticle systems due to the similarities in the structures of the oleic acid and stearic acid molecules. For simplicity, only the Au-OA nanoparticle spectrum will be discussed in detail, however, the peaks in the Au-SA nanoparticle spectrum can be easily indexed to the same vibrational modes as found for the Au-OA nanoparticle spectrum. In Figure 5.6b, the peak at  $3427\text{ cm}^{-1}$  for the Au-OA nanoparticle dispersion in DMSO is attributed to the  $\nu$  (O-H stretch) from DMSO (as was observed in the neat DMSO sample in Figure 5.4a). The peaks at  $3000\text{ cm}^{-1}$  and  $2918\text{ cm}^{-1}$  are due to the asymmetric and symmetric stretching of  $\nu$  ( $-\text{CH}_2$ ) from the oleic acid. The peak at  $1028\text{ cm}^{-1}$  results from the  $\nu$  (S=O) stretch of the sulfoxide functional group in the DMSO solvent. The remaining peaks can be assigned to either the oleic acid or to DMSO, where  $1408\text{ cm}^{-1}$  is likely from the degenerate  $\nu$  (C-H) deformation of the DMSO solvent,  $1314\text{ cm}^{-1}$  is due to the symmetric  $\nu$ (C-H) deformation of the methyl groups of the DMSO solvent or the  $\nu$  (C-O) stretch of the carboxylate ion,  $954\text{ cm}^{-1}$  likely results from the out-of-plane  $\nu$  (O-H) stretch from the oleic acid or the  $\text{CH}_3$  rocking from the DMSO solvent, and  $704\text{ cm}^{-1}$  is due to the anti-symmetric  $\nu$  (C-S-C) stretch of DMSO or  $\nu$  ( $\text{CH}_2$ ) rocking from the oleic acid (Wu et al. 2004; Nakamoto 1997; Smith 1999).

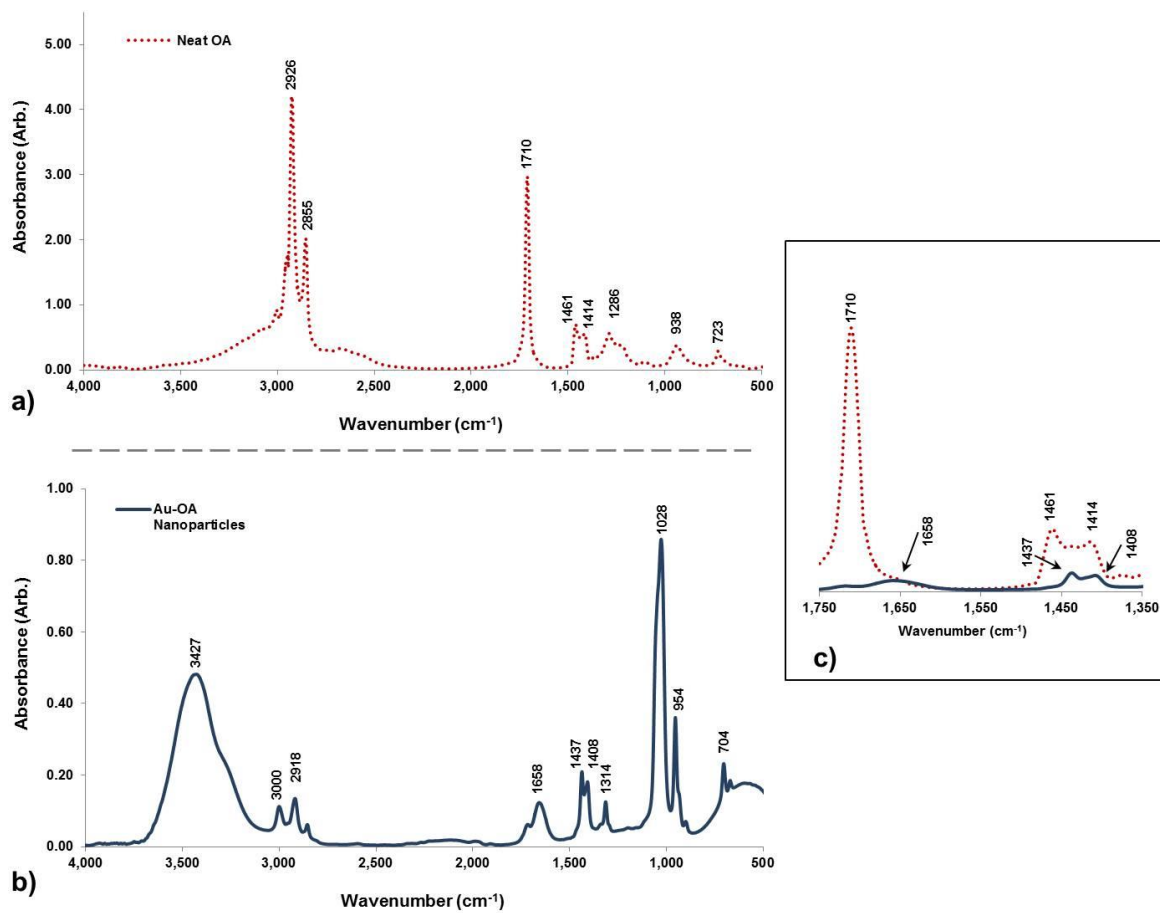


**Figure 5.6** FT-IR spectra of a) neat oleic acid, b) Au-OA nanoparticles in DMSO solvent, and c) comparison of the neat oleic acid and the Au-OA nanoparticles.

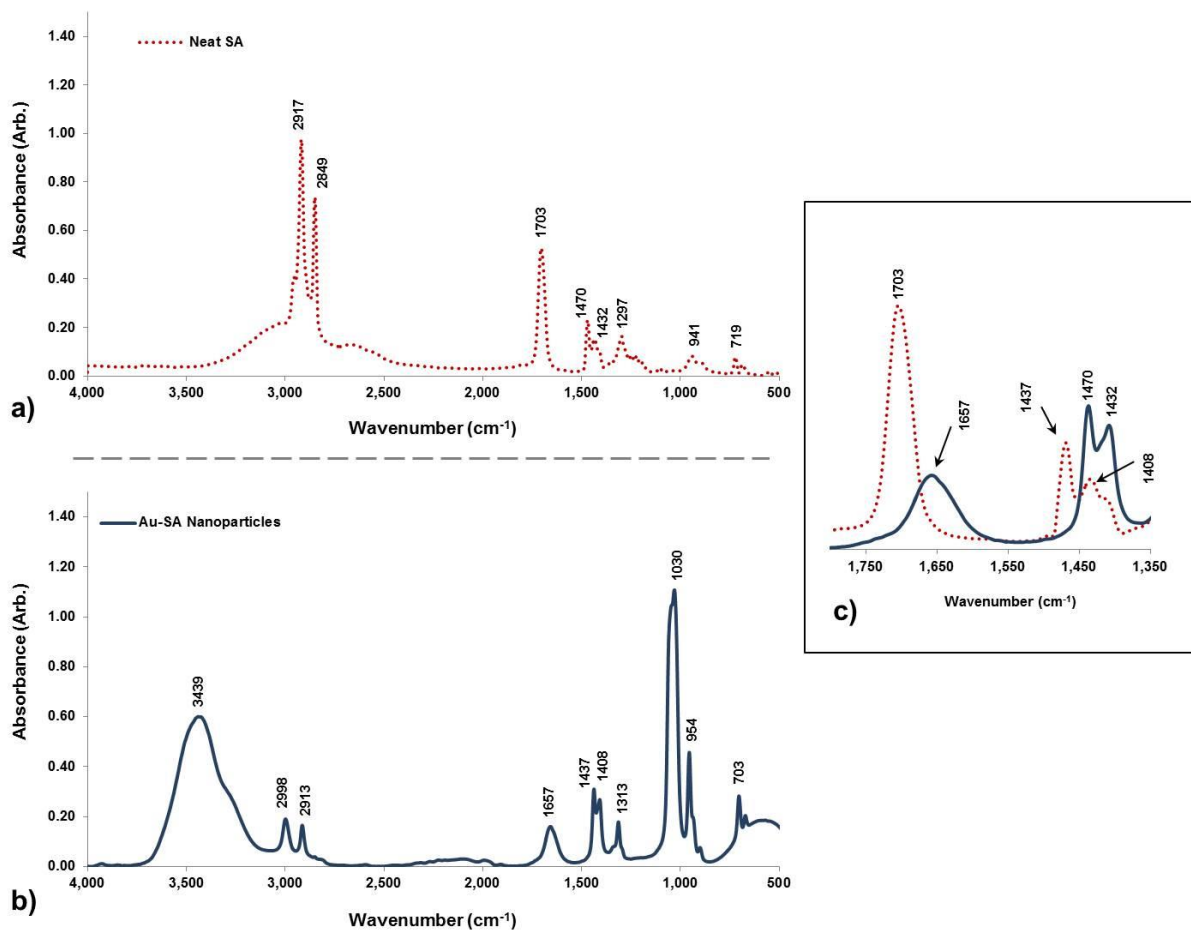


**Figure 5.7** FT-IR spectra of a) neat stearic acid, b) Au-SA nanoparticles in DMSO solvent, and c) comparison of the neat stearic acid and the Au-SA nanoparticles.



| Peak Position (cm <sup>-1</sup> ) | Assignment                         |
|-----------------------------------|------------------------------------|
| 3500 - 2500                       | O—H stretch                        |
| 2926                              | Asymmetric CH <sub>2</sub> stretch |
| 2855                              | Symmetric CH <sub>2</sub> stretch  |
| 1710                              | C = O                              |
| 1461                              | In-plane O-H band                  |
| 1414                              | CH <sub>3</sub> umbrella mode      |
| 1286                              | C—O stretch                        |
| 938                               | Out-of-plane O—H stretch           |
| 723                               | CH <sub>2</sub> rocking            |

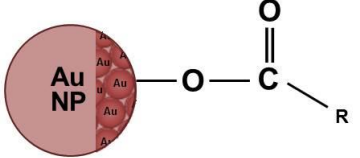
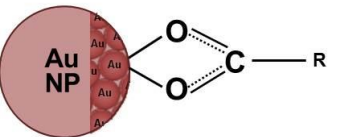
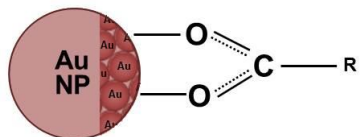
**Table 5.2** FT-IR vibrational mode assignments for neat oleic acid (Wu et al. 2004; Nakamoto 1997).

| Peak Position (cm <sup>-1</sup> ) | Assignment                         |
|-----------------------------------|------------------------------------|
| 3500 - 2500                       | O—H stretch                        |
| 2917                              | Asymmetric CH <sub>2</sub> stretch |
| 2849                              | Symmetric CH <sub>2</sub> stretch  |
| 1703                              | C = O                              |
| 1470                              | In-plane O-H band                  |
| 1432                              | CH <sub>3</sub> umbrella mode      |
| 1297                              | C—O stretch                        |
| 941                               | Out-of-plane O—H stretch           |
| 719                               | CH <sub>2</sub> rocking            |

**Table 5.3** FT-IR vibrational mode assignments for neat stearic acid (Wu et al. 2004; Nakamoto 1997; Smith 1999).

The peaks located at  $1658\text{ cm}^{-1}$  and  $1437\text{ cm}^{-1}$  from the Au-OA nanoparticle spectrum shown in Figure 5.6b (as well as the peaks located at  $1657\text{ cm}^{-1}$  and  $1437\text{ cm}^{-1}$  from the Au-SA nanoparticle spectrum in Figure 5.7b) are of particular interest because these peaks are attributed to the asymmetric and symmetric stretching of the carboxylate ion of the fatty acid ligands as they are adsorbed to the Au nanoparticle surface (Wu et al. 2004; Nakamoto 1997). The difference between the wave numbers at the peak positions for the asymmetric stretch and the symmetric stretch (i.e.,  $1658\text{ cm}^{-1}$  and  $1437\text{ cm}^{-1}$ ) provide information about the interaction between the carboxylate group of the acid stabilizing agent and the surface of the Au nanoparticle, whereby the interaction can be classified as (I) monodentate (or unidentate) chelating, (II) chelating bidentate, (III) bidentate bridging, or as an (IV) ionic association (Nakamoto 2009; Wu et al. 2004; Liu et al. 2008; Liu et al. 2007). The different modes of carboxylate complexation (I, II, and III) are illustrated in Table 5.4. The wave number separation ( $\Delta$ ) value was calculated to be  $221\text{ cm}^{-1}$  for the Au-OA nanoparticle dispersion and  $220\text{ cm}^{-1}$  for the Au-SA nanoparticle dispersion. Both of these values fall consistently within the wave number separation range for (I) monodentate chelating, as can be inferred from Table 5.4. Thus, we postulate that one of the oxygen atoms from the carboxylate head group preferentially associates with a single Au atom within a nanoparticle (i.e. one oxygen atom per Au atom in an Au nanoparticle) via an electrostatic interaction. An illustration of this phenomenon is provided in Figure 5.8. Furthermore, the intensity of the  $\nu(\text{C}=\text{O})$  peak at  $1710\text{ cm}^{-1}$  in the neat oleic acid spectrum in Figure 5.6a significantly decreased and shifted to  $1658\text{ cm}^{-1}$  for the Au-OA nanoparticle dispersion (as shown in Figure 5.6b), indicating that the oleic acid is adsorbed to the surface of the Au nanoparticle as a carboxylate. A similar

statement can be made for the Au-SA nanoparticle dispersion (Figure 5.7). These findings are analogous to other reports in the literature using FT-IR as a method to understand carboxylate ion functionalization with nanoparticle surfaces (Wu et al. 2004; Liu et al. 2007; Liu et al. 2008; deSilva et al. 2007).

| Modes of Complexation        | Wave number separation:<br>$\Delta = \nu_{as}(\text{COO}^-) - \nu_s(\text{COO}^-)$ | Nanoparticle surface interaction with $\text{COO}^-$                                 |
|------------------------------|--|--|
| (I)<br>Monodentate Chelating | $\Delta: 200 - 320 \text{ cm}^{-1}$  |   |
| (II)<br>Bidentate Chelating  | $\Delta: < 110 \text{ cm}^{-1}$  |   |
| (III)<br>Bidentate Bridging  | $\Delta: 140 - 190 \text{ cm}^{-1}$  |  |

**Table 5.4** Types of complexation, wave number separation, and illustration of the possible nanoparticle surface interaction with carboxylate functional groups.

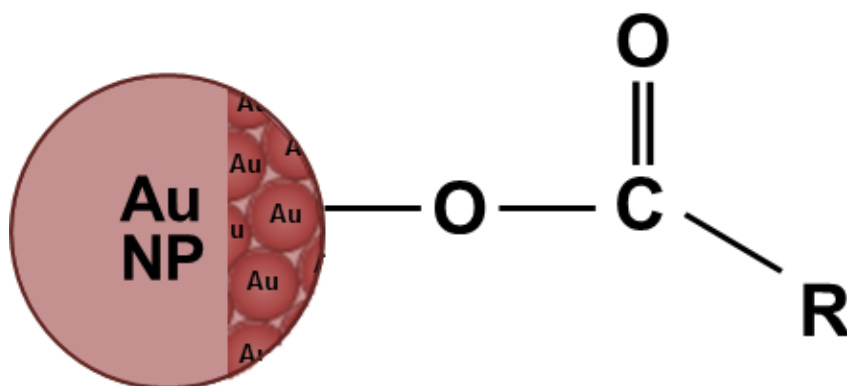


**Figure 5.8** Illustration of monodentate chelating coordination occurring between the carboxylate functional groups of the fatty acid ligands (i.e., oleic acid and stearic acid) with the Au nanoparticle surface.

### **5.3.3 Au Nanoparticle Stability as a Function of Time at Standard Ambient**

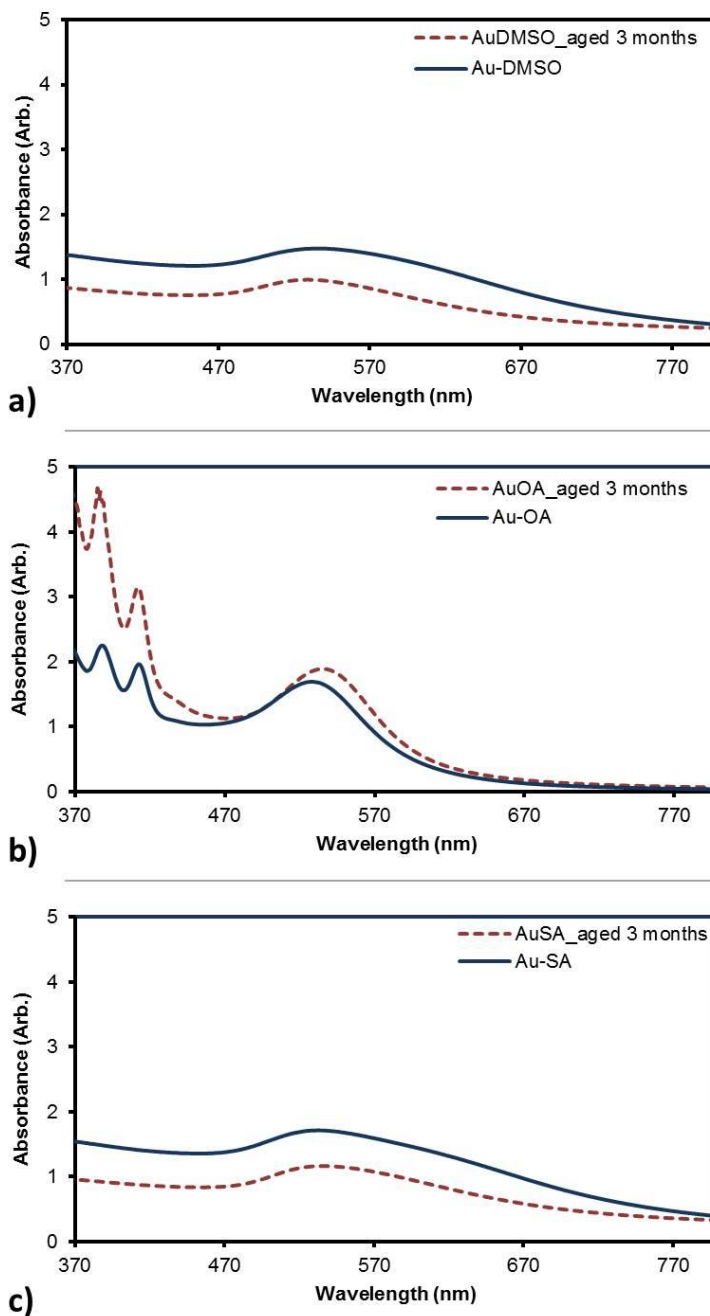
#### **Temperature and Pressure**

The stability of the three different Au nanoparticle dispersions in DMSO were studied as a function of time using UV-vis spectroscopy at standard ambient temperature and pressure. The UV-vis results of this study are presented in Figure 5.9 for each of the Au nanoparticle dispersions in DMSO. The spectra were obtained 24 hours after the synthesis was completed and again three months later in order to determine if any changes to the Au nanoparticles had occurred during an extended aging process. Figure 5.10 shows the digital images taken of each sample, and there are little-to-no color variations in each of the aged samples as compared to the fresh samples. These images and the UV-vis spectra indicate that these nanoparticles were stable for several months and did not show any physical evidence of precipitation from the solution (Figure 5.9). However, it is important to point out that the Au nanoparticles in Figure 5.9a and c show a slight decrease in the overall absorption in the spectra taken after 3 months of aging. This effect may be due to Ostwald ripening, which is part of the aging process for nanoparticles (Lifshitz & Slyozov 1961). Furthermore, the attractive van der Waals forces between nanoparticles increase with nanoparticle diameter, and steric/osmotic repulsive forces (provided by the stabilizing molecules adsorbed on the surface of the nanoparticles) counteract the attractive van der Waals forces. However, if the particles continue to grow over time, there will not be sufficient osmotic repulsive forces to prevent the largest nanoparticles from precipitating from the solution (Kitchens et al. 2003; Shah et al. 2002; Saunders & Roberts 2009). Therefore, DMSO (Figure 5.9a) and stearic acid (Figure 5.9c) likely form relatively weak interactions with the Au

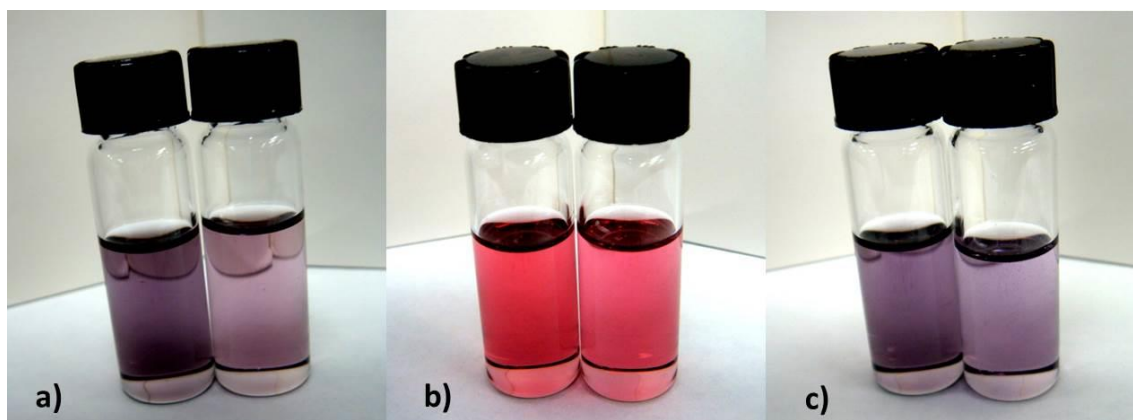
nanoparticle surface and allow for the Au nanoparticles to continue to slowly grow over time and will ultimately lead to precipitation from the DMSO solvent at standard ambient temperature and pressure.

Figure 5.9b shows the oleic acid-stabilized Au nanoparticles in DMSO. There was no significant change in the overall absorbance of these Au nanoparticles after three months of aging. This absorbance endurance (along with the TEM imaging analysis of the Au-oleic acid nanoparticles in Figure 5.2b), indicates that oleic acid is an excellent stabilizing agent for Au nanoparticles in DMSO and adequately suppresses nanoparticle aging over the time period investigated here. However, it should be noted that the peaks present around 385 nm and 410 nm are likely due to the presence of unreduced Au intermediate species in the dispersion, and similar reports for the formation of intermediates during synthesis have been found in the literature for other nanoparticle systems (McLeod et al. 2003; Henglein 1999).





**Figure 5.9** UV-vis spectra of the Au nanoparticle dispersions as a function of extended aging time at standard ambient temperature and pressure: a) DMSO as a functional solvent, b) oleic acid as the stabilizing ligand and DMSO as the solvent, and c) stearic acid as the stabilizing ligand and DMSO as the solvent.



**Figure 5.10** Digital images of the Au nanoparticle dispersions as a function of extended aging time at standard ambient temperature and pressure for a) DMSO as a functional solvent, b) oleic acid as the stabilizing ligand and DMSO as the solvent, and c) stearic acid as the stabilizing ligand and DMSO as the solvent. In each image above, the dispersion on the left has aged for 24 hours after synthesis, while the dispersion on the right has aged for 3 months.

### 5.3.4 Volume Expansion of CO<sub>2</sub>-DMSO Solutions

A series of studies were performed in order to obtain a better understanding of how the DMSO solvent influences Au nanoparticle stability. Each Au nanoparticle system was systematically pressurized using CO<sub>2</sub>, and the surface plasmon absorbance of each of the Au nanoparticle solutions were studied using UV-vis spectroscopy. Upon pressurization with CO<sub>2</sub>, the CO<sub>2</sub> gas dissolves into the DMSO solvent and creates a gas expanded liquid (Jessop & Subramaniam 2007). Figure 5.11 shows the volume expansion data at room temperature as a function of the applied CO<sub>2</sub> pressure for a solution of neat DMSO, oleic acid + DMSO, and stearic acid + DMSO. The concentration of oleic acid and stearic acid in DMSO were exactly the same as the actual concentrations of the oleic acid and stearic acid in DMSO used during Au nanoparticle synthesis. The volume expansion trend for the CO<sub>2</sub> and DMSO solvent systems observed in Figure 5.11 are consistent with the trends found in literature for other CO<sub>2</sub> gas-expanded DMSO systems (Reverchon et al. 1998; Calvignac, Rodier, et al. 2009). At room temperature, significant dissolution of CO<sub>2</sub> into each of the DMSO solvent systems occurs at approximately 28 bar for each system. Therefore, the pressure range for each nanoparticle stability study as a function of applied CO<sub>2</sub> pressure will occur in the pressure range from 28 to ~55.2 bar.

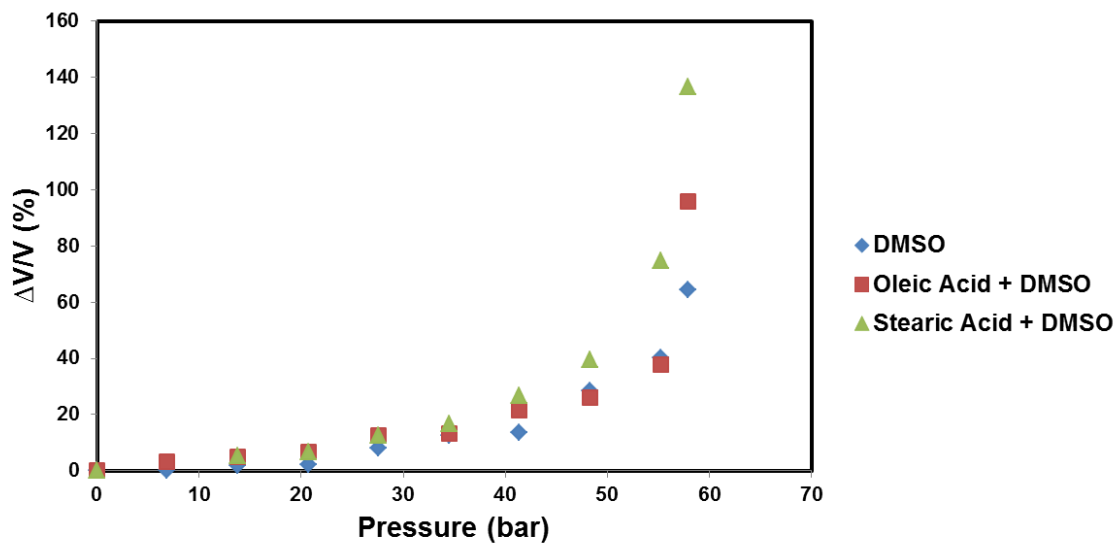


**Figure 5.11** Volume expansion as a function of applied CO<sub>2</sub> pressure for neat DMSO (◆), oleic acid + DMSO (■), and stearic acid + DMSO (▲).

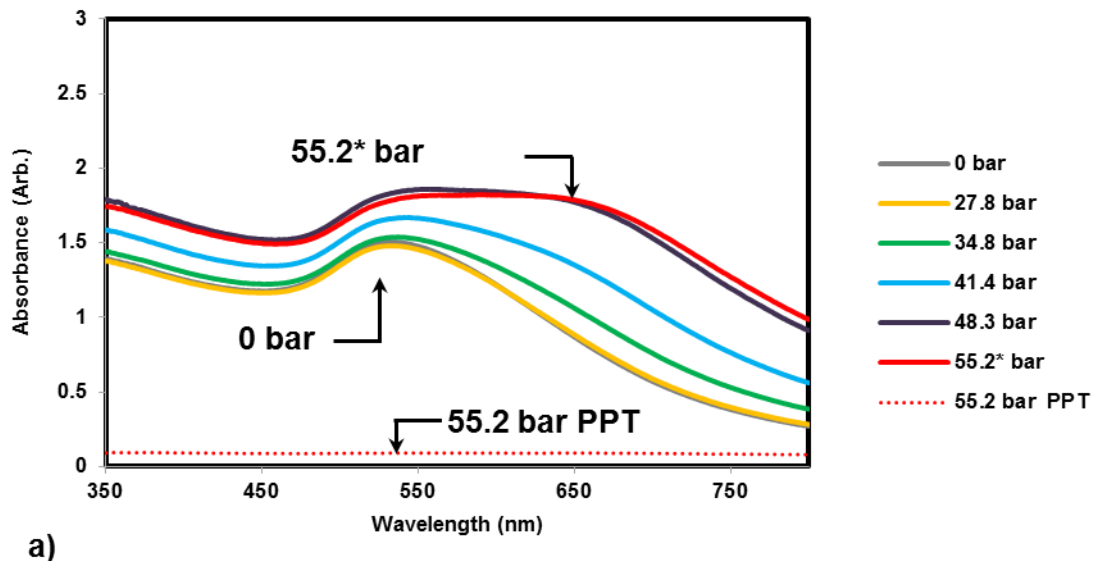
### 5.3.5 Dispersibility of Au Nanoparticles in CO<sub>2</sub>-Gas Expanded DMSO Solvent

#### Systems at Various Pressures

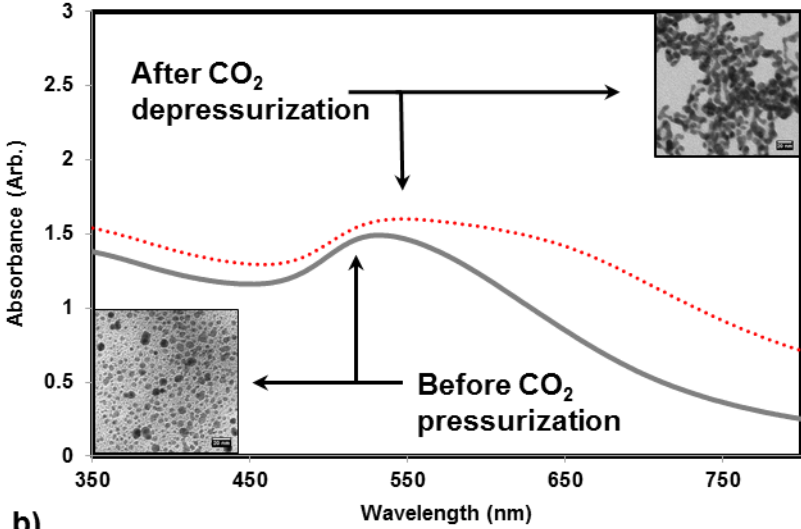
The effect of applied CO<sub>2</sub> pressure was studied for each of the three Au nanoparticle dispersions by tracking the maximum peak absorbance of the Au nanoparticle surface plasmon resonance band, which is centered at ~520 nm for each Au nanoparticle system. Each Au nanoparticle solution was loaded into the high-pressure UV-vis viewing apparatus and pressurized from 28 bar up to approximately 55.2 bar in increments of 6.9 bar. In each case, the UV-vis absorbance of the Au nanoparticle dispersion was closely monitored at each pressure interval before the CO<sub>2</sub> pressure was further increased to the next pressure setting in order to ensure the system had reached equilibrium. Ensuring the system has reached equilibrium is essential to this process because it indicates that the Au nanoparticle surface plasmon absorption bands are no longer changing due to the dissolution of CO<sub>2</sub> into the DMSO or compression of the system by the applied CO<sub>2</sub> pressure. Once there was no change in the absorbance at a given pressure, a spectrum was collected to capture the absorbance of the Au nanoparticles in the CO<sub>2</sub> gas-expanded DMSO solvent at that particular pressure, and then the CO<sub>2</sub> pressure was further increased to the next desired pressure setting up to approximately 55.2 bar.

The UV-vis spectra for the absorbance of the Au-DMSO nanoparticle dispersion as a function of applied CO<sub>2</sub> pressure are shown in Figure 5.12a. The absorbance of the Au nanoparticles in this system increases as more CO<sub>2</sub> is added from 0 bar to 55.2 bar. The peak at 525 nm significantly broadens as more CO<sub>2</sub> is added to the system. The peak labeled '55.2\* bar' corresponds to a transition pressure for the Au-DMSO nanoparticle

system. For example, in this case, 55.2\* bar is termed the 'transition pressure' because the absorbance (at that particular pressure, e.g., 55.2 bar) remains unchanged over an extended period of time before it subsequently and steadily decreases as a function of time.



a)



b)

**Figure 5.12** UV-vis spectra of a) the absorbance of the Au-DMSO nanoparticle dispersion as a function of the applied CO<sub>2</sub> pressure and b) the absorbance of the Au-DMSO nanoparticle dispersion before pressurization with CO<sub>2</sub> and after depressurization. Note that the spectrum labeled ‘55.2\* bar’ corresponds to the transition pressure, and the spectrum labeled ‘55.2 bar PPT’ corresponds to the point at which all Au nanoparticles had precipitated from the mixture.

It is important to mention that if the Au-DMSO nanoparticle solution was held at a lower pressure, i.e. 48.3 bar, the absorbance did not decrease within the time interval that was monitored (~8 hours). The amount of time spent at each pressure interval, as well as the elapsed time, are shown in Table 5.5 and the amount of time spent at each pressure interval steadily increased up to the transition pressure of 55.2\* bar as more CO<sub>2</sub> was added (i.e. more time was required at each pressure interval to ensure complete dissolution of CO<sub>2</sub> into the DMSO solvent before further increasing the pressure to the next pressure interval). However, at the pressure setting labeled 55.2\* bar (Figure 5.12a), the amount of time spent at this point (8 hours) was significantly less than the previous pressure settings (e.g. 20.5 hours at 55.2 bar). This indicates that the Au nanoparticles are effectively stable in the CO<sub>2</sub>-gas expanded DMSO dispersion for 8 hours at 55.2 bar\*, then the absorbance of the solution steadily decreased over a period of 44 hours as the particles destabilize (due to the dissolution of more CO<sub>2</sub> into the DMSO solvent mixture), and the Au nanoparticles steadily precipitate from the DMSO solvent as a function of time.



| <b>Pressure (bar)</b>       | <b>Time per Reading (hrs)</b> | <b>Time Elapsed (hrs)</b> |
|-----------------------------|-------------------------------|---------------------------|
| 0                           | <b>0</b>                      | <b>0</b>                  |
| 27.8                        | <b>7</b>                      | <b>7</b>                  |
| 34.8                        | <b>13</b>                     | <b>20</b>                 |
| 41.9                        | <b>14</b>                     | <b>34</b>                 |
| 48.3                        | <b>20.5</b>                   | <b>54.5</b>               |
| 55.2* (Transition Pressure) | <b>8</b>                      | <b>62</b>                 |
| 55.2 (Nanoparticles PPT)    | <b>44</b>                     | <b>98.5</b>               |

**Table 5.5** The amount of time spent at each CO<sub>2</sub> pressurization interval, as well as the elapsed time, for the Au-DMSO nanoparticle dispersion.

The spectra in Figure 5.12b are shown to compare the differences in the absorbance of the Au-DMSO nanoparticles before pressurization with CO<sub>2</sub> and after depressurization. As indicated by the spectra Figure 5.12a, the absorbance of the Au-DMSO nanoparticles at '55.2 bar PPT' had decreased to zero, indicating that the Au nanoparticles had completely precipitated from the solution. At this stage, the DMSO solution was colorless and transparent after depressurization (i.e., after removal of the CO<sub>2</sub> from the solution), and the precipitated Au nanoparticles could be seen at the bottom of the cuvette. The Au nanoparticles were easily re-dispersed in the DMSO solvent after sonication of the solution for approximately 15 seconds. These re-dispersed Au nanoparticles created a solution that was red in color, very similar to the original color of the Au-DMSO nanoparticle dispersion (prior to CO<sub>2</sub> pressurization). The spectra in Figure 5.12b show the absorbance of the Au-DMSO nanoparticles before the application of CO<sub>2</sub> pressure and after depressurization (and re-dispersion of the Au nanoparticles via sonication). There is an increase in the absorbance of the Au nanoparticles after depressurization, and the shape of this peak is very similar to the shape of the spectrum in Figure 5.12a for the peak describing the transition pressure of the mixture at '55.2\* bar' (e.g., as the system pressure is increased, the peak broadens). The TEM images are also provided on the inset of the spectra in Figure 5.12b and show an increase in the observed Au nanoparticle size after depressurization. After exposure to CO<sub>2</sub>, the particles agglomerated into significantly larger clusters, as can be observed from the TEM images in the insets in Figure 5.12b. It is anticipated that the sonication action disrupted what may have been even larger agglomerates within the post-depressurization solution.

The UV-vis spectra for the absorbance of the other two Au nanoparticle dispersions, Au-OA and Au-SA, are shown in Figure 5.13a and Figure 5.14a, respectively. The dispersibility of these Au-fatty acid nanoparticle solutions in CO<sub>2</sub> gas expanded DMSO is very similar to the Au-DMSO nanoparticle solution in CO<sub>2</sub> gas expanded DMSO. Figure 5.13a shows the spectra for the Au-OA nanoparticle dispersion and there is a slight increase in peak absorbance as a function of CO<sub>2</sub> pressure. In addition, the absorbance bands significantly broaden as the pressure is increased to the transition pressure of 55.2\* bar (after 9 hours at 55.2 bar, as shown in Table 5.6). Then, after the Au-OA nanoparticle dispersion is held at 55.2 bar for 9 hours, the absorbance steadily decreases to zero, indicating the Au nanoparticles have become unstable (after 45 hours at 55.2 bar) and have precipitated from the solution as a function of time. Similarly, the Au-SA nanoparticle dispersion in Figure 5.14a shows a considerable increase in absorbance and broadening of the peak as the applied CO<sub>2</sub> pressure is increased. After being held at the transition pressure (48.3\* bar) for 13 hours (pressurization times indicated in Table 5.7), the absorbance steadily decreased to zero, indicating that the Au nanoparticles had precipitated from the solution.

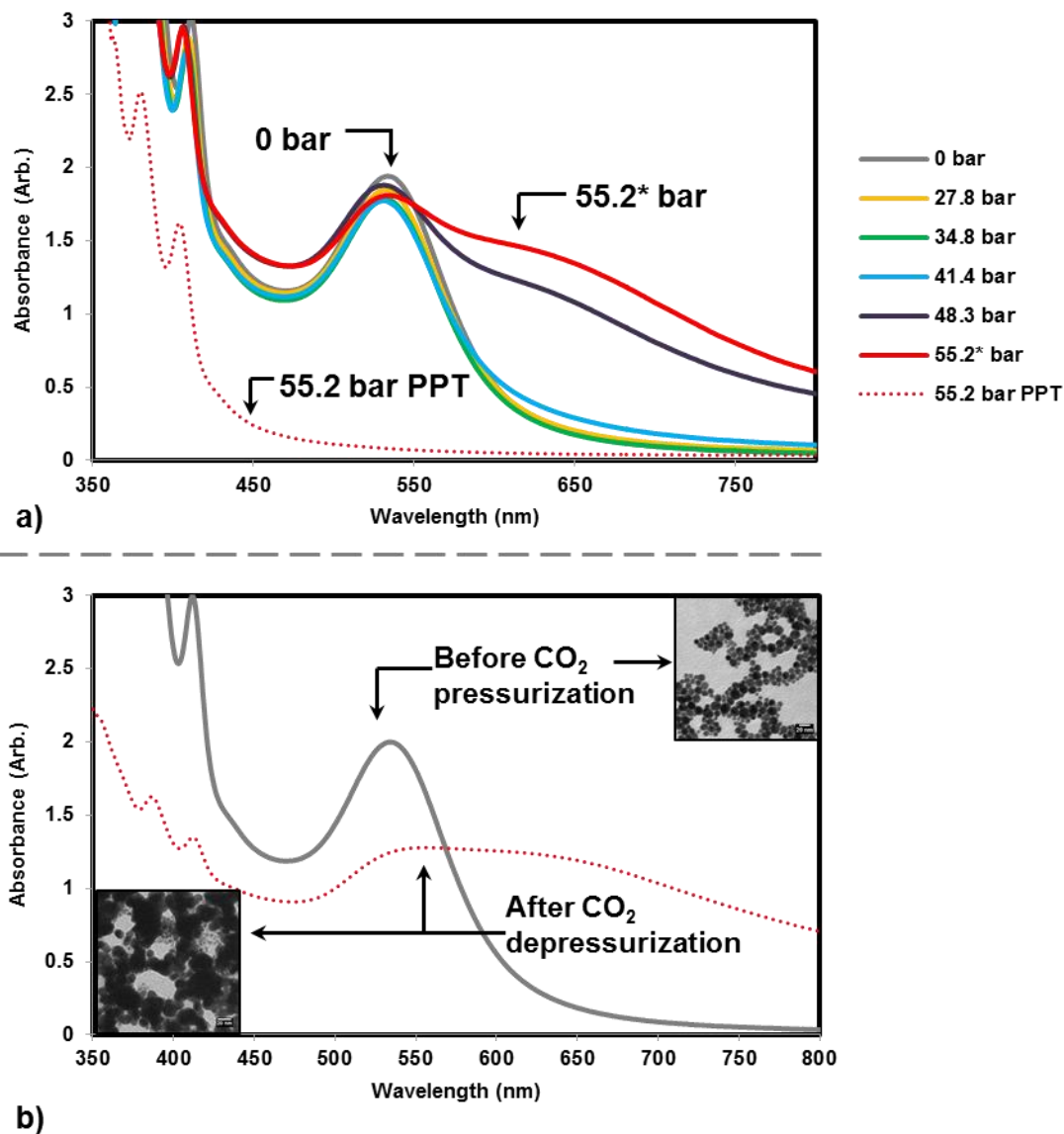


**Figure 5.13** UV-vis spectra of a) the absorbance of the Au-OA nanoparticle dispersion as a function of the applied CO<sub>2</sub> pressure and b) the absorbance of the Au-OA nanoparticle dispersion before pressurization with CO<sub>2</sub> and after depressurization. Note that the spectrum labeled '55.2\* bar' corresponds to the transition pressure, and the spectrum labeled '55.2 bar PPT' corresponds to the point at which all Au nanoparticles had precipitated from the mixture.

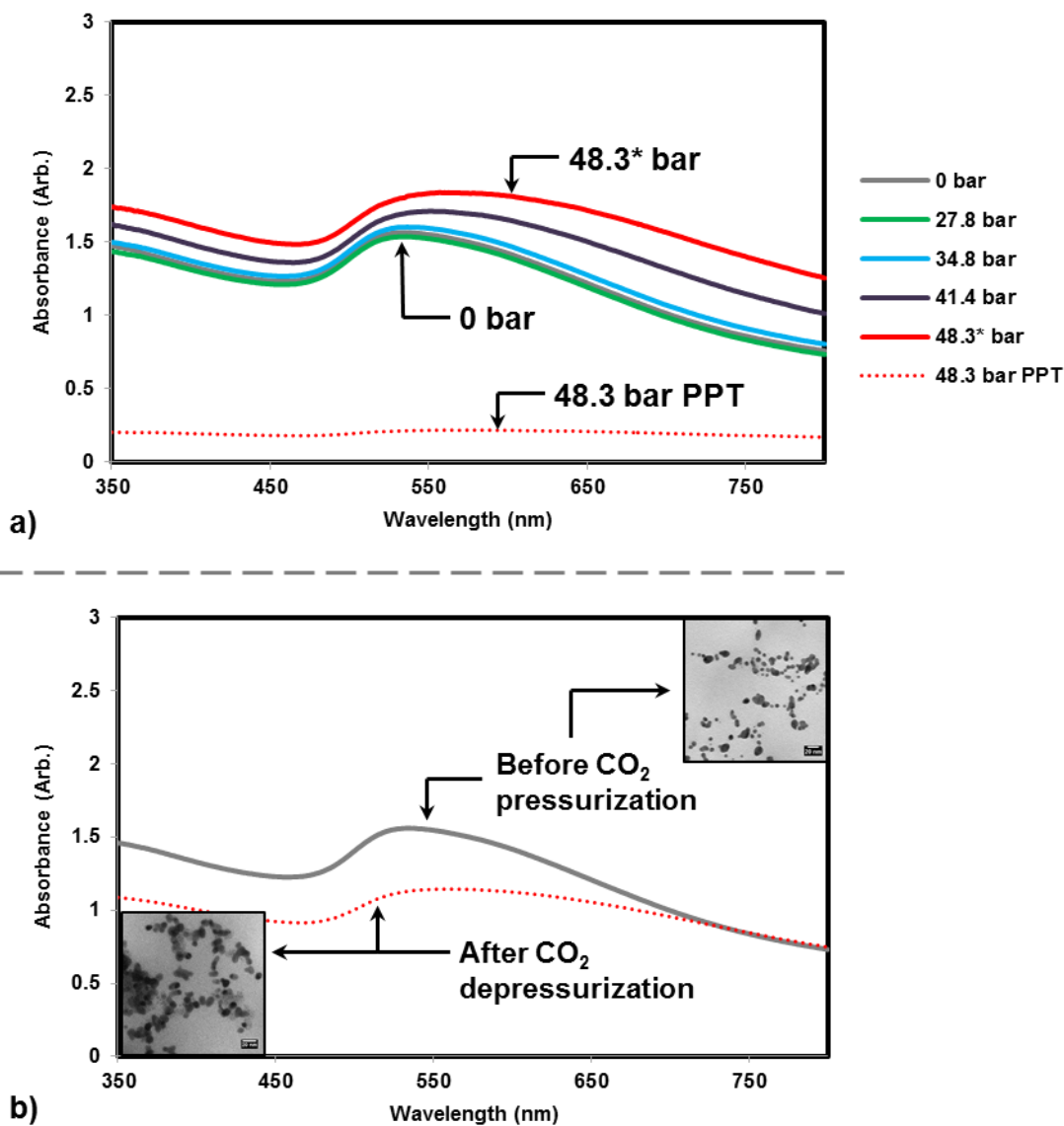


**Figure 5.14** UV-vis spectra of a) the absorbance of the Au-SA nanoparticle dispersion as a function of the applied CO<sub>2</sub> pressure and b) the absorbance of the Au-SA nanoparticle dispersion before pressurization with CO<sub>2</sub> and after depressurization. Note that the spectrum labeled '48.3\* bar' corresponds to the transition pressure, and the spectrum labeled '48.3 bar PPT' corresponds to the point at which all Au nanoparticles had precipitated from the mixture.

| <b>Pressure (bar)</b>       | <b>Time per Reading (hrs)</b> | <b>Time Elapsed (hrs)</b> |
|-----------------------------|-------------------------------|---------------------------|
| 0                           | <b>0</b>                      | <b>0</b>                  |
| 27.8                        | <b>7.5</b>                    | <b>7.5</b>                |
| 34.8                        | <b>13</b>                     | <b>20.5</b>               |
| 41.9                        | <b>20.5</b>                   | <b>41</b>                 |
| 48.3                        | <b>28</b>                     | <b>69</b>                 |
| 55.2* (Transition Pressure) | <b>9</b>                      | <b>78</b>                 |
| 55.2 (Nanoparticles PPT)    | <b>45</b>                     | <b>114</b>                |

**Table 5.6** The amount of time spent at each CO<sub>2</sub> pressurization interval, as well as the elapsed time, for the Au-OA nanoparticle dispersion.

| <b>Pressure (bar)</b>       | <b>Time per Reading (hrs)</b> | <b>Time Elapsed (hrs)</b> |
|-----------------------------|-------------------------------|---------------------------|
| 0                           | <b>0</b>                      | <b>0</b>                  |
| 27.8                        | <b>6.5</b>                    | <b>6.5</b>                |
| 34.8                        | <b>16.5</b>                   | <b>23</b>                 |
| 41.9                        | <b>22.5</b>                   | <b>45.5</b>               |
| 48.3* (Transition Pressure) | <b>13</b>                     | <b>58.5</b>               |
| 48.3 (Nanoparticles PPT)    | <b>28</b>                     | <b>73.5</b>               |

**Table 5.7** The amount of time spent at each CO<sub>2</sub> pressurization interval, as well as the elapsed time, for the Au-SA nanoparticle dispersion.

The absorbance of the other two Au nanoparticle solutions (Au-OA and Au-SA in DMSO) before pressurization with CO<sub>2</sub> and after depressurization (and subsequently redispersed via sonication in the original DMSO solvent) were studied. The spectra were very similar to the Au-DMSO nanoparticle spectra in Figure 5.12b (before pressurization with CO<sub>2</sub> and after depressurization). Figure 5.13b shows the absorbances of the Au-oleic acid nanoparticles before exposure to CO<sub>2</sub>, and the absorbance significantly decreased and the peak broadened after exposure to CO<sub>2</sub>. Likewise, the Au-stearic acid dispersion experienced a substantial decrease in absorbance and significant peak broadening after CO<sub>2</sub> depressurization (and subsequent redispersion of the nanoparticles in the solvent using sonication), as shown in Figure 5.14b. TEM images of the Au-OA and Au-SA nanoparticle solutions before and after exposure to CO<sub>2</sub> are also shown in the insets of Figure 5.13b and 5.14b, respectively. In each case, the CO<sub>2</sub>-gas expanded DMSO solution lead to large agglomerations of Au nanoparticles forming in the solution. Similar results have been reported in the literature describing a broadening of the peaks and a shift towards longer wavelengths as evidence that changes in nanostructure shape is occurring in solution (Brown & Natan 1998; N. R. Jana et al. 2001; Nikhil R. Jana et al. 2001a; Murphy et al. 2005; Lin et al. 2005).

## **5.4 Discussion of Au Nanoparticle Dispersibility in CO<sub>2</sub>-Gas Expanded DMSO**

### **Solvents**

Based on previous studies performed in the Roberts Lab and documented in the literature (Saunders & Roberts 2011a; Saunders & Roberts 2011b; Anand et al. 2005), the overall absorbance of a typical Au nanoparticle dispersion in an organic solvent with



organic/aliphatic ligands (i.e., thermodynamically-dispersed, ligand-stabilized nanoparticles) is expected to decrease as the solution is sequentially pressurized with CO<sub>2</sub>. This decrease in the absorbance of these Au nanoparticle dispersions is due to 1) the dissolution of CO<sub>2</sub> into the solvent mixture, thereby diluting the dispersion and progressively diminishing the solvent strength of the overall mixture and 2) the controlled precipitation of the Au nanoparticles from solution as a function of this applied CO<sub>2</sub> pressure (i.e., worsening solvent strength). Furthermore, these literature studies reported that the Au nanoparticles could be size-selectively precipitated from the organic dispersion by sequentially increasing the applied CO<sub>2</sub> pressure, whereby the larger nanoparticles precipitate first upon worsening solvent conditions (Saunders & Roberts 2011a; Saunders & Roberts 2011b; Anand et al. 2005).

The dispersibility of nanoparticles in an organic solvent is dependent on the interaction between the solvent and the ligands attached to the nanoparticle surface (McLeod, Anand, et al. 2005). The solvent/ligand interaction must be favorable enough to overcome the van der Waals forces of attraction between nanoparticles in a solution in order to maintain favorable nanoparticle dispersibility (Anand et al. 2008). In the case of CO<sub>2</sub> gas-expanded organic solvents, as more CO<sub>2</sub> is added via pressurization, the interaction between the solvent mixture (i.e., organic solvent plus dissolved CO<sub>2</sub>) and the ligand is weakened. Hence, the osmotic repulsive force that opposes the van der Waals attractive force (and maintains separation between nanoparticles) is reduced, which ultimately induces nanoparticle precipitation from the organic solvent (Anand et al. 2008; Saunders & Roberts 2009; Saunders & Roberts 2011b; Saunders & Roberts 2011a). Since the van der Waals forces are proportional to nanoparticle size (Hamaker 1937;

Hiemenz 1997), the largest nanoparticles precipitate first as the solvent strength is weakened by the applied CO<sub>2</sub> pressure (Anand et al. 2008; Saunders & Roberts 2009; Saunders & Roberts 2011b; Saunders & Roberts 2011a).

Contrary to the previous reports describing the controlled precipitation of aliphatic ligand-stabilized Au nanoparticles from conventional organic solvents (e.g., aliphatic hydrocarbons) (Anand et al. 2008; Saunders & Roberts 2009; Saunders & Roberts 2011a; Saunders & Roberts 2011b; Anand et al. 2005; McLeod, Anand, et al. 2005), the results presented in the present chapter illustrate that the dispersibility of Au nanoparticles in CO<sub>2</sub> gas expanded DMSO solvent systems (Au-DMSO, Au-OA in DMSO, and Au-SA in DMSO) is drastically different. In this case, the nature of the absorbance bands change as a function of applied CO<sub>2</sub> pressure (and as a function of time) in three distinct stages: Initially, at low pressure, the absorbance of each of the Au nanoparticle dispersions in the gas-expanded DMSO system increased with applied CO<sub>2</sub> pressure (in contrast to other organic systems) (Anand et al. 2008; Saunders & Roberts 2009; Saunders & Roberts 2011a; Saunders & Roberts 2011b; Anand et al. 2005; McLeod, Anand, et al. 2005), and remained stable (as evidenced by no change in the absorption spectrum) as a function of time at each applied pressure. Then, beyond a certain applied CO<sub>2</sub> pressure, the absorbance band shifted towards longer wavelengths and broadened while remaining stable as a function of time. The increase in absorbance, the broadening of the peaks, and the shift to longer wavelengths suggest that nanoparticles had agglomerated and clustered into larger (and possibly irregular) structures (Brown & Natan 1998; N. R. Jana et al. 2001; Nikhil R. Jana et al. 2001a; Murphy et al. 2005; Lin et al. 2005) as evidenced by TEM imaging analysis (insets of

Figures 5.12b, 5.13b, and 5.14b) with the increase in CO<sub>2</sub> system pressure. Eventually, a point is reached in which a ‘transition pressure’ is achieved where the absorbance then steadily decreases as a function of time at a constant pressure.

These studies have indicated that Au nanoparticles cannot be controllably precipitated from a DMSO solvent as a function of the applied CO<sub>2</sub> pressure alone at these elevated pressures; however, it was observed that the Au nanoparticles precipitate as a function of time after the application of sufficient CO<sub>2</sub> pressure. In other words, this converts to a kinetically-controlled process rather than the thermodynamically-stable solution encountered in the aliphatic hydrocarbon solvent systems (Anand et al. 2008; Saunders & Roberts 2009; Saunders & Roberts 2011a; Saunders & Roberts 2011b; Anand et al. 2005; McLeod, Anand, et al. 2005). In order to describe the eventual decrease in absorbance, which only occurred after the ‘transition pressure’ was achieved, the absorbance of each system in this region was carefully examined (starting from the transition stage to the precipitation or ‘PPT’ stage, as labeled on Figures 5.12, 5.13, and 5.14). As such, this discussion will be focused only on the spectral data collected once the ‘transition pressure’ had been reached. Since the applied CO<sub>2</sub> pressure results in the addition of CO<sub>2</sub> to the ligand-solvent mixture, the absorbance spectra must be corrected for this dilution using the Beer-Lambert Law and the associated volume expansion of the DMSO system effect (Anand et al. 2005; Saunders & Roberts 2011a; Saunders & Roberts 2011b). The corrected volumes were calculated using the Peng-Robinson Equation of State (Anand et al. 2005; Saunders & Roberts 2011a). Then, a plot of the normalized absorbances (at 550 nm, 530 nm, and 540 nm for the Au-DMSO, Au-OA, and Au-SA, respectively) was constructed at each operating pressure, and the results are presented in

Figure 5.15 for each of the Au nanoparticle solutions in DMSO. Note that the values 550 nm, 530 nm, and 540 nm were chosen because these bands correspond to the wavelength of maximum absorption for the primary band at the ‘transition pressure.’ The data in Figure 5.15 show an overall decrease in the normalized absorbance as a function of time in these Au nanoparticle CO<sub>2</sub>-expanded DMSO solvents, representing a time-resolved precipitation of the particles from solution. For example, Figure 5.15 shows graphs of the normalized absorbance versus time which can be used to monitor the destabilization of the Au nanoparticle dispersions in DMSO. The data points on each of the graphs could theoretically be used to 1) determine the amount of time at a particular pressure required to induce nanoparticle precipitation and 2) determine the amount of time necessary in order to achieve complete nanoparticle precipitation. In each of the three Au nanoparticle systems studied in Figure 5.15, the maximum peak absorbance remains relatively unchanged until approximately 10 hours.

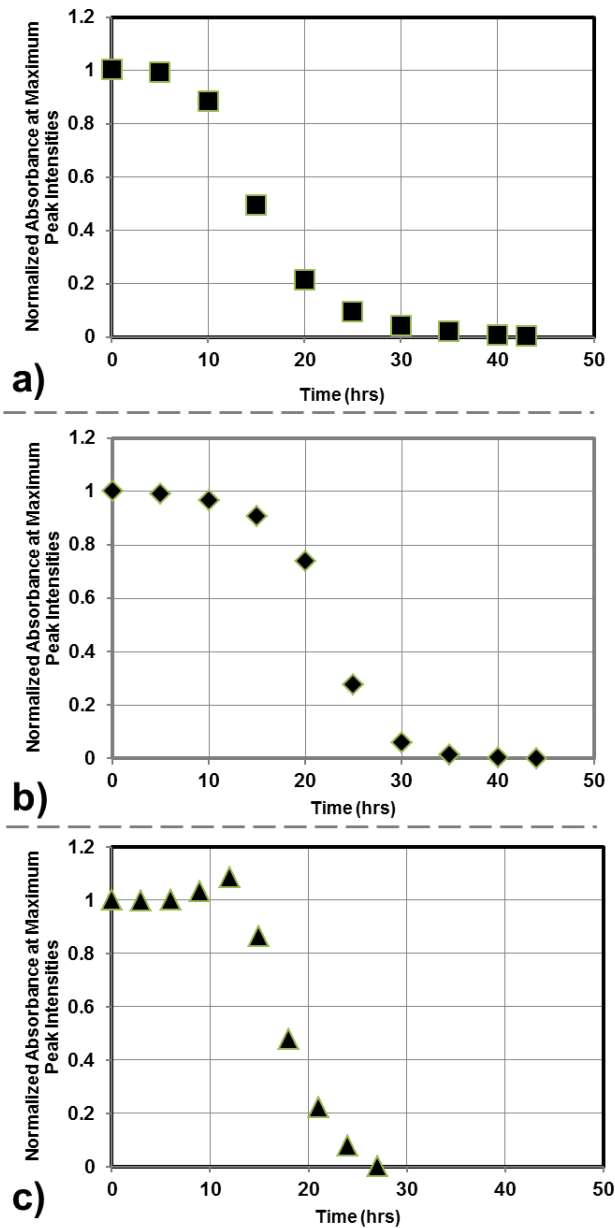


**Figure 5.15** Curves representing the precipitation of Au nanoparticles from CO<sub>2</sub>-gas expanded DMSO solvent systems as a function of time where a) is the Au-DMSO nanoparticle solution, b) is the Au-OA nanoparticle solution, and c) is the Au-SA nanoparticle solution. Pressure was held constant in each case, and the graphs represent the precipitation that occurs once the transition pressure has been reached at a) 55.2 bar for 44 hours, b) 55.2 bar for 45 hours, and c) 48.3 bar for 28 hours.

To summarize, Figure 5.16 illustrates the proposed behavior of these Au nanoparticles in the CO<sub>2</sub>-gas expanded DMSO solvent systems over the entire pressurization range studied. Figure 16a describes the Au nanoparticle dispersibility at low applied CO<sub>2</sub> pressures (e.g., 0 – 27.8 bar): the Au nanoparticles are sufficiently solvated in the DMSO+CO<sub>2</sub> solvent, and the Au nanoparticles remain dispersed in the solvent. Figure 16b portrays the Au nanoparticle dispersibility at intermediate pressures (e.g., 41.4 – 48.3 bar): the Au nanoparticles remain dispersed within the DMSO solvent, but agglomerate due to the decrease in the osmotic repulsive force which has been induced by the added CO<sub>2</sub>. At this stage, the van der Waals forces of attraction overcome the osmotic repulsive force and cause the Au nanoparticles to begin to agglomerate to a particular cluster size in solution (approximately 20 nm as shown in the insets of Figures 5.12b, 5.13b, and 5.14b). The Au nanoparticle clusters remain stable in the DMSO+CO<sub>2</sub> solvent at these intermediate pressures, and therefore remain dispersed in the DMSO+CO<sub>2</sub> solvent. This clustering phenomenon is evidenced by the observed red shift and increase in the UV-vis absorbance as a function of CO<sub>2</sub> pressure for each of the Au nanoparticle systems (Figures 5.12a, 5.13a, and 5.14a). Figure 16c illustrates the Au nanoparticle dispersibility at high CO<sub>2</sub> pressures (e.g., 48.3 – 55.2 bar): the Au nanoparticle clusters are no longer stable in the DMSO+CO<sub>2</sub> solvent, and the Au nanoparticle clusters ultimately agglomerate and precipitate from the solution as a function of time. In essence, it is proposed that at low and intermediate pressures, the added CO<sub>2</sub> can act as a co-solvent with the DMSO, thereby allowing Au nanoparticle clusters to remain dispersed in DMSO; however at higher pressures, the CO<sub>2</sub> can act as an anti-solvent in the DMSO

mixture, effectively serving as a mechanism to destabilize the Au nanoparticle clusters and induce their precipitation from the DMSO solvent.

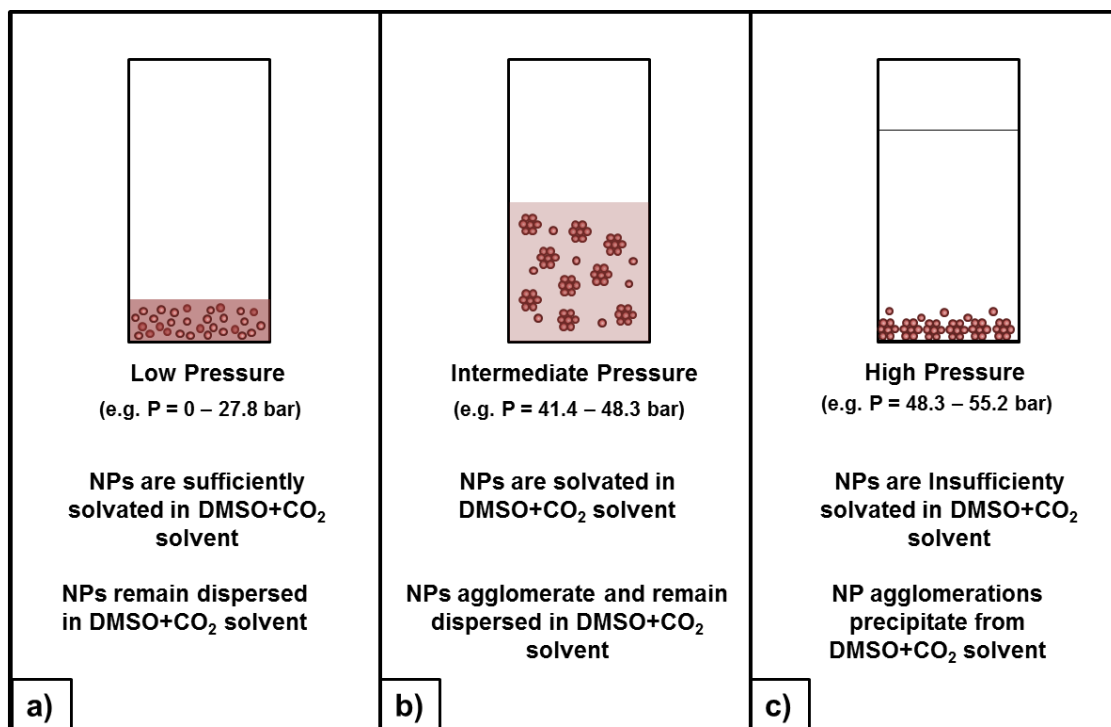


**Figure 5.16** Illustration of Au nanoparticle dispersibility in DMSO+CO<sub>2</sub> solvent systems at various applied pressures of CO<sub>2</sub>.



## 5.5 Conclusions

The studies described in this chapter have illustrated that Au nanoparticles can be sufficiently stabilized by DMSO as a functional solvent as well as by fatty acid capping ligands, such as oleic acid and stearic acid. In addition, the dispersibility of the three different Au nanoparticle solutions in CO<sub>2</sub>-gas expanded DMSO systems were examined by sequentially pressurizing the system with CO<sub>2</sub>, and simultaneously monitoring the Au nanoparticle dispersion using UV-vis spectroscopy. In each case, the particles agglomerated into clusters as more CO<sub>2</sub> was added, but these clusters remained solvated and dispersed in the DMSO+CO<sub>2</sub> solvent mixture. However, after a certain ‘transition pressure’ was reached, the Au nanoparticle clusters became unstable due to insufficient solubility in the DMSO+CO<sub>2</sub> mixture and these clusters precipitated from solution as a function of time. These findings were distinctly different from the results reported in the literature for thermodynamically-dispersed, aliphatic ligand-stabilized nanoparticles in organic solvents. This research demonstrates that the addition of CO<sub>2</sub> to the solvent mixture results in subtle changes in solvation of the nanoparticle ligands such that nanoparticle stabilization can be drastically affected.

## **Chapter 6**

### **Overall Conclusions and Future Directions**

#### **6.1 Summary and Conclusions**

In 1959, Richard Feynman challenged researchers reach further into the nanoscale in his famous lecture, “There’s Plenty of Room at the Bottom,” and since then, the scientific community has been searching for new techniques to ‘miniaturize’ technology. Over the past few decades, researchers discovered that a nanomaterial’s property is largely dependent on its size, and since this technological breakthrough, devices have been constructed using nano-scale materials and have subsequently been manufactured to be progressively smaller. Therefore, it is necessary to be able to control the size and shape of nanoparticles in order to take advantage of their unique and size-tunable properties. This can be accomplished by either judiciously controlling the nanoparticle synthesis conditions, or by performing post synthesis processing of the particles. Potential disadvantages of the more popular and current techniques that are typically used to accomplish particle size and shape control can involve using harsh and expensive reagents and solvents, and often require hours/days to complete a single synthesis experiment. Large amounts of waste are generated in typical nanoparticle post-synthesis processing techniques, and these processes yield low throughputs of particles. The research presented in this dissertation contributes to the field of nanotechnology because

of the simple techniques that were developed and described exploit the unique solvation properties of DMSO, which assists in the production of metallic and magnetic nanoparticles.

In Chapter 2, the synthesis of magnetic Co nanoparticles using DMSO as a functional solvent was presented. In this technique, the DMSO concomitantly functioned as both the solvent and the stabilizing ligand during Co nanoparticle synthesis to produce  $3.5 \pm 1.7$  nm Co nanoparticles. The interaction between the Co nanoparticle surface and the DMSO ligand was also studied, and it was found that the DMSO interacts with the Co nanoparticle surface by strong coordinations from the oxygen component of the sulfoxide functional group of DMSO. Furthermore, it was determined that the DMSO protects the Co nanoparticles from oxidation by forming a monolayer of oxygen (likely from the oxygen component of DMSO) on the surface of the particles. Upon further investigation, it was found that the Co nanoparticles possessed an amorphous structure. These findings demonstrated that DMSO is a viable solvent for the synthesis of magnetic nanoparticles.

Based on the findings of Chapter 2, the studies in Chapter 3 were focused on synthesizing Co nanoclusters using DMSO as a functional solvent by varying the reaction temperature. It was found that Co nanoparticles could be controllably aggregated into ~20 nm nanoclusters. The nanocluster sizes were directly related to the synthesis temperature. After further investigations it was confirmed that these Co nanoclusters were composed of smaller ~4 nm Co nanoparticles, which had formed due to the high temperature synthesis in DMSO. The formation of these clusters occurred at elevated temperatures likely because the interactions between the DMSO and the Co nanoparticles are weakened at higher temperatures. These smaller Co nanoparticles could then be

liberated from the clusters by adding various polar and non-polar co-solvents to the dispersion in DMSO. These results further indicated that DMSO has very unique solvation properties, such that it allows for nanoparticle clustering to occur at high temperatures. Furthermore, DMSO can form preferential interactions with other solvents to induce the deconstruction of the larger Co nanoclusters into smaller Co nanoparticles.

The studies presented in Chapter 4 described a technique to produce high-quality spinel  $\text{Co}_3\text{O}_4$  nanoparticles. These particles were produced first by synthesizing amorphous Co nanoparticles (as described in Chapter 2), and then annealing the Co nanoparticles in air up to  $800^\circ\text{C}$ . The DMSO is present on the surface of the Co nanoparticles as a monolayer (as determined by the studies in Chapter 2) up to temperatures of  $\sim 200^\circ\text{C}$ . The presence of the DMSO as a monolayer on the surface ‘protects’ the particles from oxidation in air at  $25^\circ\text{C}$ , but annealing at high temperatures removes the DMSO and allows the amorphous Co nanoparticles to transform into the ordered  $\text{Co}_3\text{O}_4$  structures. Magnetic studies indicated that these  $\text{Co}_3\text{O}_4$  structures possess high magnetic coercivity, and these results strongly suggest that these particles may have potential uses in a variety of energy and data storage devices. These interesting magnetic properties are believed to have developed due to the aggregation of the  $\sim 5$  nm nanoparticles into  $\sim 300$  nm particles that was induced by the annealing process. These findings indicate that preparing Co nanoparticles (and possibly other magnetic materials) using small molecules, such as DMSO, to function as both the ligand and the solvent can allow the particles to develop unique and distinct magnetic properties.

In Chapter 5, three different Au nanoparticle solutions were prepared in DMSO where DMSO can serve as both the solvent and the ligand: i) neat DMSO, ii) DMSO +

oleic acid, iii) DMSO + stearic acid. Then, each of the Au nanoparticle dispersions in DMSO was pressurized using CO<sub>2</sub> to create a gas-expanded DMSO system, and Au nanoparticle dispersibility was studied using *in situ* UV-vis spectroscopy. These studies were performed in order to observe the differences between nanoparticles dispersed in CO<sub>2</sub>-gas expanded non-polar organic solvents and nanoparticles dispersed in CO<sub>2</sub>-gas expanded polar aprotic solvents (e.g., DMSO). It was found that the Au nanoparticles in DMSO could be aggregated into clusters as a function of the applied CO<sub>2</sub> pressure and solubility of the clusters was maintained in the DMSO+CO<sub>2</sub> mixture at moderate pressures (e.g., 41.4 – 48.3 bar). Then upon further pressurization (e.g., 48.3 – 55.2 bar), the Au nanoparticle clusters were destabilized and precipitated from the solution as a function of time due to the poor solvation capabilities of the DMSO+CO<sub>2</sub> mixture at these elevated pressures. These results are markedly different from the reports in the literature for thermodynamically-dispersed, aliphatic ligand-stabilized nanoparticles in non-polar organic solvents, where the particles size-selectively precipitated from the organic+CO<sub>2</sub> mixture as a direct function of the applied CO<sub>2</sub> pressure. The research presented in this chapter demonstrates that the addition of CO<sub>2</sub> to the DMSO solvent mixture can result in subtle changes in nanoparticle ligand solvation such that nanoparticle stabilization can be drastically affected. Additionally, these studies may provide a foundation for the studies presented in the Future Directions of this dissertation (Section 6.2.1), which describes Au nanoparticle synthesis in CO<sub>2</sub>-gas expanded DMSO solutions. Likewise, these studies will hopefully shed light on the ability to control the dispersibility and deposition of Co<sub>3</sub>O<sub>4</sub> nanoparticles using CO<sub>2</sub>-gas expanded DMSO to

create thin films, which is of significant interest for the topics presented in the Future Directions of this dissertation (Section 6.2.2).

In conclusion, the research presented in this dissertation has been highly focused on understanding the fundamental interaction of metallic and magnetic nanoparticles with a different type of molecule, DMSO. It was repeatedly demonstrated that DMSO possesses the unique ability to behave as both a solvent and a stabilizing agent during the synthesis of Co and Au nanoparticles. Moreover, the exceptional properties of DMSO, such as high boiling point, pressure-tunable properties, and miscibility with numerous co-solvents (both polar and non-polar), have allowed for several post-synthesis processing techniques to be employed in order to produce high-quality nanoparticles. These procedures have demonstrated new methods that can be used in combination with DMSO to produce Co and Au nanoparticles that can potentially benefit a wide variety of applications.

## **6.2 Future Directions**

In this section, two different research areas are presented as possible future directions, which are based on the original findings presented in this dissertation. The first project involves the synthesis of Au nanoparticles in CO<sub>2</sub>-gas expanded DMSO solutions. The second project describes potential future directions for Co<sub>3</sub>O<sub>4</sub> thin film formation.

### **6.2.1 Synthesis of Au nanoparticles in a CO<sub>2</sub>-Gas Expanded DMSO Solvent**

The studies presented throughout this document have demonstrated that the molecule DMSO is an integral component of nanoparticle synthesis and dispersibility.

Studies have shown (Chapter 5) that the post-synthesis dispersibility of Au nanoparticles in DMSO can be manipulated by modest changes in applied CO<sub>2</sub> pressure. Specifically, the added CO<sub>2</sub> to the solvent mixture induces Au nanoparticle clustering as a function of the applied CO<sub>2</sub> pressure, and these clusters can be subsequently precipitated from the mixture as a function of time at high pressures. In addition to particle dispersibility and solvation, nanoparticle nucleation and growth may be able to be controlled by exploiting the pressure-tunable viscosity of the DMSO solvent by CO<sub>2</sub> pressurization.

The viscosity of DMSO as a function of the applied CO<sub>2</sub> pressure is shown in Figure 6.1. This data shows that as the viscosity of DMSO can be manipulated using CO<sub>2</sub> pressure, such that as the pressure of the mixture is increased, the viscosity is decreased. Literature studies have shown that solutions with high viscosity can have a direct impact on the diffusional rates of the reactants and leads to prolonged reducing rates, therefore influencing the formation of nanoclusters (King et al. 2003). Studies have also indicated that by varying the solvent viscosity, the nucleation and growth of nanoparticles can be controlled (Hu et al. 2003; Johans et al. 2008; Erdemir et al. 2009; Tannenbaum 1994; King et al. 2003; Tannenbaum 1997).

It has been discussed in the literature that by creating a nanoparticle synthesis environment which allows for the separation of the nucleation and growth regimes, monodisperse nanoparticles can be produced (LaMer & Dinegar 1950; Watzky & Finke 1997; Johans et al. 2008). Figure 6.2 provides a graphical illustration of the classical model of nucleation and growth. This figure illustrates that nanoparticle nucleation occurs when the solution becomes supersaturated with metal atoms, which occurs upon reduction of the metal ions by a reducing agent. To synthesize monodisperse

nanoparticles, the nuclei should form at the same time, ideally instantaneously (LaMer & Dinegar 1950; Viswanatha & Sarma 2007; Cao 2004). Central to the future work discussed here, control over the nucleation and growth process can be accomplished if the viscosity of the DMSO solvent is reduced (as a result of increased CO<sub>2</sub> pressure), which will allow for a burst of nucleation to occur before the growth stage begins. Thus, future work should be to perform the synthesis of Au nanoparticles in DMSO in at moderate and high CO<sub>2</sub> pressures, so as to investigate the influence of solvent viscosity on Au nanoparticle formation.



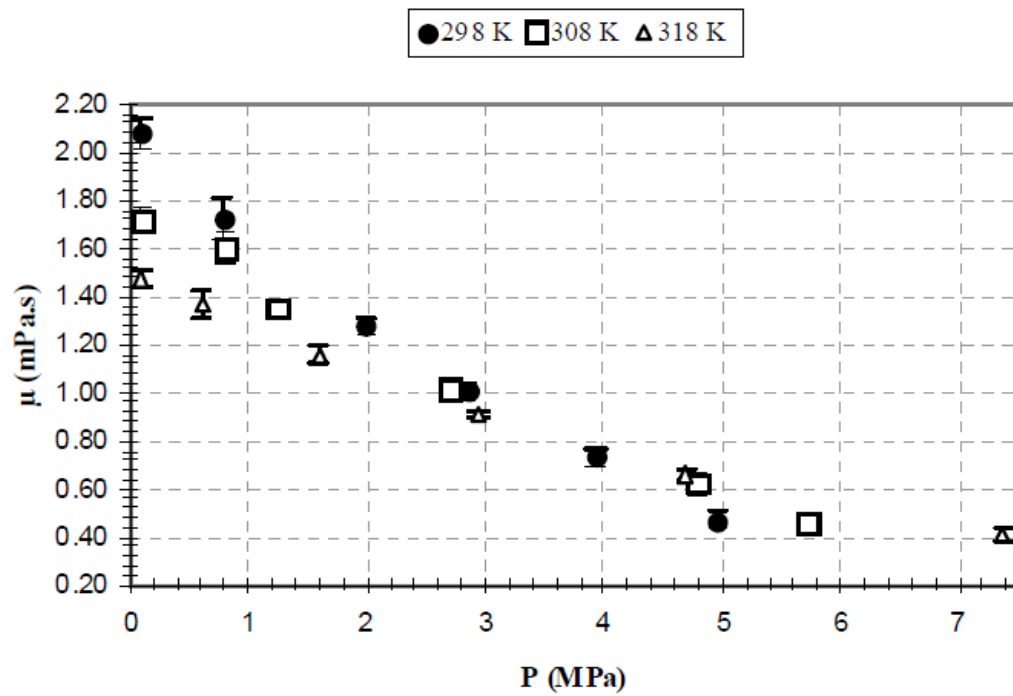


**Figure 6.1** The viscosity of DMSO as a function of the applied CO<sub>2</sub> pressure (Calvignac, Letourneau, et al. 2009; Bhuiyan et al. 2007).

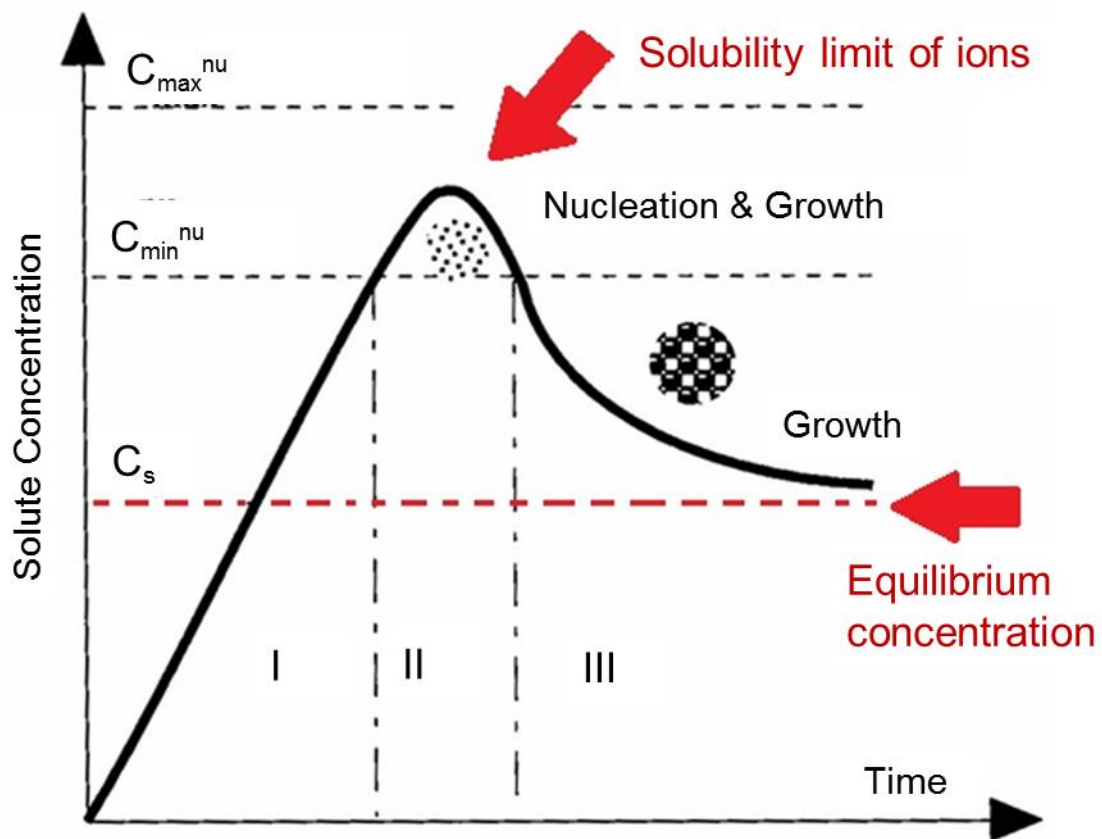


**Figure 6.2** Schematic illustration of nanoparticle formation via the processes of nucleation and growth (Cao 2004; Oskam 2006; Viswanatha & Sarma 2007).

### 6.2.2 Co<sub>3</sub>O<sub>4</sub> Thin Film Formation

The studies presented in this dissertation (Chapter 4) have shown that the crystallinity and the magnetic properties of Co nanoparticles can be altered as a function of the post-synthesis annealing temperature. Specifically, it was shown that amorphous Co nanoparticles (~5 nm) can transform into ordered structures of spinel Co<sub>3</sub>O<sub>4</sub> particles (~300 nm). The magnetism of the amorphous Co nanoparticles and the annealed samples was found to be mixtures of para- and ferromagnetic components; however, the coercivity drastically increased from 150 Oe to ~5 kOe after having been annealed in air at 800°C. Thus, these particles could potentially be used to make thin films for magnetic storage devices based on the high observed coercivity (Frey et al. 2009; Gubin et al. 2005; Coffey et al. 1995).

In a typical thin film magnetic storage device, there are thin layers of magnetic particles that are deposited onto a substrate. The magnetic layers are typically added using sputter coating (Emori et al. 2013) or by spin coating techniques (Bräuer et al. 2006). However, particle deposition techniques have been developed using CO<sub>2</sub>-gas expanded liquids which allow for the uniform deposition of nanoparticles to create wide-area thin films (McLeod, Kitchens, et al. 2005; Saunders & Roberts 2011a; McLeod, Anand, et al. 2005; Juncheng Liu et al. 2006). Figure 6.3 shows a TEM image of nanoparticles that have been deposited using the CO<sub>2</sub>-gas expanded liquid deposition technique. Thus, future work should be focused on utilizing the CO<sub>2</sub>-gas expanded particle deposition technique to create thin films of the Co<sub>3</sub>O<sub>4</sub> nanoparticles that were produced from the methods defined in Chapter 4.

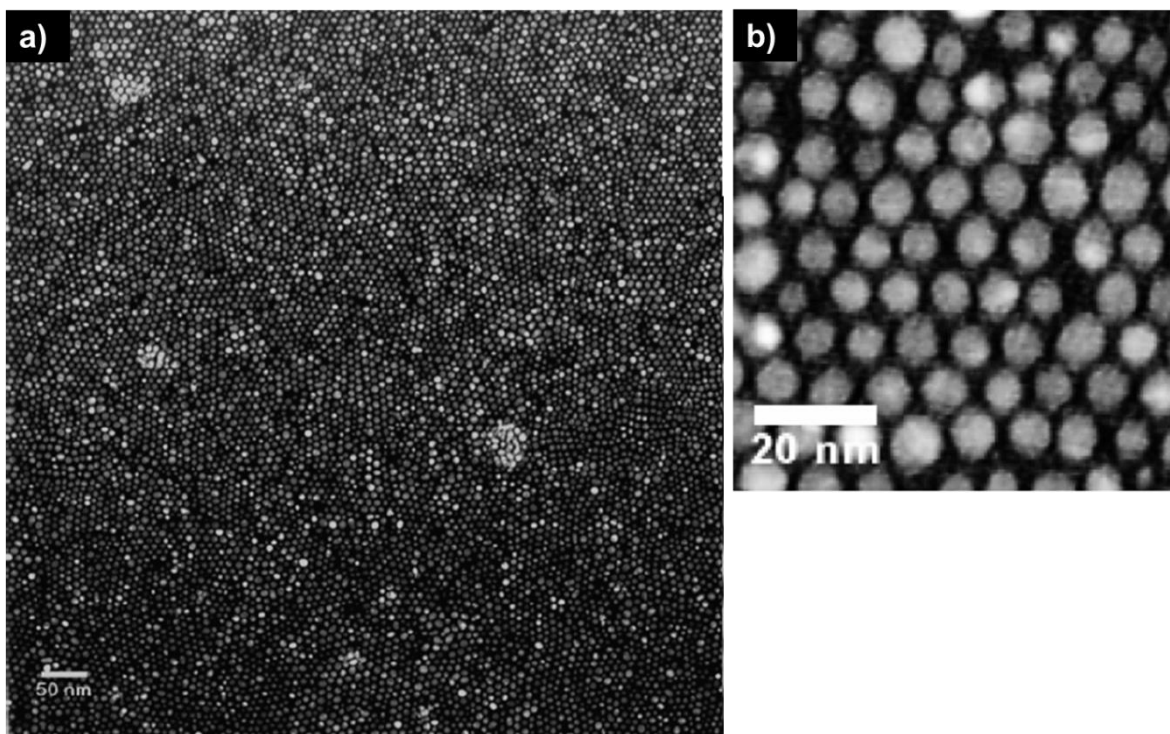


**Figure 6.3** TEM image of a) an array of dodecanethiol-stabilized Au nanoparticles that have been deposited onto a TEM grid using the CO<sub>2</sub>-gas expanded deposition technique and b) Au nanoparticle array at higher magnification to show particle deposition uniformity (Juncheng Liu et al. 2006).

## References

- Adachi, M., Tsukui, S. & Okuyama, K., 2003. Nanoparticle formation mechanism in CVD reactor with ionization of source vapor. , pp.31–37.
- Allaedini, G. & Muhammad, A., 2013. Study of influential factors in synthesis and characterization of cobalt oxide nanoparticles. *Journal of Nanostructure in Chemistry*, 3(1), p.77. Available at: <http://www.jnanochem.com/content/3/1/77>.
- Anand, M. et al., 2008. Thermodynamic Analysis of Nanoparticle Size Selective Fractionation Using Gas-Expanded Liquids. *Ind. Eng. Chem. Res.*, pp.553–559.
- Anand, M. et al., 2005. Tunable solvation effects on the size-selective fractionation of metal nanoparticles in CO<sub>2</sub> gas-expanded solvents. *The journal of physical chemistry. B*, 109(48), pp.22852–9. Available at: <http://www.ncbi.nlm.nih.gov/pubmed/16853977>.
- Anand, M., Odom, L.A. & Roberts, C.B., 2007. Finely Controlled Size-Selective Precipitation and Separation of CdSe/ZnS Semiconductor Nanocrystals Using CO<sub>2</sub>-Gas-Expanded Liquids. *Langmuir*, 23(13), pp.7338–7343.
- Andreatta, a. E. et al., 2007. Phase equilibria of dimethyl sulfoxide (DMSO)+carbon dioxide, and DMSO+carbon dioxide+water mixtures. *The Journal of Supercritical Fluids*, 42(1), pp.60–68. Available at: <http://linkinghub.elsevier.com/retrieve/pii/S0896844607000095> [Accessed September 1, 2011].
- Anon, 2007. *Dimethyl Sulfoxide ( DMSO ) Solubility Data*, Gaylord Chemical Company LLC: Gaylord Chemical Company LLC. Available at: [http://www.gaylordchemical.com/uploads/images/pdfs/literature/102B\\_english.pdf](http://www.gaylordchemical.com/uploads/images/pdfs/literature/102B_english.pdf).
- Anon, 2014. Magnetism. *Encyclopaedia Britannica*. Available at: <http://www.britannica.com/EBchecked/topic/357334/magnetism>.
- Badia, A. et al., 1997. Structure and Dynamics in Alkanethiolate Monolayers Self-Assembled on Gold Nanoparticles: A DSC, FT-IR, and Deuterium NMR Study. *Journal of the American Chemical Society*, 119(11), pp.2682–2692. Available at: <http://pubs.acs.org/doi/abs/10.1021/ja963571t>.
- Baird, D. & Shew, A., 2004. Probing the History of Scanning Tunneling Microscopy.
- Bao, S.J. et al., 2008. Shape Evolution and Magnetic Properties of Cobalt Sulfide. *Crystal Growth & Design*, 8(10), pp.3745–3749. Available at: <http://www.ncbi.nlm.nih.gov/pubmed/22072993>.
- Bao, Y. et al., 2005. Controlled crystalline structure and surface stability of cobalt nanocrystals. *The journal of physical chemistry. B*, 109(15), pp.7220–2. Available at: <http://www.ncbi.nlm.nih.gov/pubmed/16851825>.
- Bao, Y., 2003. Controlled self-assembly of colloidal cobalt nanocrystals. *Journal of Magnetism and Magnetic Materials*, 266(3), pp.L245–L249. Available at: <http://linkinghub.elsevier.com/retrieve/pii/S0304885303006498> [Accessed August 8, 2011].

- Bao, Y. et al., 2010. The critical role of surfactants in the growth of cobalt nanoparticles. *Langmuir : the ACS journal of surfaces and colloids*, 26(1), pp.478–83. Available at: <http://www.ncbi.nlm.nih.gov/pubmed/19743830> [Accessed August 8, 2011].
- Bao, Y., Calderon, H. & Krishnan, K.M., 2007. Synthesis and Characterization of Magnetic-Optical Co-Au Core-Shell Nanoparticles. *Journal of Physical Chemistry C*, 111(5), pp.1941–1944. Available at: <http://pubs.acs.org/cgi-bin/doilookup/?10.1021/jp066871y>.
- Bao, Y. & Krishnan, K., 2005. Preparation of functionalized and gold-coated cobalt nanocrystals for biomedical applications. *Journal of Magnetism and Magnetic Materials*, 293(1), pp.15–19. Available at: <http://linkinghub.elsevier.com/retrieve/pii/S0304885305001022> [Accessed November 12, 2011].
- Bean, C.P. & Livingston, J.D., 1959. Superparamagnetism. *Journal of Applied Physics*, 30(4), p.S120. Available at: <http://link.aip.org/link/JAPIAU/v30/i4/pS120/s1&Agg=doi> [Accessed March 16, 2012].
- Beecroft, L.L. & Ober, C.K., 1997. Nanocomposite Materials for Optical Applications. *Composites*, 4756(96), pp.1302–1317.
- Berry, C.C. & Curtis, A.S.G., 2003. Functionalisation of magnetic nanoparticles for applications in biomedicine. *Journal of Physics D: Applied Physics*, 36(13), pp.R198–R206. Available at: <http://stacks.iop.org/0022-3727/36/i=13/a=203?key=crossref.2b3f04f8a3947d7f67d60f2cf2c6a7fb>.
- Bhuiyan, M.M.H., Ferdaush, J. & Uddin, M.H., 2007. Densities and viscosities of binary mixtures of {dimethylsulfoxide+aliphatic lower alkanols (C1–C3)} at temperatures from T=303.15K to T=323.15K. *The Journal of Chemical Thermodynamics*, 39(5), pp.675–683. Available at: <http://linkinghub.elsevier.com/retrieve/pii/S0021961406002436> [Accessed January 25, 2014].
- Binnig, G. & Rohrer, H., 1983. Scanning Tunneling Microscopy. *Surface Science*, 126, pp.236–244.
- Borah, G. & Sharma, P., 2011. A novel route to size and shape controlled synthesis of DMSO capped ruthenium dioxide nanoparticles. , 50(January), pp.41–45.
- Bräuer, B. et al., 2006. Deposition of thin films of a transition metal complex by spin coating. *Chemical Physics Letters*, 432(1-3), pp.226–229. Available at: <http://linkinghub.elsevier.com/retrieve/pii/S0009261406015636> [Accessed January 25, 2014].
- Brown, K.R. & Natan, M.J., 1998. Hydroxylamine Seeding of Colloidal Au Nanoparticles in Solution and on Surfaces. *Langmuir*, 14(4), pp.726–728. Available at: <http://pubs.acs.org/doi/abs/10.1021/la970982u>.
- Brust, M. et al., 1994. Synthesis of Thiol-derivatised Gold Nanoparticles in. *Journal of the American Chemical Society Chemical Communications*, pp.801–802.
- Bucher, J.P. & Bloomfield, L.A., 1993. Magnetism of Free Transition Metal and Rare Earth Clusters. *International Journal of Modern Physics B*, 7(4).
- Burness, J.H., Dillard, J.G. & Taylor, L.T., 1975. An X-Ray Photoelectron Spectroscopic Study of Cobalt(II) Schiff Base Complexes and Their Oxygenation Products. *Journal of the American Chemical Society*, 97(21), pp.6080–6088.
- Calvignac, B., Rodier, E., et al., 2009. Development of Characterization Techniques of Thermodynamic and Physical Properties Applied to the CO<sub>2</sub>-DMSO Mixture. *International Journal of Chemical Reactor Engineering*, 7.

- Calvignac, B., Letourneau, J.-J., et al., 2009. Development of Characterization Techniques of Thermodynamic and Physical Properties Applied to the CO<sub>2</sub>-DMSO Mixture. *International Journal of Chemical Reactor Engineering*, 7.
- Cao, G., 2004. *Nanostructures and Nanomaterials - Synthesis, Properties, and Applications* 2nd ed., Covent Garden: World Scientific Publishing Company. Available at: <http://www.worldscibooks.com/nanosci/7885.html>.
- Chen, S. & Liu, W., 2006. Oleic acid capped PbS nanoparticles: Synthesis, characterization and tribological properties. *Materials Chemistry and Physics*, 98(1), pp.183–189. Available at: <http://linkinghub.elsevier.com/retrieve/pii/S0254058405006255> [Accessed October 5, 2012].
- Chen, Z. et al., 2002. Hydrothermal synthesis and optical property of nano-sized CoAl<sub>2</sub>O<sub>4</sub> pigment. *Materials Letters*, 55(August), pp.281–284.
- Cho, Y.W. et al., 2007. In vivo tumor targeting and radionuclide imaging with self-assembled nanoparticles: mechanisms, key factors, and their implications. *Biomaterials*, 28(6), pp.1236–47. Available at: <http://www.ncbi.nlm.nih.gov/pubmed/17126900> [Accessed January 22, 2014].
- Chou, S.-L. et al., 2008. Electrochemical deposition of porous Co<sub>3</sub>O<sub>4</sub> nanostructured thin film for lithium-ion battery. *Journal of Power Sources*, 182(1), pp.359–364. Available at: <http://linkinghub.elsevier.com/retrieve/pii/S037877530800640X> [Accessed December 11, 2013].
- Coffey, K.R., Parker, M. a. & Howard, J.K., 1995. High anisotropy L<sub>1</sub>/sub 0/ thin films for longitudinal recording. *IEEE Transactions on Magnetics*, 31(6), pp.2737–2739. Available at: <http://ieeexplore.ieee.org/lpdocs/epic03/wrapper.htm?arnumber=490108>.
- Cole, A.J., Yang, V.C. & David, A.E., 2011. Cancer theranostics: the rise of targeted magnetic nanoparticles. *Trends in biotechnology*, 29(7), pp.323–32. Available at: <http://www.pubmedcentral.nih.gov/articlerender.fcgi?artid=3210200&tool=pmcentrez&rendertype=abstract> [Accessed January 23, 2014].
- Cormode, D.P. et al., 2010. Nanotechnology in medical imaging: probe design and applications. *Arterioscler Thromb Vasc Biol*, 29(7), pp.992–1000.
- Corot, C. et al., 2006. Recent advances in iron oxide nanocrystal technology for medical imaging. *Advanced drug delivery reviews*, 58(14), pp.1471–504. Available at: <http://www.ncbi.nlm.nih.gov/pubmed/17116343> [Accessed December 19, 2013].
- Crespo, P. et al., 2004. Permanent Magnetism, Magnetic Anisotropy, and Hysteresis of Thiol-Capped Gold Nanoparticles. *Physical Review Letters*, 93(8), pp.4–7. Available at: <http://link.aps.org/doi/10.1103/PhysRevLett.93.087204> [Accessed July 13, 2012].
- Cushing, B.L., Kolesnichenko, V.L. & O'Connor, C.J., 2004. Recent advances in the liquid-phase syntheses of inorganic nanoparticles. *Chemical Reviews*, 104(9), pp.3893–3946. Available at: <http://dx.doi.org/10.1021/cr030027b>.
- Daniel-da-silva, A.L. & Trindade, T., 2011. Biofunctional Composites of Polysaccharides Containing Inorganic Nanoparticles. In *Nanotechnology and Nanomaterials*.
- Dave, S. & Gao, X., 2009. Monodisperse magnetic nanoparticles for biodetection, imaging, and drug delivery: a versatile and evolving technology. *Nanomedicine and Nanobiotechnology*, 1(6).

- Day, E.S. et al., 2010. Antibody-conjugated gold-gold sulfide nanoparticles as multifunctional agents for imaging and therapy of breast cancer. *International journal of nanomedicine*, 5, pp.445–54. Available at: <http://www.pubmedcentral.nih.gov/articlerender.fcgi?artid=2950402&tool=pmcentrez&rendertype=abstract>.
- Della, J. & Lin, W., 2010. Nanoscale Metal – Organic Frameworks : Magnetic Resonance Imaging Contrast Agents and Beyond. , pp.3725–3734.
- Demazeau, G., 1999. Solvothermal processes: a route to the stabilization of new materials. *J. Mater. Chem*, 9(8), p.15.
- Demazeau, G., 2007. Solvothermal reactions: an original route for the synthesis of novel materials. *Journal of Materials Science*, 43(7), pp.2104–2114. Available at: <http://www.springerlink.com/index/10.1007/s10853-007-2024-9> [Accessed June 1, 2011].
- Demianets, L.N., 1999. No Title. *Prog Cryst Growth Charact Mater*, 21, p.299.
- deSilva, R.M. et al., 2007. Investigation of the Influence of Organometallic Precursors on the Formation of Cobalt Nanoparticles. *Journal of Physical Chemistry C*, 111(28), pp.10320–10328. Available at: <http://pubs.acs.org/cgi-bin/doilookup/?10.1021/jp070499k>.
- Dinega, D.P. & Bawendi, M.G., 1999. A Solution-Phase Chemical Approach to a New Crystal Structure of Cobalt \*\*. *Communications*, (12), pp.1788–1791.
- Drexler, E.K., 1986. *The Coming Era of Nanotechnology*, Anchor Press/Doubleday.
- Duan, H. et al., 2008. Reexamining the Effects of Particle Size and Surface Chemistry on the Magnetic Properties of Iron Oxide Nanocrystals: New Insights into Spin Disorder and Proton Relaxivity. *Journal of Physical Chemistry C*, 112(22), pp.8127–8131. Available at: <http://pubs.acs.org/cgi-bin/doilookup/?10.1021/jp8029083>.
- Dutta, P. et al., 2007. Magnetism in dodecanethiol-capped gold nanoparticles: Role of size and capping agent. *Applied Physics Letters*, 90(21), p.213102. Available at: <http://link.aip.org/link/APPLAB/v90/i21/p213102/s1&Agg=doi> [Accessed November 8, 2010].
- Eigler, D.M. & Schweizer, E.K., 1990. Positioning single atoms with a scanning tunnelling microscope. *Nature*, 344, pp.524–526.
- El-Brolosy, T.A. et al., 2008. Shape and size dependence of the surface plasmon resonance of gold nanoparticles studied by Photoacoustic technique. *The European Physical Journal, Special Topics*, 153, pp.361–364.
- Elvassore, N. et al., 2002. On-Line Monitoring of Volume Expansion in Gas-Antisolvent Processes by UV-Vis Spectroscopy. *Journal of Chemical Engineering Data*, pp.223–227.
- Emori, S. et al., 2013. Current-driven dynamics of chiral ferromagnetic domain walls. *Nature materials*, 12(7), pp.611–6. Available at: <http://www.ncbi.nlm.nih.gov/pubmed/23770726> [Accessed January 23, 2014].
- Erdemir, D., Lee, A.Y. & Myerson, A.S., 2009. Nucleation of crystals from solution: classical and two-step models. *Accounts of chemical research*, 42(5), pp.621–9. Available at: <http://www.ncbi.nlm.nih.gov/pubmed/19402623>.



- Eustis, S. & el-Sayed, M. a, 2006. Why gold nanoparticles are more precious than pretty gold: noble metal surface plasmon resonance and its enhancement of the radiative and nonradiative properties of nanocrystals of different shapes. *Chemical Society reviews*, 35(3), pp.209–17. Available at: <http://www.ncbi.nlm.nih.gov/pubmed/16505915>.
- Farhadi, S., Safabakhsh, J. & Zaringhadam, P., 2013. Synthesis, characterization, and investigation of optical and magnetic properties of cobalt oxide (Co<sub>3</sub>O<sub>4</sub>) nanoparticles. *Journal of Nanostructure in Chemistry*, 3(1), p.69. Available at: <http://www.jnanochem.com/content/3/1/69>.
- Farokhzad, O.C. et al., 2006. Targeted nanoparticle-aptamer bioconjugates for cancer chemotherapy in vivo. *Proceedings of the National Academy of Sciences of the United States of America*, 103(16), pp.6315–20. Available at: <http://www.pubmedcentral.nih.gov/articlerender.fcgi?artid=1458875&tool=pmcentrez&rendertype=abstract>.
- Fendler, J.H., 1996. Self-Assembled Nanostructured Materials. *Chemistry of Materials*, 8(8), pp.1616–1624. Available at: <http://pubs.acs.org/doi/abs/10.1021/cm960116n>.
- Feng, S. & Li, G., 2011. Hydrothermal and Solvothermal Synthesis. In *Modern Inorganic Synthetic Chemistry*. Elsevier B.V., pp. 63–95. Available at: <http://wenku.baidu.com/view/e628ce2558fb770bf78a5562.html>.
- Feng, S. & Xu, R., 2001. New Materials in Hydrothermal Synthesis. *Acc Chem Res*, 34, p.239.
- Feng, W. et al., 2010. Synthesis and assembly of rare earth nanostructures directed by the principle of coordination chemistry in solution-based process. *Coordination Chemistry Reviews*, 254(9-10), pp.1038–1053. Available at: <http://linkinghub.elsevier.com/retrieve/pii/S001085451000038X> [Accessed February 7, 2012].
- Feynman, R., 1959. There's Plenty of Room at the Bottom. Available at: <http://www.zyvex.com/nanotech/feynman.html>.
- Finke, R.G., 2002. Transition Metal Nanoclusters. In D. L. Feldheim & C. A. Foss, eds. *Metal Nanoparticles: Synthesis, Characterization, and Applications*. New York: Marcel Dekker Inc., p. 17.
- Fischer, C.H. et al., 1989. Photochemistry of colloidal semiconductors. 30. HPLC investigation of small CdS particles. *Langmuir*, 5(2), pp.429–432. Available at: <http://pubs.acs.org/doi/abs/10.1021/la00086a024>.
- Folen, V.J. & Rado, G.T., 1958. Magnetocrystalline Anisotropy of Mg[Single Bond]Fe Ferrites: Temperature Dependence, Ionic Distribution Effects, and the Crystalline Field Model. *Journal of Applied Physics*, 29(3), p.438. Available at: <http://link.aip.org/link/JAPIAU/v29/i3/p438/s1&Agg=doi> [Accessed December 28, 2013].
- Frey, N.A. et al., 2009. Magnetic nanoparticles : synthesis , functionalization , and applications in bioimaging and magnetic energy storage. *Chemical Society Reviews*, 38, pp.2532–2542.
- Gambardella, P. et al., 2003. Giant magnetic anisotropy of single cobalt atoms and nanoparticles. *Science (New York, N.Y.)*, 300(5622), pp.1130–3. Available at: <http://www.ncbi.nlm.nih.gov/pubmed/12750516> [Accessed January 23, 2014].

- Gellissen, J. et al., 1999. Extra- and Intracellular Accumulation of Ultrasmall Superparamagnetic Iron Oxides (USPIO) in Experimentally Induced Abscesses of the Peripheral Soft Tissues and Their Effects on Magnetic Resonance Imaging. *Magnetic Resonance Imaging*, 17(4), pp.557–567.
- Ghosh, M. & Rao, C.N.R., 2004. Solvothermal synthesis of CdO and CuO nanocrystals. *Chemical Physics Letters*, 393(4-6), pp.493–497. Available at: <http://linkinghub.elsevier.com/retrieve/pii/S0009261404009248> [Accessed February 3, 2012].
- Ghosh, M., Sampathkumaran, E. V. & Rao, C.N.R., 2005. Synthesis and magnetic properties of CoO Nanoparticles. *Chem. Mater*, 17, pp.2348–2352. Available at: <http://www.ncbi.nlm.nih.gov/pubmed/21042615>.
- Glaspell, G.P. et al., 2004. Formation of Cobalt Nitrate Hydrate , Cobalt Oxide , and Cobalt Nanoparticles Using Laser Vaporization Controlled Condensation. , pp.3–6.
- Gogotsi, Y.G. & Yoshimura, M., 1994. No Title. *Nature*, 367, p.628.
- Goodsell, D., 2004. *Bionanotechnology*, New Jersey.
- Goranson, R.W., 1931. The solubility of water in granite magmas. *Am. J. Sci*, 22, p.481.
- Gray, T., Mann, N. & Whitby, M., 2013. Magnetic Type of the Elements. *Periodictable.com*. Available at: <http://periodictable.com/Properties/A/MagneticType.html> [Accessed January 18, 2014].
- Grieve, K., Mulvaney, P. & Grieser, F., 2000. Synthesis and electronic properties of semiconductor nanoparticles / quantum dots. *Current Opinion in Colloid & Interface Science*, 5, pp.168–172.
- Gubin, S.P. et al., 2005. Magnetic nanoparticles: preparation, structure and properties. *Russian Chemical Reviews*, 74(6), pp.489–520. Available at: <http://stacks.iop.org/0036-021X/74/i=6/a=R01?key=crossref.66a82224559f883728276b048a74f068> [Accessed December 15, 2013].
- Gubin, S.P. et al., 2002. Nanomaterial for High-Density Magnetic Data Storage. *Russian Journal of Inorganic Chemistry*, 47(1), pp.32–67.
- Guin, D. et al., 2006. One-pot size and shape controlled synthesis of DMSO capped iron oxide nanoparticles. *Bulletin of Materials Science*, 29(6), pp.617–621. Available at: <http://www.springerlink.com/index/10.1007/s12034-006-0013-2>.
- Habashi, F., 2005. A short history of hydrometallurgy. *Hydrometallurgy*, 79, pp.15–22.
- Hamaker, H.C., 1937. The London-van der Waals Attraction Between Spherical Particles. *Physica*, 4, pp.1058–1072.
- Hanauer, M. et al., 2007. Separation of nanoparticles by gel electrophoresis according to size and shape. *Nano letters*, 7(9), pp.2881–5. Available at: <http://www.ncbi.nlm.nih.gov/pubmed/17718532>.
- Hao, R. et al., 2010. Synthesis, functionalization, and biomedical applications of multifunctional magnetic nanoparticles. *Advanced materials (Deerfield Beach, Fla.)*, 22(25), pp.2729–42. Available at: <http://www.ncbi.nlm.nih.gov/pubmed/20473985> [Accessed January 27, 2014].

- Harris, T.J. et al., 2006. Proteolytic actuation of nanoparticle self-assembly. *Angewandte Chemie (International ed. in English)*, 45(19), pp.3161–5. Available at: <http://www.ncbi.nlm.nih.gov/pubmed/16642514> [Accessed January 22, 2014].
- Harris, V.G. et al., 2010. High coercivity cobalt carbide nanoparticles processed via polyol reaction: a new permanent magnet material. *Journal of Physics D: Applied Physics*, 43(16), p.165003. Available at: <http://stacks.iop.org/0022-3727/43/i=16/a=165003?key=crossref.d05894d43cc878735cbcd9626b220a46> [Accessed January 23, 2014].
- He, F. et al., 2007. Stabilization of Fe–Pd Nanoparticles with Sodium Carboxymethyl Cellulose for Enhanced Transport and Dechlorination of Trichloroethylene in Soil and Groundwater. *Industrial & Engineering Chemistry Research*, 46(1), pp.29–34. Available at: <http://pubs.acs.org/doi/abs/10.1021/ie0610896>.
- Heide, P. van der, 2012. *X-ray Photoelectron Spectroscopy: An Introduction to Principles and Practices* 1st ed., New Jersey: John Wiley & Sons Ltd.
- Heldebrant, D.J. et al., 2006. Liquid Polymers as Solvents for Catalytic Reductions. *Green Chemistry*, 8, p.807.
- Henglein, A., 1999. Radiolytic Preparation of Ultrafine Colloidal Gold Particles in Aqueous Solution: Optical Spectrum, Controlled Growth, and Some Chemical Reactions. *Langmuir*, 15(20), pp.6738–6744. Available at: <http://pubs.acs.org/doi/abs/10.1021/la9901579>.
- Hiemenz, P.C., 1997. *Principles of Colloid and Surface Chemistry* 3rd ed., United States: Wiley.
- Hirsch, L.R. et al., 2006. Metal nanoshells. *Annals of biomedical engineering*, 34(1), pp.15–22. Available at: <http://www.ncbi.nlm.nih.gov/pubmed/16528617> [Accessed January 21, 2014].
- Hong, R. et al., 2006. Synthesis and surface modification of ZnO nanoparticles. *Chemical Engineering Journal*, 119(2-3), pp.71–81. Available at: <http://linkinghub.elsevier.com/retrieve/pii/S1385894706000969> [Accessed July 13, 2012].
- Horrocks Jr., W.D. & Cotton, F.A., 1961. Infrared and Raman spectra and normal co-ordinate analysis of dimethyl sulfoxide and dimethyl sulfoxide-d<sub>6</sub>. *Spectrochimica Acta*, 17, pp.134 – 147.
- Hosaka, M., 1991. No Title. *Prog Cryst Growth Charact Mater*, 21, p.71.
- Hu, J. et al., 1999. A hydrothermal reaction to synthesize CuFeS<sub>2</sub> nanorods. , 2, pp.569–571.
- Hu, Z., Oskam, G. & Searson, P.C., 2003. Influence of solvent on the growth of ZnO nanoparticles. *Journal of Colloid and Interface Science*, 263(2), pp.454–460. Available at: <http://linkinghub.elsevier.com/retrieve/pii/S0021979703002054> [Accessed July 11, 2011].
- Huang, X. et al., 2006. Cancer cell imaging and photothermal therapy in the near-infrared region by using gold nanorods. *Journal of the American Chemical Society*, 128(6), pp.2115–20. Available at: <http://www.ncbi.nlm.nih.gov/pubmed/16464114>.
- Huang, X. et al., 2007. Gold nanoparticles: interesting optical properties and recent applications in cancer diagnostics and therapy. *Nanomedicine (London, England)*, 2(5), pp.681–93. Available at: <http://www.ncbi.nlm.nih.gov/pubmed/17976030>.

- Huang, X. et al., 2008. Plasmonic photothermal therapy (PPTT) using gold nanoparticles. *Lasers in medical science*, 23(3), pp.217–28. Available at: <http://www.ncbi.nlm.nih.gov/pubmed/17674122> [Accessed March 9, 2012].
- Huang, X. & El-Sayed, M.A., 2010. Gold nanoparticles: Optical properties and implementations in cancer diagnosis and photothermal therapy. *Journal of Advanced Research*, 1(1), pp.13–28. Available at: <http://linkinghub.elsevier.com/retrieve/pii/S2090123210000056> [Accessed January 13, 2014].
- Hubert, A. & Schafer, R., 2000. *Magnetic Domains*, New York: Springer Berlin Heidelberg.
- Huff, T.B. et al., 2007. Hyperthermic effects of gold nanorods on tumor cells. *Nanomedicine (London, England)*, 2(1), pp.125–32. Available at: <http://www.pubmedcentral.nih.gov/articlerender.fcgi?artid=2597406&tool=pmcentrez&rendertype=abstract>.
- Hutter, E. & Fendler, J.H., 2004. Exploitation of Localized Surface Plasmon Resonance. *Advanced Materials*, 16(19), pp.1685–1706. Available at: <http://doi.wiley.com/10.1002/adma.200400271> [Accessed January 9, 2014].
- Hyeon, T., 2003. Chemical synthesis of magnetic nanoparticles. *Chemical communications (Cambridge, England)*, (8), pp.927–34. Available at: <http://www.ncbi.nlm.nih.gov/pubmed/12744306>.
- Iijima, S., 1991. Helical microtubules of graphitic carbon. , 354, pp.56–58.
- Ingram, D.R. et al., 2010. Superparamagnetic nanoclusters coated with oleic acid bilayers for stabilization of emulsions of water and oil at low concentration. *Journal of Colloid and Interface Science*, 351(1), pp.225–232. Available at: <http://linkinghub.elsevier.com/retrieve/pii/S0021979710007071> [Accessed May 8, 2012].
- Isojima, T. et al., 2008. Reversible Clustering of pH- and Temperature-Responsive Janus Nanoparticles. *ACS Nano*, 2(9), pp.1799–1806.
- Jain, P.K. et al., 2006. Calculated absorption and scattering properties of gold nanoparticles of different size, shape, and composition: applications in biological imaging and biomedicine. *The journal of physical chemistry. B*, 110(14), pp.7238–48. Available at: <http://www.ncbi.nlm.nih.gov/pubmed/16599493>.
- Jakubovics, J.P., 1987. *Magnetism and Magnetic Materials*, Oxford: The Institute of Metals.
- Jana, N.R., Gearheart, L. & Murphy, C.J., 2001a. Evidence for Seed-Mediated Nucleation in the Chemical Reduction of Gold Salts to Gold Nanoparticles. *Chemistry of Materials*, 13(7), pp.2313–2322. Available at: <http://pubs.acs.org/doi/abs/10.1021/cm000662n>.
- Jana, N.R., Gearheart, L. & Murphy, C.J., 2001b. Seeding Growth for Size Control of 5–40 nm Diameter Gold Nanoparticles. *Langmuir*, 17(22), pp.6782–6786. Available at: <http://pubs.acs.org/doi/abs/10.1021/la0104323>.
- Jana, N.R., Gearheart, L. & Murphy, C.J., 2001. Seed-Mediated Growth Approach for Shape-Controlled Synthesis of Spheroidal and Rod-like Gold Nanoparticles Using a Surfactant Template. *Advanced Materials*, 13(18), pp.1389–1393. Available at: [http://doi.wiley.com/10.1002/1521-4095\(200109\)13:18<1389::AID-ADMA1389>3.0.CO;2-F](http://doi.wiley.com/10.1002/1521-4095(200109)13:18<1389::AID-ADMA1389>3.0.CO;2-F).

- Jessop, P.G. & Subramaniam, B., 2007. Gas-expanded liquids. *Chemical reviews*, 107(6), pp.2666–94. Available at: <http://www.ncbi.nlm.nih.gov/pubmed/17564482>.
- Ji, X. et al., 2007. Size control of gold nanocrystals in citrate reduction: the third role of citrate. *Journal of the American Chemical Society*, 129(45), pp.13939–48. Available at: <http://www.ncbi.nlm.nih.gov/pubmed/17948996>.
- Jimenez, V.L. et al., 2003. HPLC of Monolayer-Protected Gold Nanoclusters monolayers of hexanethiolate ligands ( C6 MPCs ) and with. *Science*, 75(2), pp.199–206.
- Johans, C. et al., 2008. Control of particle size by pressure adjustment in cobalt nanoparticle synthesis. *Colloids and Surfaces A: Physicochemical and Engineering Aspects*, 330(1), pp.14–20. Available at: <http://linkinghub.elsevier.com/retrieve/pii/S0927775708004640> [Accessed January 10, 2014].
- Johnston, K.P. et al., 2012. Concentrated dispersions of equilibrium protein nanoclusters that reversibly dissociate into active monomers. *ACS nano*, 6(2), pp.1357–69. Available at: <http://www.ncbi.nlm.nih.gov/pubmed/22260218>.
- Jordan, a, 1999. Magnetic fluid hyperthermia (MFH): Cancer treatment with AC magnetic field induced excitation of biocompatible superparamagnetic nanoparticles. *Journal of Magnetism and Magnetic Materials*, 201(1-3), pp.413–419. Available at: <http://linkinghub.elsevier.com/retrieve/pii/S0304885399000888>.
- Kelly, K.L. et al., 2003. The Optical Properties of Metal Nanoparticles: The Influence of Size, Shape, and Dielectric Environment. *J*, 107, pp.668–677.
- Kim, D. et al., 2007. Antibiofouling polymer-coated gold nanoparticles as a contrast agent for in vivo X-ray computed tomography imaging. *Journal of the American Chemical Society*, 129(24), pp.7661–5. Available at: <http://www.ncbi.nlm.nih.gov/pubmed/17530850>.
- King, S., Hyunh, K. & Tannenbaum, R., 2003. Kinetics of Nucleation, Growth, and Stabilization of Cobalt Oxide Nanoclusters. *The Journal of Physical Chemistry B*, 107(44), pp.12097–12104. Available at: <http://pubs.acs.org/doi/abs/10.1021/jp0355004>.
- Kita, E., 2013. Epitaxial thin film growth and control of magnetism in cobalt and iron spinel ferrite. In *3rd International Symposium on Advanced Magnetic Materials and Application*. Taiwan.
- Kitchens, C.L., Mcleod, M.C. & Roberts, C.B., 2003. Solvent Effects on the Growth and Steric Stabilization of Copper Metallic Nanoparticles in AOT Reverse Micelle Systems. *J. Phys. Chem. B.*, 107, pp.11331–11338.
- Kobayashi, Y. et al., 2003. Preparation and Properties of Silica-Coated Cobalt Nanoparticles †. *The Journal of Physical Chemistry B*, 107(30), pp.7420–7425. Available at: <http://pubs.acs.org/doi/abs/10.1021/jp027759c>.
- Koey, J., 2010. *Magnetism and Magnetic Materials*, Cambridge.
- Komarneni, S., Li, D. & Newalkar, B., 2002. Microwave-Polyol Process for Pt and Ag Nanoparticles. *Notes*, (30), pp.5959–5962.
- Kordikowski, a. et al., 1995. Volume expansions and vapor-liquid equilibria of binary mixtures of a variety of polar solvents and certain near-critical solvents. *The Journal of Supercritical Fluids*, 8(3), pp.205–216. Available at: <http://linkinghub.elsevier.com/retrieve/pii/0896844695900330>.

- Kroto, H.W. et al., 1985. C60: Buckminsterfullerene. *Nature*, 318, pp.162–163.
- LaMer, V.K. & Dinegar, R.H., 1950. Theory, Production, and Mechanism of Formation of Monodispersed Hydrosols. *Journal of the American Chemical Society*, 72(11), pp.4847–4854.
- Langer, R. & Tirrell, D. a, 2004. Designing materials for biology and medicine. *Nature*, 428(6982), pp.487–92. Available at: <http://www.ncbi.nlm.nih.gov/pubmed/15057821>.
- Larsen, E.K.U. et al., 2009. Size-Dependent Accumulation of PEGylated Silane-Coated Magnetic Iron Oxide Nanoparticles in Murine Tumors. *ACS nano*, 3(7), pp.1947–51. Available at: <http://www.ncbi.nlm.nih.gov/pubmed/19572620>.
- Lee, G.H. et al., 2002. Excellent magnetic properties of fullerene encapsulated ferromagnetic nanoclusters. *Journal of Magnetism and Magnetic Materials*, 246(3), pp.404–411. Available at: <http://linkinghub.elsevier.com/retrieve/pii/S0304885302001130>.
- Lee, W.-R. et al., 2005. Redox-transmetalation process as a generalized synthetic strategy for core-shell magnetic nanoparticles. *Journal of the American Chemical Society*, 127(46), pp.16090–7. Available at: <http://www.ncbi.nlm.nih.gov/pubmed/16287295>.
- Li, B. et al., 2011. Superparamagnetic Fe<sub>3</sub>O<sub>4</sub> nanocrystals@graphene composites for energy storage devices. *Journal of Materials Chemistry*, 21(13), p.5069. Available at: <http://xlink.rsc.org/?DOI=c0jm03717f> [Accessed December 29, 2013].
- Li, C. et al., 2013. Exciton-plasmon coupling mediated photorefractivity in gold-nanoparticle- and quantum-dot-dispersed polymers. *Applied Physics Letters*, 102(25), p.251115. Available at: <http://link.aip.org/link/APPLAB/v102/i25/p251115/s1&Agg=doi> [Accessed January 10, 2014].
- Li, Y., Afzaal, M. & O'Brien, P., 2006. The synthesis of amine-capped magnetic (Fe, Mn, Co, Ni) oxide nanocrystals and their surface modification for aqueous dispersibility. *Journal of Materials Chemistry*, 16(22), p.2175. Available at: <http://xlink.rsc.org/?DOI=b517351e> [Accessed October 5, 2012].
- Lifshitz, I.M. & Slyozov, V. V., 1961. The kinetics of precipitation from supersaturated solid solutions. *J. Phys. Chem. Solids*, 19(1-2).
- Lin, S. et al., 2005. One-Dimensional Plasmon Coupling by Facile Self-Assembly of Gold Nanoparticles into Branched Chain Networks. *Advanced Materials*, 17(21), pp.2553–2559. Available at: <http://doi.wiley.com/10.1002/adma.200500828> [Accessed November 28, 2013].
- Lin, X. & Samia, a, 2006. Synthesis, assembly and physical properties of magnetic nanoparticles☆. *Journal of Magnetism and Magnetic Materials*, 305(1), pp.100–109. Available at: <http://linkinghub.elsevier.com/retrieve/pii/S0304885305011583> [Accessed July 12, 2011].
- Link, S. & El-Sayed, M. a., 1999. Size and Temperature Dependence of the Plasmon Absorption of Colloidal Gold Nanoparticles. *The Journal of Physical Chemistry B*, 103(21), pp.4212–4217. Available at: <http://pubs.acs.org/doi/abs/10.1021/jp984796o>.
- Liu, J. et al., 2010. More Benign Synthesis of Palladium Nanoparticles in Dimethyl Sulfoxide and Their Extraction into an Organic Phase. *Ind. Eng. Chem. Res.*, pp.8174–8179.
- Liu, J. et al., 2008. Polysugar-stabilized Pd nanoparticles exhibiting high catalytic activities for hydrodechlorination of environmentally deleterious trichloroethylene. *Langmuir : the ACS journal of*

*surfaces and colloids*, 24(1), pp.328–36. Available at:  
<http://www.ncbi.nlm.nih.gov/pubmed/18044944>.

- Liu, J. et al., 2009. Precise seed-mediated growth and size-controlled synthesis of palladium nanoparticles using a green chemistry approach. *Langmuir : the ACS journal of surfaces and colloids*, 25(12), pp.7116–28. Available at: <http://www.ncbi.nlm.nih.gov/pubmed/19309120> [Accessed July 18, 2010].
- Liu, J., Anand, M. & Roberts, C.B., 2006. Synthesis and extraction of beta-D-glucose-stabilized Au nanoparticles processed into low-defect, wide-area thin films and ordered arrays using CO<sub>2</sub>-expanded liquids. *Langmuir*, 22(9), pp.3964–3971. Available at: <Go to ISI>://000236989300005.
- Liu, J., Sutton, J. & Roberts, C.B., 2007. Synthesis and Extraction of Monodisperse Sodium Carboxymethylcellulose-Stabilized Platinum Nanoparticles for the Self-assembly of Ordered Arrays. *Journal of Physical Chemistry C*, 111(31), pp.11566–11576. Available at: <http://pubs.acs.org/cgi-bin/doilookup/?10.1021/jp071967t>.
- Liu, J.C. et al., 2006. Facile “Green” Synthesis, Characterization, and Catalytic Function of b-d-Glucose-Stabilized Au Nanocrystals. *Chem. Eur. J.*, 12(8), p.2131. Available at: <http://www.ncbi.nlm.nih.gov/pubmed/16358347> [Accessed February 3, 2012].
- Liu, J.C. et al., 2006. No Title. *Chem. Eur. J.*, 12, p.2131.
- Liu, Y., 2006. Hydro/Solvothermal Route to Growth of Nanocrystals. In G. V. Karas, ed. *New Topics in Crystal Growth Research*. New York: Nova Science Publishers, Inc.
- Liu, Z.P. et al., 2003. Synthesis of copper nanowires via a complex-surfactant-assisted hydrothermal reduction process. *Journal of Physical Chemistry B*, 107, pp.12658–661.
- Lu, A.-H., Salabas, E.L. & Schüth, F., 2007. Magnetic nanoparticles: synthesis, protection, functionalization, and application. *Angewandte Chemie (International ed. in English)*, 46(8), pp.1222–44. Available at: <http://www.ncbi.nlm.nih.gov/pubmed/17278160>.
- Ma, L.L. et al., 2009. Small Multifunctional Nanoclusters (Nanoroses) for Targeted Cellular Imaging and Therapy. *ACS Nano*, 3(9), p.2686.
- Mattoussi, H. et al., 1998. Electroluminescence from heterostructures of poly(phenylene vinylene) and inorganic CdSe nanocrystals. *Journal of Applied Physics*, 83(12), p.7965. Available at: <http://link.aip.org/link/JAPIAU/v83/i12/p7965/s1&Agg=doi> [Accessed December 2, 2013].
- McConnell, W.P. et al., 2000. Electronic and Optical Properties of Chemically Modified Metal Nanoparticles and. *Society*, pp.8925–8930.
- McLeod, M.C., Anand, M., et al., 2005. Precise and rapid size selection and targeted deposition of nanoparticle populations using CO<sub>2</sub> gas expanded liquids. *Nano letters*, 5(3), pp.461–5. Available at: <http://www.ncbi.nlm.nih.gov/pubmed/15755095>.
- McLeod, M.C. et al., 2003. Synthesis and Stabilization of Silver Metallic Nanoparticles and Premetallic Intermediates in Perfluoropolyether / CO<sub>2</sub> Reverse Micelle Systems. *Society*, pp.2693–2700.
- McLeod, M.C., Kitchens, C.L. & Roberts, C.B., 2005. CO<sub>2</sub>-expanded liquid deposition of ligand-stabilized nanoparticles as uniform, wide-area nanoparticle films. *Langmuir : the ACS journal of surfaces and colloids*, 21(6), pp.2414–8. Available at: <http://www.ncbi.nlm.nih.gov/pubmed/15752033>.

- Michalet, X. et al., 2005. Quantum dots for live cells, in vivo imaging, and diagnostics. *Science (New York, N.Y.)*, 307(5709), pp.538–44. Available at: <http://www.pubmedcentral.nih.gov/articlerender.fcgi?artid=1201471&tool=pmcentrez&rendertype=abstract> [Accessed July 31, 2010].
- Moore, G.E., 1965. Cramming more components onto integrated circuits. *Electronics*, 38(8).
- Mornet, S. et al., 2004. Magnetic nanoparticle design for medical diagnosis and therapy. *Journal of Materials Chemistry*, 14(14), p.2161. Available at: <http://xlink.rsc.org/?DOI=b402025a>.
- Muir, M., 2005. DMSO : Many Uses , Much Controversy. , pp.1–9. Available at: <http://www.dmsolab.org/articles/information/muir.htm>.
- Mukhopadhyay, M., 2003. Partial molar volume reduction of solvent for solute crystallization using carbon dioxide as antisolvent. , 25.
- Mulvaney, P., 1996. Surface Plasmon Spectroscopy of Nanosized Metal Particles. *Langmuir*, 12(3), pp.788–800. Available at: <http://pubs.acs.org/doi/abs/10.1021/la9502711>.
- Murphy, C.J. et al., 2005. Anisotropic metal nanoparticles: Synthesis, assembly, and optical applications. *The Journal of Physical Chemistry B*, 109(29), pp.13857–70. Available at: <http://www.ncbi.nlm.nih.gov/pubmed/16852739>.
- Murphy, C.J., Gole, A.M., Hunyadi, S.E., et al., 2008. Chemical sensing and imaging with metallic nanorods. *Chemical communications (Cambridge, England)*, (5), pp.544–57. Available at: <http://www.ncbi.nlm.nih.gov/pubmed/18209787> [Accessed April 22, 2011].
- Murphy, C.J., Gole, A.M., Stone, J.W., et al., 2008. Gold nanoparticles in biology: beyond toxicity to cellular imaging. *Accounts of chemical research*, 41(12), pp.1721–30. Available at: <http://www.ncbi.nlm.nih.gov/pubmed/18712884>.
- Murray, C.B., Kagan, C.R. & Bawendi, M.G., 2000. Synthesis and Characterization of Monodisperse Nanocrystals and Close-Packed Nanocrystal Assemblies. *Annual Review of Materials Science*, 30, pp.545–610.
- Murray, C.B., Norris, D.J. & Bawendi, M.G., 1993. Synthesis and Characterization of Nearly Monodisperse CdE (E = S, Se, Te) Semiconductor Nanocrystallites. *Journal of the American Chemical Society*, 115, pp.8706–8715.
- Na, H. Bin, Song, I.C. & Hyeon, T., 2009. Inorganic Nanoparticles for MRI Contrast Agents. *Advanced Materials*, 21(21), pp.2133–2148. Available at: <http://doi.wiley.com/10.1002/adma.200802366> [Accessed January 22, 2014].
- Nadagouda, M.N. & Varma, R.S., 2007. Synthesis of thermally stable carboxymethyl cellulose/metal biodegradable nanocomposites for potential biological applications. *Biomacromolecules*, 8(9), pp.2762–7. Available at: <http://www.ncbi.nlm.nih.gov/pubmed/17665946>.
- Nakamoto, K., 1997. *Infrared and Raman Spectra of Inorganic and Coordination Compounds Part A*. 5th ed., New York: John Wiley & Sons Ltd.
- Nakamoto, K., 2009. *Infrared and Raman Spectra of Inorganic and Coordination Compounds: Part B* 6th ed., New Jersey: John Wiley & Sons Ltd.



- Narayanan, R. & El-Sayed, M. a, 2005. Catalysis with transition metal nanoparticles in colloidal solution: nanoparticle shape dependence and stability. *The journal of physical chemistry. B*, 109(26), pp.12663–76. Available at: <http://www.ncbi.nlm.nih.gov/pubmed/16852568>.
- Niu, H.L. et al., 2004. Hydrothermal formation of magnetic Ni–Cu alloy nanocrystallites at low temperatures. *Nanotechnology*, 15(8), pp.1054–1058. Available at: <http://stacks.iop.org/0957-4484/15/i=8/a=034?key=crossref.0227ff0e9037e0056e66381fec75b31e> [Accessed December 16, 2011].
- Oskam, G., 2006. Metal oxide nanoparticles: synthesis, characterization and application. *Journal of Sol-Gel Science and Technology*, 37(3), pp.161–164. Available at: <http://www.springerlink.com/index/10.1007/s10971-005-6621-2> [Accessed August 4, 2011].
- Pankhurst, Q. a, 2003. Applications of magnetic nanoparticles in biomedicine. *Journal of Physics D: Applied Physics*, 20(13), pp.816–R181.
- Panyam, J., 2003. Biodegradable nanoparticles for drug and gene delivery to cells and tissue. *Advanced Drug Delivery Reviews*, 55(3), pp.329–347. Available at: <http://linkinghub.elsevier.com/retrieve/pii/S0169409X02002284>.
- Park, J. et al., 2005. One-Nanometer-Scale Size-Controlled Synthesis of Monodisperse Magnetic Iron Oxide Nanoparticles. *Angewandte Chemie*, 117(19), pp.2932–2937. Available at: <http://doi.wiley.com/10.1002/ange.200461665> [Accessed July 28, 2011].
- Park, J.-I. et al., 2002. Superlattice and magnetism directed by the size and shape of nanocrystals. *Chemphyschem : a European journal of chemical physics and physical chemistry*, 3(6), pp.543–7. Available at: <http://www.ncbi.nlm.nih.gov/pubmed/12465496>.
- Perezjuste, J. et al., 2005. Gold nanorods: Synthesis, characterization and applications. *Coordination Chemistry Reviews*, 249(17-18), pp.1870–1901. Available at: <http://linkinghub.elsevier.com/retrieve/pii/S0010854505000287> [Accessed January 9, 2014].
- Pérez-Mayoral, E. et al., 2008. Chemistry of paramagnetic and diamagnetic contrast agents for Magnetic Resonance Imaging and Spectroscopy pH responsive contrast agents. *European journal of radiology*, 67(3), pp.453–8. Available at: <http://www.ncbi.nlm.nih.gov/pubmed/18455343> [Accessed January 22, 2014].
- Petit, C., Wang, Z.L. & Pileni, M.P., 2005. Seven-nanometer hexagonal close packed cobalt nanocrystals for high-temperature magnetic applications through a novel annealing process. *The journal of physical chemistry. B*, 109(32), pp.15309–16. Available at: <http://www.ncbi.nlm.nih.gov/pubmed/16852940>.
- Polshettiwar, V., Nadagouda, M.N. & Varma, R.S., 2009. Microwave-Assisted Chemistry: a Rapid and Sustainable Route to Synthesis of Organics and Nanomaterials. *Australian Journal of Chemistry*, 62(1), p.16. Available at: <http://www.publish.csiro.au/?paper=CH08404>.
- Poole, C. & Owens, F., 2003. *Introduction to Nanotechnology*, New Jersey: Wiley.
- Puntes, V.F. et al., 2002. Synthesis of hcp-Co Nanodisks. *Journal of the American Chemical Society*, 124(43), pp.12874–80. Available at: <http://www.ncbi.nlm.nih.gov/pubmed/12392435>.
- Puntes, V.F., Krishnan, K.M. & Alivisatos, P., 2001. Synthesis, self-assembly, and magnetic behavior of a two-dimensional superlattice of single-crystal  $\epsilon$ -Co nanoparticles. *Applied Physics Letters*, 78(15),

- p.2187. Available at: <http://link.aip.org/link/APPLAB/v78/i15/p2187/s1&Agg=doi> [Accessed August 3, 2011].
- Qiang, Y. et al., 2004. Synthesis of Core-Shell Nanoclusters With High Magnetic Moment for Biomedical Applications. *IEEE Transactions on Magnetics*, 40(6), pp.3538–3540. Available at: <http://ieeexplore.ieee.org/lpdocs/epic03/wrapper.htm?arnumber=1353462>.
- Rabenau, A. & Rau, H., 1969. No Title. *Philips Tech Rev*, 30, p.89.
- Rajamathi, M. & Seshadri, R., 2003. Oxide and Chalcogenide Nanoparticles from Hydrothermal/Solvothermal Reactions. *ChemInform*, 34(49), pp.337–345. Available at: <http://doi.wiley.com/10.1002/chin.200349235>.
- Rajasingam, R. et al., 2004. Solubility of carbon dioxide in dimethylsulfoxide and N-methyl-2-pyrrolidone at elevated pressure. *Carbon*, 31, pp.227–234.
- Ramos, J., 2012. Gold Nanoparticle Mediated Photo-Chemotherapy. *Journal of Nanomedicine & Nanotechnology*, 03(08). Available at: <http://www.omiconline.org/2157-7439/2157-7439-3-e125.digital/2157-7439-3-e125.html> [Accessed January 21, 2014].
- Raveendran, P., Fu, J. & Wallen, S.L., 2006. A simple and “green” method for the synthesis of Au, Ag, and Au–Ag alloy nanoparticles. *Green Chemistry*, 8(1), p.34. Available at: <http://xlink.rsc.org/?DOI=b512540e> [Accessed July 7, 2011].
- Raveendran, P., Fu, J. & Wallen, S.L., 2003. Completely “green” synthesis and stabilization of metal nanoparticles. *J. Am. Chem. Soc*, 125, p.13940.
- Raveendran, P., Fu, J. & Wallen, S.L., 2003. Completely “green” synthesis and stabilization of metal nanoparticles. *J. Am. Chem. Soc*, 125(46), p.13940. Available at: <http://www.ncbi.nlm.nih.gov/pubmed/14611213>.
- Raveendran, P., Fu, J. & Wallen, S.L., 2006. No Title. *Green Chemistry*, 8, p.34.
- Reverchon, E. et al., 1998. Supercritical Antisolvent Precipitation of Nanoparticles of Superconductor Precursors. *Ind. Eng. Chem. Res*, 37(9), pp.952–958.
- Robert, V., 2000. Dimethyl Sulfoxide (DMSO) A “New” Clean, Unique Superior Solvent. In *American Chemical Society Annual Meeting*. Washington, D. C.
- Rodríguez-Gattorno, G. et al., 2002. Metallic Nanoparticles from Spontaneous Reduction of Silver(I) in DMSO. Interaction between Nitric Oxide and Silver Nanoparticles. *J. Phys. Chem. B*, 106(10), pp.2482–2487. Available at: <http://pubs.acs.org/doi/abs/10.1021/jp012670c>.
- Salavati-Niasari, M., Fereshteh, Z. & Davar, F., 2009. Synthesis of cobalt nanoparticles from [bis(2-hydroxyacetophenato)cobalt(II)] by thermal decomposition. *Polyhedron*, 28(6), pp.1065–1068. Available at: <http://linkinghub.elsevier.com/retrieve/pii/S0277538709000412> [Accessed August 15, 2012].
- Sandhyarani, N. & Pradeep, T., 2001. Oxidation of alkanethiol monolayers on gold cluster surfaces. *Chemical Physics Letters*, 338, pp.33–36.
- Sarathy, K.V. et al., 1997. Thiol-Derivatized Nanocrystalline Arrays of Gold, Silver, and Platinum. , 36(9), pp.9876–9880.

- Saunders, S.R. & Roberts, C.B., 2011a. Nanoparticle separation and deposition processing using gas expanded liquid technology. *Current Opinion in Chemical Engineering*, 1(2), pp.1–11. Available at: <http://linkinghub.elsevier.com/retrieve/pii/S2211339811000311> [Accessed January 11, 2012].
- Saunders, S.R. & Roberts, C.B., 2009. Size-selective fractionation of nanoparticles at an application scale using CO<sub>2</sub> gas-expanded liquids. *Nanotechnology*, 20(47), p.475605. Available at: <http://www.ncbi.nlm.nih.gov/pubmed/19875872> [Accessed September 1, 2011].
- Saunders, S.R. & Roberts, C.B., 2011b. Tuning the Precipitation and Fractionation of Nanoparticles in Gas-Expanded Liquid Mixtures. *Journal of Phys*, pp.9984–9992.
- Savitzky, A. & Golay, M.J.E., 1964. Smoothing and Differentiation of Data by Simplified Least Squares Procedures. *Analytical Chemistry*, 36, pp.1627–1636.
- Schoepf, U. et al., 1998. Intracellular magnetic labeling of lymphocytes for in vivo trafficking studies. *BioTechniques*, 24(4), pp.642–6, 648–51. Available at: <http://www.ncbi.nlm.nih.gov/pubmed/9564539>.
- Scofield, J.H., 1973. *Lawrence Livermore Laboratory Report No. UCRL-51326*,
- Scurto, A.M., Hutchenson, K. & Subramaniam, B., 2009. Gas-Expanded Liquids : Fundamentals and Applications. *Symposium A Quarterly Journal In Modern Foreign Literatures*, pp.3–37.
- Seehra, M.S. et al., 2012. Core-shell model for the magnetic properties of Pd nanoparticles. *Materials Letters*, 68, pp.347–349. Available at: <http://linkinghub.elsevier.com/retrieve/pii/S0167577X11012614> [Accessed May 25, 2012].
- Shafer-Peltier, K.E. et al., 2003. Toward a glucose biosensor based on surface-enhanced Raman scattering. *Journal of the American Chemical Society*, 125(2), pp.588–93. Available at: <http://www.ncbi.nlm.nih.gov/pubmed/12517176>.
- Shafi, K.V.P.M. et al., 2001. Sonochemical Synthesis of Functionalized Amorphous Iron Oxide Nanoparticles. , (13), pp.5093–5097.
- Shah, P.S. et al., 2002. Size-Selective Dispersion of Dodecanethiol-Coated Nanocrystals in Liquid and Supercritical Ethane by Density Tuning. *J. Phys. Chem. B.*, 106, pp.2545–2551.
- Shi, Z. et al., 2006. Antibacterial and mechanical properties of bone cement impregnated with chitosan nanoparticles. *Biomaterials*, 27, pp.2440–2449.
- Shields, S.P., Richards, V.N. & Buhro, W.E., 2010. Nucleation Control of Size and Dispersity in Aggregative Nanoparticle Growth. A Study of the Coarsening Kinetics of Thiolate-Capped Gold Nanocrystals. *Chemistry of Materials*, 22(10), pp.3212–3225. Available at: <http://pubs.acs.org/doi/abs/10.1021/cm100458b> [Accessed January 10, 2014].
- Sigman, M.B., Saunders, A.E. & Korgel, B.A., 2004. Metal nanocrystal superlattice nucleation and growth. *Langmuir*, 20(3), pp.978–983. Available at: <Go to ISI>://000188660600065.
- Skomski, R. & Coey, J.M.D., 1999. *Permanent Magnetism*, Bristol; Philadelphia: Institute of Physics Publishing.
- Smith, B., 1999. *Infrared Spectral Interpretation: A Systematic Approach*, Boca Raton: CRC Press.

- Steiner, E.C. & Gilbert, J.M., 1965. The acidities of weak acids in Dimethyl Sulfoxide. II. The Hammett Acidity Function. *Journal of the American Chemical Society*, 87(2), pp.382–384.
- Su, Y., OuYang, X. & Tang, J., 2010. Spectra study and size control of cobalt nanoparticles passivated with oleic acid and triphenylphosphine. *Applied Surface Science*, 256(8), pp.2353–2356. Available at: <http://linkinghub.elsevier.com/retrieve/pii/S0169433209015116> [Accessed October 27, 2011].
- Sun, S. & Murray, C.B., 1999. Synthesis of monodisperse cobalt nanocrystals and their assembly into magnetic superlattices (invited). *Journal of Applied Physics*, 85(8), p.4325. Available at: <http://link.aip.org/link/JAPIAU/v85/i8/p4325/s1&Agg=doi> [Accessed September 19, 2013].
- Sweeney, S.F., Woehle, G.H. & Hutchison, J.E., 2006. Rapid purification and size separation of gold nanoparticles via diafiltration. *Journal of the American Chemical Society*, 128(10), pp.3190–7. Available at: <http://www.ncbi.nlm.nih.gov/pubmed/16522099>.
- Takahashi, M. & Suzuki, T., 1979. Temperature Dependence of Magnetic Domain Structures in H.C.P. Cobalt Single Crystals. *Japanese Journal of Applied Physics*, 18(6), pp.1071–1078.
- Tam, J.M. et al., 2010. Controlled Assembly of Biodegradable Imaging and Therapeutic Applications. *ACS Nano*, 4(4).
- Tam, J.M. et al., 2010. Kinetic Assembly of Near-IR-Active Gold Nanoclusters Using Weakly Adsorbing Polymers to Control the Size. *Langmuir*, 26(11), pp.8988–8999. Available at: <http://pubs.acs.org/doi/abs/10.1021/la904793t> [Accessed May 8, 2012].
- Tanase, M. et al., 2007. Structure Optimization of FePt Nanoparticles of Various Sizes for Magnetic Data Storage. *Metallurgical and Materials Transactions A*, 38(4), pp.798–810. Available at: <http://link.springer.com/10.1007/s11661-006-9081-6> [Accessed December 28, 2013].
- Taniguchi, N., 1974. On the basic concept of nanotechnology. In *Proc. Int. Conf. Prod. Eng. Tokyo Part 2*. Tokyo, pp. 18–23.
- Tannenbaum, R., 1997. Polymer Matrix Influence on the Kinetics of Some Fundamental Inorganic Colloidal Reactions. *Langmuir*, 13(19), pp.5056–5060. Available at: <http://pubs.acs.org/doi/abs/10.1021/la9701992>.
- Tannenbaum, R., 1994. Thermal decomposition of cobalt carbonyl viscous media. *Inorganica Chimica Acta*, 227, pp.233–240.
- Thorat, A. a. & Dalvi, S. V., 2012. Liquid antisolvent precipitation and stabilization of nanoparticles of poorly water soluble drugs in aqueous suspensions: Recent developments and future perspective. *Chemical Engineering Journal*, 181-182, pp.1–34. Available at: <http://linkinghub.elsevier.com/retrieve/pii/S1385894711015944> [Accessed July 20, 2012].
- Tong, L. et al., 2009. Gold nanorods as contrast agents for biological imaging: optical properties, surface conjugation and photothermal effects. *Photochemistry and photobiology*, 85(1), pp.21–32. Available at: <http://www.pubmedcentral.nih.gov/articlerender.fcgi?artid=2818790&tool=pmcentrez&rendertype=abstract>.
- Turkevich, J., 1985. Colloidal Gold. Part II. *Gold Bulletin*, 18(4), pp.125–131.

- Underwood, S. & Mulvaney, P., 1994. Effect of the Solution Refractive Index on the Color of Gold Colloids. *Langmuir*, 10(10), pp.3427–3430. Available at: <http://pubs.acs.org/doi/abs/10.1021/la00022a011>.
- Vengsarkar, P.S. & Roberts, C.B., 2013. Effect of Ligand and Solvent Structure on Size-Selective Nanoparticle Dispersibility and Fractionation in Gas-Expanded Liquid (GXL) Systems. *Journal of Physical Chemistry C*, 117, p.14362.
- Vijaykumar, T., Sanketh, R. & Kulkarni, G.U., 2007. Polar-solvent mediated phase-transfer of nanocrystals of metals and semiconductors from an aqueous to an organic phase. *Chemical Physics Letters*, 436(1-3), pp.167–170. Available at: <http://linkinghub.elsevier.com/retrieve/pii/S0009261407000462> [Accessed June 17, 2011].
- Viswanatha, R. & Sarma, D.D., 2007. *Nanomaterials Chemistry: Recent Developments and New Directions* C. N. R. Rao, A. Muller, & A. K. Cheetham, eds., Federal Republic of Germany: Wiley-VCH.
- Vossmeier, T. et al., 1994. CdS Nanoclusters : Synthesis , Characterization , Size Dependent Oscillator Strength , Temperature Shift of the Excitonic Transition Energy , and Reversible Absorbance Shift. , pp.7665–7673.
- Wang, D., Wang, Q. & Wang, T., 2011. Morphology-controllable synthesis of cobalt oxalates and their conversion to mesoporous Co<sub>3</sub>O<sub>4</sub> nanostructures for application in supercapacitors. *Inorganic chemistry*, 50(14), pp.6482–92. Available at: <http://www.ncbi.nlm.nih.gov/pubmed/21671652>.
- Wang, X. et al., 2004. One-Dimensional Arrays of Co<sub>3</sub>O<sub>4</sub> Nanoparticles: Synthesis, Characterization, and Optical and Electrochemical Properties. *The Journal of Physical Chemistry B*, 108(42), pp.16401–16404. Available at: <http://pubs.acs.org/doi/abs/10.1021/jp048016p>.
- Warne, B. et al., 2000. Self assembled nanoparticulate Co:Pt for data storage applications. *IEEE Transactions on Magnetics*, 36(5), pp.3009–3011. Available at: <http://ieeexplore.ieee.org/lpdocs/epic03/wrapper.htm?arnumber=908658>.
- Watzky, M.A. & Finke, R.G., 1997. Transition Metal Nanocluster Formation Kinetic and Mechanistic Studies . A New Mechanism When Hydrogen Is the Reductant : Slow , Continuous Nucleation and Fast Autocatalytic Surface Growth. *Faraday Discussions*, 7863(i), pp.10382–10400.
- Wayland, B.B. & Schramm, R.F., 1969. Cationic and Neutral Chloride Complexes of Palladium(II) with the Nonaqueous Solvent Donors Acetonitrile, Dimethyl Sulfoxide, and a Series of Amides. Mixed Sulfur and Oxygen Coordination Sites in a Dimethyl Sulfoxide Complex. *Inorganic chemistry*, 8(4), p.971.
- Weissleder, R., 2001. A clearer vision for in vivo imaging. *Nature Biotechnology*, 19.
- Wetenschappén, F. & Chemie, D., 2006. *An experimental study on the preparation of gold nanoparticles and their properties*,
- Von White, G. & Kitchens, C.L., 2010. Small-Angle Neutron Scattering of Silver Nanoparticles in Gas-Expanded Hexane. *Society*, 114, pp.16285–16291.
- Wilcoxon, J.P. et al., 1998. Photoluminescence from nanosize gold clusters. *The Journal of Chemical Physics*, 108(21), p.9137. Available at: <http://link.aip.org/link/JCPSA6/v108/i21/p9137/s1&Agg=doi>.

- Wu, J. et al., 2013. A Nanotechnology Enhancement to Moore's Law. *Applied Computational Intelligence and Soft Computing*, 2013, pp.1–13. Available at: <http://www.hindawi.com/journals/acisc/2013/426962/>.
- Wu, N. et al., 2004. Interaction of Fatty Acid Monolayers with Cobalt Nanoparticles. *Nano Letters*, 4(2), pp.383–386. Available at: <http://pubs.acs.org/doi/abs/10.1021/nl035139x>.
- Www.gaylordchemical.com, 2007. *Dimethyl Sulfoxide (DMSO) Solubility Data*, Slidell. Available at: [http://www.gaylordchemical.com/uploads/images/pdfs/literature/102B\\_english.pdf](http://www.gaylordchemical.com/uploads/images/pdfs/literature/102B_english.pdf).
- Xie, J. et al., 2011. Surface-engineered magnetic nanoparticle platforms for cancer imaging and therapy. *Accounts of chemical research*, 44(10), pp.883–92. Available at: <http://www.pubmedcentral.nih.gov/articlerender.fcgi?artid=3166427&tool=pmcentrez&rendertype=abstract>.
- Xie, J., Zheng, Y. & Ying, J.Y., 2009. Protein-directed synthesis of highly fluorescent gold nanoclusters. *Journal of the American Chemical Society*, 131(3), pp.888–9. Available at: <http://www.ncbi.nlm.nih.gov/pubmed/19123810>.
- Yamasaki, N. et al., 1986. No Title. *J Mater. Sci. Lett.*, 5, p.355.
- Yang, H., 2004. Mechanochemical synthesis of cobalt oxide nanoparticles. *Materials Letters*, 58(3-4), pp.387–389. Available at: <http://linkinghub.elsevier.com/retrieve/pii/S0167577X0300507X> [Accessed July 26, 2011].
- Yang, H.T. et al., 2003. Self-assembly and magnetic properties of cobalt nanoparticles. *Applied Physics Letters*, 82(26), p.4729. Available at: <http://link.aip.org/link/APPLAB/v82/i26/p4729/s1&Agg=doi> [Accessed November 2, 2011].
- Yuan, C. et al., 2009. Electrochemically Induced Phase Transformation and Charge-Storage Mechanism of Amorphous CoS<sub>x</sub> Nanoparticles Prepared by Interface-Hydrothermal Method. *Journal of The Electrochemical Society*, 156(3), p.A199. Available at: <http://jes.ecsdl.org/cgi/doi/10.1149/1.3065086> [Accessed April 9, 2013].
- Van der Zee, J., 2002. Heating the patient: a promising approach? *Annals of Oncology*, 13(8), pp.1173–1184. Available at: <http://annonc.oxfordjournals.org/cgi/doi/10.1093/annonc/mdf280> [Accessed January 20, 2014].
- Zhang, H., Liu, Y. & Sun, S., 2010. Synthesis and assembly of magnetic nanoparticles for information and energy storage applications. *Frontiers of Physics in China*, 5(4), pp.347–356. Available at: <http://link.springer.com/10.1007/s11467-010-0104-9> [Accessed December 29, 2013].
- Zhang, J. et al., 2001. A new method to recover the nanoparticles from reverse micelles: recovery of ZnS nanoparticles synthesized in reverse micelles by compressed CO<sub>2</sub>. *Chemical Communications*, (24), pp.2724–2725. Available at: <http://xlink.rsc.org/?DOI=b109802k> [Accessed January 12, 2012].
- Zhang, M. & Singh, R.P., 2004. Mechanical reinforcement of unsaturated polyester by AL<sub>2</sub>O<sub>3</sub> nanoparticles. *Scanning*, 58, pp.408 – 412.

## **Appendix A**

### **Appendix A1 - TEM Imaging Analysis for Co Nanoparticles**

TEM imaging analysis was performed on each of the solutions resulting from the Co nanoparticle synthesis at different  $[\text{Co}^{2+}]:[\text{NaBH}_4]$  ratios. TEM images and the size histograms of each of the solutions are shown in Figure A1.1. It is noted that there is no notable variation in average Co nanoparticle size resulting from these experiments.

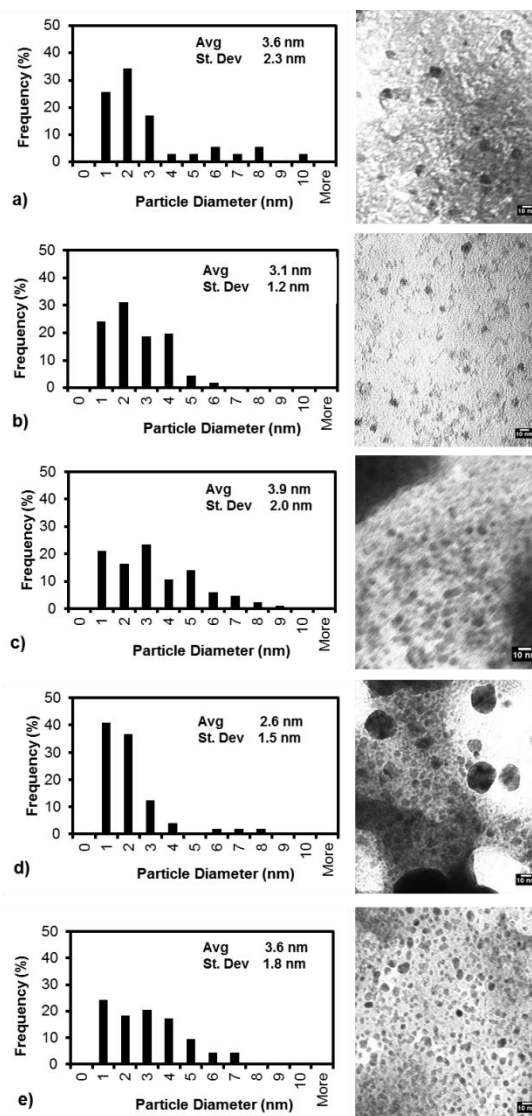


**Figure A1.1** TEM images and corresponding histograms for Co nanoparticles stabilized by the functional solvent, DMSO, where the ratio of [Co<sup>2+</sup>]:[NaBH<sub>4</sub>] is a) 4:1, b) 4:3, c) 4:5, d) 4:6, e) 4:9.



## Appendix A2 - Temperature Programmed Desorption (TPD) Data

This data was obtained from Micromeritics (Norcross, GA), where the desorption of materials present in the Co nanoparticle sample was monitored in the temperature range from 25°C to 1000°C (Figure A1.2) using 0.0050 g of dried Co nanoparticle powder. Figure A1.1 shows the TPD data of the Co nanoparticle powder, where there is a small aberration in the data (pink line) which corresponds to mass = 18 from the beginning of the experiment to approximately 50 minutes. This peak is attributed to the desorption of water from the Co nanoparticle sample and the broadness of the peak is likely due to the removal of water from within the pores of the Co nanoparticle powder. It is important to note that mass = 78 corresponding to the DMSO molecules were not detected using TPD (evidenced by the flat line in Figure A1.1). This is due to the limitations associated with the TPD detector, which is unable to detect the small amount of DMSO present on the surface of the Co nanoparticles. Recall that a monolayer of DMSO was expected to be on the surface of the Co nanoparticles, as determined by FT-IR studies (in Chapter 2).

Sample: JD-CoNP-1  
Operator: LD/DS  
Submitter: Auburn University  
File: C:\2920\DATA\2013\02\FEB\1300489D.SMP

Started: 2/20/2013 3:16:24PM  
Completed: 2/20/2013 5:27:31PM

Sample Mass: 0.0050 g  
Report Time: 3/6/2013 1:19:12PM

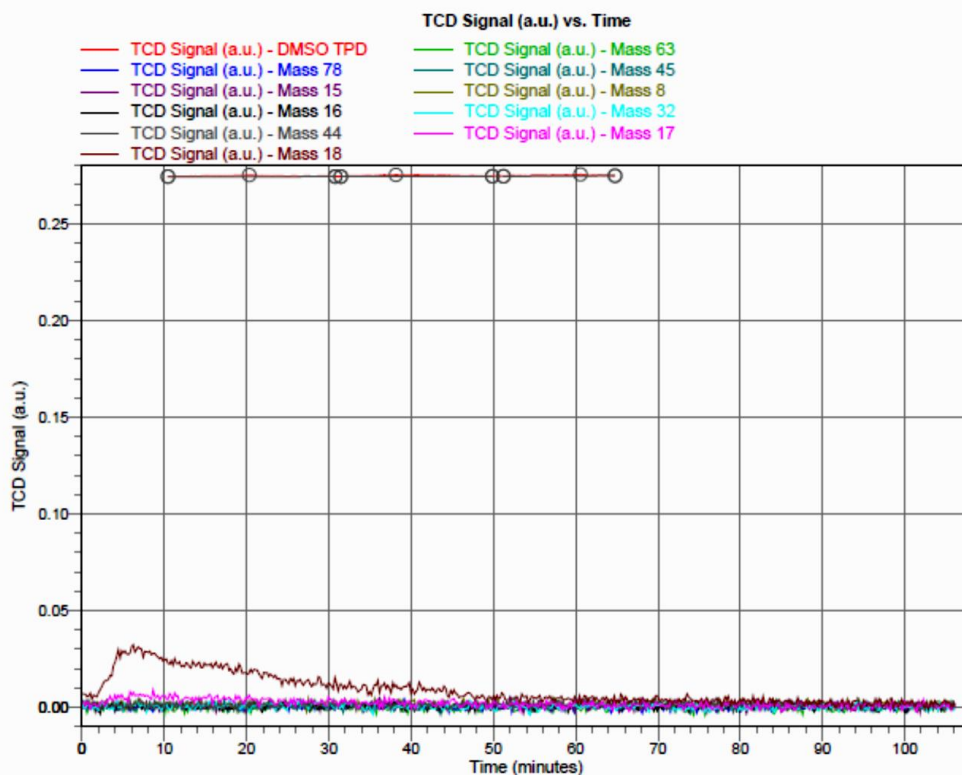


**Figure A2.1** TPD data as obtained from Micromeritics, where the TCD signal is plotted as a function of time.

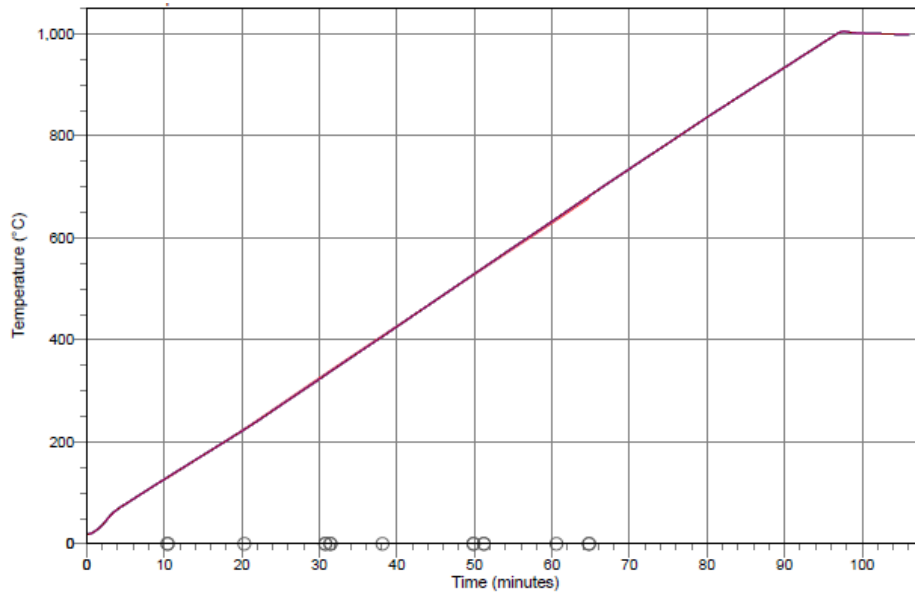


**Figure A2.2** TPD data as obtained from Micromeritics, where the measurements were carried out over the range from 0°C to 1000°C.

## **Appendix B**

### **Appendix B1 - The Effect of Gold Coating on SEM Imaging Analysis**

Each of the Co nanoparticle samples (resulting from room temperature synthesis and after annealing at 200°C, 400°C, 600°C and 800°C for 2 hours) was adhered to a standard SEM pin stub mount using double-carbon tape. Some of the mounted Co nanoparticle samples were coated with a thin layer of gold (~14 nm) using an EMS 550X Sputter Coating Device, where indicated, while other samples were left uncoated. SEM images were obtained for uncoated samples (Figure B1.1) and samples coated with gold (Figure B1.2). Prior to sputter coating with gold, (Figure B1.1) the resolution of the images was poor, and it was difficult to observe the particles' morphology in each sample. However, after sputter coating each sample with gold (Figure B1.2) the resolution of each image improved drastically. This is likely due to the ability of the gold coating to shield the oxidative layer on the Co particles, and allow for more electron scattering to occur from the gold, thereby providing a more detailed SEM image to be obtained.

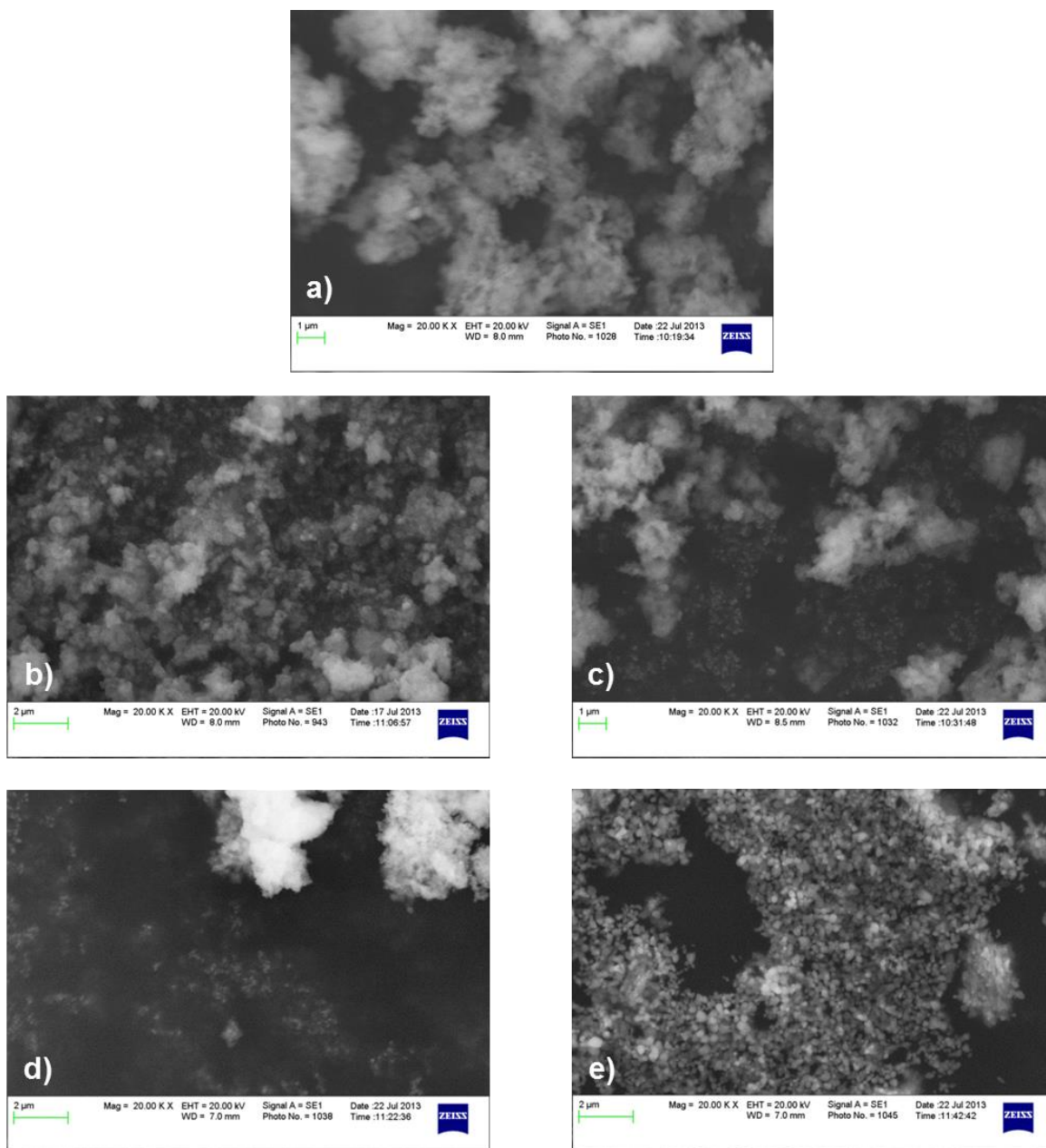


**Figure B1.1** SEM images of Co nanoparticles without gold coating a) prior to annealing, b) annealed at 200°C, c) annealed at 400°C, d) annealed at 600°C, and e) annealed at 800°C. All images were taken at 20,000X magnification.

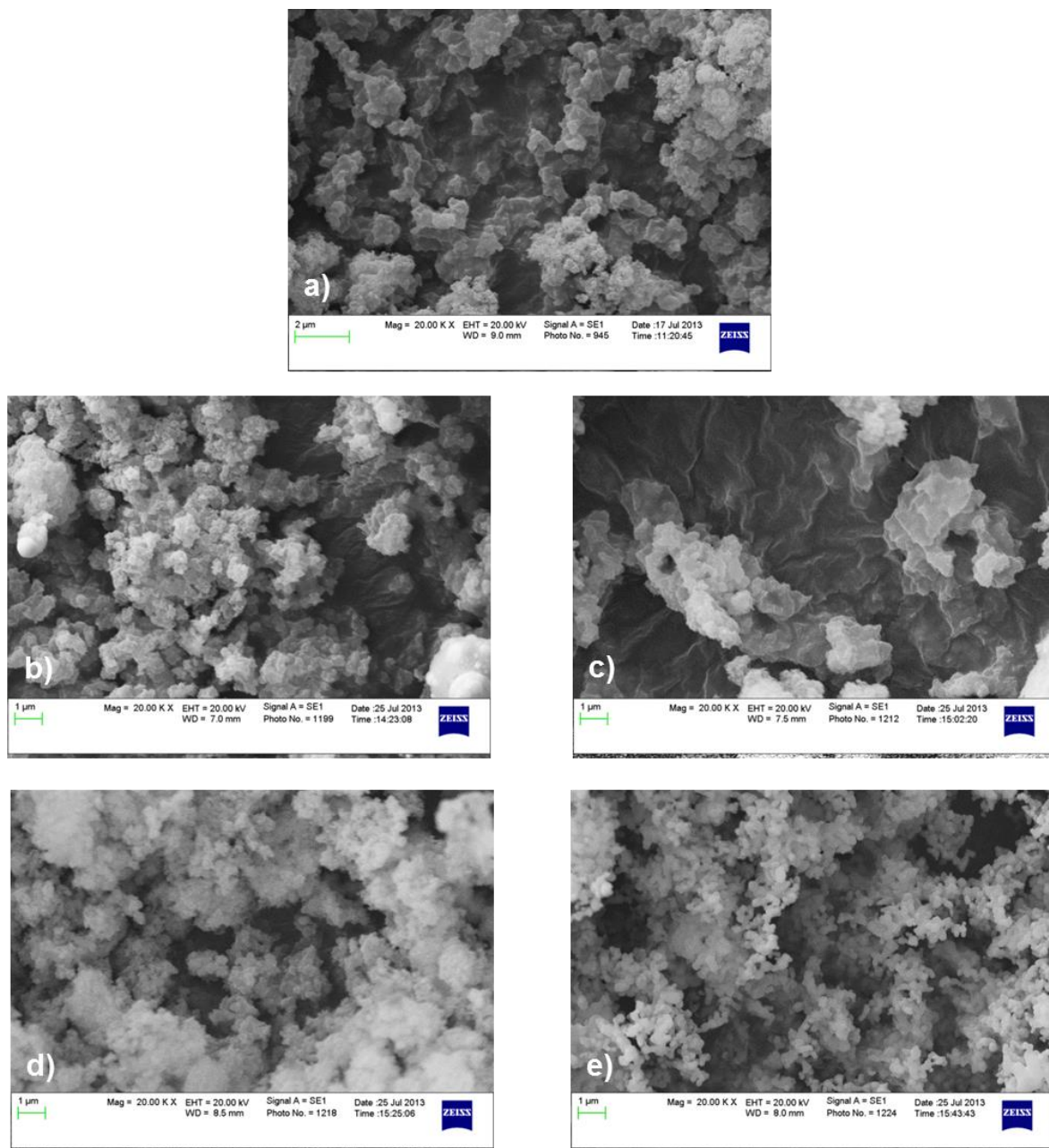


**Figure B1.2** SEM images of Co nanoparticles that have been sputter coated with gold a) prior to annealing, b) annealed at 200°C, c) annealed at 400°C, d) annealed at 600°C, and e) annealed at 800°C. All images were taken at 20,000X magnification.

## Appendix C

### Appendix C1 - Determining the Amount of Reagents Necessary to Produce Au Nanoparticles

A series of experiments were performed in order to determine the amount of reducing agent which needed to be added to the  $\text{Au}^{3+}$  salt solution in order to achieve complete  $\text{Au}^{3+}$  reduction and therefore produce Au nanoparticles. ). For example, to achieve a ratio of 4:1 of  $[\text{Au}^{3+}]:[\text{NaBH}_4]$ , 500 mL of  $\text{Au}^{3+}$  salt was combined with 125 mL  $\text{NaBH}_4$  in 50 mL of DMSO. It is noted that the amount of  $\text{Au}^{3+}$  salt added to each of the experiments remained unchanged (500 mL). After stirring for 24 hours, the reaction was removed from the stir plate, and an aliquot of the solution was transferred to a cuvette to be examined using UV-vis spectroscopy. The results of the UV-vis analysis of these experiments are shown in Figure C1.1. The disappearance of the  $\text{Au}^{3+}$  salt absorbance band at 330 nm and the appearance of the strong band centered around 540 nm indicates the formation of Au nanoparticles. TEM imaging analysis was also performed on the solutions, and the results are shown in Figure C1.2. Note that there is no significant difference in average size for any of the various reagent ratios studied.

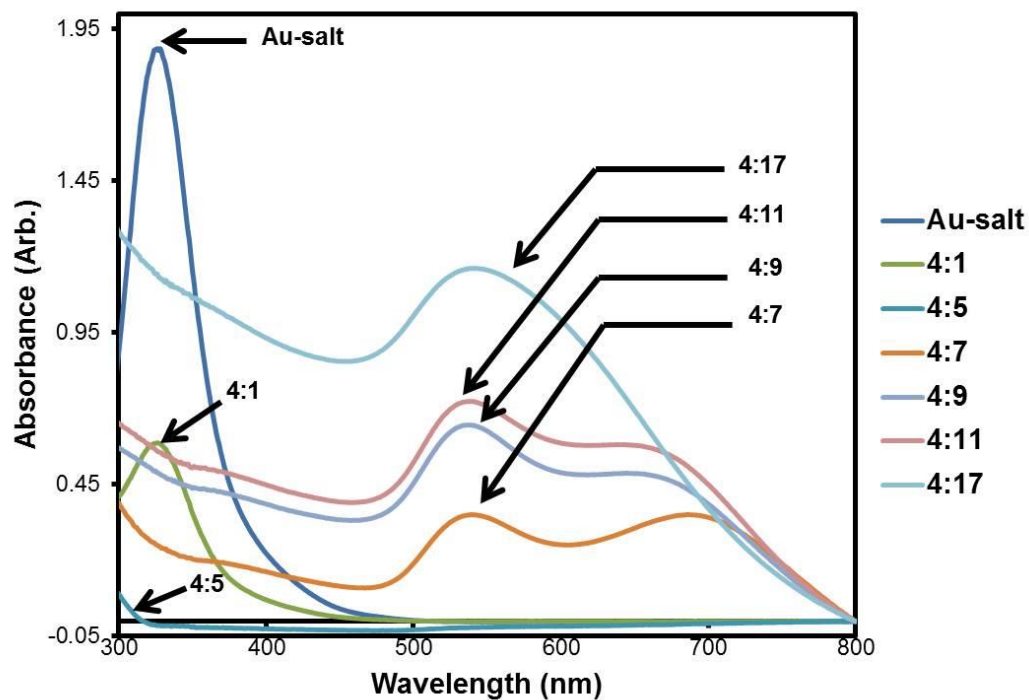


**Figure C1.1** UV-vis absorption spectra of the Au nanoparticle synthesis in DMSO using different ratios of salt to reducing agent: 4:1, 4:5, 4:7, 4:9, 4:11, 4:17. (Experiments were also performed at 4:3, 4:13, and 4:15 which are not shown in this figure for clarity, but fall consistently within these trends.)



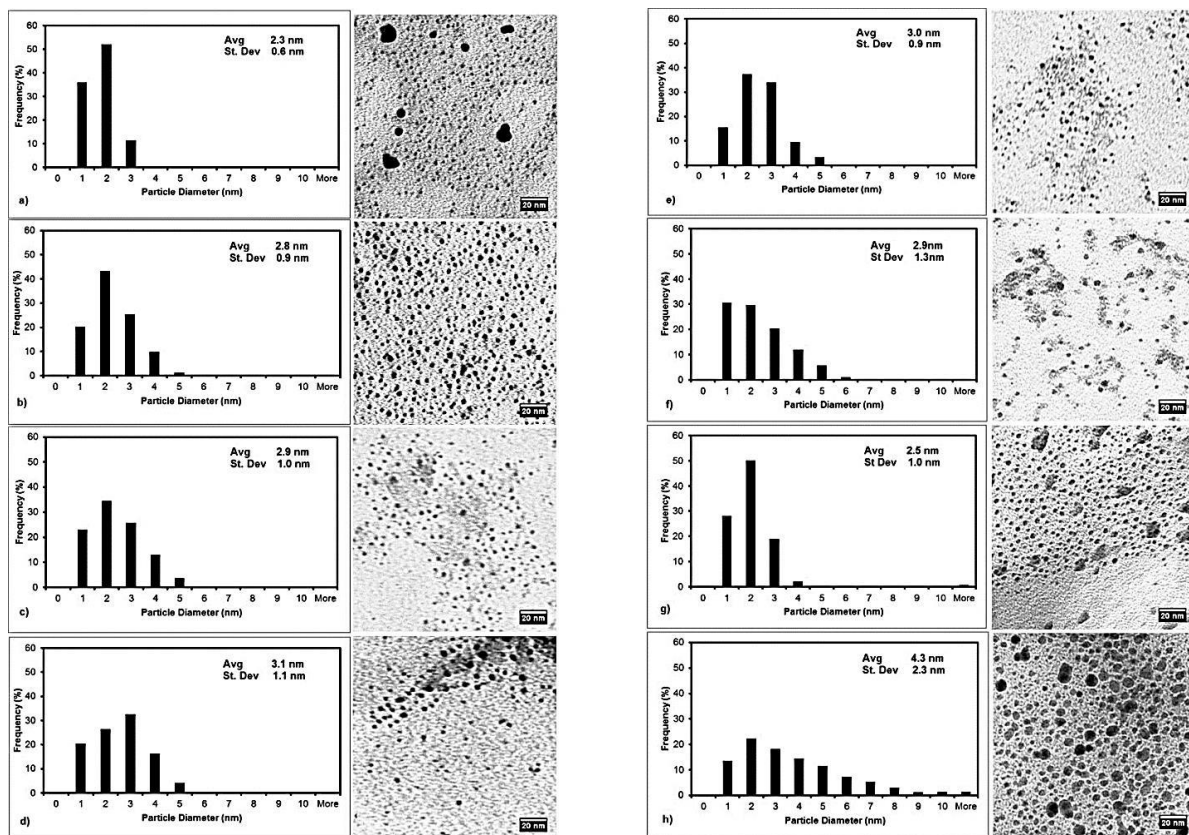


**Figure C2.2** TEM images and histograms of the Au nanoparticles synthesized in DMSO using different ratios of salt to reducing agent: a) 4:1, b) 4:3, c) 4:7, d) 4:9, e) 4:11, f) 4:13, g) 4:15, h) 4:17.

## **Appendix C2 - High Temperature Synthesis of Au Nanoparticles**

Au nanoparticles were synthesized in DMSO solvent at 150°C in order to determine if the synthesis temperature had any effect on the Au nanoparticle size (similar to the high temperature experiments performed in Chapter 3 where it was determined that the high synthesis temperature of Co nanoparticles in DMSO produced particles of larger sizes). The results for these experiments are shown in the figures below. Figure C2.1 shows the TEM imaging results from the synthesis of Au nanoparticles at 150°C where oleic acid is used as the ligand. Figure C2.2 shows the TEM imaging results from the synthesis of Au nanoparticles at 150°C where stearic acid is the solvent. The oleic acid-stabilized and the stearic-acid stabilized particles are roughly 100 nm in size. Due to the irregular particle morphologies observed in the images, it can be inferred that the Au nanoparticles have clustered to form these larger Au structures (similar to the results described in Chapter 3 for Co nanoparticle clustering at high synthesis conditions). However, it is important to point out that larger structures were also visible in the solution, which could be observed using the naked eye. It is also noted that the results for the synthesis of Au nanoparticles in DMSO at 150°C are not shown because particles on the nano-scale were not found in this particular solution of Au-DMSO using TEM imaging analysis. In each of these images, it can be inferred that increasing the synthesis temperature induces an increase in particle size.

These findings also reveal more information about the surface chemistries of the Co nanoparticles (Chapter 3) and the Au nanoparticles (Chapter 5): Chapter 2 indicated that Co nanoparticle clusters (~20 nm) could be formed under high synthesis conditions. The study with high-temperature synthesis of Au nanoparticles in this section showed

that Au nanoparticles could be clustered, but into much larger clusters than the Co nanoparticles. This is likely due to the fact that the interaction between the DMSO molecules and the Co nanoparticles is much ‘stronger’ than the interaction between the DMSO/fatty acid ligands and Au nanoparticles. This difference may be attributed to the variation between the surface of Co (an inherently oxidic metal and the surface of Au (a noble metal). In the Co nanoparticle high-temperature synthesis experiments, it was postulated that the particles clustered because the increased synthesis temperature weakened the interaction occurring between the DMSO and Co particles, thereby allowing the Co nanoparticles (~4 nm) to cluster into the ~20 nm clusters as a function of temperature. Furthermore, the Co nanoparticles were found to be ‘protected’ by an oxidic layer that was formed due to the interaction of the oxygen component of DMSO with the surface of the Co. The general clustering process is the same with Au nanoparticle clustering at high temperatures in DMSO, but there is no oxide layer on the Au nanoparticle surface (Au does not have a tendency to be oxidized) and the DMSO molecules adsorb to the Au surface with a relatively ‘weak’ interaction with DMSO (where Au nanoparticle stabilization occurs presumably by an equal contribution from the S- and O- components of the DMSO sulfidic bond). This interaction allows very large Au structures to form within the solution (as was visible with the naked eye). These results ultimately demonstrate that increasing the reaction temperature during synthesis using DMSO as a solvent may be a viable method to increase the overall cluster size of other metallic nanoparticles.

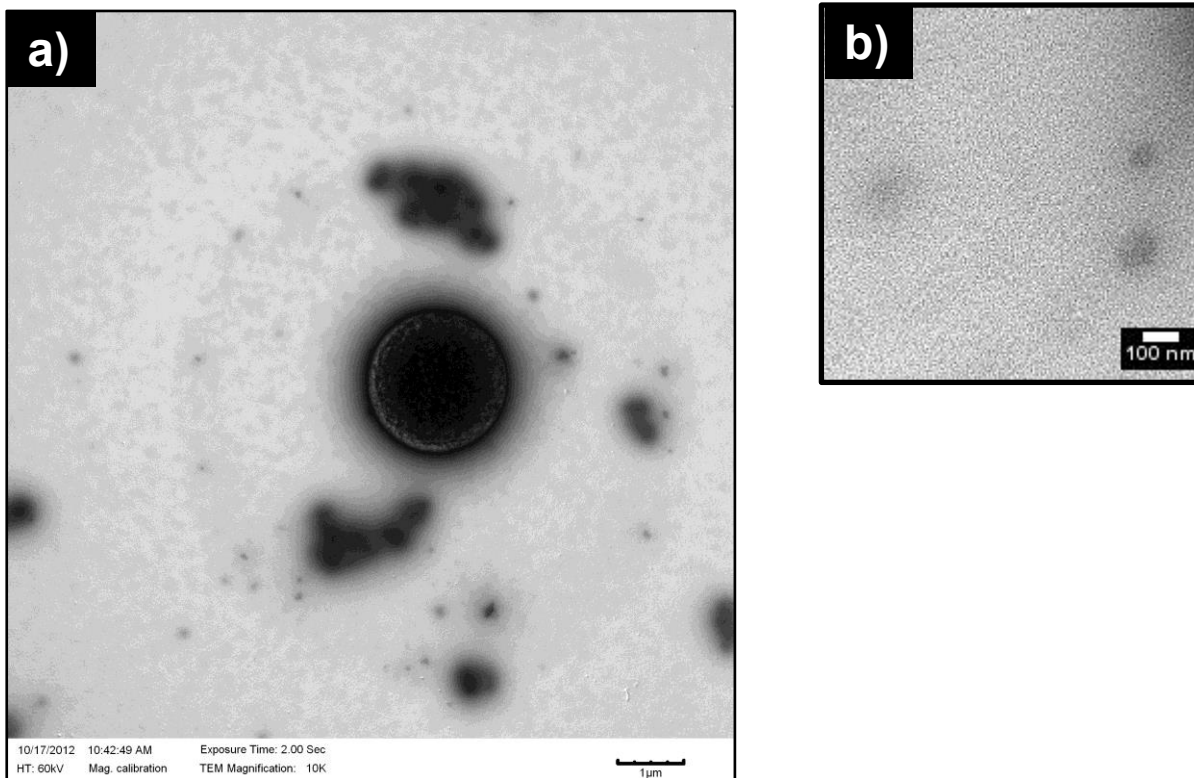


**Figure C2.1** TEM image of Au nanoparticles that were synthesized at 150°C using DMSO as the solvent and oleic acid as the ligand where a) is an image taken at 10,000 times magnification and b) is an image that has been zoomed in on a particular region of the image.

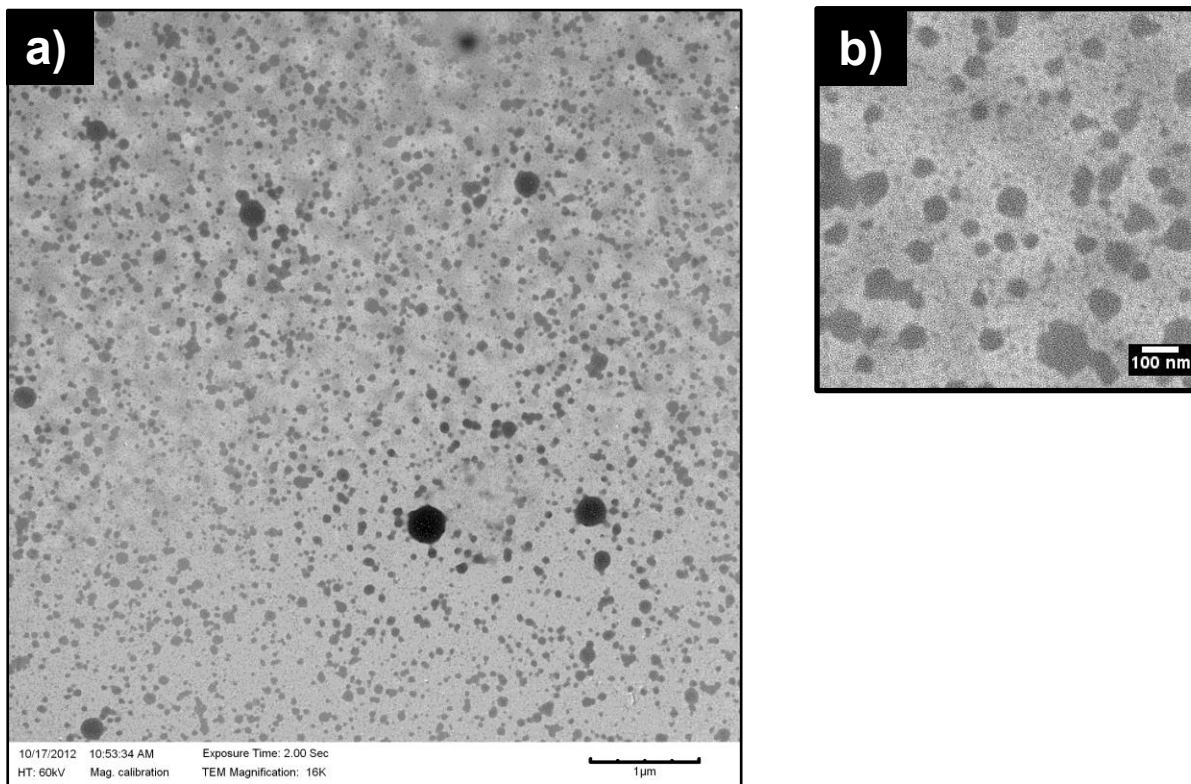


**Figure C2.2** TEM image of Au nanoparticles that were synthesized at 150°C using DMSO as the solvent and stearic acid as the ligand, where a) is an image taken at 16,000 times magnification and b) is an image that has been zoomed in on a particular region of the image.

## Appendix D

### Patents

1. Jennifer N. Duggan, Anurag Chaturvedi, Takao Suzuki, and Christopher B. Roberts, "Metal Nanoparticles with Novel Magnetic Properties," *Provisional Status*, (2014).

### List of Publications

1. Jennifer N. Duggan, Anurag Chaturvedi, Takao Suzuki, and Christopher B. Roberts, "Controlling the Crystallinity and Magnetism of Cobalt Nanoparticles via Thermal Oxidative Treatment," *Completed – To Be Submitted*, (2014).
2. Jennifer N. Duggan and Christopher B. Roberts, "Aggregation and Precipitation of Gold Nanoparticle Clusters in CO<sub>2</sub>-Gas Expanded Liquid DMSO Solvent Systems," *Completed – To Be Submitted*, (2014).
3. Jennifer N. Duggan and Christopher B. Roberts, "Clustering and Solvation of Cobalt Nanostructures in Dimethyl Sulfoxide," *Completed – To be Submitted*, (2014).
4. Jennifer N. Duggan, Michael J. Bozack, and Christopher B. Roberts, "The Synthesis and Arrested Oxidation of Cobalt Nanoparticles using DMSO as a Functional Solvent," *Journal of Nanoparticle Research*, (2013) 15: 2089.
5. Juncheng Liu, Jennifer N. Duggan, Joshua Morgan, and Christopher B. Roberts, "Seed-Mediated Growth and Manipulation of Au Nanorods via Size-Controlled Synthesis of Au Seeds," *Journal of Nanoparticle Research*, (2012) 12: 1289.
6. Jennifer N. Boice, Pranav S. Vengsarkar, and Christopher B. Roberts, "Nanoparticle Dispersibility in a DMSO/CO<sub>2</sub> – Gas Expanded Liquid System," 10<sup>th</sup> *International Symposium on Supercritical Fluids, Conference Proceeding*, (2012).
7. Pranav S. Vengsarkar, Jennifer N. Boice, and Christopher B. Roberts, "Tunable Steric Stabilization Effects on Size-Selective Nanoparticle Dispersability in Gas

8. Expanded Liquid Systems,” 10<sup>th</sup> *International Symposium on Supercritical Fluids, Conference Proceeding*, (2012).

### **List of Presentations**

1. “Magnetic Properties of Co<sub>3</sub>O<sub>4</sub> Nanoparticles Fabricated by Chemical Synthesis using Molecular Dimethyl Sulfoxide,” Anurag Chaturvedi, Jennifer N. Duggan, Christopher B. Roberts, and Takao Suzuki, International Magnetics Conference, Oral Presentation, Dresden, Germany, To be presented in May 2014.
2. “Controlling the Crystallinity, Morphology, and Magnetic Properties of DMSO-Stabilized Cobalt Nanoparticles Using Progressive Thermal Treatment Methods,” Jennifer N. Duggan and Christopher B. Roberts, 247<sup>th</sup> American Chemical Society National Meeting, Invited Oral Presentation, Dallas, TX, United States, To be presented in March 2014, E.V. Murphree Award in Industrial and Engineering Chemistry 107.
3. “A Straightforward Technique to Control the Oxidation of Amorphous Cobalt Nanoparticles during Synthesis using DMSO,” Jennifer N. Duggan, Anurag Chaturvedi, Takao Suzuki, and Christopher B. Roberts, 2013 American Institute of Chemical Engineers Annual Meeting, Oral Presentation, San Francisco, CA, United States, November 2013, 503g.
4. “Synthesis and Characterization of Metallic and Magnetic Nanoparticles in a Multi-Functional Solvent System,” Jennifer N. Duggan and Christopher B. Roberts, 246<sup>th</sup> American Chemical Society National Meeting, Oral Presentation, Indianapolis, IN, United States, September 2013, COLL 183.
5. “Tunable Assembly of Metallic and Magnetic Nanoparticle Clusters in DMSO Solvent Systems,” Jennifer N. Duggan, Pranav S. Vengsarkar, Christopher B. Roberts, 2012 American Institute of Chemical Engineers Annual Meeting, Oral Presentation, Pittsburgh, PA, United States, October 2012, 705a.
6. “Manipulating Size-Selective Dispersibility of Gold Nanoparticles in Gas Expanded Liquid Systems using Ligand/Solvent Steric Effects,” Pranav S. Vengsarkar, Jennifer N. Duggan, Christopher B. Roberts, 2012 American Institute of Chemical Engineers Annual Meeting, Oral Presentation, Pittsburgh, PA, United States, October 2012, 158b.

7. "Exploring the Dispersibility of Gold Nanoparticles in DMSO using Gas-Expanded Liquid Systems," Jennifer N. Duggan, Pranav S. Vengsarkar, Christopher B. Roberts, American Institute of Chemical Engineers Annual Meeting, Oral Presentation, Pittsburgh, PA, United States, October 2012, 393w.
8. "Tunable Steric Stabilization Effects on Iron Oxide Nanoparticle Dispersibility in Gas Expanded Liquid Systems," Pranav S. Vengsarkar, Jennifer N. Duggan, Christopher B. Roberts, 2012 American Institute of Chemical Engineers Annual Meeting, Oral Presentation, Pittsburgh, PA, United States, October 2012, 393v.
9. "Nanoparticle Dispersibility in a DMSO/CO<sub>2</sub> –Gas Expanded Liquid System," Jennifer N. Boice, Pranav S. Vengsarkar, Christopher B. Roberts, 10th International Symposium on Supercritical Fluids, Poster Presentation, San Francisco, CA, United States, May 2012.
10. "Tunable Steric Stabilization Effects on Size-Selective Nanoparticle Dispersability in Gas Expanded Liquid Systems," Pranav S. Vengsarkar, Jennifer N. Boice, Christopher B. Roberts, 10th International Symposium on Supercritical Fluids, Poster Presentation, San Francisco, CA, United States, May 2012.
11. "A Simple and Sustainable method to synthesize magnetic nanoparticles using a functional solvent," Jennifer N. Boice, Juncheng Liu, Christopher B. Roberts, 2011 American Institute of Chemical Engineers Annual Meeting, Oral Presentation, Minneapolis, MN, United States, October 2011, 398f.
12. "Green synthesis of magnetic nanoparticles using a "functional solvent" for use as contrasting agents in MRI," Jennifer N. Boice, Juncheng Liu, Christopher B. Roberts, 15th Annual GC&E Meeting, Poster Presentation, Washington, D.C., United States, June 2011, GCE284.
13. "Green synthesis of cobalt nanoparticles to be used as contrast agents for MRI," Jennifer N. Boice, Juncheng Liu, Christopher B. Roberts, Auburn University Graduate Research Symposium, Oral Presentation, Auburn, AL, March 2011.
14. "Size-Selective Processing of Metal Nanoparticles Using CO<sub>2</sub>-Expanded Liquids," Jennifer N. Boice, Steven R. Saunders, Auburn University Graduate Research Symposium, Oral Presentation, Auburn, AL, February 2010.